Otto-von-Guericke-Universität Magdeburg

Fakultät für Informatik
Institut für Simulation und Graphik

Visual Analysis, Clustering, and Classification of Contrast-Enhanced Tumor Perfusion MRI Data

Dissertation

zur Erlangung des akademischen Grades
Doktoringenieurin (Dr.-Ing.)

angenommen durch die Fakultät für Informatik
der Otto-von-Guericke-Universität Magdeburg

von Dipl.-Ing. Sylvia Glaßer
geb. am 26. Mai 1984 in Jena

Gutachterinnen / Gutachter
Prof. Dr. Bernhard Preim
Prof. Dr. Heidrun Schumann
Prof. Dr. Silvia Miksch

Magdeburg, den 04. Juli 2014

Abstract

This thesis presents the visual analysis, clustering, and classification of contrast-enhanced tumor perfusion magnetic resonance imaging (MRI). Perfusion MRI data plays an important role for diagnosis of cancer. Cancer is a malignant tumor which can grow uncontrollably and threaten life when therapy is not effective or started too late. For the evaluation of contrast-enhanced perfusion MRI, a contrast agent is intravenously injected. It works as tracer of perfusion and tumorous tissue can be identified due to its increased microvasculature. This thesis focuses on two major clinical research areas. The first one is the evaluation of dynamic contrast enhanced MRI (DCE-MRI) data for improved breast cancer diagnosis. The second one is the evaluation of longitudinal brain tumor studies, covered by dynamic susceptibility contrast MRI (DCS-MRI) scans. The specialty of this thesis is the underlying set of medical image data. For both application areas, clinical image data was available and the developed methods were carefully adapted to the clinical scope. Two frameworks were presented that allow for visual analysis and exploration of the data sets.

As a special property of the available databases, a report for each breast tumor data set was available. Thus, an automatic classification could be carried out. Therefore, this thesis presents clustering techniques for breast DCE-MRI data including an automatic classification approach based on this clustering results. As a result, the presented methods identified important features associated with tumor heterogeneity that can be employed in clinical practice and research. In addition, the brain tumor database contains rare cases of patients where a transformation from low grade gliomas into high grade gliomas was monitored with DSC-MRI within a longitudinal study. The thesis contributes a carefully adapted framework for this database. The framework allows for visual analysis of the tumor progression. Furthermore, it contains a pre-processing pipeline which maintains the analysis of different longitudinal DSC-MRI scans, acquired at different points in time with different MRI scanners and scanning protocols. In conclusion, although many properties of cancer are known, a fully automatic tumor classification for the specific tumor types based on perfusion MRI does not exist in literature. This thesis will not close this gap but make it smaller by providing heterogeneity-based features that were indicative for tumor malignancy as well as sophisticated visual analysis techniques, and clustering approaches for an improved cancer evaluation and a possible detection of new discriminative features.

Zusammenfassung

Die vorliegende Dissertation präsentiert Techniken zur visuellen Analyse, sowie Clusteringkonzepte, und automatische Klassifizierungansätze zur verbesserten Auswertung von Tumorherden in Kontrastmittel-verstärkten magnetresonanztomographischen (MRT) Perfusionsdaten. Diese Daten sind ein wichtiger Bestandteil für die Diagnose von Krebs. Krebs ist ein bösartiger Tumor, der unkontrolliert wuchern kann und zum Tode führt, sofern keine effektive Therapie möglich ist oder eine Therapie zu spät begonnen wurde. Bösartige Tumore zeichnen sich durch erhöhte Mikrovaskulatur aus und können daher mit Kontrastmittel detektiert werden. Die Dissertation behandelt zwei Hauptanwendungsgebiete der klinischen Forschung. Das erste Anwendungsgebiet ist die Evaluation von *dynamic contrast-enhanced* (DCE) MRT Daten für eine verbesserte Brustkrebsdiagnose. Das zweite Anwendungsgebiet ist die Evaluation von longitudinalen Kopftumorstudien, akquiriert mit *dynamic susceptibility contrast* (DSC) MRT Daten. Für beide Anwendungsgebiete gab es eine besondere Sammlung von Datensätzen, die eine zielgerichtete Entwicklung von Methoden ermöglichten um klinische Forschungsfragen zu beantworten. Für die visuelle Analyse und Exploration wurden zwei verschiedene Software-Prototypen im Rahmen dieser Arbeit entwickelt.

Die Brustkrebstumordatenbank ist für die Computer-gestützte Auswertung besonders wertvoll, da für jeden Tumor ein Befund zur Verfügung gestellt wurde. Somit konnten zusätzlich Clusteringtechniken weiterentwickelt und angepasst werden, die die Ausgangslage für die Adaption von komplexen Klassifizierungansätzen bildeten. Ein Ergebnis dieser Arbeit ist die Identifikation von wichtigen Tumorattributen (welche eine automatische Abschätzung der Tumorheterogenität erlauben), die in der klinischen Forschung und Praxis Anwendung finden können. Weiterhin enthält die Kopftumordatenbank eine Sammlung von seltenen Fällen, in denen Patienten mit einem niedriggradigem Gliom regelmäßig mittel MRT-gestützter Perfusionsbildgebung über einige Jahre kontrolliert wurden. Alle niedriggradigen Gliome entwickelten sich zu einem höhergradigem Gliom während dieses Zeitraums. In dieser Arbeit wird ein Framework vorgestellt, welches die visuelle Analyse der Tumorprogression (und somit der Gliomtransformation) unterstützt. Außerdem wurde eine Vorverarbeitungskette entwickelt, die es ermöglicht verschiedene Perfusionsdaten einer Longitudinalstudie miteinander zu vergleichen. Dabei müssen verschiedene MRT-Scanner und Scanningprotokollparameter berücksichtigt werden. Obwohl viele Eigenschaften von bösartigen Tumoren bekannt sind, existiert keine exakte automatische Klassifikation für die präsentierten Spezialfälle in der Literatur. Die vorliegende Dissertation leistet einen wichtigen Beitrag für die verbesserte automatische Klassifikation, in dem Heterogenitätsbasierte Eigenschaften identifiziert werden, welche mit der Tumorbösartigkeit korrelieren. Weiterhin ermöglicht die visuelle Analyse in Kombination mit Clustering eine verbesserte Auswertung der Krebsdaten.

Ehrenerklärung

Ich versichere hiermit, dass ich die vorliegende Arbeit ohne unzulässige Hilfe Dritter und ohne Benutzung anderer als der angegebenen Hilfsmittel angefertigt habe; verwendete fremde und eigene Quellen sind als solche kenntlich gemacht. Insbesondere habe ich nicht die Hilfe eines kommerziellen Promotionsberaters in Anspruch genommen. Dritte haben von mir weder unmittelbar noch mittelbar geldwerte Leistungen für Arbeiten erhalten, die im Zusammenhang mit dem Inhalt der vorgelegten Dissertation stehen. Ich habe insbesondere nicht wissentlich:

- Ergebnisse erfunden oder widersprüchliche Ergebnisse verschwiegen,
- statistische Verfahren absichtlich missbraucht, um Daten in ungerechtfertigter Weise zu interpretieren,
- fremde Ergebnisse oder Veröffentlichungen plagiiert,
- fremde Forschungsergebnisse verzerrt wiedergegeben.

Mir ist bekannt, dass Verstöße gegen das Urheberrecht Unterlassungs- und Schadensersatzansprüche des Urhebers sowie eine strafrechtliche Ahndung durch die Strafverfolgungsbehörden begründen kann. Die Arbeit wurde bisher weder im Inland noch im Ausland in gleicher oder ähnlicher Form als Dissertation eingereicht und ist als Ganzes auch noch nicht veröffentlicht.

Magdeburg, 18.12.2013

Sylvia Glaßer

Danksagung

Mein großer Dank gilt meinem Doktorvater Bernhard Preim, der mich schon während meines Studiums für die medizinische Visualisierung begeistert hat. Während der Promotionszeit stand er mir stets mit Anregungen, Hilfestellungen, Kritik und vielen Tipps zur Seite. Dabei hat mich nicht nur seine fachliche, sondern auch menschliche Kompetenz stark beeindruckt. Er hatte stets eine offene Tür und ein offenes Ohr für *alle* Probleme rund um die Dissertation. Einen besonderen Dank möchte ich Uta Preim aussprechen. Sie hat mir nicht nur die klinischen Brustkrebsperfusionsdaten zur Verfügung gestellt, sondern zu Beginn meiner Promotionszeit auch Einblicke in den klinischen Alltag ermöglicht. Weiterhin hat sie mich stets an ihrem Fachwissen teilhaben lassen und alle im Rahmen der Promotion entwickelten Techniken ausführlich evaluiert. Weiterhin bedanken möchte ich mich bei Helwig Hauser. Der Aufenthalt in Bergen war nicht nur fachlich eine große Bereicherung. Es war eine sehr schöne Zeit, was neben der hervorragenden Betreuung auch an der netten Arbeitsgruppe lag. Ein großes Dankeschön geht auch an Atle Bjørnerud vom Rikshospitalet-Radiumhospitalet Medical Centre in Oslo, Norwegen, für die Bereitstellung der Kopftumorperfusionsdaten und das detaillierte fachliche Feedback. Mein Forschungsaufenthalt wurde durch das norwegische Austauschprogramm Yggdrasil ermöglicht. Ein besonderer Dank gilt Myra Spiliopoulou und Uli Niemann. Aus der schönen Zusammenarbeit mit Euch sind gemeinsame Publikationen entstanden. Meine Promotion wurde durch das DFG Schwerpunktprogramm Scalable Visual Analytics ermöglicht. Bedanken möchte ich mich daher auch bei Sebastian Schäfer aus der AG Bildverarbeitung. Gemeinsam ist die visuelle Analyse von Brusttumorperfusionsdaten im Rahmen unser Projekts Efficient Visual Analysis of Dynamic Medical Image Data entstanden. Weiterhin möchte ich mich insgesamt bei allen Kollegen des ISG für die schöne Arbeitsatmosphäre bedanken. Insbesondere meinen Kollegen der AG Visualisierung, die stets für fachliche Diskussionen oder motivierende Kaffeepausen zur Verfügung standen. Ein großer Dank gilt auch dem Fraunhofer MEVIS für die Bereitstellung von MeVisLab. Hier ist besonders die Auswertung co-registrierter T_1 und T_2 gewichteter Brustkrebsdaten in Zusammenarbeit mit Tobias Böhler ewähnenswert. Weiterhin bedanken möchte ich bei Kathrin Scheil und Sophie Roscher die mit großem Engagement an der Umsetzung des Karteikartenbrowsers und des spektralen Clusterings mitgewirkt haben. An dieser Stelle möchte ich noch meinen hervorragenden Informatiklehrer Herr Thiele nennen. Er hat in seinem Leistungskurs meine Liebe zur Informatik geweckt: vielen lieben Dank! Für die schönen gemeinsamen Projekte geht ein besonders großer Dank an Kai sowie an Bettina und Peter für die moralische Unterstützung.

Zum Schluss möchte ich mich bei den wichtigsten Menschen in meinem Leben bedanken. Mein großer Dank gilt meiner Familie, die mich mein Leben lang unterstützt hat und mir den Weg zu dieser Promotionsschrift geebnet hat. Mein Sohn Oliver, ich danke dir für die Freude, die du mir jeden Tag schenkst.

Contents

1. Introduction

1 Introduction

In these early years of the 21^{st} century, the broad group of cancer-related diseases often leading to cancer-related deaths is a major challenge for clinicians and biomedical researchers. Cancer is a malignant tumor which can grow uncontrollably and threaten life when therapy is not effective or started too late. With the development in the area of medical imaging, detection of cancer has been improved and diagnoses as well as therapies benefit from the newly available information. However, a manifold of challenges still remains when interpreting the medical image data. An important clinical research area is the evaluation of perfusion magnetic resonance imaging (MRI). A contrast agent is injected that works as tracer of perfusion. Even early stages of cancer develop an increased demand for oxygen and nutrients causing angiogenesis, the growing and sprouting of new or existing vessels. Angiogenesis is the key for perfusion imaging, as it causes increased perfusion in tumorous tissue. Two variants are exploited for perfusion MRI acquisition: the T_2 effect, covered with a dynamic susceptibility contrast MRI (DCS-MRI) scan, and the T_1 effect, covered with a dynamic contrast enhanced MRI (DCE-MRI) scan. This thesis focuses on the improved evaluation of breast cancer based on DCE-MRI data, and longitudinal brain tumors monitored with DSC-MRI. The diagnosis based on time-varying 4D MRI perfusion data benefits from dedicated support by computer-aided systems. Although many cancer properties are known, a fully automatic tumor classification for the mentioned specific tumor types does not exist in literature. This is why the thesis will not close the gap but make it smaller. A great variety still exists among these diseases, and the application scenario is narrowed down to two important clinical research areas:

- Small breast lesions, only detectable in perfusion MRI and not conventional X-ray mammography.
- Low grade gliomas of the brain which in special cases are subject to lifelong monitoring to detect a transformation into a high grade glioma.

Regarding breast cancer, two major aspects are analyzed in more detail. First, the manual and error-prone placement of regions of interest by an expert could mislead the tumor classification as well as further diagnosis like core needle biopsy. Second, the high sensitivity of DCE-MRI is the main reason for employing it in breast cancer detection, but its low specificity (when compared to conventional X-ray mammography) demands for computer-aided improvement. For gliomas of the brain, many studies in the literature reported a correlation between tumor progression, surveillance rate, and tumor grade with a specific perfusion parameter - cerebral blood volume - that can only be extracted from perfusion DSC-MRI scans. However, the analysis of longitudinal scans involves many preprocessing steps and challenges when comparing different scans, acquired at different points in time, different MRI scanners, and even different scanning protocols.

The contribution of this thesis is the improvement of these aspects via visual analysis-based exploration and visualization, clustering methods to extract a tumor's most malignant part, and classification analyses to extract a feature set that is most indicative for tumor malignancy regarding the heterogeneity of contrast enhancement kinetics. In particular, the combination of these techniques tailored to tumor perfusion data sets is based on two very specific databases. This is in contrast with many computer science-motivated approaches where only a small number of cases is available for initial tests or exploration. The breast tumor database is a clinical study comprising small suspicious breast tumors detected in perfusion MRI where a ground truth was discovered via histopathologic reports or follow-up studies. The tumors could not be detected in X-ray mammography and thus represent a very special and important collection of tumors. Likewise, the longitudinal brain tumor perfusion database is important for clinical research. In clinical practice, these data sets are not evaluated with visual analytic methods. However, they bear great potential for such an evaluation, which will be presented later on. In summary, the amount of data and the clinical background information allow for a target-oriented combination of computer science algorithms for the clinical research and practice.

This thesis was created within the priority program “Scalable Visual Analytics” (DFG SPP 1335) of the German research council. The goal of the project “Efficient Visual Analysis of Dynamic Medical Image Data” was not only the visual exploration of the time-dependent medical perfusion data but the integration from sophisticated data mining methods as well, yielding the visual analytics approaches. Based on a thorough cooperation with Dr. Uta Preim, a professional radiologist with many years of experience, this thesis’ contribution is the visual analysis of brain and breast tumor perfusion data, including carefully application-adapted sophisticated clustering and classifier algorithms for the radiologists in clinical practice and clinical research. The thesis at hand is organized as follows:

- Chapter 2 covers the medical imaging of tumor perfusion data restricted to breast and brain tumors. In addition to the medical background and MR imaging modalities, the calibration of signal intensities and the extraction of perfusion parameters are described. Goals for this thesis are listed at the end of this chapter.

- Chapter 3 is dedicated to the clustering of medical perfusion data due to the importance of this subject for the subsequent analyses. Hence, a general categorization of cluster analysis is presented with focus on density-based clustering, detection of attribute dependency dimensional reduction, and region merging.

- Chapter 4 covers the related work that has been presented in literature, starting from a more general aspect - the visualization of high-dimensional data - and proceeding to the evaluation of breast tumors in DCE-MRI data as well as the evaluation of low and high grade gliomas in DSC-MRI data.

- Chapter 5 introduces the PerfusionAnalyzer framework. This framework was developed in this thesis to allow for a 2D visual exploration of breast tumor perfusion data including a lesion detection method, a glyph visualization, a region merging approach and the new *File-Card-Browser View*. Furthermore, a combination of the DCE-MRI perfusion data set with T_2-weighted MRI data is suggested.

- Chapter 6 comprises 3D exploration techniques for breast perfusion data, including a new scatterplot technique to explore a tumor clustering result. This technique is not restricted to breast perfusion data and can be adapted to other medical tomographic data as well.

- Chapter 7 covers four classification approaches that allow for an automatic classification of small breast tumors, only detectable in perfusion DCE-MRI. Hence, the focus is set to the analysis of heterogeneity regarding the contrast enhancement kinetics. The classification approaches can be integrated in current breast evaluation systems in clinical practice.

- Chapter 8 focuses on the visual analysis of longitudinal brain perfusion tumor scans for characterization of low grade gliomas and their transformation into high grade gliomas. The presented framework visualizes the longitudinal studies and highlights perfusion parameter changes.
- Chapter 9 holds the conclusion of this thesis including a discussion of the presented methods and future application areas for the designated techniques.

2.

Medical Imaging of Tumor Perfusion

2 Medical Imaging of Tumor Perfusion

Medical imaging of tumor perfusion plays a more and more important role for tumor diagnosis. This thesis covers two important medical research areas: the evaluation of breast tumor perfusion and brain tumor perfusion with magnetic resonance imaging (MRI). For perfusion MRI, basically two variants are exploited: the T_2^* effect, covered with a dynamic susceptibility contrast (DSC) MRI scan, and the T_1 effect, covered with a dynamic contrast enhanced (DCE) MRI scan.

In this chapter, the reader is introduced to breast and brain tumor diagnosis as well as the MRI sequences, dedicated to these application scenarios. Section 2.1 refers to breast tumors. Medical background information is provided to understand tumors and their neoangiogenetic activity that is fundamental for perfusion imaging.

Afterwards, Perfusion MRI is explained and the different weighted DSC-MRI and DCE-MRI scans are described in more detail. For breast tumor perfusion imaging, T_1-weighted DCE-MRI data sets are acquired and the image acquisition as well as the calibration of the acquired MRI signal intensities are explained.

Likewise, the Section 2.2 covers the medical background of brain tumors. Due to the specific cerebral vasculature system encompassed by the blood brain barrier, the human brain provides a unique environment, favoring a T_2^*-weighted MRI sequence and dedicated methods for the conversion from time-intensity curves to concentration-time curves. This chapter is concluded with a summary and the identification of the important goals for this thesis.

2.1 Perfusion Imaging for Breast Cancer Diagnosis

This section comprises the anatomy of the breast and the medical background for breast tumors including diagnosis and treatment planning. In the second part of this section, DCE-MRI and DSC-MRI are described in more detail, revealing the advantages of each method for the specific medical application area. Afterwards, a more detailed analysis of DCE-MRI of breast tumors, including the image acquisition, calibration of signal intensities, and MR-based tumor classification, is provided.

2.1.1 Medical Background

This section deals with the anatomy of the breast. Furthermore, breast cancer and the accompanying *neoangiogenesis* is described, followed by a short description of diagnosis and treatment planning.

Anatomy of the Breast

The human breasts (mammae) overlay the pectoralis muscles and cover the chest area and chest wall. The male breasts are in a rudimentary state, whereas the female breasts equal two hemispherical eminences. In adult women, breasts are milk-producing, tear-shaped glands and their primary function is the nourishing of an infant child. In Figure 2.1, the anatomy of the breast is illustrated. The breast consists of gland, fibrous, and fatty tissue. These tissue types hold and sustain the inner parts of the breast, like the lobes and the ducts. In general, each breast has 12 to 20 lobes that are arranged in a circular manner. Each lobe comprises many lobules which end with tiny bulb like glands, where milk is produced in response to hormonal signals. The lobes are covered by fatty tissue, that gives the breast its size and shape. The ducts connect the glands and lobes. After child birth, milk is produced in the lobules and transported to the nipple (papilla mamilla), the tip of the breasts, via the ducts. As a mammary gland, the breast is an inhomogeneous anatomic structure.

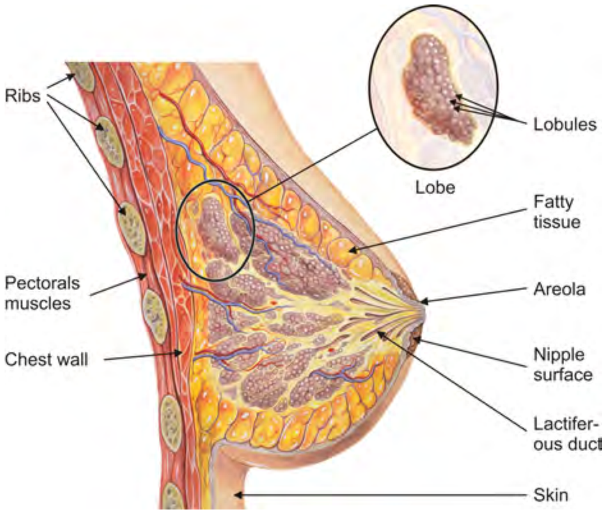

Figure 2.1: *Anatomy of the human female breast. The ducts connecting the lobules to the tip of the nipple. The areola is the darker-pigmented area around the nipple. (Adapted from an illustration by Patrick J. Lynch, medical illustrator.)*

The breasts' blood supply is maintained by arteries from the thoracic branches of the axillary artery, the intercostal artery and the internal thoracic artery. The veins are ordered in an anastomotic circle around the nipple. Deriving from this circle, large branches transmit blood to the circumference of the gland before they end in the axillary and internal mammary veins.

Breast Cancer

Like all cancers, breast cancer is caused by a cell mutation and it originates from breast tissue. Ductal carcinomas refer to cancers originating from the ducts. Lobular carcinomas denote cancer originating from the lobules.

After invasive breast cancers grow beyond a size of a few *mm*, they have a higher oxygen and nutrients demand that exceeds the supply through normal vessels of the glandular tissue. With increasing tumor growth, the gap between demand and supply is increasing as well. Therefore peptide hormones, like the vascular endothelial growth factor (VEGF), are released, causing the formation of new vessels and or sprouting of existing vessels [Folkman, 1990, 1995]. This process is called *angiogenesis* or *neoangiogenesis* and is depicted in Figure 2.2. These newly formed vessels are very permeable. Thus, they allow for a leakage of proteins or contrast agent, a very important effect for breast cancer imaging. During neoangiogenesis and tumor growth, breast cancer may reach an advanced stage and may spread metastasis to lymph nodes or more distant parts of the body, mostly the bones, the lung, the liver or the brain.

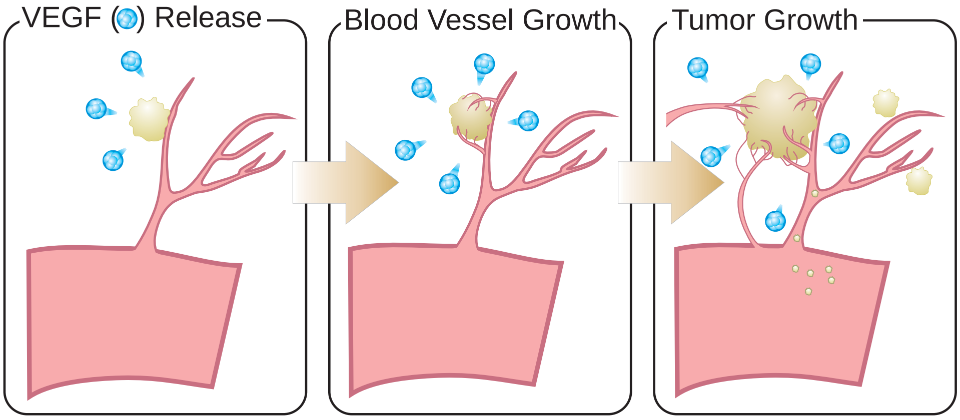

Figure 2.2: *Illustration of angiogenesis. The tumor's increased demand for oxygen and nutrients causes the release of proteins, mainly the VEGF, which in turn causes formation of new vessels and sprouting of existing ones. These vessels allow for tumor growth.*

Breast cancer is the most common incident cancer and cause of cancer-related death in women. In Germany, incidence and mortality rates (for women in 2008) were 171.1 per 100,000 and 41.1 per 100,000 [The Robert Koch-Institute, 2012]. For international comparison, age-standardization is carried out to account for the national age distribution. Age-standardized incidence and age-standardized mortality was 123.1 per 100,000 and 24.6 per 100,000 for the year 2008 [The Robert Koch-Institute, 2012]. Similar age-standardized rates were reported for developed countries. The age-standardized survival rates from breast cancer slowly increased in developed countries to 85% due to improved screening practices and treatments, whereas the survival rates remains 50-60% in developing countries [International Agency for Research on Cancer, 2008]. Furthermore, the incidence rate is increasing in developed countries. This rise (in contrast to the mortality rate) is interpreted as direct consequence of the improved screening practices. This disease mostly occurs in women, i.e., less than 1% of all breast cancer patients are male [Sasco et al., 1993].

The risk factors for breast cancer are female sex, age, the lack of childbearing (or late child birth), the lack of breastfeeding, and the age at menarche and menopause (i.e., the risk of breast cancer increases with cumulative number of ovarian cycles) [Collaborative Group on Hormonal Factors in Breast Cancer, 2002, International Agency for Research on Cancer, 2008]. The family history, i.e., a family relative that developed breast cancer, does also lead to an increased breast cancer risk. This relationship may be caused by low-penetrance genes, particularly the CYP19 gene, or high-penetrance genes, e.g., BRCA1, BRCA2, and p53, but these genes are rare in most populations and only cause a small fraction of total cases [International Agency for Research on Cancer, 2008]. Although the incidence and mortality for breast cancer varies between countries, it is assumed that environmental factors are of greater importance than the genetic factors [McPherson et al., 2000].

For the exact description of breast cancer and its properties, like size or shape, a classification is carried out. There are different ways based on several underlying classification systems. The three most common approaches are:

- The histopathological analysis.
- The tumor grading.
- The staging of the tumor's spread.

For histopathological analysis, breast tissue is removed and histopathological characteristics are evaluated with light microscopy. The three major histopathological types are the invasive ductal carcinoma, the ductal carcinoma in situ, and the invasive lobular carcinoma. The World Health Organization recommends detailed pathological types for histopathological classification in [Tavassoli and Devilee, 2003].

For tumor grading, the microscopic similarity of a breast cancer cell to normal breast tissue cells is evaluated. Three categories are possible:

(1) Low grade, for well differentiated cancer cells.

(2) Intermediate grade, for moderately differentiated cancer cells.

(3) High grade, for poorly differentiated / undifferentiated cancer cells.

Lower graded tumors have a better prognosis and can be treated more aggressively, whereas higher grades indicate a worse prognosis, since the associated tumor cells will divide more rapidly and tend to spread. Elston and Ellis [1991] refine this system by defining an overall score based on tubule formation, nuclear pleomorphism, and mitotic count.

Beyond grading, the *TNM classification system* allows for assigning a tumor stage to describe the extent of a person's cancer and cancer spread. Hence, the extent of a primary tumor (T), the existence of regional lymph node metastasis (N), and the presence of distant metastasis (M) are taken into account [Sobin and Wittekind, 2002]. The TNM classification system is developed and maintained by the *Union for International Cancer Control*.[1] Since this system includes therapy guidelines for the different TNM stages, it is important in clinical practice for further therapy of breast cancer.

Diagnosis and Treatment Planning of Breast Cancers

Investigation of the breast comprises a clinical study, i.e., inspection and palpation of breasts and axillary lymph nodes. If there is a unclear finding and suspicion of cancer, an imaging-based technique is taken into account. During the last decades, several image acquisition techniques have been employed for breast cancer diagnosis.

X-ray mammography is the most conventional and wide-spread image modality. In contrast to other imaging techniques, it allows for detection of micro-calcification. However, the density of the breast tissue strongly influences accuracy of X-ray mammography, which is why supplemental modalities are taken into account. Beyond X-ray mammography, breast ultrasound is carried out. This modality is especially well suited for dense fibrous breast tissue that occurs in younger women. However, breast ultrasound is limited due to its resolution.

---

[1] Non-governmental organization *Union for International Cancer Control*; www.uicc.org (12/01/2013)

Breast MRI is currently the most sensitive imaging modality for invasive breast cancer [Kuhl, 2007]. It allows for differential diagnosis after ambiguous X-ray mammography findings. The images provide tissue information and cross-sectional morphology. DCE-MRI is acquired for the analysis of local perfusion and described in more detail in the following.

Once, the exact localization of the breast cancer was determined and classification took place, further treatment can be planned. In clinical practice, the treatment is dependent of specific cancer attributes. In general it consists of surgery, radiation therapy, medication, or any combination thereof.

Due to its prevalence as most common incident cancer in women and the importance of an early detection for the further treatment planning, breast cancer awareness campaigns aim at getting attention for the disease. The pink ribbon, see Figure 2.3, is the symbol of these campaigns. With the increased knowledge and attention, more women participate in screening studies, which in turn leads to an earlier breast cancer detection. Due to these detections of very small lesions in early tumor stages, the demand for computer-aided diagnosis for an automatic classification increases.

Figure 2.3: *A pink ribbon is the worldwide symbol for the breast cancer awareness campaign.*

2.1.2 Breast Tumor Perfusion Imaging with DCE-MRI

Over the past 20 years, perfusion DCE-MRI of the breast has gained increasing importance due to its unsurpassed sensitivity for the detection of invasive breast cancer [Heywang-Köbrunner, 1994, Kuhl, 2007]. Thus, the number of malignant cancers which are not detected (false negatives) with MRI and DCE-MRI is lower compared to other imaging modalities. However, compared to conventional X-ray mammography, DCE-MRI only exhibits a moderate specificity, i.e., a relative high rate of tumors are incorrectly classified as being malignant (false positives). Therefore, many benign tumors could not be correctly classified as benign tumors and there is a great demand for further improvements to predict malignancy in DCE-MRI [Kuhl, 2007]. DCE-MRI has the ability to reveal small tumors that could not be detected with X-ray mammography. This might be necessary in case of an existing primary tumor, detected with X-ray. Hence, additional small tumors in the primary tumor's environment as well as in the bilateral breast have to be found and identified with DCE-MRI for further treatment planning. Moreover, suspicious tumors that could not be classified with X-ray or sonography, will be evaluated with DCE-MRI, since additional information about the tumor's enhancement kinetics could be provided. In conclusion, the advantage of DCE-MRI of providing morphologic and functional information makes it important for differential diagnosis.

Role of Perfusion Imaging in the Clinical Workflow

As it was stated in Section 2.1.1, DCE-MRI data is acquired after suspicious findings during palpation or X-ray mammography. If the evaluation of the data set reveals contrast agent enhancement, the further treatment depends on the properties / attributes, see Figure 2.4.

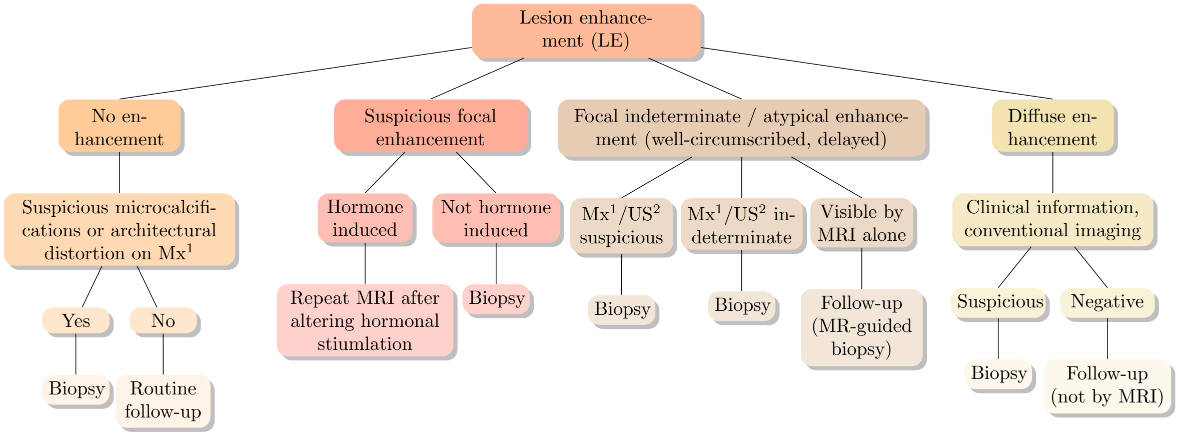

Figure 2.4: *A guideline for the interpretation of lesion enhancement in breast MRI of the breast in the clinical routine (adapted from [Heywang-Köbrunner and Schreer, 2001]).*
[1] *Mx denotes X-ray mammography,*
[2] *US denotes ultrasound.*

Image Acquisition

Perfusion MRI allows for the acquisition of sequential sets of morphological data, which are widely used for oncology and thus breast cancer diagnosis [Kuhl et al., 1999, Knopp et al., 2001]. It is based on the MRI technique that exploits the nuclear magnetic resonance, i.e., the electromagnetic interaction of nuclei in a magnetic field. The relaxation times differ due to the hydrogen proton density and cause different signal intensities for the different tissue types. For the specific aim of perfusion analysis, a contrast agent is administered as a single intravenous bolus injection and its enhancement is tracked. Hence, it is also referred to as a tracer.

As it was stated earlier, tumor growth is strongly related to angiogenesis and thus an increased perfusion. This effect is exploited by perfusion imaging and illustrated in Figure 2.5. Hence, the contrast agent accumulates in the extravascular-extracellular space before it diffuses back into the vasculature. From there, it is excreted via the kidneys. In Figure 2.5(a), tumor growth in combination with angiogenesis and the resulting new blood capillaries are depicted. A single voxel of the MR image is shown in Figure 2.5(b). The voxel's extent and thus the resolution of the resulting 4D image is characterized by the image matrix, i.e., how many pixels are acquired in one slice, and the slice thickness. In the inlet of Figure 2.5(c), the contrast agent administration is depicted. The MRI signal intensity changes due to contrast agent administration yield a contrast agent enhancement curve, see Figure 2.5(d). This curve covers the enhancement kinetics during the passage of the contrast agent. The curve shape for the scheme from line 1 to 2 refers to the time before contrast agent injection, which took place right after at line 2. The scheme from line 2 to 4 illustrates contrast agent leakage in extravascular-extracellular space and its diffusion back into the vasculature. The patterns of increased signal intensities in perfusion MRI depend from physiological factors like vessel density, blood flow, endothelial permeability, and the size of the extravascular-extracellular space in which the contrast agent is distributed [Hayes et al., 2002].

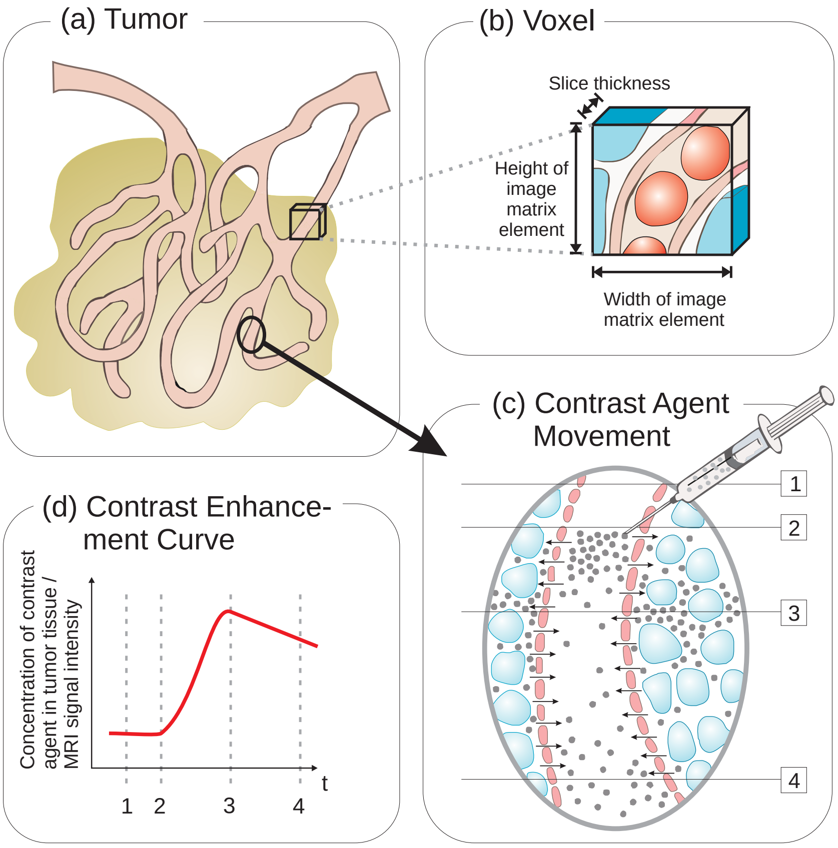

Figure 2.5: *Illustration of diffusible contrast agent administration. In (a), a tumor and its permeable vasculature are depicted. The box inlet visualizes a single voxel in (b), whose size depends on the image matrix and the slice thickness of the MRI protocol. In (c), the contrast agent administration is depicted, where the contrast agent bolus injection is carried out at line 2. The agent leaks into the extravascular-extracellular space (line 2 to 3) and diffuses back into vasculature (line 3 to 4), resulting in a MR signal intensity change that is represented in (d). (Adapted from [Gribbestad et al., 2005].)*

At this point, the difference between types of contrast agent are explained. Two main types of contrast agent exist:

- *Diffusible contrast agents* pass the border between the intravascular and the extravascular-extracellular space, as depicted in Figure 2.5.
- *Intravascular contrast agents* do not leak into the extravascular-extracellular space but stay inside the vessel lumen.

The first property is necessary for DCE-MRI. In contrast, DSC-MRI requires an intravascular contrast agent. Since no intravascular contrast agents have been approved for assessing cerebral perfusion in the clinical routine, intravascular agents are employed for DSC-MRI as well. However, in case of an intact blood-brain barrier, the diffusible contrast agents behave equally.

The most commonly used group of diffusible contrast agents are the paramagnetic gadolinium chelates, e.g., gadolinium diethylene triamine pentacetic acid (Gd-DTPA) [Caravan et al., 1999].

For different MRI sequences, different effects of the contrast agent are exploited. The tracer's paramagnetic properties cause a decrease in the T_1 and the T_2 / T_2^* properties of the water yielding a signal enhancement in T_1-weighted sequences, and a signal loss in T_2 / T_2^*-weighted sequences. In contrast to T_2 sequences, the T_2^* sequences also depend on the magnetic field gradient irregularities, but have a shorter relaxation time. The signal enhancement increase in T_1-weighted sequences is caused by dipole-dipole interaction, which only occurs in short distances to the contrast agent. Thus, the T_1 enhancement is only present in areas with direct access to the contrast agent and a tracer that diffuses in the extravascular-extracellular space is well suited for this purpose. In contrast, the T_2 effect is caused by strong susceptibility-induced gradients surrounding the contrast agent. Therefore, it is more prominent if the contrast agent is compartmentalized [Villringer et al., 1988]. As a conclusion, these effects arise in a complementary manner. As a first example, an area with a uniform and homogeneously distributed contrast agent will cause a very large T_1 effect due to the direct access, but only a very small T_2 effect due to the missing gradients. On the contrary, an area with contrast agent in small compartments will cause a strong T_2 effect, whereas the T_1 effect is negligible. Thus, intermediate contrast agent distributions causes both effects and they both compete against each other.

In conclusion, breast T_1-weighted DCE-MRI sequences are acquired with a diffusible tracer due to the direct access of breast tissue to the tracer. The signal intensity increase in T_1-weighted sequences is based on various physiological and physical factors, like tissue perfusion, vessel density, angiogenesis-induced pathological capillary permeability, and volume of the extracellular leakage space. Signal intensities arising from T_2-weighted first-pass perfusion images are more directly related to vessel density and angiogenesis-induced pathological vessel permeability. T_2-weighted MRI scans are applied to improve differential diagnosis for the T_1 sequence [Kuhl et al., 1997], e.g., the differentiation of small tumor lesions and cysts. The T_1-weighted sequence is adjusted such that a high spatial resolution is maintained to allow for evaluation of the lesion's morphology. However, any increase in spatial resolution causes an increased acquisition time. Typically, dynamic MRI protocols comprise a dynamic acquisition time from 60 - 120 s, with 5 - 6 acquistions, an image matrix of 512×512 resulting in $0.5 \times 0.5\ mm^2$ to $0.8 \times 0.8\ mm^2$, a through-plane pixel size (section thickness) of 1-3 mm and use fast gradient echo sequences [Kuhl, 2007]. Even with the largest image matrix, a voxel always contains a set of different cells. Thus, the voxel's signal intensity accumulates the different tissue cells covered by this voxel, which is defined as partial volume effect.

Motion Correction

Perfusion DCE-MRI data sets exhibit severe motion artifacts mainly due to thorax expansion through breathing and patient's movement. To establish a better inter-pixel correspondence and to reduce the interference, motion correction via image registration is carried out.

The scope of image registration of different medical image data sets is the geometrically alignment of these data sets. For example, the images may arise from:

- different imaging modalities (e.g., T_1-weighted and T_2-weighted sequences),
- different patients (e.g., from a cohort study), or

- from the same patient but acquired at different time steps (e.g. perfusion image data or follow-up studies).

In general, for perfusion data sets, the registration is the process of transforming the different images arising from different points in time such that they optimally fit to the first acquired image at the first point in time. This first image is referred to as *reference image* and the others are referred to as *target* or *template images*. The optimal fit is usually quantified by a similarity criterion based on the comparison of the reference image and the target image. The similarity criterion can be subdivided into intensity-based criteria and geometry-based criteria. Intensity-based criteria are based on the MR intensity of the perfusion data sets, whereas the geometry-based criteria are based on the geometrical position of landmarks. The transformation model of the registration can be divided into global transformations and local transformations. Global transformations are carried out over the whole target image, whereas local transformations are only carried out on a part of the target image. Hence, the global models are further divided into:

- Rigid transformation, where only translation, rotation, and a combination thereof are applied to the target image.
- Affine transformation, where translation, rotation, scaling, shearing, and a combination thereof are applied to the target image.
- Polynomial transformations, where thin plate splines are applied to the target image.

Local transformations models include a variety of different techniques and parameters to locally fit parts of the template image to the reference image, e.g., via cubic B-spline transformations [Rueckert et al., 1999]. The motion correction of breast perfusion data is a special application of medical image registration. A survey about breast image registration is presented by Guo et al. [2006]. Motion correction and registration of perfusion data is also discussed in Preim and Botha [2013].

For the optimal registration of breast DCE-MRI data, the deformation cannot be described by affine transformations adequately due to the soft tissue of the breast. A similarity criterion to characterize the similarity between the time step images is defined and optimized. Sophisticated approaches apply a combination of rigid and non-rigid transformations [Rueckert et al., 1999, Fischer and Modersitzki, 2002, Rohlfing et al., 2003].

A challenge in breast DCE-MRI registration is the contrast enhanced-induced increase of signal intensities. Further approaches do not only take the MR signal intensity but also pharmacokinetic modeling into account, as presented by Hayton [1998]. Their framework employs the pharmacokinetic model by Tofts et al. [1995]. Schäfer et al. [2011] apply a combination of rigid and non-rigid transformations and a pharmacokinetic modeling of breast DCE-MRI enhancement as presented by Radjenovic et al. [2008]. However, the pharmacokinetic modeling may be hampered due to the very low temporal resolution of breast DCE-MRI data comprising only five to six acquisitions.

Calibration of Signal Intensities and Perfusion Parameter Extraction

For the interpretation of the dynamic contrast enhancement of breast DCE-MRI, the following questions arise [Kuhl and Schild, 2000]:

- How fast does the lesion enhance?
- When does the lesion start to enhance?
- Where (within the lesion) does the lesion start to enhance?
- What happens after the initial signal increase?

For the evaluation of these criteria, different approaches exist, including a prior calibration of signal intensities, the extraction of perfusion related parameters, and the evaluation of the enhancement curves.

The signal intensities of breast DCE-MRI perfusion data depend on different parameters and the MR scanning protocol. For the quantification of contrast enhancement, different normalization schemes were suggested, e.g., a normalization based on the signal of fatty tissue [Heywang et al., 1989] or a normalization based on the initial signal intensity at the first acquired time step [Kaiser and Zeitler, 1989]. The latter approach is widely used in clinical practice [Kuhl et al., 1999]. Hence, the *relative enhancement* (RE), i.e., the percentaged signal intensity increase is calculated:

$$RE = \frac{(SI_c - SI)}{SI} \times 100, \tag{2.1}$$

where SI is the pre-contrast and SI_c is the post-contrast signal intensity. Pre-contrast refers to the early phase of enhancement. In general, a strong uptake due to the bolus injection can be observed in the beginning of contrast enhancement. Post-contrast refers to the phase following. The RE of a voxel can be plotted over time, which is illustrated in Figure 2.6. Hence, the pre- and post-contrast phase are also illustrated.

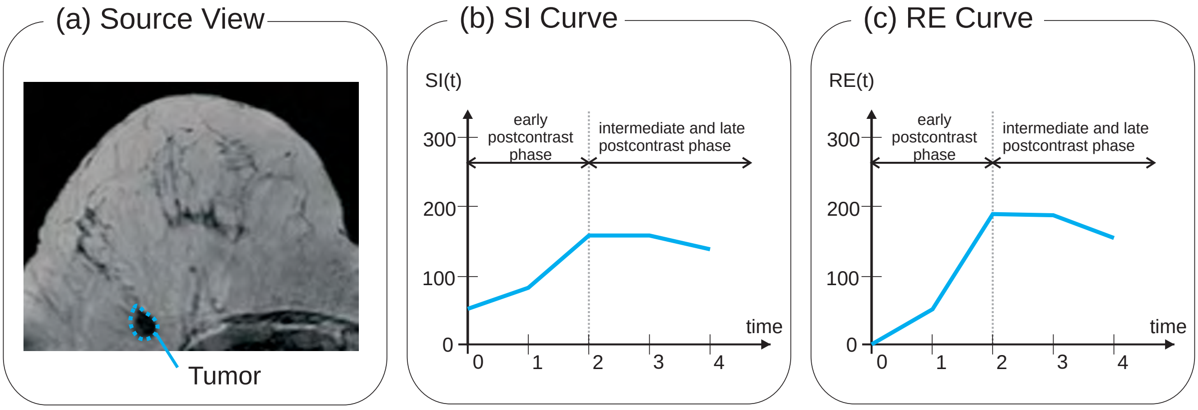

Figure 2.6: *Example of a T_1-weighted DCE-MRI breast data set. In (a), the T_1 source view at the first time step is presented. The blue shape masks a tumor, whose average signal-intensity (SI) curve is depicted in (b). In (c), the corresponding RE curve is visualized. (Data is courtesy of U. Preim, Municipal Hospital Magdeburg, Germany.)*

In clinical practice, the RE curves are classified into three different types [Kuhl et al., 1999]:

- steady or continuously increasing curves (also referred to as washin curves),
- plateau curves, and
- washout curves.

See the examples in Figure 2.7(a). A steady curve is characterized by continuously increasing RE values. The plateau curve exhibits a plateau shape during the intermediate and late post-contrast phase. The washout curve is a descending curve after the initial contrast agent washin. The washout curve, with a rapid and intense enhancement, is indicative for permeable capillaries and neoangiogenesis and thus malignancy [Kuhl et al., 1999].

A further classification of RE curves was presented by Degani et al. [1997] and Furman-Haran et al. [1998], who evaluated the contrast enhancement behavior at three points in time yielding the *three-time-point* (3TP) method. The three time steps t'_1, t'_2, and t'_3 are extracted with model-based calculations and depend on the MRI protocol that they used. Hence, t'_1 refers to the first point in time before the contrast agent injection, t'_2 to the point in time $2min$ after t'_1, and t'_3 to the point in time $4min$ after t'_2 and thus $6min$ after t'_1. With the 3TP method, the initial contrast agent accumulation (CA_{early}) in the early post-contrast phase is classified into

$$CA_{early} = \begin{cases} slow & if \quad 0\% \leq RE(t'_2) < 50\% \\ normal & if \quad 50\% \leq RE(t'_2) < 100\% \\ fast & if \quad RE(t'_2) \geq 100\%. \end{cases} \tag{2.2}$$

Furthermore, the contrast accumulation (CA_{late}) in the intermediate and late post-contrast phase is classified based on the curve's behavior between t'_2 and t'_3:

$$CA_{late} = \begin{cases} steady & if \quad RE(t'_3) - RE(t'_2) > 10\% \\ plateau & if \quad |RE(t'_3) - RE(t'_2)| \leq 10\% \\ washout & if \quad RE(t'_3) - RE(t'_2) < -10\%. \end{cases} \tag{2.3}$$

By applying Eq. 2.2 and Eq. 2.3 to the RE values at the three time steps t'_1, t'_2, and t'_3, nine different classes of RE curves are obtained, see Figure 2.7(b).

Beyond the classification of the RE curve shape, the RE curves are further characterized by descriptive perfusion parameters. For breast perfusion imaging, the following parameters are derived from the RE curve (see Fig. 2.7(c)):

- *Peak enhancement (PE)*: the RE curve's maximum value.
- *Time to peak (TTP)*: the point in time where *PE* occurs. Washin takes place between the first time step and *TTP*, whereas the washout occurs between *TTP* and the last point in time. Thus, steady curves will exhibit *TTP* values that equal the last point in time.
- *Integral*: the approximated area under the curve for the whole time period.
- *UpSlope*: the curve's steepness during the early postcontrast phase. Synonyms of UpSlope are *washin*, *curve slope*, *early phase enhancement rate*, and *enhancement velocity*.
- *DownSlope*: the steepness of the descending curve during the intermediate and late post-contrast phase. A synonym for this parameter is *washout*.

Integral and PE yield important information about how much the lesion enhances, whereas TTP indicates an early or late enhancement. Naturally, these parameters are well suited for breast perfusion data because of the low temporal resolution. However, other image modalities like brain perfusion data exhibit a higher temporal resolution and thus a more complex time-intensity curve. Then, additional descriptive perfusion parameters may be derived, see [Preim et al., 2009] for more information.

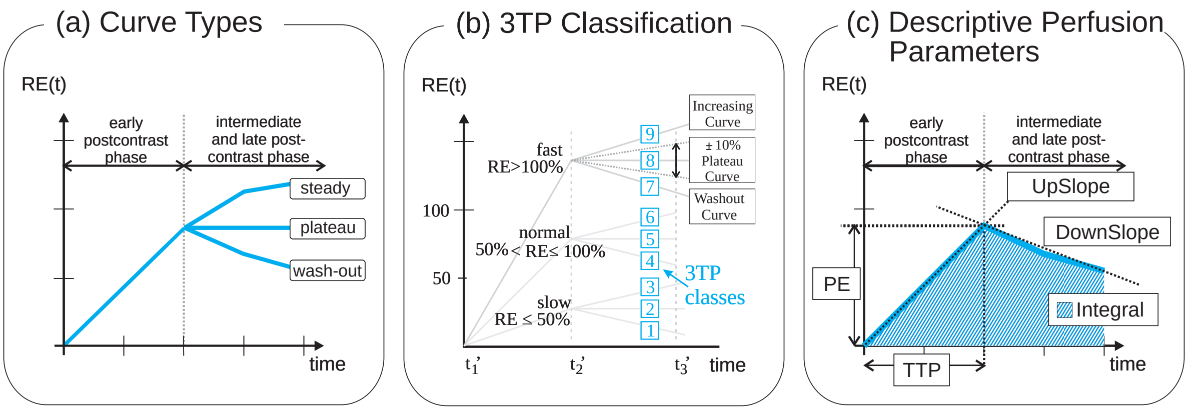

Figure 2.7: *In (a), the schematic drawings of the RE curve shapes steady, plateau, and washout are presented. In (b), the 3TP classification is shown. Each curve is classified based on the contrast enhancement between t_1' and t_2' (slow, normal, and fast) and between t_2' and t_3' (steady, plateau, and washout) yielding nine different classes. In (c), an RE curve with a washout shape and the annotated perfusion parameters PE, TTP, Integral, UpSlope, and DownSlope is depicted.*

The extraction of physiological parameters is based on the pharmacokinetic analysis which in turn is in general applied to the T_2 sequence. Hence, the enhancement curve is fitted to a pharmacokinetic modeled curve, e.g., based on the model described by Radjenovic et al. [2008]. The benefit of a pharmacokinetic model fit is the possibility to extract values that are proportional to physiological parameters like the volume of the leakage space and capillary permeability [Tofts et al., 1999]. However, appropriate model fitting requires a high temporal resolution, which is not available for breast perfusion data yet.

In clinical practice, the radiologist places a region of interest (ROI) in the most suspect part of the lesion. Next, the averaged RE curve of the ROI is extracted and the shape of the RE curve is evaluated qualitatively, i.e., the referring radiologist visually interprets the whole RE curve. More advanced workstations do also offer automatically extracted parameter maps. However, different recommendations for the optimal ROI size and placement exist, ranging from 3-4 pixels to the whole enhancing lesion [Mussurakis et al., 1997, Kuhl et al., 1999, Kuhl, 2007] resulting in a substantial inter-observer variability.

Classification of Breast MRI Lesions

For the categorization of a breast lesion in MRI, the *Breast Imaging Reporting and Data System* (BI-RADS) for MR imaging is applied [American College of Radiology, 2003].

The MR BI-RADS lexicon classifies a lesion as:

- mass,
- area of non-masslike enhancement, or
- a focus.

Mass refers to a space-occupying tumor. The non-masslike enhancement does not occupy any space, but describes an enhancing area that appears normal on the pre-contrast images. The focus is a small enhancing area of less than 5 *mm* size. Based on this classification and the

Table 2.1: *Categories of the MR BI-RADS by American College of Radiology [2003].*

Category	Assessment	Follow-Up
0	Need additional imaging evaluation	Additional imaging needed before a category can be assigned
1	Negative	Continue annual screening X-ray mammography (for women over age 40)
2	Benign (non-cancerous) finding	Continue annual screening X-ray mammography (for women over age 40)
3	Probably benign	Receive a 6-month follow-up X-ray mammography
4	Suspicious abnormality	May require biopsy
5	Highly suggestive of malignancy (cancer)	Requires biopsy
6	Known biopsy - proven malignancy (cancer)	Biopsy confirms presence of cancer before treatment begins

evaluation of shape, margin, and enhancement kinetics, the lesion is categorized into one of the seven categories in Table 2.1. For masses, the shape and margin of the mass are analyzed. Furthermore, enhancement kinetics of masses and non-masslike enhancement are evaluated, where special care must be taken since non-masslike enhancement may also include ductal carcinoma in situ and lobular cancers that exhibit inconsistent angiogenetic activity.

Benign tumors are predominantly more homogeneous [Okafuji et al., 2008] than malignant ones. They also exhibit a lower vessel density than recurrent invasive breast cancer [Obermair et al., 1994]. However, fibroadenomas as well may display a heterogeneous internal enhancement in contrast enhanced perfusion imaging due to mucinous or myxoid degeneration [Kuhl, 2007]. Malignant lesions often exhibit necrosis and fibrosis in the tumor center in an advanced tumor stage. Thus, they show rim enhancement or heterogeneous enhancement in their centers and angiogenetic activity predominantly at their peripheries [Buadu et al., 1996]. The study of Mavroforakis et al. [2005] identifies the *tumor shape type* and the *boundary sharpness* as important features for classification of benign and malignant tumors in X-ray mammography, see Figure 2.8. The same holds for DCE-MRI, and smooth borders and well-defined margins are associated with benign diseases, whereas irregular and spiculated borders are indicative for malignancy. Recent studies divide the tumor's margin into [Fischer et al., 1999]:

- well defined and
- ill defined

and the tumor's shape into [Szabo et al., 2003]:

- smooth,
- lobulated,
- irregular, and
- spiculated.

As a prerequisite, a contrast-enhancing lesion must be present in the DCE-MRI data set. Furthermore, ring enhancement of contrast agent and a more heterogeneous enhancement over

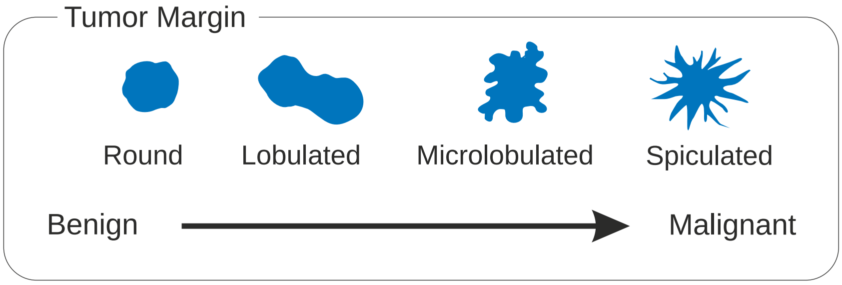

Figure 2.8: *Illustration of morphological shape types of breast tumors. (Adapted from [Mavroforakis et al., 2005].)*

time in general is considered to be indicative for malignancy [Behrens et al., 2007]. The morphology of lesions without contrast enhancement cannot be adequately evaluated.

2.2 Perfusion Imaging for Brain Tumor Diagnosis

This section provides medical background information about the human brain and the most common brain tumors: gliomas. In the second part, T_2^*-weighted MRI acquisition is explained in more detail, including the calibration of signal intensities and the extraction of perfusion parameters.

2.2.1 Medical Background

In this section, the reader gets familiar with the basic terms for anatomical structures of the brain. Afterwards, important aspects of the brain tumor epidemiology and the brain tumor classification are described. Finally, the brain tumor diagnosis and the treatment planning with focus on gliomas is presented.

Anatomy of the Brain

The human brain is the center of the nervous system, placed into cerebrospinal fluid and protected by the skull. Its structure is depicted in Figure 2.9. The brain is divided into the cerebrum, cerebellum, and brain stem. Cerebrum and cerebellum are covered with the cerebral cortex, the outermost thick layer of neural tissues. The cerebral cortex is folded to increase the surface of this layer in the available volume in the skull. A cortical fold is referred to as sulcus and the smooth areas between the folds are named gyri. The cortex is divided in the four lobes: the frontal lobe, parietal lobe, temporal lobe, and occipital lobe, see Figure 2.9(b). Each lobe comprises several cortical areas that process different information and are associated with a particular function like language or vision.

The cortex is nearly symmetrical and it is divided into a left and a right hemisphere, see Figure 2.10. The central nervous system has two major components: gray matter and white matter. The gray matter can be found at the surface of the cerebral cortex and surrounds the white matter. It consists of neuronal cell bodies for muscle control, sensory perception such as seeing and hearing, memory, emotions, and speech. The white matter transmits signals

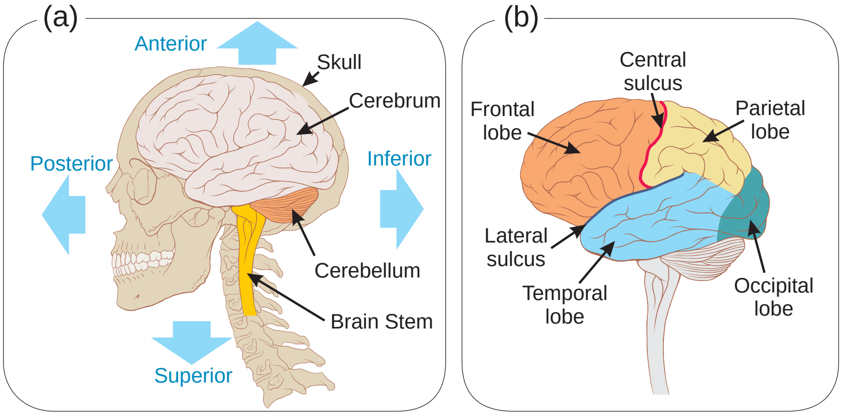

Figure 2.9: *Anatomy of the human brain. In (a), the brain comprising the cerebrum, cerebellum, and the brain stem as well as the anatomical directions are depicted. In (b), the four lobes of the cortex and the central and lateral sulcus are illustrated. (Adapted from an illustration by Patrick J. Lynch, medical illustrator.)*

from one region of the cerebrum to another. The cerebral cortex is covered by the meninges, a membrane system consisting of the dura mater, the arachnoid mater, and the pia mater.

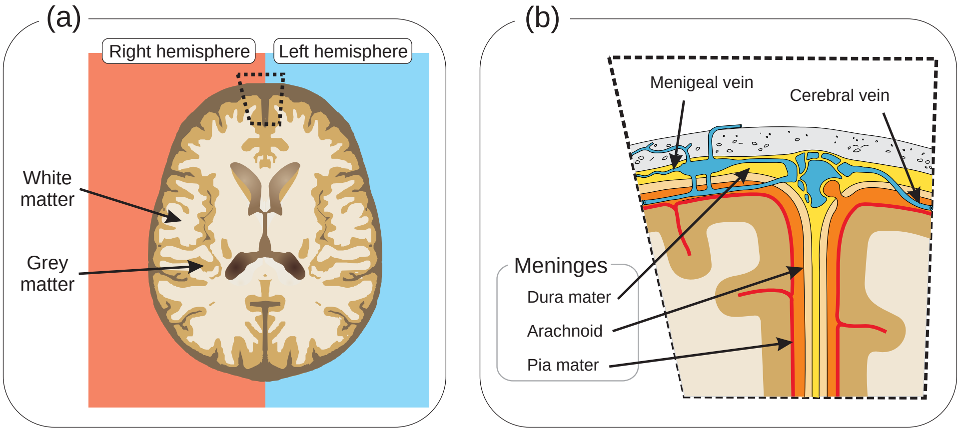

Figure 2.10: *In (a), a cross section of the brain illustrates its division into the right and the left hemisphere as well as the white and the gray matter. The inlet is shown in (b) and visualizes the meninges, consisting of the arachnoid, dura mater, and pia mater.*

The human brain is the organ with highest demand for blood and oxygen supply. The arterial system of the brain is illustrated in Figure 2.11. The arterial cerebral circulation comprises the anterior and the posterior cerebral circulation. The anterior cerebral circulation is built up by the right and left internal carotid artery that branch from the left and right common artery. From each internal carotid artery, the ophthalmic artery is branching, supplying the eye and parts of the nose, face and the meninges. Next, the internal carotids split into the middle cerebral arteries and the anterior cerebral arteries. They are connected via the anterior communicating artery and supply the lateral and medial portions of the brain. In contrast, parts of the temporal lobe and the occipital lobe are supplied by the posterior cerebral circulation. Inner parts of the brain, like basal ganglia and thalamus are supplied by both, the anterior and the posterior cerebral circulation. The posterior cerebral circulation is created by the left and the right vertebral artery. They unite to the basilar artery. Branches of the vertebral arteries and the basilar artery supply the brain stem and the cerebellum. The basilar artery splits into two posterior cerebral arteries, which supply the occipital lobe. The basilar artery is connected via the bilateral posterior communicating arteries to the internal carotid arteries on each side: forming the Circle of Willis, see Figure 2.11(b). The Circle of Willis serves as backup circulation of the brain if the blood supply is hampered, i.e., if one of the supply arteries is occluded. The anatomical manifestation of the described arteries may vary among different patients, e.g., underdeveloped communicating arteries.

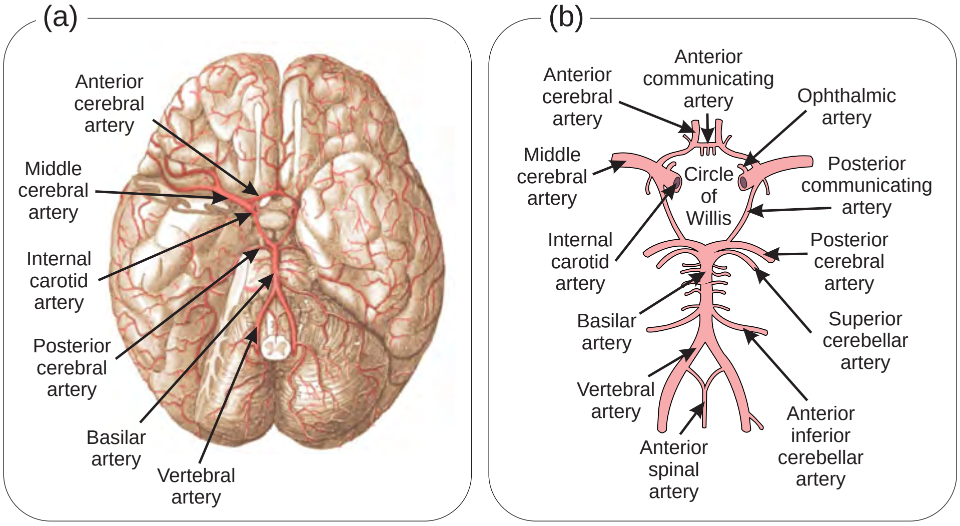

Figure 2.11: *The blood supply of the brain is maintained by the anterior and the posterior cerebral circulation, see (a), and the Circle of Willis, see (b), as backup circulation. (Adapted from illustrations in [Gray, 2000].)*

Brain Tumors and Their Epidemiology and Classification

Brain tumors are masses of abnormally growing cells in the brain or the skull. Like breast tumors, they can be benign (i.e., non-cancerous) or malignant (i.e., cancerous). However, on clinical grounds, also benign tumors are very dangerous, since a growing tumor will damage or compress other brain structures, see Figure 2.12.

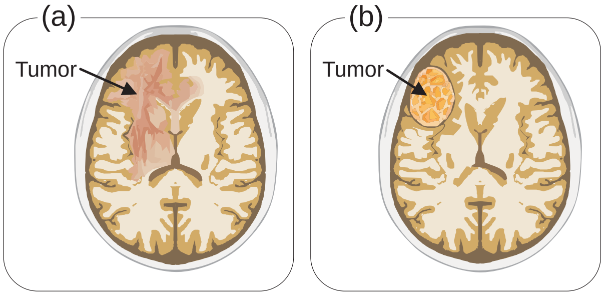

Figure 2.12: *Illustration of negative tumor impact. In (a), the brain tumor invades and destroys normal brain tissue. In (b), the brain tumor does not infiltrate brain tissue but causes increased pressure within the brain as well as pressure on the surrounding tissue.*

Brain tumors that are arising from brain tissue are referred to as primary brain tumors. Unlike other cancers, they do rarely spread. However, they could be caused by the spreading of other tumors in the body, like breast or colon cancer, which is referred to as secondary or metastatic brain tumors.

Primary brain tumors are much less common than secondary ones. They are named based on the cell types they are arising from. Brain tumors that arise from the meninges are called meningiomas, while schwannomas (also called neurilemomas) arise from the Schwann cells of the nerve sheath. Both tumor types are mainly benign.

Gliomas - tumors with a glial cell origin - are the most common primary brain tumors [International Agency for Research on Cancer, 2008]. Even worse, they are the most lethal forms of this tumor kind [Ohgaki and Kleihues, 2005]. Glioma cells are highly invasive and infiltrate the brain parenchyma. Furthermore, the tumor growth can be rather fast.

Pathological classification divides gliomas into astrocytomas, also prescribed with low grade gliomas (LGG) and glioblastomas, i.e., high grade gliomas (HGG). LGGs may transform into HGGs at some point in time and an early detection of such a transformation is of significant clinical importance. The incidence of gliomas is slightly higher in men than in women with a male to female ratio of approximately 1.3. The age distribution of brain tumors has a maximum peak incidence in adults between 45 and 70 years and a smaller peak in children [International Agency for Research on Cancer, 2008]. The prognosis for patients with gliomas is very bad and, only 3% of patients with a glioblastoma survive longer than 3 years, the majority dies within 9-12 months [Ohgaki and Kleihues, 2005].

The classification of tumors of the nervous system by the world health organization (WHO) covers more than 50 clinicopathological entities. LGGs are classified as WHO grade I and II, HGGs are assigned with WHO grade III to IV, depending on the tumor type. The most frequent tumor types, their grade, and their typical location are listed in Table 2.2.

Table 2.2: *The most frequent tumors of the nervous system, from [International Agency for Research on Cancer, 2008].*

Tumor	WHO Grade	Typical location
Pilocytic astrocytoma	Grade I	Cerebellum, optic nerve
Low grade diffuse astrocytoma	Grade II	Cerebral hemispheres
Glioblastoma	Grade IV	Cerebral hemispheres
Oligodendroglioma	Grade II / Grade III	Cerebral hemispheres
Ependymoma	Grade II	Ventricles, spinal cord
Medulloblastoma	Grade IV	Cerebellum
Neuroblastoma	Grade IV	Abdomen

The incidence of primary brain tumors has been increased in the developed countries during the last few decades. However, this increase correlates with improved diagnostic methods and imaging technologies [International Agency for Research on Cancer, 2008].

Brain Tumor Diagnosis and Treatment Planning

There is no specific clinical singular symptom for brain tumors. Symptoms depend on the tumor's size, location, and rate of growth. Commonly, the first symptom may be an epileptic seizure. The list of symptoms may further include unusual or more frequent and more severe headaches, difficulties with vision, balance, speech, or hearing, as well as unexplained nausea or vomiting. If the patient suffers from such symptoms or a combination thereof, diagnostic investigation starts with an anamnesis. Next, clinical and laboratory investigations can exclude infections. Non-invasive, high-resolution imaging techniques like MRI and computer tomography scans may identify brain tumors since they often exhibit different colored masses in the image data. However, brain tumor detection is hardened by the blood-brain barrier (BBB). Since the BBB separates blood from the brain, many contrast agents could not reach the tumor at its very early stage. Once the tumor causes a BBB disruption, a stronger contrast agent enhancement will occur. This will also influence the signal intensity calibration, a problem that is discussed later on. Finally, only the histopathological examination of tumor tissue, extracted by brain biopsy or open surgery, can confirm or reject a brain tumor diagnosis. After this diagnosis, the standard treatment is similar to many malignancies and includes surgery (when feasible), radiation therapy, and adjuvant chemotherapy during and after radiation.

Surgery aims at the removal of the brain tumor and thus the diminishing of the mass effect and the compression of brain structures. Furthermore, normal cerebrospinal fluid pathways should be restored. Brain tissue is removed for pathological diagnosis and the tumor burden is reduced for other therapies. Glioma cells are highly invasive and infiltrate normal functioning brain parenchyma. First, the resection of this tissue could cause unacceptable neurological deficits. Second, the exact spatial extent of the tumor cannot be precisely determined. Thus, a total excision of a glioma is rarely possible [Mamelak and Jacoby, 2007].

Gliomas are not radiosensitive, but radiation is effective in retarding the glioma progression. A general cure of long-term control of the disease cannot be achieved. Radiation is further limited since normal brain parenchyma is also sensitive to radiation effects and a radiation injury and radiation-induced cell death is often as damaging as the primary tumor itself [Mamelak and Jacoby, 2007].

Also, systematic chemotherapy does not perform very well, since the blood-brain barrier hampers the distribution of the drug into the brain. Combination of radiation and chemotherapy has been found to increase the median survival by two months when compared to radiation alone for patients with newly diagnosed glioblastoma multiforme [Stupp et al., 2005].

The very bad prognosis for patients with an HGG and the lack of meaningful therapies has led to a continued research for better treatment. In addition, the differentiation between LGGs and HGGs plays an important role for treatment planning and patient outcome [Covarrubias et al., 2004]. Further, LGGs may transform to HGGs at some point in time and patients with LGGs are commonly subject to a life long monitoring.

2.2.2 Brain Perfusion Imaging with DSC-MRI

Conventional MRI is widely used for the diagnosis and follow-op of brain tumor patients. The MRI protocol used for brain tumor diagnosis comprises several acquisitions, structural T_1 and T_2-weighted sequences with high spatial resolution for morphologic analysis and the T_2^*-weighted perfusion series, with high temporal resolution. In this section, the image acquisition, the motion correction, the calibration of signal intensities, and the extraction of perfusion parameters are described.

Image Acquisition

The developments in perfusion-sensitive MRI in the last decades made it possible to assess the cerebral microvasculature including brain tumor perfusion. The neoangiogenetic tumor activity is exploited, which causes increased microvasculature and perfusion of tumorous tissue. In contrast to breast perfusion imaging with DCE-MRI (recall Section 2.1.2), the perfusion imaging of the brain is carried out with DSC-MRI. Due to the existence of the BBB, the human brain provides a unique environment for tracers, where the contrast agent remains compartmentalized, i.e., the agent remains intravascular. Thus, it causes a significant T_2 and T_2^* effect. The diffusible Gd-DTPA-based contrast agents (which are also employed for breast DCE-MRI, recall Sect. 2.1.2) behave like intravascular tracers, and are used for brain perfusion imaging as well.

When comparing T_2 and T_2^* sequences, it can be stated that the latter is sensitive to microvasculature whereas the T_2 sequence is more sensitive to the total vasculature [Weisskoff et al., 1994, Boxerman et al., 1995]. Recent studies [Donahue et al., 2000, Sugahara et al., 2001] favor the gradient-echo T_2^* sequence for brain tumor perfusion imaging since large, tortuous vessels are often present in tumors. Furthermore, T_2^* sequences are accompanied with shorter relaxation times than T_2 sequences (recall also Sect. 2.1.2). Thus, T_2^* DSC-MRI is the most established method for brain perfusion imaging [Provenzale et al., 2002].

The contrast agent is injected with an intravenous catheter such that a tight bolus of contrast material will pass through the brain. Successive images are acquired to analyse the first pass of contrast agent through the capillary bed of the brain, see Figure 2.13. The susceptibility effect causes a drop of the T_2^* signal intensities and its magnitude depends on the local blood volume and flow. Furthermore, the signal intensity decrease does not only occur inside the vessel lumen but extends in to the surrounding tissue as well [Villringer et al., 1988]. The signal intensity decrease is acquired on a voxel-by-voxel basis to extract a time-intensity curve, see Figure 2.14.

The most common sequences are adapted to the short transit times (only a few seconds) of the contrast agent's travel through the tissue. Hence a rapid MRI technique is required, like echo-planar imaging (EPI) and fast low-angle single-shot (FLASH) sequences. Thus, the repetition time ranges from one to two seconds, which in turn limits the number of slices that can be covered within this period. Typical spatial parameters of EPI sequences with this repetition time are: 128 × 128 image matrix, 2 *mm* spatial resolution and 7 *mm* slice distance for 10-15 acquired slices per point in time. Image acquisition covers about 40 - 80 time steps. FLASH sequences are used to overcome EPI image distortions (which may occur in areas with different susceptibility properties like tissue-air boundaries). However, a repetition time of 1-2 *s* only allows for a few slices of spatial coverage. One of these slice is positioned such that a major artery for extraction of the arterial input function is covered (this function will be described later on) with only a few slices left for the tissue of interest [Rempp et al., 1994]. In conclusion, the selection of temporal and spatial resolution is in general a compromise accounting for the particular application and the tissue that has to be studied. In contrast to the MR BI-RADS protocol, there is no equivalent MRI rating protocol for brain tumors available.

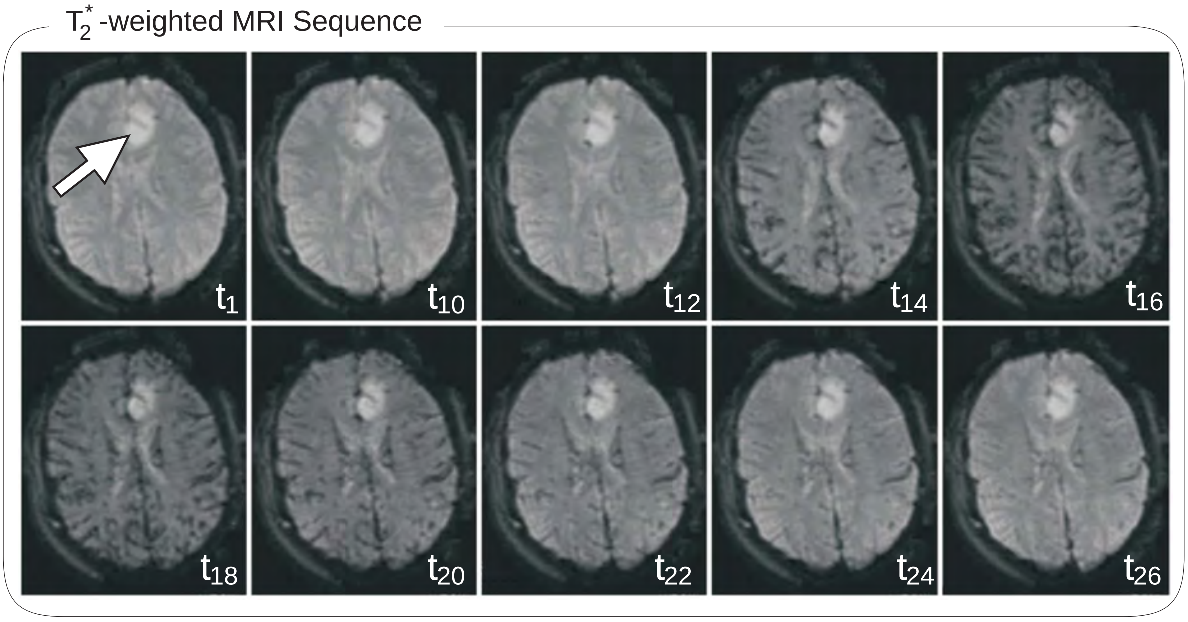

Figure 2.13: *Views of a T_2^*-weighted sequence of an HGG (see arrow). The MRI views illustrate the decrease of signal intensity at selected time steps with a repetition time of* 1.45 *s. Two ROIs have been defined for further analysis, see Figure 2.14. (Data is courtesy of Atle Bjørnerud, Department of Medical Physics, Rikshospitalet-Radiumhospitalet Medical Centre and Department of Physics, University of Oslo, Norway.)*

Motion Correction

The motion correction of DSC-MRI perfusion data of brain tumors is less complicated than breast perfusion registration (recall Sect. 2.1.2) due to the shorter acquisition time, i.e., less patient movement, and the skull as static reference object. Motion artifacts may arise due to head movement. However, this movement does not change the shape of the brain. Thus, a rigid body registration is sufficient to generate satisfying results. Hence, summarized information about perfusion data registration is also provided in [Preim and Botha, 2013].

Calibration of Signal Intensities

The T_2^* effect, i.e., the signal intensity decrease per voxel, yields a time-intensity curve, recall Figure 2.14. The transverse relaxation rate R_2^*, with $R_2^* = 1/T_2^*$, is proportional to the time-dependent concentration of contrast agent $C(t)$, a relation that has been determined theoretically and experimentally in the studies by Villringer et al. [1988], Rosen et al. [1990], and Weisskoff et al. [1994]. For the quantification of $C(t)$, a conversion from time-intensity to concentration-time curve is carried out:

$$C(t) = \kappa_t \Delta R_2^*(t) = \frac{\kappa_t}{TE} \cdot \ln\left(\frac{S(t)}{S_0}\right), \tag{2.4}$$

where $S(t)$ denotes the MRI signal intensity at time t and S_0 is the signal intensity of the baseline of the time-intensity curve. An illustration is provided in Figure 2.15. TE denotes the echo-time of the MRI scan. The proportionality constant κ_t depends on [Weisskoff et al., 1994, Boxerman et al., 1995]:

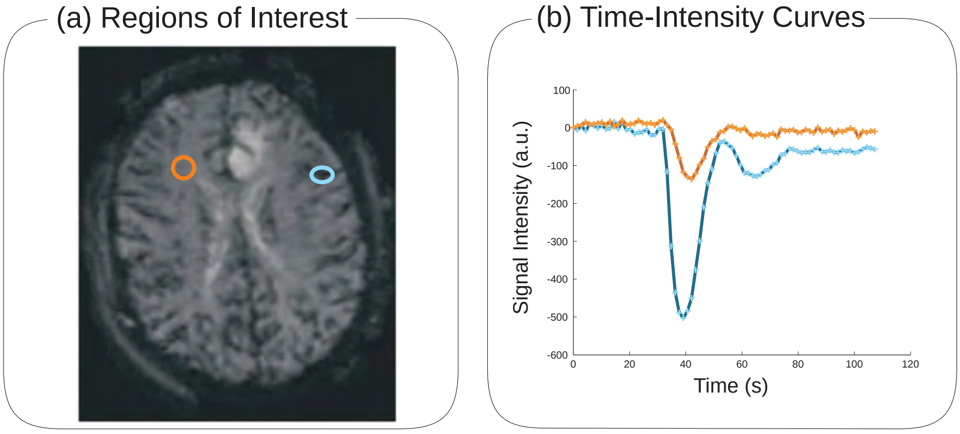

Figure 2.14: *Two ROIs and their corresponding time-intensity curves are presented, extracted from the data set shown in Figure 2.13. The first region covers a vessel (blue), whereas the second one covers white matter in the contralateral brain side to the tumor (orange). The average time-intensity curves (a.u., arbitrary units) are depicted in (b). The arterial region exhibits a larger signal intensity decrease than the white matter region. (Data is courtesy of Atle Bjørnerud, Department of Medical Physics, Rikshospitalet-Radiumhospitalet Medical Centre and Department of Physics, University of Oslo, Norway.)*

- the contrast agent,
- the pulse sequence parameters, and
- the MR field strength.

For the relationship of $C(t)$ and R_2^*, expressed by Eq. (2.4), negligible T_1 effects are assumed. This assumption is in general fulfilled with intravascular contrast agents and thus, with diffusible contrast agents and an intact BBB.

The calibration of signal intensities is only applicable for the first pass of the tracer. In Figures 2.14 and 2.15, also the recirculation phase, i.e., the second pass of the contrast agent, is illustrated. The relationship between $C(t)$ and $R_2^*(t)$ expressed by Eq. (2.4) is not maintained in this phase. In practice, two approaches exist. First, the calibration is only carried out until the last time step before recirculation begins. Second, the contrast agent's first pass concentration-time curve is fitted to a gamma variate function to model an ideal bolus shape function, see again Figure 2.15. The gamma variate fitting is conducted via [Thompson et al., 1964]:

$$C(t) = s \cdot (t - t_{BA})^r \cdot e^{-b \cdot (t - t_{BA})}, \tag{2.5}$$

where t_{BA} is the arrival time of the contrast agent, s a constant scaling factor, and r and b the coefficients determining the gamma variate function's shape.

Extraction of Brain Tumor Perfusion Parameters

To characterize perfusion of cerebral microvasculature, the quantitative hemodynamic parameters cerebral blood volume (CBV), cerebral blood flow (CBF), and the mean transit time (MTT) are extracted based on the concentration-time curve, i.e., the $C(t)$ curve. CBV is approximated as the area under a voxel's concentration-time-curve due to the compartmentalization of the tracer within the intravascular space. It is defined as the total volume of blood

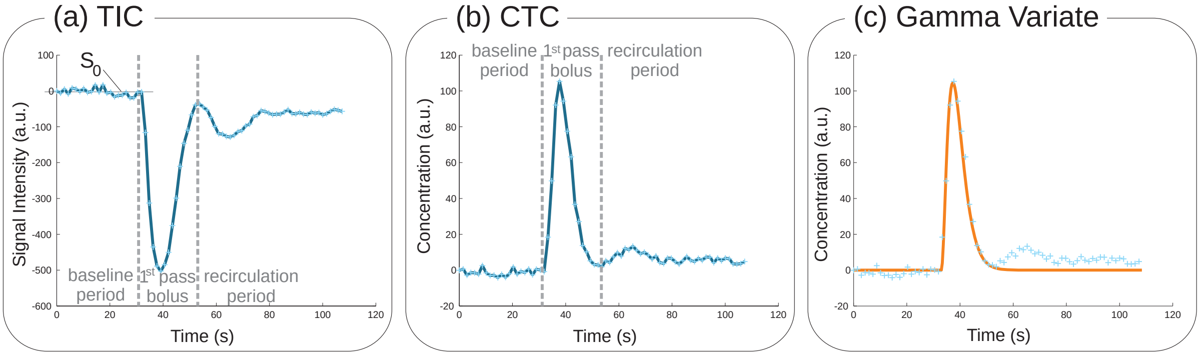

Figure 2.15: *Illustration of the conversion from the time-intensity curve (TIC) in (a) to the concentration-time curve (CTC) in (b) and a gamma variate fitting in (c). The time-intensity curve equals the curve extracted for the vessel in Figure 2.14. The time-intensity curve shape illustrates the different periods of contrast agent washin: the baseline period (before the arrival of the contrast agent bolus), the first passage of the contrast agent, and the period of recirculation. Hence, the second pass of the contrast agent is indicated with the smaller peak. The conversion from signal intensity (a.u., arbitrary units) to concentration yields the concentration-time curve depicted in (b). To eliminate the influence of recirculation, gamma variate fitting is carried out according to Eq.* (2.5).

traversing a given region of brain, measured in *ml* of blood per 100 *g* of brain tissue. CBV is proportional to the integral of $C(t)$, normalized to the total amount of tracer:

$$CBV = \frac{1}{\alpha} \frac{\int C(t)}{\int C_{AIF}(t)}, \tag{2.6}$$

where α is a proportionality constant. It depends on:

- the density of brain tissue and
- the difference in haematocrit levels between capillaries and large vessels.

The second issue arose since only the plasma volume is accessible to the contrast agent [Calamante et al., 1999]. $C_{AIF}(t)$ denotes the concentration-time curve of the arterial input function (AIF), i.e., the contrast agent concentration that reaches the cerebral tissue at the time t. $C_{AIF}(t)$ is in general extracted from a major cerebral artery, like the middle cerebral artery [Østergaard et al., 1996a] or the internal carotid artery [van Osch et al., 2001] (recall Fig. 2.11). The extraction of $C_{AIF}(t)$ is conducted with Eq. (2.4) with a corresponding proportionality constant κ_a. Hence, the same dependancies hold for κ_a as for κ_t, recall Eq. (2.4). The more contrast agent is injected, the greater contrast concentration will reach the cerebral tissue, independently of the actual CBV. This is the reason why, the normalization to the $C_{AIF}(t)$ is carried out for CBV approximation.

The parameter CBF denotes the cerebral blood flow and describes the volume of blood traversing a given region of brain per unit time, measured in *ml* of blood per 100 *g* of brain tissue per minute. For the CBF analysis, the indicator dilution theory for intravascular contrast agents is applied. Thereby, the contrast agent concentration $C(t)$ can be described as [Østergaard et al., 1996b, Calamante et al., 1999]:

$$C(t) = \alpha \cdot CBF \cdot (C_{AIF}(t) \otimes R(t)) = \alpha \cdot CBF \cdot \int_0^t (C_{AIF}(\tau) R(t-\tau)) \mathrm{d}\tau, \tag{2.7}$$

where $C_{AIF}(t)$ is the concentration of the AIF and $R(t-\tau)$ denotes the residue function, i.e., the fraction of contrast agent that remains in the tissue at time t after the contrast agent bolus injection at time τ. Thus, $R(0) = 1$ since no contrast agent particles have left the tissue at time $t = \tau$, and $R(\infty) = 0$ since no contrast agent particles remain in the tissue due to the intact BBB and the washout of the contrast agent through normal perfusion. Hence, the convolution of two functions is denoted with the $\otimes$ operator. Its expression as integral is provided by the last term in Eq. (2.7). As introduced in Eq. (2.6), α is a proportionality constant.

To extract the CBF, the term $CBF \cdot R(t)$ is isolated via deconvolution of Eq. (2.7). Next, CBF is obtained with $CBF \cdot R(t)$ and $R(0) = 1$ at time $t = 0$. For the deconvolution operation, different mathematical approaches exist and a more detailed description can be found in [Østergaard et al., 1996b]. The most wide-spread method is the singular value decomposition [Rosen et al., 1990, Østergaard et al., 1996b].

The parameter MTT describes the average time for a molecule of contrast agent to pass through the cerebral vasculature. Since the three physiological parameters CBV, CBF, and MTT are related through the central volume theorem [Stewart, 1894], MTT can be extracted via:

$$MTT = \frac{CBV}{CBF}. \tag{2.8}$$

In theory, the equations (2.4), (2.6), and (2.7) can provide absolute units of CBV, CBF and MTT. However, the proportionality constants α, κ_t, and κ_a would have to be acquired. Yet, an absolute and correct measurement of CBV, CBF, and MTT is not available. This issue is addressed by Calamante [2005] in more detail. The following problems were identified:

- potential errors due to the presence of delay and dispersion on the estimated AIF,
- partial volume effects in the quantification of the AIF,
- a change in the proportionality constants or scaling factors, and
- changes in haematocrit levels.

Although absolute measurements of CBV, CBF, and MTT are not possible yet, the extracted parameters approximated with the described methods are closely related, i.e., proportional, to the underlying absolute parameter values.

When it comes to brain tumor perfusion analysis, a disruption of the BBB has to be taken into account due to infiltrating tumor growth. Because of a disrupted BBB, the contrast agent could leak into the extravascular space and the assumption of the intravascular tracer is incorrect. Furthermore, the second assumption of a negligible T_1 effect is not valid. To solve this problem, it has been suggested to apply a small pre-loading dose of contrast agent to tissue with moderate contrast extravasation such that the T_1 effect of the main bolus, i.e., the second bolus, is negligible [Kassner et al., 2000]. Another approach is the modeling of the combined T_1 and T_2 effects, to extract ΔR_2^* values that are not contaminated by T_1 enhancement [Weisskoff et al., 1994]. Furthermore, studies suggest to employ a dual-echo T_2^*-weighted sequence to extract ΔR_2^* without T_1 enhancement [Barbier et al., 1999]. These methods are explained in more detail in [Calamante, 2005].

In general, the evaluation of brain tumor perfusion MRI is based on the parameter CBV, whereas CBF and MTT are more important for the assessment of cerebral ischemic stroke

[Covarrubias et al., 2004]. The term *relative* refers to a normalization of CBV values. Different approaches exist and the most general consists of the normalization with the averaged white matter's CBV values of the contralateral side [Wetzel et al., 2002], yielding relative CBV (rCBV) values. The parameter rCBV is an important indicator for a patient's survival since tumor growth induces angiogenesis and thus elevated rCBV values. It can further be employed for brain tumor grading into LGG and HGG, since rCBV correlates with the tumor grade [Law et al., 2004]. Like the ROI-based evaluation of contrast enhancement, rCBV is extracted as average value of a ROI as well. Since the ROI is placed such that it includes highest rCBV values but no brain vessels, the ROI is also referred to as hot spot.

Beyond the extraction of quantitative parameters, descriptive perfusion parameters (also called summary parameters) are calculated for characterization of brain perfusion data. They are illustrated in Figure 2.16, including the parameters TTP, PE, Integral, UpSlope, and DownSlope that have been introduced for breast perfusion, recall Section 2.1.2. Additionally, the following parameters are extracted: full width at half maximum (FWHM), the first moment of the concentration-time curve (FMC), and the time points t_{BA} and t_{end}, representing the arrival of the contrast agent and the end of the first pass of the bolus, respectively. In the survey by Preim et al. [2009], the reader becomes acquainted with a more detailed description of summary parameters in perfusion imaging. The main advantage of these parameters is the fast and straightforward approximation without extracting the AIF. Summary perfusion parameters in general are widely employed in clinical applications like stroke diagnosis. The parameters may provide important clinical information. However, none of these parameters can provide a direct measurement of the underlying perfusion. Furthermore, they may be prone to errors due to the lack of the integration of the AIF and the residue function. As a result, the parameters may be hampered by the injection conditions of the contrast agent, the patient's vascular structures and the patient's cardiac output [Perthen et al., 2002].

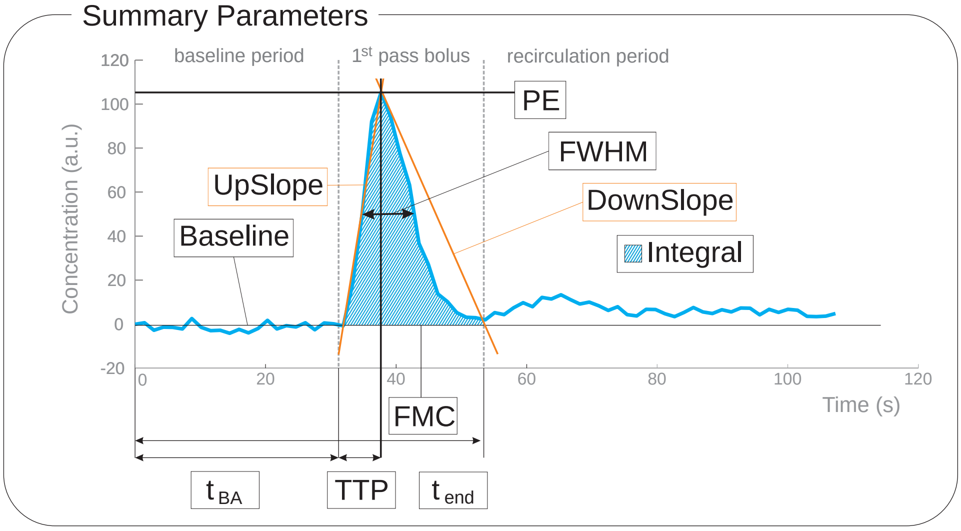

Figure 2.16: Illustration of the summary parameters PE, Integral, UpSlope, DownSlope, FWHM, and the time related parameters TTP, FMC, t_{BA} and t_{end}. Summary parameters are only extracted for the first pass of the contrast agent from the concentration-time curve (as illustrated) or even from the time-intensity curve.

2.3 Summary and Implications for this Thesis

Evaluation of perfusion MRI plays an important role to narrow down the differential diagnosis of tumors in medical imaging. This thesis focuses on two application scenarios: the evaluation of breast tumor perfusion data and brain perfusion data. These pathologies fundamentally differ concerning the underlying vasculature: the breast tissue and thus a breast tumor have direct access to the contrast agent, whereas the blood in the brain remains compartmentalized due to the BBB. Therefore, T_1-weighted as well as T_2^*-weighted MR sequences are acquired, each accompanied by its own advantages and disadvantages.

The breast MR perfusion analysis is strongly intertwined with the evaluation of the shape of the corresponding RE curve courses. Thus, the main focus of this thesis is the optimal evaluation of the contrast enhancement of a tumor, under consideration of finding the best ROI for RE curve extraction. The forming of these ROIs is adapted to the detection of similarly perfused regions. Hence a tumor subdivision has to be carried out via clustering. Due to the limited number of time steps, the approximation of the similarity of perfusion characteristics rather based on the summary perfusion parameters instead of pharmacokinetic modeling parameters. Furthermore, the tumor subdivision via clustering allows for automatic detection of a most suspect ROI as well as the extraction of specific features. Since heterogeneity is indicative for tumor malignancy, the clustering result will be employed to extract features that describe the tumor's heterogeneity.

For glioma diagnosis, promoted by brain tumor perfusion MRI, it is important to differentiate between LGG and HGG since important attributes, e.g., progression time and survival rate, are associated to the tumor types. Hence, quantitative parameters, predominantly CBV, should be evaluated in more detail, especially when MR perfusion scans of the brain are compared to characterize a longitudinal progression. To examine the transformation from an LGG into an HGG, this thesis focuses on the visual analysis of longitudinal brain tumor MR perfusion studies that comprise such transformations. Due to the need of comparison from perfusion studies arising from different time steps of the same patients, the usage of summary parameters is avoided, and the analysis is mainly based on the evaluation of the parameter CBV due to its high importance for LGG and HGG characterization.

In summary, this thesis has the following goals:

1. The improved (visual) evaluation of breast tumor DCE-MRI data, including a subdivision via clustering in similarly perfused regions.
2. The 3D visualization of breast tumor DCE-MRI data, including the 3D view of the clustered tumor.
3. A thorough cluster analysis of breast tumor DCE-MRI data as well as the discriminative power of clustering results for an automatic classification with focus on heterogeneity and kinetic features.
4. The visual analysis of transformation from LGGs into HGGs within a longitudinal brain tumor MRI study.

These goals will be tackled (in this order) in Chapters 5, 6, 7, and 8.

3. Clustering of Medical Perfusion Data

3 Clustering of Medical Perfusion Data

For biomedical research, increasing sets of data have to be evaluated. Clustering is carried out to provide insight in the natural grouping or structure of these data sets. In general, it is applied to create groups of meaningful subclasses of a set of objects. Alternatively, it can be employed as a preprocessing tool such that further algorithms evaluate the attributes of detected clusters, e.g., for biomedical purposes.

In this chapter, the importance of clustering for perfusion data is explained in Section 3.1. Afterwards, a general clustering categorization is provided in Section 3.2, including advantages and disadvantages of the clustering algorithms with respect to medical perfusion data. Particular important concepts for this thesis are identified. These concepts are:

- density-based clustering approaches, described in Section 3.3,
- the reduction of feature space dimensionality via a principal component analysis as well as clustering in the spectral domain, explained in Section 3.4, and
- the region merging approach, presented in Section 3.5.

Finally, a conclusion of this chapter in given in Section 3.6.

3.1 The Importance of Clustering for Evaluation of Perfusion Data

As it was explained in Chapter 2, the evaluation of perfusion MRI data is based on the evaluation of the contrast enhancement. Hence, a region of interest (ROI) is manually placed for the clinical evaluation of breast tumor perfusion as well as brain tumor perfusion. The ROI covers voxels with similar relative enhancement (RE) kinetics. Next, the contrast agent kinetics are evaluated via averaging the voxels' RE values. Such ROIs need to contain at least a few voxels and yet they must not contain too many voxels. This is reasoned by:

1. A single voxel could be an outlier and the ROI is assumed to be more robust against artifacts.
2. Large ROIs could cover different tumor parts, e.g., benign and malignant ones.

These problems are illustrated in Figure 3.1. Hence, single voxels show arbitrary enhancement kinetics and it is difficult to rate the tumor's malignancy, see Figure 3.1(c). Furthermore, the large ROI does not reflect the washout characteristics, see Figure 3.1(i). Since the intra- and inter-observer variability of the manual ROI placement is identified as drawback in many classification approaches (e.g., [Stoutjesdijk et al., 2005]), this thesis will come up with an automatic ROI identification. The automatic ROI identification is based on an automatic subdivision of the tumor into similarly perfused tumor parts and the detection of the most suspicious or malignant tumor part of this subdivision. For the subdivision of the tumor, clustering is essential. Furthermore, each of the clusters of an appropriate clustering algorithm fulfills both reasons above.

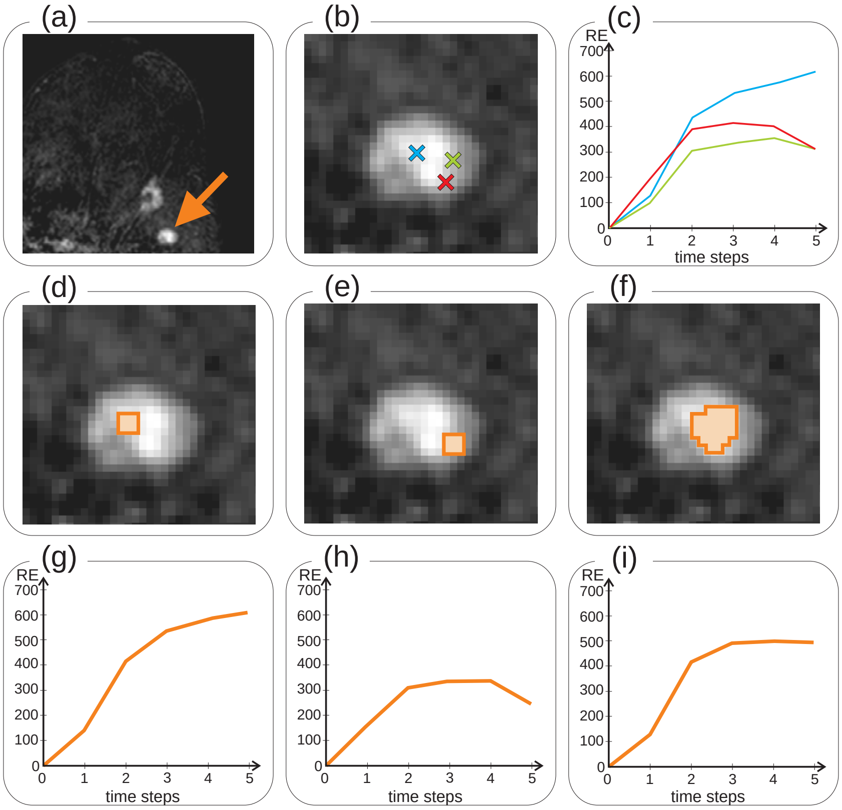

Figure 3.1: *The challenges of tumor perfusion enhancement evaluation. In (a), the subtract view reveals two tumors, focus is set on the round one (marked with an arrow). In (b), three single voxels have been marked and their corresponding RE curves are depicted in (c). Note that exactly three different curves are presented: a washout curve, a plateau curve, and a continuously increasing one. In (d) - (f), the pitfalls of ROI placement are illustrated. The ROI in (d) covers benign tumor parts with an average increasing curve, see (g). The ROI in (e) covers malignant tumor parts with an average washout curve, see (h). The ROI in (f) covers both tissue types and the averaged curve is distorted, yielding an average plateau curve. This lesion was histopathological proven to be malignant. (Data is courtesy of U. Preim, Municipal Hospital Magdeburg, Germany.)*

Beyond the automatic ROI determination for clinical practice, the clustering of tumor perfusion data is important for clinical research. Many automatic classification systems, which automatically divide into benign and malignant tumors, employ features extracted from a clustering result. For example, the study by Chen et al. [2006a] automatically classifies breast DCE-MRI tumors into benign and malignant based on features from a fuzzy c-means clustering. There is no gold standard for clustering of perfusion data available yet and each clustering-based classification approach is heavily dependent on the clustering result.

One further property of the underlying data is the small size of tumors ($30-1000$ voxels). Therefore, the runtimes of the different clustering algorithms were almost irrelevant for all developed methods. Thus, no further discussion about the runtimes are provided in this chapter and the reader is encouraged to have a look at the referenced algorithms for a detailed algorithm's runtime specification.

3.2 Categorization of Cluster Analysis

In this section, the concept of clustering is explained in detail. Therefore, a categorization of clustering approaches is presented, including the adaption of the clustering concepts to the perfusion data, on which this thesis is based upon.

Clustering is the partitioning of a set of objects into distinct groups, i.e., clusters, such that two objects from the same cluster are similar to each other and two objects from distinct clusters are not. The objects exhibit certain *features* in their *feature space*. The similarity between objects is calculated with a *distance function* over their features, e.g., the Euclidean distance or a correlation coefficient that approximates the dependency between two variables. For perfusion data, each voxel is interpreted as an *object* and its perfusion parameter values (e.g., DownSlope) are interpreted as *features*. All tumor voxels form the *database* for the actual clustering run. The number of features that are employed for the clustering process defines the dimensionality of the *feature space*.

Various cluster analysis techniques have been presented: each one with advantages and disadvantages when applied to solve a specific problem. The categorization of cluster algorithms is not standardized since different researchers need to extract different clusters on different databases. Clustering algorithms rely on different concepts. The two most fundamental concepts are the *partitioning* and *hierarchical* approach [Kaufman and Rousseeuw, 1990]. In [Han et al., 2011], two more concepts are added: the grid-based and the density-based concept. Therefore, they yield four basic clustering concepts:

- Partitioning clustering algorithms,
- Hierarchical clustering algorithms,
- Grid-based clustering algorithms, and
- Density-based clustering algorithms.

Beyond these basic concepts, Han et al. [2011] introduce advanced clustering concepts, see Figure 3.2:

- Fuzzy and probabilistic model-based approaches,
- Clustering of high-dimensional data, including the subspace clustering and the dimensionality reduction,
- Clustering of graph and network data, and
- Clustering with constraints, including hard and soft constraints.

This categorization is only one of many possible categorizations due to the complexity of data clustering in general. For a more comprehensive overview the reader is referred to the survey by Jain et al. [1999].

3.2.1 Basic Clustering Concepts

The first part of this section provides an overview of the four basic clustering concepts. Furthermore, for each concept, a clustering algorithm is introduced and applied to an artificially

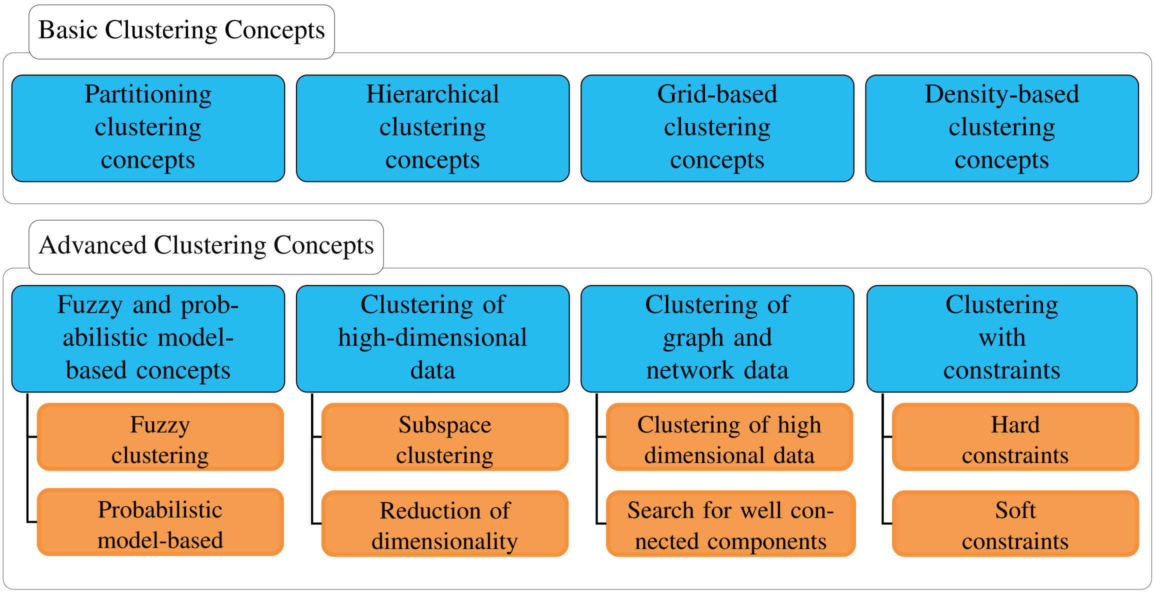

Figure 3.2: *Overview of basic and advanced clustering concepts based on [Han et al., 2011].*

generated data set, see Figure 3.3. Next, the adaption to perfusion data is described. The categorization of clustering concepts is not exclusive, and as it will be described in the following, many clustering algorithms combine different concepts.

Partitioning Clustering Algorithms

Partitioning clustering algorithms create k clusters from a set of n objects, $k \leq n$. Furthermore, k is an input parameter and domain knowledge is needed to define the appropriate number of clusters k in advance. The algorithm starts in general with an initial partition of the database's feature space by creating k representatives in this feature space. Next, each object is assigned to its closest representative in terms of the similarity function. The cluster result is optimized by iteratively adjusting the representatives (e.g., as a centroid or mediod calculation) and assigning the objects to clusters. Hence, the clusters are convex w.r.t. the distance function, which is very restrictive for some applications. Note that the term *convex clusters* describes a clustering result where the intersection of the convex hulls for each pair of two clusters is always empty.

The most wide-spread example for the group of partitioning clustering algorithms is the k-means algorithm [MacQueen, 1967]. Each cluster is defined by its mean, i.e., its centroid. Initially, the k centroids are randomly distributed. Next, an optimization is carried out by iteratively assigning objects to their closest centroid and updating the centroids' positions based on the actual assigned objects. Thus, the assignment of objects may change due to the updated centroids' positions. The clustering is finished if the algorithm converges or the change is sufficiently small. In Figure 3.3 (b), the clustering result of k-means with $k = 2$ is presented. Due to the convex clusters, the two groups of objects could not adequately be identified. Furthermore, an unfavorable initialization of initial cluster centers may hamper the clustering result. For example, one cluster contains the object near the origin and the second cluster contains all remaining objects in the example of Figure 3.3 (b).

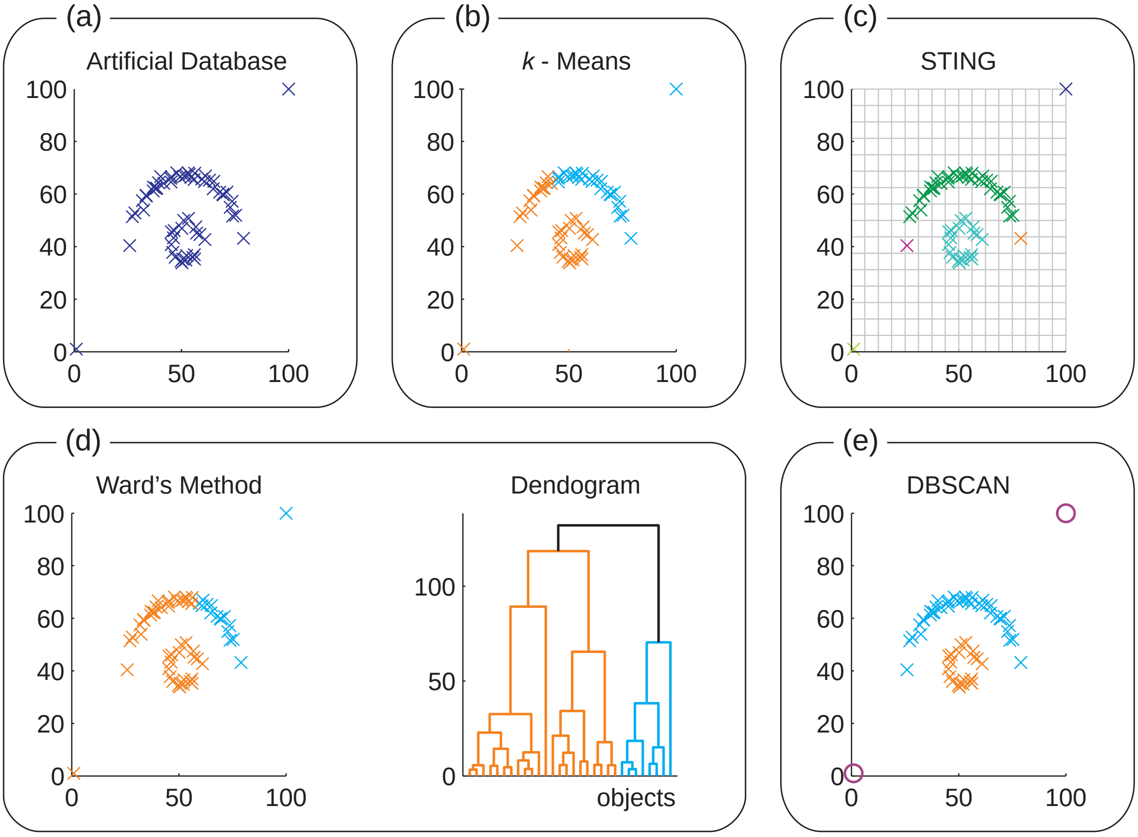

Figure 3.3: *Illustration of the four basic clustering concepts [Han et al., 2011]. In (a), the 2D feature space of the data is presented in the scatterplot. The data was artificially generated for illustration purpose. In (b), the partitioning k-means cluster result is depicted. In (c), the grid-based STING algorithm is presented. In (d), the hierarchical clustering result, based on Ward's method, and the corresponding dendrogram are depicted. In (e), the density-based DBSCAN algorithm is illustrated. For all basic clustering concepts an Euclidean distance function was employed.*

Hierarchical Clustering Algorithms

Hierarchical clustering algorithms yield a hierarchical decomposition of the database, represented by a dendrogram. They are subdivided in agglomerative and divisive approaches. Agglomerative approaches initially group each object into one cluster. Then, similar clusters are iteratively combined into a new cluster until all objects are contained in one remaining cluster. Alternatively, divisive approaches start with a cluster comprising all objects and iteratively split them up until each object forms a single cluster. Hierarchical algorithms need a termination condition that indicates when the merging or splitting approach has to be stopped. In contrast to partitioning algorithms, the number of clusters is not needed as input, but the finding of an appropriate termination condition can be challenging. However, based on the application scenario, the termination condition can be defined such that the user aims at a partition with k clusters. Hierarchical clustering approaches are also referred to as connectivity clustering approaches since the dendrogram connects the clusters.

Ward's method [Ward, 1963] is an agglomerative hierarchical clustering where the similarity function is based on the within-cluster variance. The within-cluster variance for each pair of clusters is extracted based on their sum of squared errors. Iteratively, the pair with minimum within-cluster variance is merged. In Figure 3.3 (d), the clustering result of Ward's method is depicted as well as the dendrogram representing the hierarchical decomposition of the data. The termination condition was set to a certain threshold for within-cluster variance to obtain two clusters.

Grid-Based Clustering Algorithms

Grid-based clustering algorithms divide the database's feature space in a limited number of cells - the grid. Grid-based methods are feature space-driven. This is in contrast to the other basic concepts, which are in general data-driven and adapted to the distribution of objects in the feature space. The partitioning of the feature space into cells is independent of the distribution of the objects and yields a multi-resolution grid data structure. Since all operations are carried out along the grid, a fast execution time is achieved that depends on the grid resolution instead of the number of objects. However, for the application of perfusion data, the fast execution time is not mandatory.

The statistical information grid (STING) approach [Wang et al., 1997] stores statistical information for each cell like the minimum and maximum of the cell's objects. These statistical information are employed for query processing and other data analysis tasks. To obtain the hierarchical structure of grid cells, the first cell contains the whole feature space. Next, this cell is iteratively split into a given number n of children by dividing the parent cell in n equally sized regions until a user-defined resolution is achieved. To group similar objects as answer for a query process, only relevant cells (i.e., whom statistical information met the query) are analyzed in the hierarchy. Irrelevant cells as well as their children are not examined. Naturally, the quality of STING depends on the granularity of the bottom layer. The cluster shapes are isothetic, i.e., they depend on the grid cell. Figure 3.3(c) illustrates the STING clustering result, including the bottom layer of the hierarchy.

Density-Based Clustering Algorithms

Density-based algorithms identify clusters as regions with increased density separated by areas with lower density in the feature space. Objects of these sparse areas are usually considered to be noise (outliers) or part of the cluster border. The extraction of the density is based on the neighborhood of an object in the feature space. The size of this neighborhood has to be provided as input parameter. However, the identification of the number of clusters as well as outlier identification is automatically carried out.

The most prominent algorithm is the density-based spatial clustering of application with noise (DBSCAN), presented by Ester et al. [1996]. Each object's neighborhood is analyzed in the feature space. Depending on the number of objects in the neighborhood, the object is defined as core object, border object, or outlier. If core objects and border objects are connected, they form a cluster, a process that will be described in more detail in Section 3.3. In Figure 3.3(e), the clustering result of the DBSCAN algorithm is illustrated. The algorithm has no problems to detect arbitrarily shaped clusters, since DBSCAN is based on the density of objects in the feature space. Furthermore, the two objects in the origin and top right of the database are identified as outliers (see the red circles in Fig 3.3(e)).

Adaption of Basic Clustering Concepts to Perfusion Data

The medical scope of this thesis is the analysis of tumor perfusion data. The presented algorithms will be compared regarding their suitability for the underlying data. The results are listed in Table 3.1, and the criteria: global optimum, automatic extraction of cluster number, the cluster shape, and outlier detection are explained in the following. With respect to the clinical requirements, the employed clustering technique always needs to produce the same results and find the global optimum instead of a local optimum. Local optima are produced due to the order of the processed objects. For example, the k-means algorithm may not find the global optimum due to the random initial k seeds. The next criterion covers the number of clusters. Contrast-enhanced tumor data sets exhibit very different concentration time-curves and each tumor is different from others. Thus, a pre-defined amount of clusters is not feasible. Furthermore, the amount of clusters would depend on malignancy since malignant tumors are in general more heterogeneous than benign ones, requiring more clusters for an appropriate subdivision of the tumor tissue. However, malignancy of a tumor is not always known and sometimes it is the goal of the clustering to predict this malignancy and not vice versa. The third criterion deals with the cluster shape. Clusters should be arbitrarily shaped and a restriction to convex clusters would be misleading, since the tumors strongly vary in shape, size, and attributes. Hence, the disadvantages of grid-based methods become apparent. For example the cluster borders of a clustering result extracted with STING are aligned to the bottom layer grid granularity and consist of horizontal or vertical pieces only. The last criterion is assigned to the detection and identification of outliers. Outlier detection favors the evaluation of tumor perfusion data since motion artifacts could cause outliers in these type of data. As a first result, density-based concepts seems best suited when considering the basic clustering concepts.

Table 3.1: *Suitability of the basic clustering algorithm concepts for medical tumor perfusion data based on four empirical criteria.*

	Partitioning concepts	Hierarchical concepts	Grid-based concepts	Density-based concepts
Global maximum	no	yes	yes	yes
Automatic no. of clusters	no	yes	yes	yes
Cluster shape	convex	arbitrary	box-shaped	arbitrarily
Outlier detection	no	no	no	yes

3.2.2 Advanced Clustering Concepts

Advanced clustering concepts are designed to cope with various challenges. First, the concept of probabilistic model-based clustering approaches is explained, recall Figure 3.2. Next, advanced techniques for the clustering of high-dimensional data are described. This is followed by a brief description of clustering of graph and network data and concluded by a short introduction of clustering with constraints. Afterwards, the adaption to perfusion data is described.

Fuzzy and Probabilistic Model-Based Clustering Algorithms

Fuzzy and probabilistic model-based clustering concepts contain objects and clusters where an object can be part of multiple clusters. This is in contrast to the previously discussed basic concepts where each object of the database exclusively belongs to one cluster. Fuzzy concepts or probabilistic model-based concepts replace this binary membership with a probability, i.e., an object belongs with a certain probability to each cluster. A fuzzy clustering is a fuzzy set of clusters and the object's membership probability lies in the interval $[0,1]$. Thus, a fuzzy clustering is also referred to as soft clustering. The quality of a fuzzy clustering, i.e., how well a fuzzy clustering fits a database, can be assessed by analyzing the sum of the squared distances to all cluster centers weighted by the degrees of membership that the object belongs to this distance.

The probabilistic model-based clustering concept is similar to the fuzzy clustering concept. A probabilistic cluster C is defined via a probability density function f. Hence, for an object o of the database, $f(o)$ is the relative likelihood that an instance of C appears at the location of o in the feature space. Thus, the complete database is interpreted as finite sample of the possible instances of the clusters. Consequently, probabilistic model-based cluster analysis aims at determining a set of k probabilistic clusters with k probability density functions that most likely generated this database. Similar to the fuzzy approach, each object has a certain membership of each of the clusters. In theory, the probability density function covers background knowledge of the specific application and may be of arbitrary complexity. Practically, these functions are modeled with parametrized distributions, e.g., a Gaussian distribution. The quality of a probabilistic model-based clustering can be assessed by extracting the likelihood that all objects of the database were generated with the probability density functions weighted by the membership degrees.

For example, the expectation maximization (EM) algorithm [Dempster et al., 1977] can be employed as framework for fuzzy clustering or probabilistic model-based clustering. It consists of two steps: the expectation step and the maximization step. In the first step, objects are assigned to clusters based on the current fuzzy clustering or the current parameters of the probabilistic density functions. In the maximization step, the new clustering is determined. For fuzzy clusterings, the sum of membership-weighted squared distances for each object is minimized. For probabilistic model-based clusterings, the expected likelihood is maximized by adjusting the parameters of the employed distributions. These steps are iterated until the clustering cannot be further improved due to the converging of the clustering or a sufficiently small change of the clustering. Hence, the EM algorithm only detects a local optimum.

Clustering of High-Dimensional Data

The clustering of high-dimensional data is often affected by noise in many dimensions of the feature space. Hence, the similarity measure may be strongly influenced or even dominated by the noise in certain dimensions. Therefore, the clustering of high-dimensional data aims at the detection of meaningful clusters and their embedding space. Two general concepts exist to reduce the high-dimensional data space: the subspace clustering concept and the reduction of the dimensionality. Representatives of the first class aim at cluster detection in subspaces of the full feature space, whereas the representatives of the second class aim at the generation of a new lower dimensional feature space.

The subspace clustering idea can be further divided into bottom-up and top-down approaches. Bottom-up methods start with the analysis of low-dimensional subspaces and analyze only high-dimensional subspaces that are expected to hold meaningful clusters. Top-down approaches start with the high-dimensional, complete attribute space and recursively search in lower dimensional subspaces. For example, the subspace clustering SUBCLU algorithm [Kailing et al., 2004] employs the same density-based concepts like the DBSCAN approach and carries out a bottom-up method. That means, if a subspace without any meaningful clusters is detected, this subspace is not included in any further cluster analysis.

For dimensionality reduction, the original dimensions are combined or transformed into a new feature space. A common approach is the application of a principal component analysis (PCA) since it accounts for possible correlated attributes of the objects. The PCA yields an orthogonal linear transformation of the feature space into a new data space such that the greatest variance of the database is expressed by the first dimension - the first principal component. The second dimension is defined by the second principal component, which is orthogonal to the first principal component and expresses the second greatest variance possible. Due to the reduced correlation, only a few principal components are necessary to cover the major part of the database's variance, e.g., 95%, yielding a transformed feature space with a much lower dimensionality. In the projected feature space, a standard clustering algorithm can be applied and the clustering result is back-projected in the high-dimensional feature space afterwards.

Clustering of Graph and Network Data

Clustering of graph and network data plays an important role in visual analytic tasks due to its wide-spread use in online social networks or the World Wide Web in general. Hence, a special challenge arise from the lack of different attributes. In general, only the objects are given as graph vertices and the relationships between them via connecting edges form the set of attributes. Clustering concepts for graph and network data aim to identify clusters such that vertices within a cluster are similar to each other, i.e., all vertices are well connected and vertices of different clusters are not similar to each other, i.e., they are connected in a much weaker way. Mostly, the clustering is carried out either by dimension reduction or by a search for well-connected components, like the structural clustering algorithm for networks (SCAN) algorithm [Xu et al., 2007]. Similar to DBSCAN, the SCAN algorithm defines core vertices in dense graph parts and grows clusters from these.

Clustering with Constraints

Clustering with constraints allow for special relationships in the database and incorporate advanced domain knowledge via *hard constraints* and *soft constraints*. Hard constraints maintain a certain relationship, e.g., the *must-link* constraint. If a must-link constraint is assigned to two objects o_1 and o_2 then o_1 and o_2 must be grouped into the same cluster. Hard constraints have to be taken into account during the clustering process. For example, the COP-k-means algorithm [Wagstaff et al., 2001] works similar as the general k-means algorithm, but maintains the must-link constraints during initialization of the cluster centers first and prevents a must-link constraint violation during cluster center assignment by carrying out the nearest feasible center assignment, afterwards. Due to conflicting hard constraints, it is sometimes impossible to fulfill all hard constraints. Therefore, soft constraints assign a certain penalty for violated hard constraints of a specific clustering result. Thus, the clustering process becomes an optimization problem where the penalties have to be reduced and the clustering quality score has to be maximized. An example was presented by Davidson and Ravi [2005] with the Constrained Vector Quantization Error (CVQE) algorithm, which is based on k-means.

Adaption of Advanced Clustering Concepts to Perfusion Data

Further challenges of the clustering of perfusion data arise from the high-dimensionality of the feature space. Therefore, advanced cluster techniques may be useful, see Table 3.2. Hence, a fuzzy or probabilistic model-based approach is rejected since this thesis focuses on an exclusive tumor subdivision. Thus, the clinical expert can better interpret an exclusive subdivision. In addition, the tumor voxels underlay an unknown distribution, which can not be easily predicted due to tumor heterogeneity. When it comes to the dimensionality of the feature space, a dimensionality reduction or subspace clustering may be favorable. Dependent on the amount of extracted perfusion parameters, the feature space may exhibit more or less dimensions. However, there will be in general no benefit obtained by applying a concept for clustering of graph or network data, but the clustering with constraints may be well suited. In detail, the tumor data should be grouped in regions of spatially connected voxels. Thus, a hard constraint could prevent the merging of objects into a cluster if the objects are not spatially connected.

Table 3.2: *The suitability of the advanced clustering concepts for medical perfusion data.*

	Useful for clustering of tumor perfusion data?
Fuzzy and probabilistic model-based	no
Clustering of high-dimensional data	yes
Clustering of graph and network data	no
Clustering with constraints	yes

As a result of this informative comparison, the following concepts will be explained in more detail:

- the density-based clustering concepts, including DBSCAN, OPTICS, and SUBCLU (Sect. 3.3),
- the statistical analysis of attributes, including the dependency of attributes and the PCA for dimension reduction based on the redundancy of attributes (Sect. 3.4),
- the clustering in the spectral domain, including the dimension reduction (also described in Sect. 3.4), and
- the hierarchical clustering approach region merging (Sect. 3.5) combined with the constraint that only spatially connected voxels can be grouped.

Due to the complexity and the wide-spread use for data mining and knowledge discovery in databases, a multitude of clustering concepts exists. The reader is referred to [Han et al., 2011] for a more comprehensive discussion about clustering concepts considering different application areas.

3.3 Density-Based Clustering

Density-based clustering methods merge objects into regions, if they have a high density in the database's feature space. The most wide-spread approach is the *Density Based Spatial Clustering of Application with Noise* (DBSCAN), developed by Ester et al. [1996]. The *Subspace Clustering* (SUBCLU) [Kailing et al., 2004] algorithm employs the density concepts of DBSCAN in subspaces of the feature space. The *Ordering Points To Identify the Clustering Structure* (OPTICS) [Ankerst et al., 1999] algorithm will be introduced as third concepts.

3.3.1 DBSCAN

The DBSCAN approach is based on the *density* of objects. The density of an object o is the number of objects (including o) in the ε-neighborhood of o in the feature space, see the illustration in Figure 3.4. Based on their densities in the ε-neighborhoods, and a parameter *minPoints*, objects are classified into core objects, border objects, and outliers (see Fig. 3.4):

- core objects have at least a density of *minPoints*,
- border objects have a smaller density than *minPoints*, but can be found in the ε-neighborhood of a core object, and
- outliers have a smaller density than *minPoints* and are not in any ε-neighborhood of a core object

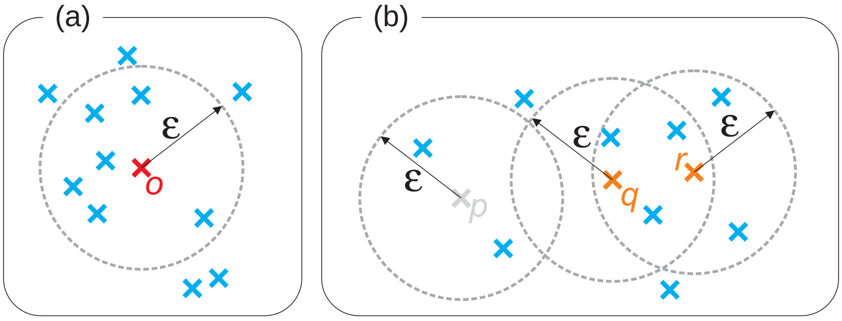

Figure 3.4: *Illustration of the object classification based on the density of the* ε*-neighborhood. In (a), the density of object o is depicted. The density equals seven, i.e., the number of objects (including o) in the* ε*-neighborhood of o. In (b), the objects p with density three, q with density five, and r with density seven, are depicted. By setting the parameter minPoints to six, r is identified as core object. Since q and p have a smaller density than minPoints, they are not classified as core objects. However, q is in the* ε*-neighborhood of r, making q a border object. The object p is classified as outlier and q and r form a cluster.*

For the DBSCAN algorithm, the following relationships have been defined (w.r.t. a given ε and *minPoints*) [Ester et al., 1996]:

- The object p is *directly density-reachable* from object q if p lies inside the ε-neighborhood of q and q is a core object.
- The object p is *density-reachable* from q if q is a core object, and there is a chain of objects $p_1, \ldots, p_n$ with $p_1 = q$ and $p_n = p$ such that p_{i+1} is always directly density-reachable from p_i.
- The object p is *density-connected* with object q if there is another object o such that p and q are both density-reachable from o.

The density-connectivity, density-reachability, and direct density-reachability are illustrated in Figure 3.5. Finally, a *density-based* cluster is a set of density-connected objects that is maximal regarding the density-reachability, i.e., all density-connected objects of the database are contained in the cluster.

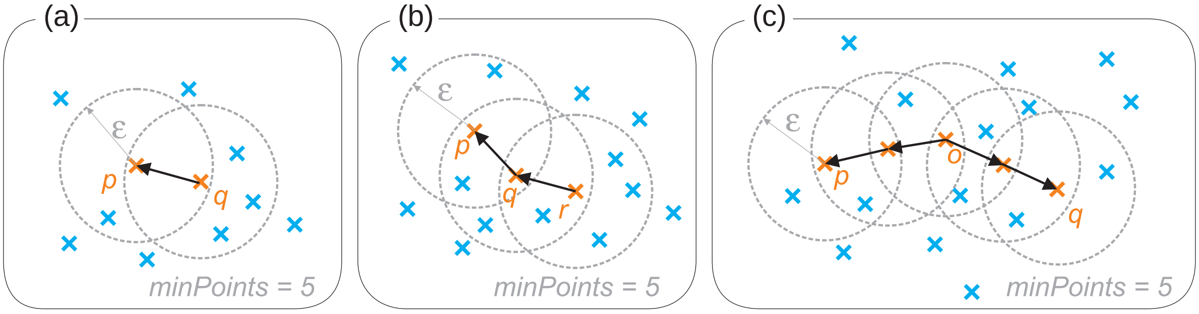

Figure 3.5: *Illustration of the relationships between objects. In (a), the object p is directly density-reachable from object q, but q is not directly density-reachable from p. In (b), p is density reachable from r, but r is not density-reachable from p. In (c), the objects p and q are density-connected to each other via object o.*

DBSCAN creates clusters from a database by starting with an arbitrarily chosen object p from the database, see the Algorithm 1. Next all objects that are density-reachable from p w.r.t. ε and *minPoints* are retrieved via the ExpandCluster function, see Algorithm 2. If p is a core point, i.e., p has a density $\geq$ *minPoints*, a cluster is extracted by proceeding with p's neighbors. Alternatively, if p is a border point or an outlier (and no points are density-reachable from p) then DBSCAN proceeds with the next (unvisited) object from the database.

Algorithm 1 Pseudocode DBSCAN from [Ester et al., 1996]. *SetOfObjects* is either the whole database or a discovered cluster from a previous run.

```
function DBSCAN(SetOfObjects, $\varepsilon$, minPoints)
    // SetOfObjects is UNCLASSIFIED
    ClusterId := nextId(NOISE)
    for $i \leftarrow 1$ to SetOfObject.size do
        Object := SetOfObjects.get(i)
        if Object.ClusterId = UNCLASSIFIED then
            if ExpandCluster(SetOfObjects, Object, ClusterID, $\varepsilon$, minPoints) then
                ClusterId := nextId(ClusterId)
            end if
        end if
    end for
end function
```

Algorithm 2 Pseudocode ExpandCluster from [Ester et al., 1996].

```
function ExpandCluster(SetOfObjects, Object, ClusterId, $\varepsilon$, minPoints):Boolean
    seeds := SetOfObjects.regionQuery(Object, $\varepsilon$)
    if seeds.size < minPoints then
        SetOfObjects.changeClusterId(Object, NOISE)
        return FALSE
    else
        // All Objects in seeds are density-reachable from Object
        SetOfObjects.changeClusterId(seeds,ClusterId)
        seeds.delete(Object)
        while seeds $\neq \emptyset$ do
            currentO := seeds.first()
            result := SetOfObjects.regionQuery(currentO,$\varepsilon$)
            if result.size $\geq$ minPoints  then
                for i $\leftarrow$ 1  to  result.size do
                    resultO := result.get(i)
                    if resultO.ClusterId $\in$ {UNCLASSIFIED,NOISE} then
                        if resultO.ClusterId = UNCLASSIFIED then
                            seeds.append(resultO)
                        end if
                        SetOfObjects.changeClusterId(result,ClusterId)
                    end if // UNCLASSIFIED or NOISE
                end for
            end if // result.size $\geq$ minPoints
            seeds.delete(currentO)
        end while // result.size $\neq$ minPoints
        return TRUE
    end if
end function
```

The main advantage of DBSCAN is the detection of arbitrarily shaped clusters based on the density of objects in the feature space. Hence, the number of clusters is automatically determined during the clustering process. Also, the clustering result is in general deterministic. Exceptional the assignment of border points, each run will obtain the same core points in the same clusters and the same outliers. The identification of outliers is an important advantage of the DBSCAN. A limitation of this method is the restriction to similar dense areas for cluster detection. If two two clusters exist, one with much lower density than the other, DBSCAN may not detect both. This initial condition is illustrated in Figure 3.7 of the next section. There will also be an appropriate solution presented, provided with the OPTICS algorithm.

3.3.2 OPTICS

OPTICS can be interpreted as a generalization of the DBSCAN algorithm where an *ordering of objects* is created instead of a clustering [Ankerst et al., 1999]. This ordering of objects comprises information that represents density-based clustering results with multiple parameter choices and effectively replaces the ε parameter with a maximum search radius. Thus, also clusters with different densities can be identified.

The algorithm requires the input parameters ε and *minPoints*. However, ε is an upper threshold value and different neighborhood sizes are considered. Furthermore, OPTICS employs the concepts of an object's *core distance* and *reachability distance*, which are illustrated in Figure 3.6 and explained in the following:

- The *core distance* of object p is the smallest distance ε' between p and an object from its ε-neighborhood such that p is a core object. If p exhibits a density less than *minPoints*, it is not a core object and its corresponding core distance is undefined.
- The *reachability distance* of an object q to the object p is the maximum of the core distance of p and the Euclidean distance between p and q. If p is not a core object, the reachability distance is not defined.

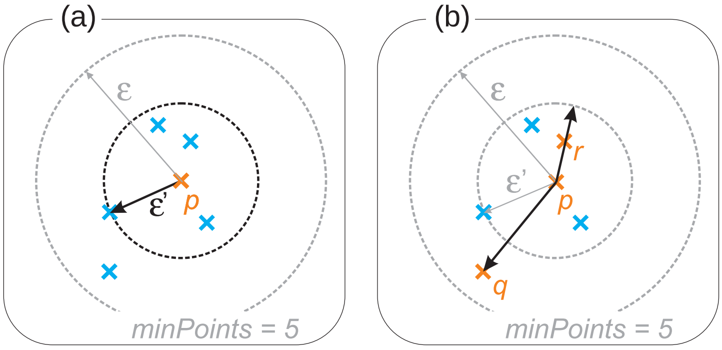

Figure 3.6: *Illustration of the core and reachability distances. In (a), the core distance ε' of object p is illustrated, w.r.t. minPoints and ε. In (b), the reachability distances of objects r and q to p are depicted.*

In contrast to a general clustering approach, OPTICS extracts an ordering of the objects *OrderedFile* (in combination with each object's core distance and reachability distance) instead of the explicit assignment of objects to clusters. For the ordering, OPTICS starts with an arbitrary object of the database and determines all neighbors in the object's ε-neighborhood, see Algorithm 3. Sorted by their reachability distance, the object and its neighbors are stored in a priority queue (starting with the smallest reachability distance). Now, the priority queue is processed such that the first element is analyzed with the *ExpandClusterOrder* function and stored in the ordering structure, see Algorithm 4. Hence, the object's neighbors are extracted and sorted (with respect to their reachability distance) into the queue. If the reachability distances of objects, which are already contained in the queue, will improve due to the processing of the queue's first element, these reachability distances will be updated, see the function *OrderSeeds::update* in Algorithm 5. If the priority queue is empty, the next, yet unprocessed, object of the database will be analyzed. This procedure maintains the complete extraction of an entire cluster before the next cluster is extracted.

The ordering structure can be visually presented with a reachability diagram, which depicts the exact ordering of the points, see Figure 3.7(b). The y-values illustrate the reachability distances for objects, which are ordered along the abscissa. The diagram's valleys are clusters and outliers are characterized by an increased reachability distance. To extract a cluster structure with a certain ε'-neighborhood, a user-defined threshold for ε' is applied (see red line in Fig. 3.7). This line separates outliers (exhibiting reachability distances larger than ε') from clusters (valleys between outliers). In practice, the clustering result is extracted via DBSCAN clustering from the ordering structure for a given ε' with $\varepsilon' \leq \varepsilon$.

Algorithm 3 Pseudocode OPTICS from [Ankerst et al., 1999].

```
function OPTICS(SetOfObjects, $\varepsilon$, minPoints, OrderedFile)
    OrderedFile.open()
    for $i \leftarrow 1$ to SetOfObjects.size do
        Object := SetOfObjects.get(i)
        if not Object.Processed then
            ExpandClusterOrder(SetOfObjects, Object, $\varepsilon$, minPoints, OrderedFile)
        end if
    end for
    OrderedFile.Close
end function
```

Algorithm 4 Pseudocode ExpandClusterOrder from [Ankerst et al., 1999].

```
function EXPANDCLUSTERORDER(SetOfObjects, $\varepsilon$, minPoints, OrderedFile)
    neighbors := SetOfObjects.neighbors(Object, $\varepsilon$)
    Object.Processed := TRUE
    Object.reachabilityDistance := UNDEFINED
    Object.setCoreDistance(neighbors, $\varepsilon$, minPoints)
    OrderedFile.write(Object)
    if Object.coreDistance $\neq$ UNDEFINED then
        OrderSeeds.update(neighbors, Object)
        while not OrderSeeds.empty() do
            currentObject := OrderSeeds.next( )
            neighbors := SetOfObjects.neighbors(currentObject, $\varepsilon$)
            currentObject.Processed := TRUE
            currentObject.setCoreDistance(neighbors, $\varepsilon$, minPoints)
            OrderedFile.write(currentObject)
            if currentObject.coreDistance $\neq$ UNDEFINED  then
                OrderSeeds.update(neighbors, currentObject)
            end if
        end while
    end if
end function
```

The advantages of OPTICS are similar to DBSCAN: arbitrarily shaped clusters can be detected and outliers can be identified. The main advantage is the extracted ordering of objects. Instead of one global parameter setting, different ε values can be set to extract the clustering result based on the reachability distances diagram (recall Fig. 3.7). Hence, this diagram also features a 2D presentation of high-dimensional databases. However, like most clustering algorithms, OPTICS may exhibit difficulties when it comes to clustering of high-dimensional data sets due to the lack of adequate similarity functions in these feature spaces.

3.3.3 SUBCLU

The main idea of the SUBCLU approach is the analysis of subspaces of the high-dimensional parameter space [Kailing et al., 2004]. As it was already discussed in Section 3.2.2, high-dimensional feature spaces complicate the clustering process due to the hardened process of

Algorithm 5 Pseudocode OrderSeeds::update from [Ankerst et al., 1999].

```
function ORDERSEEDS::UPDATE(neighbors, CenterObject)
    $c_{dist}$ := CenterObject.coreDistance
    for each Object ∈ neighbors do
        if not Object.Processed then
            newRdist := max($c_{dist}$, CenterObject.dist(Object))
            if Object.reachabilityDistance = UNDEFINED then
                Object.reachabilityDistance := newRdist
                insert(Object, newRdist)
            else
                // All Objects in seeds are density-reachable from Object
                if newRdist < Object.reachabilityDistance then
                    Object.reachabilityDistance := newRdist
                    decrease(Object, newRdist)
                end if
            end if
        end if
    end for each
end function
```

finding meaningful clusters and appropriate similarity functions. Hence, the SUBCLU algorithm is based on the assumption that meaningful clusters of high-dimensional data can be found in some cluster subspaces.

In more detail, the subspaces of the feature space of the database are analyzed with the density-based concepts that were introduced for the DBSCAN algorithm. Adapting the formal definitions to a subspace S of the high-dimensional feature space, a density-connected set (w.r.t. ε and *minPoints*) is defined: a set of objects is a density-connected set in S if all objects of the set are density-connected in S with each other. The density-connected sets are monotonic. For example, if $C \subseteq DB$ is a density-connected set of objects of the database DB in the subspace S, then C is also a density-connected set in any subspace $T \subseteq S$, see also Figure 3.8. This monotonicity may not hold for clusters, since clusters have to be maximal w.r.t. density-reachability, see the detailed description of SUBCLU and the density-based definitions in [Ester et al., 1996] and [Kailing et al., 2004], respectively. Thus, SUBCLU first detects density-connected sets in all 1D subspaces of the high-dimensional feature space with DBSCAN, see Algorithm 6. Next, if a subspace does not contain any density-connected set and thus any density-connected cluster, this subspace is excluded from further analysis. For all detected clusters in the subspaces, SUBCLU checks if these clusters are also contained in the next higher dimensional subspace, see Algorithm 7.

The advantages of the SUBCLU algorithm are the same advantages associated with the DBSCAN algorithm since it is closely related to this approach. Additionally, SUBCLU allows for clustering in subspaces and is suitable for high-dimensional feature spaces. However, a disadvantage is the global parameter choice. Hence, the same values for ε and *minPoints* are employed independent from the number of dimensions of the feature space. Naturally, objects are more dense in low dimensional spaces than in high-dimensional spaces. Thus, appropriate small ε and *minPoints* values for the low dimensional space might be inappropriate for the high-dimensional spaces.

Algorithm 6 Pseudocode SUBCLU from [Kailing et al., 2004].

```
function SUBCLU(SetOfObjects, $\varepsilon$, minPoints)
    // Step 1: Generate all 1D clusters
    $S_1 := \emptyset$ // Set of 1D subspaces containing clusters
    $C_1 := \emptyset$ // Set of all sets of clusters in 1D subspaces
    for each $a_1 \in$ Attributes do
        // set of all clusters in subspace $a_i$
        $C^{\{a_i\}}$ := DBSCAN(SetOfObjects, $\{a_i\}$, $\varepsilon$, minPoints)
        if $C^{\{a_i\}} \neq \emptyset$ then // at least one cluster in subspace $a_i$
            $S_1 := S_1 \cup \{a_i\}$
            $C_1 := C_1 \cup C^{\{a_i\}}$
        end if
    end for each
    // Step 2: Generate $(k+1)$D candidate subspaces
    $k := 1$
    while $C_k \neq \emptyset$ do
        // Step 2.1: Generate $(k+1)$D subspace candidates
        $CandS_{k+1}$ = GenerateCandidates($S_k$)
        // Step 2.2: Test candidates and generate $(k+1)$D clusters
        for each $cand \in CandS_{k+1}$ do
            // Search $k$D subspace of $cand$ with minimal number of objects in the clusters
            bestSubspace := $\min_{s \in S_k \wedge s \subseteq cand} \sum_{C_i \in C^s} |C_i|$
            $C^{cand} := \emptyset$
            for each cluster $\in C^{bestSubspace}$ do
                $C^{cand} := C^{cand} \cup$ DBSCAN(cluster, cand, $\varepsilon$, minPoints)
                if $C^{cand} \neq \emptyset$ then
                    $S_{k+1} := S_{k+1} \cup cand$
                    $C_{k+1} := C_{k+1} \cup C^{cand}$
                end if
            end for each
        end for each
    end while
end function
```

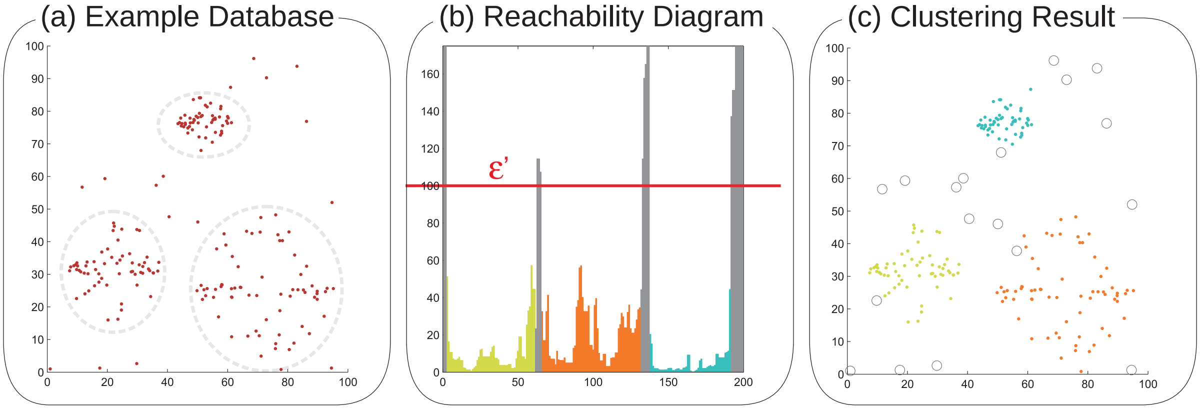

Figure 3.7: *Illustration of the OPTICS' reachability diagram and cluster extraction. In (a), a 2D example database is presented that was artificially generated for illustration purpose. Hence, three clusters can be intuitively perceived, see dashed ellipses. Note that the cluster at the top exhibits a higher density than the cluster at bottom right. In (b), reachability distances for each object in the extracted ordering are displayed. The user-defined threshold ε' was set to 100 and this threshold yields three clusters (yellow-green, orange, and cyan colored) that are separated by outliers (gray colored). Naturally, the outliers exhibit highest reachability distances. As it can be inferred from (b), the cyan cluster is more dense than the orange one (see the smaller reachability distances). In (c), the resulting clustering based on ε' is depicted with the same color scheme. Outliers are furthermore marked with circles.*

3.4 Statistical Analysis of Attribute Dependency and Dimensional Reduction

In contrast to the subspace clustering, many concepts aim at the construction of a new and lower dimensional feature space. A dimensionality reduction concept like the PCA is based on the assumption that many features interfere with each other or measuring somehow the same system variables. In this case, a certain redundancy occurs when extracting the attributes. To be more precise, descriptive perfusion parameters extracted from concentration-time curves in the setting of tumor diagnosis based on perfusion MRI often correlate. The correlation can be present because the amount of contrast agent concentration influences several perfusion parameters at once. This section provides important background information for the analysis of redundancy between two parameters, followed by the description of the PCA and spectral clustering.

3.4.1 Redundancy of Two Attributes

To characterize the redundancy between two attributes, two approaches are employed: the extraction of the correlation coefficient and the covariances [Han et al., 2011]. Both measures depend on the mean and the variance of the objects' attributes. Hence, the mean $\overline{x}$ of a certain attribute x of n objects of the database, is also referred to as expected value $E(x)$ of x. It is calculated by:

$$\overline{x} = E(x) = \frac{\sum_{i=1}^{n} x_i}{n}, \tag{3.1}$$

where x_i denotes the value of attribute x for the ith object.

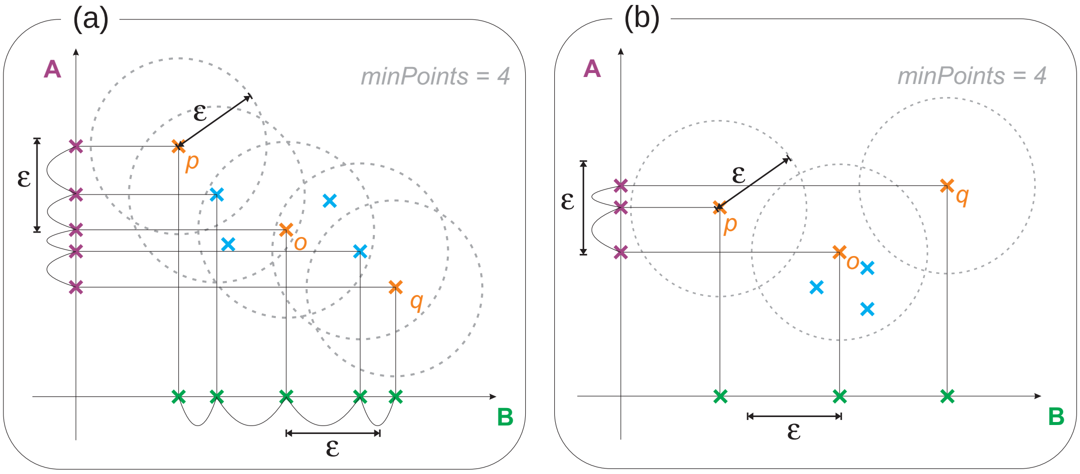

Figure 3.8: Illustration of the monotonicity of density-connected sets with minPoints = 4. In (a), the objects p and q are density-connected via o in the 2D subspace spanned by the attributes A and B. Therefore, they are also density-connected via o in each 1D subspace A and B. In (b), the objects p and q are not density-connected in the 1D subspace B. Thus, they are also not density-connected in the 2D subspace AB. However, they are density-connected via o in the 1D subspace A. (Adapted from [Kailing et al., 2004].)

The sample variance σ^2 of the attribute x can be expressed by:

$$\sigma^2 = \frac{1}{(n-1)} \sum_{i=1}^{n} (x_i - \bar{x})^2 \tag{3.2}$$

Hence, we interpret the objects of our database as samples of a collected data set, e.g., breast tumor perfusion data sets in a clinical workflow from the population. On the contrary, the variance $\sigma^{*2} = \frac{1}{n}\sum_{i=1}^{n}(x_i - \bar{x})^2$ should be employed when the sample would include the whole population. The equations for σ^* and σ differ only in the $n-1$ and n divisor. Furthermore, σ is called the sample standard deviation. The same holds for σ^*.

The Correlation Coefficient

The correlation coefficient determines how strong two attributes x and y of n objects are correlating. The correlation coefficient, also called Pearson's product moment coefficient, is defined by:

$$r_{x,y} = \frac{\sum_{i=1}^{n}(x_i - \bar{x})(y_i - \bar{y})}{n\sigma_x\sigma_y} = \frac{\sum_{i=1}^{n}(x_i y_i) - n\bar{x}\,\bar{y}}{n\sigma_x\sigma_y}. \tag{3.3}$$

The values of $r_{x,y}$ lie in the interval of $[-1,1]$. Hence, values > 0 indicate a positive correlation, i.e., the values of x increase as the values of y increase and values < 0 indicate a negative correlation, i.e., the values of one attribute decrease as the values of the other attribute increase. An $r_{x,y}$ value of 0 indicates no correlation between the two attributes.

Algorithm 7 Pseudocode GenerateCandidates from [Kailing et al., 2004]. S_k is the set of subspaces

```
function GENERATECANDIDATES($S_k$)
    // Step 2.1.1: Generate $(k+1)$D candidate subspaces
    $CandS_{k+1} := \emptyset$
    for each $s_1 \in S_k$ do
        for each $s_2 \in S_k$ do
            if $s_1.attr_1 = s_2.attr_1 \&\& \ldots \&\& s_1.attr_{k-1} = s_2.attr_{k-1} \&\& s_1.attr_k < s_2.attr_k$ then
                insert$\{s_1.attr_1, \ldots, s_1.attr_k, s_2.attr_k\}$ into $Cand_{k+1}$
            end if
        end for each
    end for each
    // Step 2.1.2: Prune irrelevant candidate subspaces
    // Step 2.1.1: Generate $(k+1)$D candidate subspaces
    for each $cand \in CandS_{k+1}$ do
        for each $s \subset cand$ with $|s| = k$ do
            if $s \notin S_k$ then
                delete $cand$ from $CandS_{k+1}$
            end if
        end for each
    end for each
end function
```

The Covariance of Attributes

The covariance Cov of numeric data is the second possibility to assess how similar two attributes change together in probability theory and statistics. It is defined as

$$Cov(x,y) = E((x-\bar{x})(y-\bar{y})) = \frac{\sum_{i=1}^{n}(x_i-\bar{x})(y_i-\bar{y})}{n}. \tag{3.4}$$

For further characterization, $Cov(x,y)$ can be expressed as:

$$Cov(x,y) = E(x \cdot y) - \bar{x}\,\bar{y}. \tag{3.5}$$

Interpreting the last equation, a positive value of $Cov(x,y)$ indicates the following relationship. If x is larger than its expected value $\bar{x}$, then y is likely to be larger than $\bar{y}$. Contrary, a negative value of $Cov(x,y)$ equals the relationship that one attribute is above its expected value as the other attribute is below the expected value. If x and y are independent regarding their correlation, then $Cov(x,y)$ equals 0. However, the covariance covers a linear relationship. Thus, if the attributes x and y may exhibit a certain relationship (e.g., a non-linear dependency), the value of $Cov(x,y)$ can be equal to 0.

Covariance and correlation coefficient exhibit the following relationship:

$$r_{x,y} = \frac{Cov(x,y)}{\sigma_x \sigma_y} \tag{3.6}$$

Furthermore, the variance σ^2 equals the covariance covering two identical attributes ($Cov(x,x)$).

3.4.2 PCA for Dimensional Reduction

The PCA is an orthogonal transformation from the original feature space into a new feature space of equal dimension. The new feature space is spanned by the principal components. The first principal component equals the first axis of the new feature space and expresses the maximum variance possible among all options for this first axis. The second principal component is perpendicular to the first one and expresses the possible maximum of the data's variance under the constraint to be perpendicular to the first principal component. This holds also for the following principal components such that all principal components are mutually perpendicular.

A PCA can be analytically determined by maximizing the variances expressed by the principal components. For a statistical setting of a database with n objects with m attributes, the PCA can be carried out by exploiting the attributes' covariances. Therefore, the covariance matrix Σ is extracted. The element in the ith row and jth column $(\Sigma)_{i,j}$ represents the covariance of the values of attribute i and attribute j, i.e., $(\Sigma)_{i,j} = Cov(i,j)$. The m attributes yield a covariance matrix with dimension $m \times m$. From Σ, the normalized eigenvectors and eigenvalues are extracted. Next, they are ordered by eigenvalue, from highest to lowest, yielding the components in order of significance. The ordered eigenvectors form the principal components. To obtain the positions of the objects in the new feature space, the attribute values are shifted such that their mean lies in the origin. Next, they are multiplied with the principal components. The centering around their means is inevitable for the transformation into the new space, which is also automatically carried out by Σ.

Since the principal components are ordered by significance, i.e., the amount of variance they are covering, it is in general sufficient to employ only the first few principal components to construct a new feature space. Thus, the dimension of the feature space can be effectively reduced with only a small loss of information. Clustering is then carried out in the lower dimensional feature space and the clustering result is assigned to the original data.

Due to the dependency on the covariance, PCA is sensitive to the relative scaling of the original variables. Increased importance will be assigned to attributes with larger domain ranges than to attributes with smaller domain ranges. To reduce the influence of the attributes' domain ranges, the attribute values are normalized such that each attributes domain range covers the same range. Different normalization techniques exist, for example the min-max normalization and the z-score normalization. The first one maps the values of attribute x lying in the interval $[x_{min}, x_{max}]$ to the new values x' in the range $[x'_{min}, x'_{max}]$:

$$x' = \frac{x - x_{min}}{x_{max} - x_{min}} (x'_{max} - x'_{min}) + x'_{min}. \tag{3.7}$$

Z-scoring maps the values x to the new values x' by applying the mean $\bar{x}$ and the standard deviation σ_x:

$$x' = \frac{x - \bar{x}}{\sigma_x}. \tag{3.8}$$

Thus, the values of x' have a mean equal to 0 and a variance equal to 1. However, the PCA can only detect linear dependencies between the variables.

The PCA is illustrated with the flea beetle database. This database contains 74 samples with 7 attributes and was published by [Lubischew, 1962]. The first attribute determines the type of flea beetle and equals one of the three different types of chaetocnema: ch. concinna, ch. heptapotamica, and ch. heikertingeri. The six remaining attributes (units are given in brackets) cover:

- D_1: the size of the first joint of the foot of the first leg [μm],
- D_2: the size of the second joint of the first tarsus [μm],
- D_3: maximum width of the head between the external edges of the eyes [$0.01 mm$],
- D_4: maximum width of the aedeagus in the fore-part [μm],
- D_5: front angle of aedeagus [in $7.5°$], and
- D_6: aedeagus width from the side [μm].

Since they express physiological features, a certain redundancy can be expected.

The feature space reduction with the PCA is illustrated in Figure 3.9. In Figure 3.9(a), the covariance matrix Σ of the attributes $D_1 - D_6$ is shown, where z-scoring was applied to the original attributes. Thus, each original attribute exhibits variances equal to 1, see diagonal entries of Σ. Higher values for the covariance values of two attributes are highlighted with a gray background. The percentage variances of the principal components are listed in Figure 3.9(b). Note that the first three principal components cover 90% of the overall data variance. In Figure 3.9, the database's feature space is visualized. For each different type, a different color was chosen (orange was assigned to ch. concinna, cyan to ch. heptapotamica, and green to ch. heikertingeri). In Figures 3.9(c)-(d), 3D scatterplots are presented, employing the attributes $D_1 - D_3$ or $D_4 - D_6$, respectively. In Figure 3.9(e) only the first three principal components are employed. Cluster algorithms can be employed in the new constructed 3D feature space and three well separated clusters can be obtained. Note that the color mapping is only based on the beetle type, no clustering approach was carried out.

3.4.3 Clustering in the Spectral Domain

In spectral clustering, the clustering is reformulated as a graph cut problem. The objects of the database are considered as nodes of a connected graph. The similarity of two objects' features is expressed via the weight of their connecting edge. A graph cut is a partition of the graph's nodes into two disjoint subsets which are joined by at least one edge. For spectral clustering, these cuts should partition the graph such that edges between different groups (i.e., clusters) have very low weights and edges within the same cluster have high weights. It is approximated with the eigenvectors and eigenvalues of a specific matrix: the Laplacian matrix. Thus, the original data points are mapped into a lower dimensional space. In this new representation, clusters can be easier separated (regarding the high-dimensional space) by applying simple clustering techniques like k-means.

In the following, the spectral clustering is briefly explained. For a more detailed review, see the tutorial of Von Luxburg [2007]. First, a weighted, undirected graph is constructed from the initial database with n objects. Hence, each graph node represents an object and each edge represents the similarity between two objects based on a symmetric and non-negative

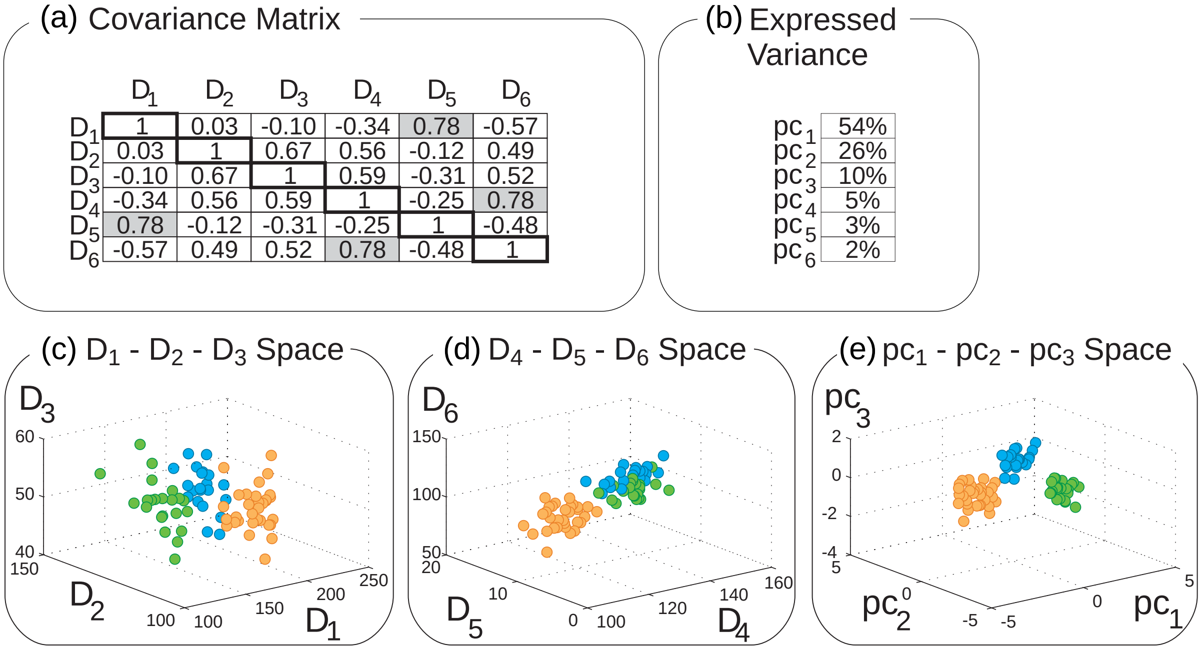

(a) Covariance Matrix

	D_1	D_2	D_3	D_4	D_5	D_6
D_1	1	0.03	-0.10	-0.34	0.78	-0.57
D_2	0.03	1	0.67	0.56	-0.12	0.49
D_3	-0.10	0.67	1	0.59	-0.31	0.52
D_4	-0.34	0.56	0.59	1	-0.25	0.78
D_5	0.78	-0.12	-0.31	-0.25	1	-0.48
D_6	-0.57	0.49	0.52	0.78	-0.48	1

(b) Expressed Variance

pc_1	54%
pc_2	26%
pc_3	10%
pc_4	5%
pc_5	3%
pc_6	2%

Figure 3.9: *Illustration of the PCA over the flea beetle data set [Lubischew, 1962]. In (a), Σ of the attributes $D_1 - D_6$ is presented. In (b), the percentage variances expressed by the principal components pc_1 - pc_6 are listed. In (c), (d), and (e), 3D scatterplots are presented where orange was assigned to ch. concinna, cyan to ch. heptapotamica, and green to ch. heikertingeri. In (c), the 3D subspace comprising the features D_1-D_3 is depicted. In (d), the subspace of features D_4-D_6 is shown. In (e), the new feature space of pc_1-pc_3 is depicted.*

similarity function, e.g., the Euclidean distance function. The similarity between two nodes o_i and o_j is employed as weight w_{ij}. The object's o_i degree d_i is extracted as:

$$d_i = \sum_{j=1}^{n} w_{ij} \tag{3.9}$$

Next, a Laplacian matrix L is constructed from the graph. L is based on the *degree matrix* D and the *weighted adjacency matrix* W, see [Von Luxburg, 2007] for various variants. Here, D is the diagonal matrix with degrees $d_1, \ldots, d_n$ on the diagonal and $W = (w_{i,j})_{i,j=1\ldots n}$. As it is stated in the tutorial by Von Luxburg [2007], an unique definition of the exact graph Laplacian does not exist. Different approaches exist, for example the normalized spectral clustering according to Ng et al. [2002], which is also referred to as Ng-Jordan algorithm.

Hence, a normalized Laplacian matrix is constructed based on W and D and a spectral decomposition is performed. Based on a pre-defined k, the k biggest eigenvalues and corresponding eigenvectors $u_1, \ldots, u_k$ are extracted. Then, the matrix U containing $u_1, \ldots, u_k$ as columns is constructed. The matrix T is extracted from U by normalizing the rows to transform the objects into the spectral space: the object y_i corresponds to the ith row of T. Now, the clustering can be carried out in the space spanned by T and the objects y can be clustered, e.g., with the k-means algorithm. The final cluster results are projected back such that the clustering result of objects x is yielded.

The main advantage of the spectral clustering approach for tumor perfusion data is the influence of the local neighborhood. Hence, a modification of the similarity function that deter-

Algorithm 8 Pseudocode for the Ng-Jordan algorithm [Ng et al., 2002] from [Von Luxburg, 2007].

```
Input: Similarity matrix $S \in \mathbb{R}^{n\times n}$, number $k$ of clusters to construct.
Construct a similarity graph and let $W$ be its weighted adjacency matrix.
Compute the normalized Laplacian $L_{sym}$.
Compute the first $k$ eigenvectors $u_1,\dots,u_k$ of $L_{sym}$.
Let $U \in \mathbb{R}^{n\times k}$ be the matrix containing the vectors $u_1,\dots,u_k$ as columns.
Form the matrix $T \in \mathbb{R}^{n\times k}$ from $U$ by normalizing the rows
    that is set $t_{ij} = u_{ij} / \sqrt{\sum_k u_{ik}^2}$.
For i = $1,\dots,n$ let $y_i \in \mathbb{R}^k$ be the vector corresponding to the i$^{th}$ row of $T$.
Cluster the points $y_i$ $(i = 1,\dots,n)$ with the $k$-means algorithm into clusters $C_1,\dots,C_k$.
Output: Clusters $A_1,\dots,A_k$ with $A_i = \{j|y_j \in C_i\}$.
```

mines the weights is carried out. With the modified similarity function, e.g., the Gaussian similarity function

$$s(o_i,o_j) = exp\left(-\frac{||o_i - o_j||^2}{2\sigma^2}\right), \tag{3.10}$$

the neighborhood size is controlled with the parameter σ. Then, a similarity equal to zero is assigned to spatially non-connected voxels yielding only spatially connected clusters.

3.5 Region Merging

Region merging is a basic concept to extract homogeneous regions of an image. The algorithm comprises the following steps: initially, each pixel forms a single region. Next, two adjacent regions are merged into a new region if they fulfill a certain homogeneity criterion. The algorithm converges if no pair of adjacent regions exists that fulfills this criterion anymore. Hence, the homogeneity criterion also defines the termination condition. Although originally associated with the 2D digital image processing, this concept can be interpreted as agglomerative hierarchical clustering where each region corresponds to a cluster.

For a 3D tomographic medical data set, voxels are clustered and the homogeneity criterion is replaced by the similarity function. The merging of adjacent regions is modeled by a hard constraint. Region merging is a straight-forward approach and thus easy to understand and implement. The result of the region merging usually depends on the order in which the regions are merged. Advanced concepts include the split-and-merge algorithm, which employs a multi-scale-strategy and combines region splitting and merging, or the statistical region merging concept [Nock and Nielsen, 2004].

3.6 Conclusion

In this chapter, the reader was acquainted with the process of clustering to detect meaningful groups of data. The categorization of clustering is a challenging aspect since clustering concepts are often adapted to the specific problem and many clustering algorithms combine more than one clustering concept. Therefore, in the first part of this chapter, a short description of basic and advanced clustering techniques was presented. In combination with medical imaging of perfusion data, different aspects were compared to identify promising clustering concepts for this purpose.

The selected concepts were presented in more detail in Sections 3.3-3.5. Hence, the demand for arbitrarily shaped clusters and the ability of the detection of outliers, strongly favors density-based approaches. The DBSCAN algorithm is one of the most often employed clustering algorithm in literature and closely related to SUBCLU and OPTICS. Further, statistical characterization of the redundancy of attributes, the PCA for dimensionality reduction, and spectral clustering was presented. When considering lots of perfusion parameters, the concept of dimension reduction is in particular interesting. The region merging approach, a rather simple approach for clustering, has the strong advantage of including the hard constraint of spatially connected data. The region merging approach allows for the creation of spatially connected regions, an advantage in clustering of tomographic image data.

When applied to medical perfusion data and the right initial conditions, clustering yield grouped voxels with similar perfusion characteristics. Thus, a group of automatically determined voxels redeems the manual ROI placement of the clinician or the biomedical researcher. Further, it reduces the intra- and inter-observer variability, which is the main motivation for employing clustering to medical perfusion data. In the next chapter, an overview of related work including clustering approaches of medical (perfusion) image data is provided.

4. Visual Analysis of High-Dimensional Clustered Medical Image Data

4 Visual Analysis of High-Dimensional Clustered Medical Image Data

This chapter is dedicated to the state of the art of visual analysis techniques for medical perfusion data sets. Due to the time dimension and the diagnosis-induced grouping of voxels to region of interests (ROIs), this chapter covers a number of research areas. The following concepts contribute to this topic: the visualization of high-dimensional and time-varying data, the combination with clustering of these visualizations, as well as multiple linked views, including scatterplots and parallel coordinate plots to explore the high-dimensional data, see Figure 4.1.

In Section 4.1, these concepts are presented and illustrated with current state of the art approaches. Hence, the breast and brain perfusion magnetic resonance imaging (MRI) data can be interpreted as time-varying data, as well as high-dimensional data (with a set of derived perfusion parameters, as described in Sect. 2.1.2). The voxels are interpreted as objects of a database and their perfusion parameter values or contrast agent concentration at different points in time are assigned to the attributes yielding a high-dimensional feature space. Further, each data set contains a set of voxels and due to noise and motion artifacts, the evaluation of contrast enhancement kinetics of single voxels is not feasible. Therefore, clinical evaluation involves grouping of voxels into ROIs. Related concepts of grouping or clustering of voxels for the visual exploration is also covered in Section 4.1. The section ends with specific concepts for the visualization of medical perfusion data, i.e., breast and brain perfusion data.

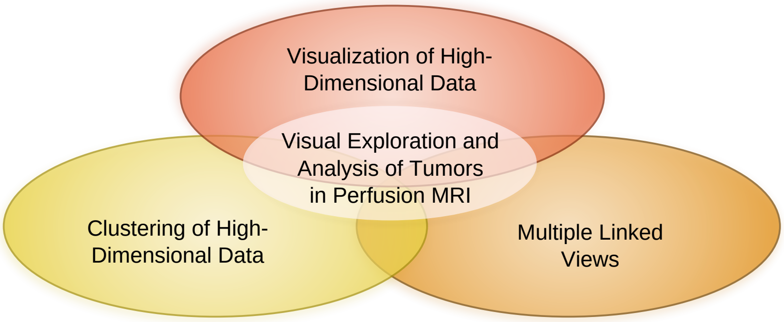

Figure 4.1: *The main visualization research areas that influence the visualization and exploration of tumor perfusion MRI data.*

Afterwards, related work for the clinical evaluation of breast tumors and brain tumors with focus on DCE-MRI and DSC-MRI is presented and selected concepts are discussed in more detail. Section 4.2 covers the detection and the classification of breast lesions in DCE-MRI. Section 4.3 contains related work for quantitative perfusion parameter-based differentiation between low grade gliomas and high grade gliomas for DSC-MRI as well as a short discussion of the optimal ROI size for glioma evaluation.

This chapter ends with a short summary that highlights important aspects of the medical image interpretation and visual analysis-based exploration.

4.1 Visual Analysis and Visualization of High-Dimensional Data

The visualization of a data set, e.g., the set of voxels of a tumor with different attributes, is the process which generates a visual representation of this data set. Medical image data sets become larger and more complex. To improve and support the radiologist's work, advanced methods including visual analytic solutions are promising. Thus, a focus is set on visual analysis and visualization of these data sets. The visualization of high-dimensional data, i.e., medical image data, can be carried out with two different approaches:

1. Dimension reduction via clustering is employed for the high-dimensional data. Next, visualizations are generated for the low-dimensional clustering results.
2. Multiple linked views are applied to the high-dimensional data. Hence, attribute subspaces can be explored in a 2D or 3D way. Each subspace exploration is linked such that the user can extract subspaces of the whole data set.

Therefore, in Section 4.1.1, related work for the visualization and clustering of medical high-dimensional data is presented. In Section 4.1.2, state of the art for visual analysis and exploration of high-dimensional data based on multiple linked views is provided. Finally, in Section 4.1.3, visualization techniques especially for perfusion datasets are presented. For a comprehensive overview for the area of visual data mining with special focus on visual analytics, the reader is referred to [Keim et al., 2008].

4.1.1 Clustering of Medical High-Dimensional Data

This section provides examples of appropriate adoptions of clustering algorithms to medical image data with focus on medical perfusion data. As it was illustrated in Figure 4.1, the different research areas are overlapping. Therefore, in Section 4.1.2 the multiple linked views frameworks are described. Related work for clustering of high-dimensional data in combination with visualization of high-dimensional data is presented afterwards.

For example, an important application area for clustering is the analysis and visualization of functional MRI (fMRI) data. In general, peaks in the histogram of all voxels' signal intensities of a medical data set often represent different tissue types and are well suited to detect important signal intensity ranges. These ranges are important for further visualization. However, in fMRI data, histogram peaks may represent overlaps of tissue types that are not particularly interesting. Therefore, Maciejewski et al. [2009] employed clustering to analyze the gradient versus the intensity histogram space. Furthermore, cluster analysis was carried out to generate transfer functions for this type of data by Maciejewski et al. [2013].

Diffusion tensor MRI data forms another important medical application area for clustering. In the work by Moberts et al. [2005] fiber tracts were clustered to provide a visualization for neurosurgeons. O'Donnell and Westin [2005] adapted spectral clustering to identify fiber tract correspondences over a population of brains. Tiwari et al. [2009] employed hierarchical spectral clustering to magnetic resonance spectroscopy to supplement MRI. Thus, they could automatically identify suspicious regions on the prostate in the spectroscopy data. In addition, clustering (of curvature-related measures) was successfully employed to detect regions of the colon for a further polyp detection in virtual colonoscopy by Zhao et al. [2006]. Schultz and Kindlmann [2013] presented the *Open-Box Spectral Clustering*, see Figure 4.2. This interactive framework for spectral clustering in medical image analysis applications suggested parameter values and provided immediate feedback to support the user. Furthermore, the high-dimensional feature space was mapped to the three-dimensional data space. Thus, the complex parameter choices for spectral clustering could be effectively supported. The approach by Marrocco et al. [2012] was adapted to conventional X-ray mammography. They carried out a watershed transform to define areas of microcalcifications that form ROIs. Next, they input the ROIs' geometrical and textural features to decision tree classifiers, which filter out uninteresting ROIs. The remaining regions are clustered into spatially contiguous clusters. Similar to DCE-MRI perfusion data, dynamic nuclear image data of the heart allows for extraction of time-activity curves per voxel. Tönnies et al. [2003] employed region merging to cluster voxels with similar time-activity curves. Furthermore, they employed a similarity criterion based on a reduced set of features. This reduced feature set was obtained via a principal component analysis (PCA).

Clustering of medical image data is closely related to the visualization of high-dimensional data since the clustering often serves as dimension reduction method. Further, the clustering allows for an intelligent grouping of the data and the detection of the most relevant information. Zhang et al. [2006] et al. presented a method to visualize gene clusters in 3D. First, they used the spring model to locate genes within a cluster into InfoCubes. Afterwards, they employed the same method to allocate the InfoCubes in 3D space. Their algorithm avoids the space partition problem. When transferred to tomographic perfusion MRI data, it must be stated that clusters could be entwined around each other such that this approach becomes inappropriate. The approach by Quigley [2001] deals with large data sets and generates hierarchical compound graphs. The clusters are represented as a graph where the nodes act as the clusters. Yang et al. [2003] presented a system for the processing of DNA microarray data. They introduced a space-undivided and a space-divided 3D gene plot. In the first plot, every gene is assigned to a sphere and the cluster membership is color-coded. The second plot splits the 3D space into cubes and puts the clusters into these cubes. In the first case, clusters seem to be huge point clouds and in the second case, no spatial information about the clusters exists. Aono and Kobayashi [2011] developed a visual interface for non-technical users to understand the output from clustering algorithms. Their algorithm displays clusters which are projected on a 3D subspace based on the user's keyword input. Thus, the computed recommendations for the 3D visualization cannot present the spatial relationships.

Similar to DCE-MRI perfusion data, dynamic nuclear image data of the heart allows for extraction of time activity curves per voxel. Tönnies et al. [2003] employed region merging to cluster voxels with similar time-activity curves. Furthermore, they used a similarity criterion based on a reduced set of features. This reduced feature set was obtained via a principal component analysis (PCA). The approach by Marrocco et al. [2012] was adapted to conventional X-ray mammography. They carried out a watershed transform to define areas of microcalcifications that form ROIs. Next, they input the ROIs' geometrical and textural features to decision tree classifiers, which filtered out uninteresting ROIs. The remaining regions were clustered into spatially contiguous clusters.

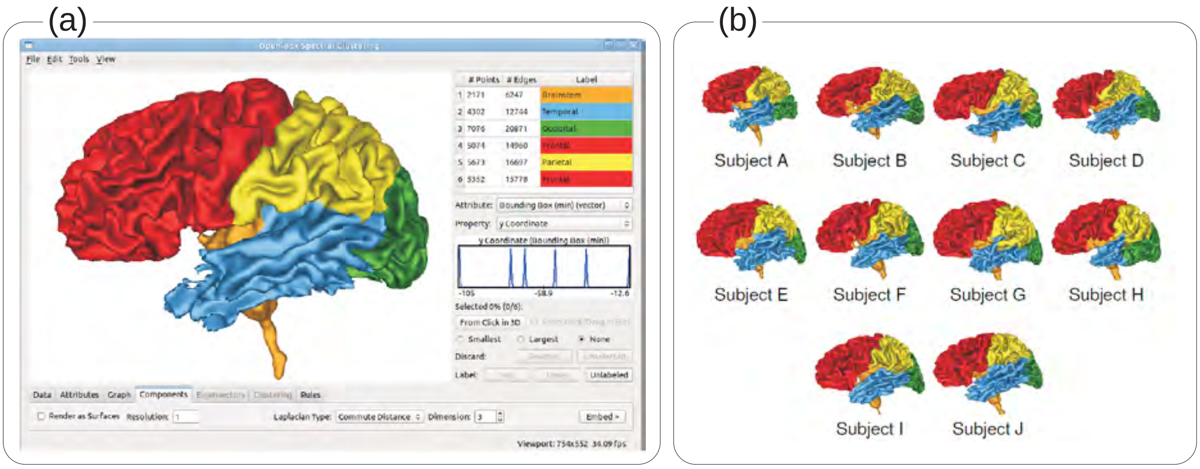

	# Points	# Edges	Label
1	2171	6247	Brainstem
2	4302	12744	Temporal
3	7076	20871	Occipital
4	5074	14960	Frontal
5	5673	16697	Parietal
6	5352	15778	Frontal

Attribute: Bounding Box (min) (vector)
Property: y Coordinate
Selected 0% (0/6):
○ Smallest ○ Largest ● None
☐ Render as Surfaces Resolution: 1
Laplacian Type: Commute Distance
Dimension: 3
Viewport: 754x552 34.09 fps

Figure 4.2: *The open-box framework for interactive spectral clustering (Image adapted and reprinted from [Schultz and Kindlmann, 2013] © IEEE 2013 with kind permission from IEEE). In (a), the framework is depicted and in (b), the parameter choices were automatically applied for the clustering of other patients.*

Since the clustering concepts for dimension reduction may contain a loss of spatial information in the high-dimensional space, different approaches were presented to visualized these high-dimensional data in combination with the clustering results. The concepts overlap with concepts of visualizing high-dimensional data in general. In particular, they are also combined with multiple linked views. Therefore, these concepts are presented in the next section.

4.1.2 Multiple Linked Views

Multiple linked views are a well-established information visualization tool [Wong and Bergeron, 1997]. Hence, the views provide different portions of the data and thus allow for exploration of relationships between different attributes. Furthermore, the user can select some portion of the data, e.g., by placing a ROI in the first view, and the contained objects are dynamically highlighted in the other views. For example, the WEAVE (workbench environment for analysis and visual exploration) system [Gresh et al., 2000] links scientific views (represented by multidimensional statistical representations) by brushing facilities applied to scatterplots. The *SimVis* framework [Doleisch et al., 2003] extends the WEAVE framework and also employs scatterplots and parallel coordinates plots. Hence, interaction is possible via smooth brushing [Doleisch and Hauser, 2002]. An example is provided at the end of this section where the *SimVis* framework was successfully employed for analysis of cerebral perfusion MRI data sets to assess ischemic stroke by Oeltze et al. [2009]. The most important and most common views of such multiple linked frameworks are listed in this section:

- The first part contains related work for scatterplot views.
- The second part presents parallel coordinates plots.
- The third part describes the Radviz view.
- The fourth part lists general approaches for the visualization of (clustered) high-dimensional data within a multiple view framework.

The Scatterplot View

Scatterplots [Wong and Bergeron, 1997] are an established technique to visualize objects in an *n*-dimensional space where each axis of the space corresponds to a dimension of the *n*-dimensional feature space. Naturally, only 2D and 3D scatterplots can be intuitively perceived. Mostly, the scatterplot covers a 2D plane where the horizontal and vertical coordinates equal to two of the feature space dimensions. A scatterplot matrix [Cleveland, 1985] comprises all combinations of two dimensions from the feature space. Kosara et al. [2004] presented the VoxelPlot, a 3D scatterplot that interactively links scientific and information visualization with multiple views similar to the WEAVE system [Gresh et al., 2000]. Sanftmann and Weiskopf [2009] introduced the illuminated scatterplot where shape perception is improved by applying a dedicated illumination technique to the 3D scatterplot's point cloud representation. Piringer et al. [2004] mapped the distance to color and the point size of the scatterplots. These approaches only employed color or shading to the data objects to represent the type of cluster. In contrast, Healey et al. [2001] included contextual cues in the final 3D scatterplot-based visualizations. Furthermore, the scatterplot concept has been extended to continuous scatterplots by Bachthaler and Weiskopf [2008] to account for spatially continuous input data instead of discrete data sets.

The Parallel Coordinates Plot

The parallel coordinates plot [Inselberg and Dimsdale, 1990] employed vertical axes for each dimension of the feature space. In general, all axes are parallel to each other and arranged in a 2D view. The objects are presented as line segments where each line segment connects two attributes of the object. The work by Theisel [2000] introduced free-form curves instead of line segments for connection of points on adjacent axes. First, visual clutter was reduced. Second, the replacement of line segments by curves provided more space between two adjacent axes and more information like correlation between more than two dimensions could be encoded. Matkovič et al. [2007] applied color to 2D parallel coordinate plots to highlight similar curves. Furthermore, the illustrative parallel coordinates presented by McDonnell and Mueller [2008] applied artistic rendering techniques to convey a large amount of information. They employed edge-bundling through splines to visualize so-called branched clusters, opacity-hints to support cluster density perception, opacity, shading effects as well as silhouettes and shadows. Wegenkittl et al. [1997] presented 3D parallel coordinates plots for the scientific visualization of high-dimensional data based on the trajectories of high-dimensional dynamical systems which form a data set of a smooth-dimensional flow. As a last example, the *pargnostics* approach by Dasgupta and Kosara [2010] included screen-space metrics like line crossings, crossing angles or overplotting, to quantify the different visual structures in parallel coordinates plots and to construct an optimized display of the plot.

The Radviz View

Further visualization techniques of high-dimensional data exist, like the radial coordinate visualization (Radviz) and multi-dimensional scaling. The Radviz approach was presented by Hoffman et al. [1997] to classify DNA sequences. Hence, for each dimension of the feature space, a line emanates radially from the center of the circle and terminates at the perimeter where the special end points form equally distanced anchor points. The objects of the data set are then arranged in the circle center by attaching springs to the object and the anchor points. Hence, the spring constant is assigned to the (normalized) attribute value of the object for the specific anchor point, i.e., specific feature. The data points are placed at the positions where the spring forces sum up to zero. Multidimensional scaling comprises visualization techniques that place objects in an n-dimensional feature space in a lower dimensional space (like 2D or 3D) such that the objects' distances are preserved as much as possible.

Visualization of (Clustered) High-Dimensional Data with Multiple Linked Views

Since the clustering process for dimension reduction may contain a loss of spatial information, Linsen et al. [2008] presented a surface extraction approach that includes spatial information of multifield clustered data. Hence, boundary surfaces are extracted and semi-transparently visualized in a 3D star coordinate layout to reveal nested clusters. Poco et al. [2011] employed a least square projection to map high-dimensional data to 3D visual spaces. Their framework allowed for the visualization of multidimensional non-spatial data and integrates the feature space of multi-variate spatial data. Both approaches employed surface representations for their cluster results.

The *DimStiller* framework presented by Ingram et al. [2010] allows for analysis and dimensionality reduction of high-dimensional data. Hence, the user can define workflows that can be re-used for different databases. Tatu et al. [2012] provided a subspace and search visualization approach where not only one subspace is created, but a candidate set of subspaces. Also, the brushing concept was employed for high-dimensional data such that the user can jointly study the structure of the dimensions space as well as the distribution of data items with respect to the dimensions by Turkay et al. [2011a]. The combination of parallel coordinates and large time-varying data can be visually explored with *meta parallel coordinates*, a parallel coordinates plot based on perceptually motivated visual metrics [Dasgupta et al., 2012]. Another visualization technique for large, time-dependent data was introduced by Walker et al. [2012] where the parallel coordinates are combined with spherical coordinates. For more information about parallel coordinates, the survey by Heinrich and Weiskopf [2013] is recommended. The *TiMoVa* framework supported domain experts during model selection in time series analysis through an interactive visual interface [Bögl et al., 2013]. The approach by Krstajic et al. [2011] visualized large and dynamic event data sets with so-called *CloudLines*. Their technique revealed visual clusters in a compressed view of multiple time series and also included interactive distortion techniques for an individual data item analysis. Zhao et al. [2011] presented the *ChronoLenses* framework for the visual analysis of time series. For a closer look on visual methods for analyzing time-oriented data, the reader is referred to Aigner et al. [2008].

The framework by Younesy et al. [2013] allowed for visual analysis of epigenomic data including grouping of the data by k-means clustering or the querying based on presence or absence of signals in different epigenomic experiments. For the interactive visual analysis of temporal cluster structures, Turkay et al. [2011b] presented two novel visualization techniques, the temporal cluster view and the temporal signatures, to analyze and evaluate temporal clusters. The approach by Hadlak et al. [2013] allows for clustering of temporal attributes for visual analysis of dynamic networks. Hence, the supergraph is visualized in combination with the clustered nodes that share a similar trend over time. The *Microarray Time-Series Explorer* framework was presented by Craig et al. [2012], and is dedicated for exploratory analysis of large scale microarray time series data. The work by Zachow et al. [2009] employed the *SimVis* framework for visual analysis of nasal air flow. Hence, the attribute views of this framework, e.g., the parallel coordinates plot, curve views of the temporal data, or scatterplots, were linked with each other and the user can highlight certain attributes via brushing and linking. In summary, the visualization of (clustered) high-dimensional data with multiple linked views is an active research area. A comprehensive overview of the visualization of high-dimensional data is presented in Chapter 6 in the visualization book of Schumann and Müller [2000]. Furthermore, the survey by Kehrer and Hauser [2012] holds an important overview about visualization and visual analysis of multi-faceted scientific data.

4.1.3 Visualization of MRI Perfusion Data

In this section, the visualization of perfusion data is described in more detail. Therefore, it is divided into three parts:

- The first part introduces commercially available software workstations for perfusion data.
- The second part introduces the three-time-point (3TP) method in more detail, since this method has been employed for the techniques developed in this thesis.
- The third part holds related work for the visualization and visual analysis of perfusion MRI data.

Commercially Available Software Workstations for Perfusion

Many commercially available perfusion software systems comprise these basic visualization techniques. The *CADstream software*[1] provides colored parameter maps and highlights voxels with a relative enhancement (RE) value above a given threshold. Hence, the color represents the post-initial change of the voxel's RE curve. A washout curve is color-coded red, a plateau curve is color-coded green, and a continuous enhancing curve is coded blue. Furthermore, the percentage of curve types in comparison to the whole lesion is presented. As a prerequisite step, the radiologist must manually mark the lesion or define a ROI that contains the whole lesion [Lehman et al., 2006]. The SIEMENS Syngo, Neuro Perfusion Software allow for evaluation of brain tumors. Hence, the concentration time curve as well as color-coded parameter maps are provided. The *nordicICE* software package[2] allows for direct co-registration of anatomical and functional brain data sets. Furthermore, the extraction of quantitative perfusion parameters is supported and the parameter maps are presented in 2D color-coded views [Bjørnerud, 2003].

The 3TP Breast Software Packacke

The 3TP breast software package was employed in the approach by Hauth et al. [2006a]. Hence, the curve shape is mapped to color and the RE of the contrast agent is mapped to

---

[1] Product of Confirma, Kirkland, USA; www.confirma.com (10/01/2013)

[2] Product of NordicNeuroLab, Bergen, Norway; www.nordicneurolab.com (12/08/2013)

intensity. This is based on the 3TP method introduced by Degani et al. [1997] and illustrated in Figure 4.3.

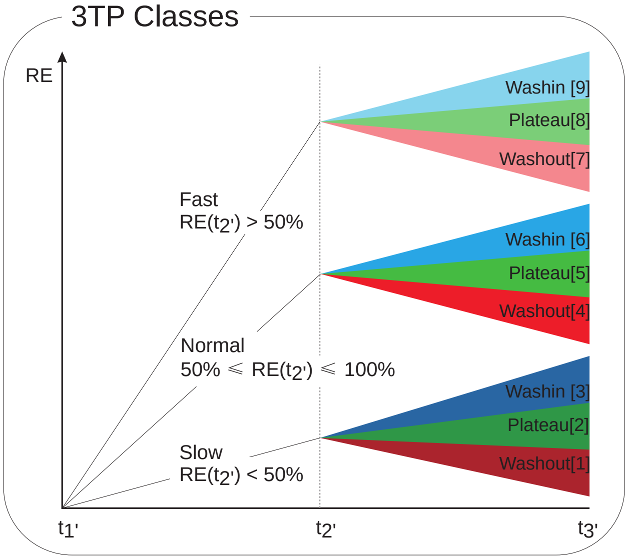

Figure 4.3: *Mapping of the 3TP classes to colors and intensity.*

In Figure 4.4, the software interface is depicted. A limitation of this software package is the missing assessment of lesion heterogeneity. Also, besides the percentage distribution of the nine clusters over the whole tumor no additional information about cluster attributes is available. In Section 4.2.2, related studies that employ this software package for automatic feature breast classification are presented.

Visualization and Visual Analysis of MRI Perfusion Data.

First, the visualization of perfusion data is described. Afterwards, the visual analysis is presented.

Visualization of MRI Perfusion Data. For the specific application area of perfusion data sets, the general evaluation approaches comprises conventional techniques, like cine-movies, subtraction images, color-coded parameter maps as well as more sophisticated visual analysis methods [Preim et al., 2009]. Cine-movies describe an animation of 2D views of the perfusion MRI data sets through all time steps of the acquisition. They are well suited to detect enhancement patterns of the contrast agent. Subtraction images show the contrast enhancement or contrast concentration differences between two points in time, revealing contrast enhancing regions and non-enhancing tissue. In general, color-coded parameter maps for perfusion MRI map the voxel values of a single parameter to color. These maps represent a 2D slice of the data set. Based on these parameter maps, the radiologist can identify ROIs with similar parameters and extract time-intensity curves from these ROIs.

Kohle et al. [2002] presented a new approach for volume visualization of breast DCE-MRI data. A color mapping for the highlighting of perfusion abnormalities and the closest vessel projection to add depth information to maximum intensity projections are employed. Englmeier et al. [2004] also employed a mapping of parameters to color and intensity, but the

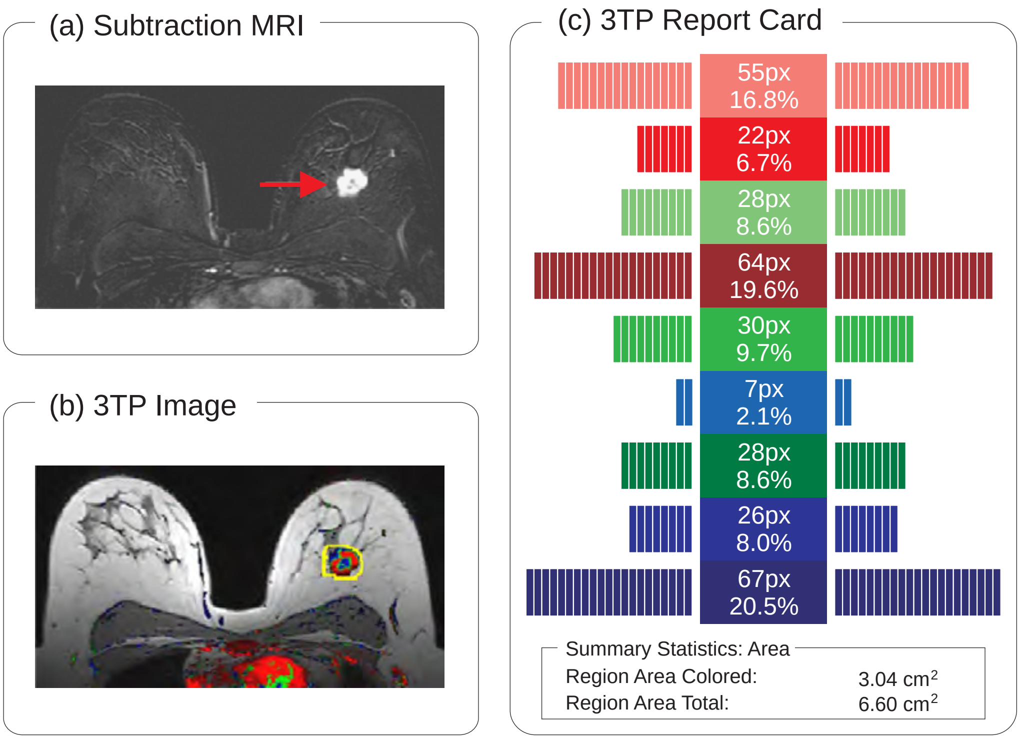

Figure 4.4: *Illustration of the 3TP color-coded image (Image adapted and reprinted from [Hauth et al., 2008] © 2007 Elsevier Ireland Ltd with kind permission from Elsevier). In (a), the subtraction image of breast DCE-MRI reveals a contrast-enhancing lesion in the left breast (see arrow). In (b), the 3TP color-coded image is presented where the lesion has been encircled (see yellow outline). Furthermore, the software employed in the study provides the 3TP report card that presents the total number and percentages of the nine 3TP classes, i.e., the color hue and color intensity of the voxels in the encircled area, see (c).*

user has to infer the parameter value from the associated color and intensity component. Oeltze et al. [2008a] combined color with glyphs to map more than one perfusion parameter to convey information about the coronary heart disease based on myocardial perfusion MRI. Hence the glyph combined color, shape and orientation to map the information, similar to color icons, which were introduced by Levkowitz [1991]. A further approach employed glyphs for visual exploration of cerebral perfusion MRI, including multi-resolution glyphs to improve readability and different glyph shapes [Oeltze et al., 2008b]. For the state of the art about glyphs, the reader is referred to the taxonomy-based glyph design by Maguire et al. [2012]. Also, isolines, height fields, or orientations of textures might be employed to combine several parameters within a single image, see the survey of visual exploration and analysis of perfusion data for more detail [Preim et al., 2009]. Here, for example, the application of colored height fields for the analysis of myocardial perfusion data was presented. Hence, the descriptive perfusion parameter peak enhancement was mapped to height, and washin was mapped to color. As a second example, the usefulness of movable viewing lenses [Bier et al., 1993], also called *Magic Lenses*, was demonstrated for breast perfusion and cerebral perfusion MRI. Hence, one parameter value was presented as context visualization, and the lens visualized another parameter as focus map to allow for a multi-parameter exploration.

Visual Analysis of MRI Perfusion Data. Medical image data sets become larger and more complex. The study by Lundström and Persson [2011] characterized the visual analytic tasks in diagnostic imaging. They stated that the increasing complexity of medical image data induces an increasing demand for visual analytic solutions. Their study revealed that the key issue remains the diagnosis of primary and secondary findings. Albeit their work identified the diagnosis of primary and secondary findings in the image data in an efficient way as key issues, the determination of shape, size, and relative position of different parts of the anatomy were identified as important component of a radiologist's image review work

As a result, advanced methods including visual analytic solutions are required to improve and support the radiologist's work. The Profile Flag approach is an example for a more advanced exploration approach for breast MRI perfusion data. It was presented by Mlejnek et al. [2006] and allowed for the intuitive probing and annotation of temporal data. The visualization of the temporal curves is closely connected to the rendering of the anatomic structure of the data without removing any parts thereof. Mostly, a preselection of voxels or a segmentation is created, as a basis for further analyses. Coto et al. [2005] employed enhancement scatterplots of the pre-contrast intensity and the RE for such a preselection in breast DCE-MRI data. They developed the *MammoExplorer* - a multidimensional view framework comprising these techniques. The user can select voxels of interest for a visual exploration of the breast perfusion data set where cutaway views reveal the suspicious breast tumor embedded in its surrounding tissue. The exploration can also be improved by brushing and linking. This is similar to the work by Oeltze et al. [2007] where brushing and linking was also applied to perfusion data sets. This was carried out with the *SimVis* framework, presented by Doleisch et al. [2003] (recall Sect. 4.1.2). Furthermore, they carried out correlation analysis and a PCA for dimension reduction and analysis of the inter-parameter relations for descriptive perfusion parameters.

Related to this work, Oeltze et al. [2009] presented a visual analysis of longitudinal cerebral perfusion data sets to evaluate ischemic stroke. Again, they employed the *SimVis* framework. The exploration of the brain was carried out to assess how much of the brain tissue is affected by an ischemic stroke and if the tissue is irreversibly damaged (no contrast agent will arrive) or if it is tissue-at-risk (delayed contrast agent washin). Hence, the authors brushed over the first two principal components of a PCA carried out over the descriptive perfusion parameters. They reported that the first and second principal components reflect the magnitude of enhancement and the time to enhancement, respectively. With the brushing, brain tissue with a delayed washin (increased time to enhancement) and only little contrast agent arriving (small magnitude of enhancement) could be selected. Applied to three consecutive scans of a stroke patient revealed a decreased amount of infected brain tissue, indicating that the tissue-at-risk benefited from the thrombolytic therapy that was carried out between the scans.

Similar to the adaption of the *SimVis* framework to medical image data, Blaas et al. [2007] presented a system for analyzing and exploring medical multifield data and integrated techniques from pattern analysis to enhance the data exploration process. The software assistant *MeVisCardioPerfusion* by Kühnel et al. [2006] allowed for analysis of cardiac MR perfusion data. Hence, the evaluation of myocardial tissue for diagnosis and assessment of severity of cardiac stroke is supported. The work by Hennemuth et al. [2007] extended this framework with different exploration modes based on the evaluation of perfusion parameters, enhancement curves, and user-defined thresholds in automatically selected regions. Then, a more accurate detection of distorted regions of the left ventricle was possible. In [Preim and Botha, 2013], an extensive description including state of the art for perfusion data visualization and analysis is provided. Finally, the PhD-thesis by Oeltze [2010] “Visual Exploration and Analysis of Perfusion Data” with focus on brain and cardiac perfusion MRI for assessment of ischemic stroke and heart attacks comprehensively aggregates important techniques for perfusion data sets. The thesis at hand is closely related to this work. However, the strong application-oriented methods (including the clinical research question about importance of tumor heterogeneity), the large collection of data sets as well as integration of sophisticated clustering and classification approaches are the fundamental differences.

4.2 Evaluation of Breast Tumors in DCE-MRI Data

This section focuses on breast DCE-MRI from a clinical point of view. When compared to conventional X-ray mammography, breast perfusion DCE-MRI exhibits high sensitivity, but only a moderate specificity. Thus, a crucial task is to improve this specificity by means of computer-based classification approaches and the automatic classification into benign and malignant tumors is an active clinical research area. As a prerequisite, the lesions have to be detected in the DCE-MRI data set. Lesion detection approaches are listed in Section 4.2.1. Afterwards, the classification of breast lesions is analyzed in more detail in Section 4.2.2. Therefore, the related studies are roughly categorized based on the features that were employed for the classification: features that mainly cover kinetic analysis, features covering the lesion margin and morphology, and the combined features of both aspects.

4.2.1 Breast Lesion Detection in DCE-MRI Data

Due to the principle of DCE-MRI, suspect lesions are identified as contrast-enhancing lesions. Therefore, the enhancing lesion can be approximated with a primitive volume growing algorithm.

In general, subtraction images allow for the identification and the extraction of enhancing lesions. Also, the RE values of voxels can be employed for a primitive segmentation. Lucas-Quesada et al. [1996] introduced two semi-automatic methods for the segmentation of breast lesions in DCE-MRI data. The first approach is based on temporal correlation, whereas the second approach employs a multi-spectral analysis to generate a feature map. Chen et al. [2006a] proposed a fuzzy *c*-means algorithm followed by binarization and optimization steps to automatically segment tumors. Hence, the user had to select a ROI on which further analysis is carried out. They compared the fuzzy *c*-means lesion detection with a volume-growing method and with a reference segmentation that was manually extracted by an expert radiologist. They reported better results for the first mentioned technique. In [Ertaş et al., 2007], the lesion segmentation was carried out by generating a normalized maximum intensity-time ratio projection of the data set. Behrens et al. [2007] proposed a method combining region growing and morphologic operations on subtraction images of the breast.

For further reading, the survey on real-time breast lesion characterization in DCE-MRI by Suri et al. [2006] is recommended. Hence, additional techniques for tumor detection and analysis are presented as well. However, this thesis focuses more on the lesion characterization and exploration than the lesion detection itself.

4.2.2 Classification of Breast Lesions in DCE-MRI Data

In many approaches, the lesion detection and the classification process are interleaved. Therefore, some of the following approaches also include the lesion detection as a prerequisite step. The state of the art of breast tumor classification comprises various feature sets on which the classification is carried out. These feature sets are linked to:

- the kinetic contrast enhancement,
- the texture of the tumorous tissue in the medical MRI data,
- the tumor's boundary and morphology, and
- a combination thereof.

Each of these four aspects will be discussed in more detail in the following. However, the automated image analysis methods do not only aim at the extraction of the relevant information from breast perfusion MRI but also at the reduction of the inter-observer variability [Chen et al., 2007]. Thus, a more accurate and consistent image interpretation is possible, which is very important due to the absence of standardized interpretation guidelines in the clinical routing of breast lesion imaging.

Classification with Focus on Kinetic Analysis

For the extraction of kinetic features, the strong variations of different tumor parts have to be taken into account. That means, a tumor is a heterogeneous lesion containing different tissue parts with different perfusion characteristics. To reduce the influence of outliers, a set of voxels is selected and their RE curves are analyzed. Furthermore, averaging over similarly perfused tissue parts is possible. Thus, in general a preselection of voxels has to be carried out.

Chen et al. [2006b] employed a fuzzy c-means clustering algorithm to the segmented 3D breast lesion to obtain clusters that describe prototypic curves. This was an extension of their previous work Chen et al. [2006a]. Next, the prototypic curve with the highest initial enhancement, i.e. the highest washin, was chosen to be the representative *characteristic kinetic curve* (CKC) of the lesion. Classification was carried out by applying the receiver operating characteristic (ROC) curve analysis to four features of the CKC: the descriptive perfusion parameters peak enhancement, time to peak, washin rate, and washout rate. The classification result based on the CKC was compared with a second and third classification. The second classification was carried out on features that were extracted from the whole lesion's average curve. The third classification was carried out on features extracted from a ROIs average curve, where the ROI was manually placed by an experienced radiologist. As a result, the first classification yielded better results than the second one. It yielded similar results to the third classification. As conclusion, the automatically determined CKC had a better discriminating power than the whole lesion's average curve.

The work by Baltzer et al. [2009] compared the classification result when taking the whole lesion instead of a single curve into account. Hence, the authors employed two features describing the curve types:

1. The initial contrast enhancement of the RE curve was classified into significant, $< 50\%$; intermediate, $50\% - 100\%$; strong, $> 100\%$.

2. The curve shape after initial contrast enhancement was classified (based on the difference of the last RE value and the RE value after initial contrast enhancement) into continuously increasing $> 10\%$; plateau stable RE $\pm 10\%$; washout $> 10\%$.

This is similar to the 3TP classification, recall Figure 4.3. Classification was carried out via ROC analysis by employing only the most suspect curve based on highest washin, or the feature distribution percentage of the whole lesion. Furthermore, a logistic regression analysis was carried out based on the combined features of the most suspect curve and the whole lesion. As a result, the integration of the whole lesion improved the specificity when compared to analysis of the features of the single most suspect curve, but no statistical significance for this finding was found. Note that this stands in contrast to the previous study [Chen et al., 2006b], where the CKC achieved best classification results.

As it was already described, the 3TP method by Degani et al. [1997] extracted nine classes of RE curves, recall Figure 4.3. Hauth et al. [2006b] applied this method for classification purposes by combining the extracted classes per lesion and the whole class distribution per lesion. In the study by Hauth et al. [2008], this work was extended, and next to the 3TP method, pharmacokinetic model-derived variables are employed, recall the example in Figure 4.4. To extract the pharmacokinetic parameters vascular permeability and extracellular volume fraction, the Tofts model [Tofts and Kermode, 1991] was adapted to the data sets. Feature extraction was carried out over the whole 3D lesion and a 2D part of a lesion. The 2D part was extracted by considering the 2D slice of the DCE-MRI data set where the lesion's diameter was maximal. As a result, the kinetic and pharmacokinetic features showed significant differences between benign and malignant lesions, and the 3D analysis achieved better results than the 2D analysis.

The study by Williams et al. [2007] comprised a classification based on the kinetic features: presence or absence of threshold enhancement of 50% and 100% minimum thresholds; peak of initial enhancement and the percentage distribution of curve shape (washout, plateau, and increasing) of the whole lesion. The initial peak enhancement value was extracted from the most suspicious curve (with washout > plateau > persistent w.r.t. suspiciousness, and highest initial enhancement). The presence of the threshold enhancement was very sensitive for malignancy compared to the manual evaluation of an experienced radiologist, whereas the initial peak enhancement and the curve distribution did not demonstrate further improvements.

Classification with Focus on Lesion Margin and Morphology

Numerous studies comprise a DCE-MRI breast cancer classification with integration of lesion margin and morphology. As it was stated in Section 2.1.2, ill-defined margins and irregular morphologies are indicative for malignancy. Usually these features are combined with kinetic analysis. Liang et al. [2012] carried out a classification based on lesion shape and lesion margin. However, these features are extracted from the minimum volume-enclosing ellipsoid of lesions that are segmented manually. The study by Wedegärtner et al. [2001] focused on lesion morphology by employing the features lesion shape, irregularity of contour, homogeneity of contrast enhancement, and presence of ring enhancement. As a result, the morphological criteria were useful features, but prone to errors due to a high inter-observer variability. Hence, a standardization of the terminology of the morphological features could solve this problem. The morphologic lesion analysis is also discussed by Behrens et al. [2007] in more detail, including a summary of important morphology features presented in literature. The authors highlight the strong influence of the preceding processing, image resolution and applied protocols for the extraction of these features and demand a thorough evaluation for a larger scale of data to truly assess their discriminative power.

Classification with Combined Features

A combination of texture, morphology, and kinetic features for DCE-MRI classification is promising since malignant tumors are associated with rim or heterogeneous enhancement due to necrosis and fibrosis mainly in the tumor center, and thus an angiogenetic activity predominantly at the periphery [Buadu et al., 1996]. Texture and morphologic features were combined in the study by Nie et al. [2008]. As a result, benign lesions showed a rounder shape and smoother margins than benign ones, which can be assessed with the morphologic feature *compactness*. The texture features were associated with heterogeneity patterns and enhancement intensity. They could be successfully employed since the malignant lesions were more heterogeneous in terms of these features. Gibbs and Turnbull [2003] focused on texture features for classification, including the entropy and the sum entropy. When combining them with lesion size, average time to peak of the lesion, and patient's age, a diagnostic accuracy of 0.92 ± 0.05 (approximated with area under curve analysis) was achieved.

Chen et al. [2007] also employed texture features for classification. Instead of a slice-wise analysis of the texture features (extracted from 2D slices), they employed a volumetric analysis, which is reported to achieve better results. Sinha et al. [1997] combined kinetic features with boundary and texture features. They also included the patient's age in the feature set. Best values for sensitivity and specificity were achieved by combing the three feature classes and including the patient's age. When a restriction to only one feature class was carried out, boundary features were identified as best suited, followed by kinetic features and texture features. This is similar to the work by Chen et al. [2004], who combined morphology features, kinetic features and the time course of contrast enhancement variation over the whole lesion. They reported better results for automatic classification when compared to results based on manual evaluation of experienced radiologists. However, Fusco et al. [2012] performed manual tumor segmentation and then studied different subsets of region features: dynamic ones, spatio-temporal ones, and texture features. They showed that the subset of dynamic features achieved highest discriminative power.

Wiener et al. [2005] combined morphologic features and kinetic features based on the 3TP classification. Okafuji et al. [2008] analyzed lesions that were detected as circumscribed masses on conventional mammography. For classification of these lesions in DCE-MRI, the rim enhancement, the heterogeneity of enhancement, the washout dynamic pattern, and combinations thereof were considered, revealing an increased importance of the washout dynamic pattern.

The scoring system that was first described by Fischer et al. [1999] - the Göttinger score - comprises pre-defined choices for initial peak signal intensity increase, signal intensity in the late contrast phase, lesion margin, lesion shape, and contrast material kinetics. For each feature, a certain amount of points is assigned. These points are summed up as score. Classification is then carried out via a cut-off value for this score. They reported sensitivity, specificity, and accuracy rates for the DCE-MRI-based evaluation of 93%, 65% and 85%, respectively. They tested their approach with a database containing 548 breast lesions.

An interesting combination of kinetic and texture features was introduced by Karahaliou et al. [2010]. They extracted three parameter maps of the breast lesion based on the three kinetic parameters: initial enhancement, post-initial enhancement, and signal enhancement ratio. Afterwards, they applied texture analysis to the parameter maps to assess the lesion's heterogeneity. Best classification results were achieved with the signal enhancement ratio map. In addition, the multi-center study introduced by Schnall et al. [2006] showed the importance of the combination of features from morphology and kinetic enhancement. They concluded that the multivariate models comprising feature assessment have a diagnostic accuracy superior to that of qualitative characterization of the kinetic enhancement in breast DCE-MRI. Stoutjesdijk et al. [2005] reported a considerable inter-observer variability for kinetic and morphologic enhancement features. In their study, different observers evaluated breast DCE-MRI lesions and chose attributes from a standardized terminology. Furthermore, the manual ROI placement was identified as major source of variability for the extraction of kinetic features.

A short summary of the presented classification studies will be presented in Section 4.4 at the end of this chapter. Also, the most important aspects for this thesis will be expressed. The next section focuses on the evaluation of brain DSC-MRI data of longitudinal glioma studies.

4.3 Evaluation of Low and High Grade Gliomas in DSC-MRI Data

The main focus of this thesis is not the diagnosis and evaluation of brain tumors in general, but the analysis of gliomas in DSC-MRI data, especially the differentiation of high grade gliomas (HGGs) from low grade gliomas (LGGs). This is motivated by the importance of DSC-MRI for tumor differentiation rather than detection [Covarrubias et al., 2004]. In clinical research regarding neurological impairments, longitudinal studies are becoming more and more important [Ashburner et al., 2003]. For the evaluation of LGGs and HGGs, the evaluation of the relative cerebral blood volume (rCBV) is a clinical research focus. It is an important indicator for a patient's survival and gliomas with high rCBV values have a significantly faster progression time [Law et al., 2008]. Since patients with LGGs may transform to HGGs at some point in time, these patients are commonly subject to a life long MRI-based monitoring. To detect a transformation from an LGG into an HGG, computer-aided methods are employed to analyze the acquired medical image data.

For longitudinal studies, rCBV maps of different acquisitions have to be compared, which is a complex and exploratory analysis task due to the absence of standardized intensity values and the high variability of MRI scanners and patient data. When taking a series of perfusion data (in the context of a longitudinal study) into account, the complexity gets even higher. As one challenge, inter-voxel correspondence has to be established between scans of different time steps. This is further complicated by tumor growth and increasing tumor heterogeneity. At last, MRI scans from longitudinal studies are acquired over a period of several years and thus employ different scanning protocols, image resolutions, and sequence parameters. This is in contrast to cohort studies, e.g., the SHIP study [Völzke et al., 2011] where many patients are examined in a short time period and extra care is taken to avoid image parameter changes. Currently, longitudinal studies are assessed with software intended for the diagnosis of a patient at one point in time. Hence, no dedicated support for longitudinal studies, i.e., normalization of image data and visual comparison of data from different points in time, is provided. In the work of Steenwijk et al. [2010], visual analysis techniques were applied to cohort study image data to explore parameters across patients. So far, visual analysis has seen limited use in medical research, although many applications would strongly benefit from these methods due to the magnitude and heterogeneity of the data.

This section introduces important studies that examine the suitability of perfusion parameters for differentiation between glioma type in its first part. The second part covers more general concepts, like the optimal ROI size or the tumor heterogeneity.

4.3.1 Evaluation of Perfusion Parameters for Glioma Grade Differentiation

When focusing on perfusion MRI of the brain, many studies have shown that rCBV highly correlates with the tumor grade [Law et al., 2004] and can be employed for differentiation between LGGs and HGGs [Shin et al., 2002, Law et al., 2003, Hakyemez et al., 2005, Emblem et al., 2008, Law et al., 2008]. For evaluation of gliomas, a representative ROI is placed and the average rCBV values of the ROI are analyzed. However, a gold standard for a cut-off value between LGGs and HGGs of a ROI's average rCBV value is still missing [Bjørnerud and Emblem, 2010]. Shin et al. [2002] identified 2.93 *ml* / 100 *g* as best rCBV cut-off value, and Hakyemez et al. [2005] 1.98 *ml* / 100 *g* for differentiation between LGGs and HGGs. Covarrubias et al. [2004] suggest an rCBV value of 1.5 *ml* / 100 *g* and Law et al. [2003] 1.75 *ml* / 100 *g* as cut-off value. These cut-off values are reported to have high sensitivity but low specificity by Emblem et al. [2008]. They suggest cut-off values between $3.75 - 5.58$ *ml* / 100 *g* after minimizing the number of glioma grade misclassification and maximizing the average sensitivity and specificity Law et al. [2007] propose an rCBV histogram analysis. They extract 14 different measures from the normalized histogram based on the method described in [Ge et al., 2001]. A ROI is used to mark the tumor voxels (not a single hot spot) and features like the mean, median and standard deviation are extracted from the ROI's histogram. The histogram-derived features yields similar results to conventional rCBV ROI-based analysis w.r.t. the correlation with glioma grade. Likewise, Friedman et al. [2012] propose a similar method. Again, histogram-based rCBV features are compared with the maximal rCBV value of a ROI within the brain tumor. In addition, they also examined the results from specialist and non-specialist operators. They reported that for the feature extraction with highest correlation to tumor grade (with their semi-automatic approach) no specialized operator was necessary.

Despite the widespread application of the perfusion parameters cerebral blood flow (CBF) and mean transit time (MTT) in stroke imaging, the concepts of these parameters have not been as fully studied in the context of brain tumor perfusion analysis as has CBV [Covarrubias et al., 2004]. However, the studies by Shin et al. [2002] and Hakyemez et al. [2005] did not only employ CBV but also CBF. They reported significant differences of CBF between LGG and HGG. Other studies employed the tumor permeability extracted from T_1-weighted permeability imaging [Roberts et al., 2000] and extracted from T_2^* DSC-MRI [Provenzale et al., 2002]. They report strong correlation of permeability and tumor grade. However, the study by Law et al. [2004] compared the correlation of rCBV and permeability with the tumor's grade. They identified rCBV to be a more significant predictor for high-grade gliomas than permeability. In another study, Law et al. [2006] carried out different approaches for tumor grade differentiation, including rCBF as well as rCBV. Again, they identified rCBV as best predictor of glioma grade. Järnum et al. [2010] compared a 3D pseudo-continuous arterial spin labeling technique with the DSC-MRI to cope with the susceptibility artifacts. They employed the *nordicICE* software package (recall Sect. 4.1.3) and extracted CBF parameter maps for both sequences, see Figure 4.5. They reported a good correlation between the parameter maps. Thus, they suggested 3D pseudo-continuous arterial spin labeling technique as an alternative for patients with renal failure since no contrast agent injection is needed.

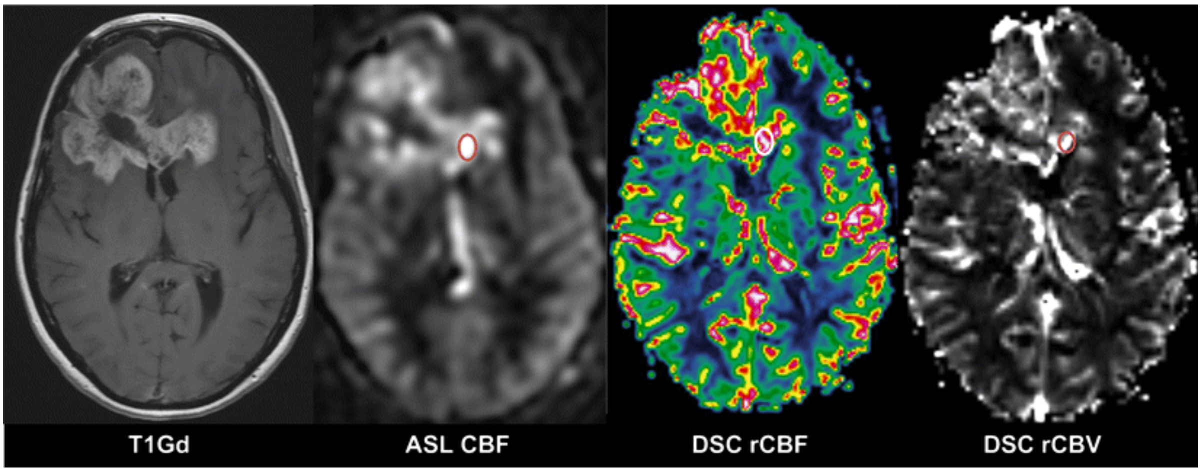

Figure 4.5: *Patient with glioblastoma in the frontal lobes (Image reprinted from [Järnum et al., 2010] © 2009, Springer-Verlag with kind permission from Springer Science and Business Media). On the left, the T_1 sequence reveals the contrast enhance glioblastoma. The images ASL CBF and DSC rCBF show the CBF and rCBF parameter maps for the arterial spin labeling sequence (gray scale) and the DSC-MRI sequence (color coding), respectively. On the right, the rCBV parameter map from the DSC-MRI sequence is presented.*

4.3.2 Influence of ROI Size and Heterogeneity Evaluation

This part focuses on two important aspects when evaluating brain tumors in DSC-MRI data beyond the parameter based evaluation:

- the optimal placement of ROIs and
- the tumor's heterogeneity.

For ROI placement, rCBV parameter maps are analyzed. In general, color coding highlights rCBV values higher than 1.25 *ml* / 100 *g* [Covarrubias et al., 2004]. The ROI is placed such that highest spatially connected rCBV values - the hot spot - are included with exclusion of brain vessels. This method is therefore called hot spot method. However, it suffers from inter-observer variability. Furthermore, different recommendations about the optimal ROI's size exist [Wetzel et al., 2002]. For example, Hakyemez et al. [2005] employed the hot spot method with at least 16 pixels in their study, whereas Bisdas et al. [2009] recommended 6×6 pixels. In the study by Wetzel et al. [2002], different methods for creating a representative ROI regarding intra- and interobserver reproducibility were analyzed. Best results were achieved if each observer selects four ROIs (with radius 1.8 *mm*) and applies the maximum averaged CBV value for glioma grading. However, LGGs do vary regarding their size as well as their amount and extent of foci with high rCBV. Furthermore, Emblem et al. [2008] presented a histogram analysis of rCBV heterogeneity leading to increased diagnostic accuracy and inter-observer agreement. Lupo et al. [2005] extracted the spatial heterogeneity of a brain tumor's concentration-time curves to further distinguish microvasculature characteristics.

4.4 Concluding Remarks

This chapter illustrated the different aspects that influence the visual analysis of MRI perfusion data with respect to brain and breast tumors. Inherent to this problem is the grouping of voxels into regions. Furthermore, the set of tumor voxels can be interpreted as set of objects in a high-dimensional feature space. Such data is in general visualized by representing (lower dimensional) clustering or examined via multiple linked views that allow for interactive exploration of different subspaces of the data. Most techniques consist of one (or all) approaches. They reduce the high-dimensional space to a lower dimensionality (e.g., via clustering), they employ multiple and interactively linked views with an interaction between the attribute space and the physical domain (e.g., via brushing), or they try to visualize all variables at once (e.g., by glyphs). However, visualization and exploration of high-dimensional data sets remains a challenging task due to the missing spatial information in the low-dimensional space. Furthermore, problems with visual clutter or non-intuitive presentations of the derived low-dimensional space might occur.

Section 4.2 provided related work for breast cancer detection and classification in DCE-MRI perfusion data. Since breast perfusion DCE-MRI has a high sensitivity, but only moderate specificity when compared to conventional X-ray, an important goal of breast cancer evaluation is an automatic classification into benign and malignant lesions to increase the specificity. Due to its high importance, many breast cancer classification studies exist that are based on features extracted from DCE-MRI data. Morphological criteria are useful features but suffer from inter-observer variability due to a missing standardization of terminology. In summary, studies with combined textural, morphology, and kinetic features are superior to conventional manual analysis by experienced radiologists for breast cancer classification.

Important Breast Cancer Classification Aspects. For this thesis, the following aspects are of great importance for breast cancer classification:

$\boxed{1}$ Kinetic features are very important for automatic breast tumor classification (recall Sect. 4.2.2). Features extracted of the most suspect curve are better suited than features from an averaged curve of the whole lesion and it is important to detect this most suspicious curve [Chen et al., 2006b]. However, features of the whole lesion (instead of the averaged curve of the whole lesion), like curve shape distribution, further improve the classification result [Baltzer et al., 2009, Williams et al., 2007].

$\boxed{2}$ The heterogeneity of malignant breast lesions is very important for breast classification and was employed in the studies by Issa et al. [1999], Gibbs and Turnbull [2003], Chen et al. [2007], Ertaş et al. [2007], Nie et al. [2008], Karahaliou et al. [2010]. The heterogeneity analysis based on regions of the breast lesion was carried out in the last study. This region analysis is also part of the third aspect. Furthermore, the heterogeneity analysis is *not* part of current commercially available workstations.

3 A region-based analysis seems to be most appropriate for extracting relevant features since the data sets are noisy by nature. The importance of a ROI-based analysis can also be referred from the first aspect since additional features of the whole lesion or a part of the lesion improve classification results. However, different recommendations for the optimal ROI size and placement exist, ranging from 3-4 pixels to the whole enhancing lesion [Mussurakis et al., 1997, Kuhl et al., 1999, Kuhl, 2007]. Thus, the inter-observer variability is a substantial limitation for manual placement.

4 Many studies employ perfusion parameters for kinetic feature analysis. For example, pharmacokinetic parameters are extracted in the studies by Hauth et al. [2008] and Englmeier et al. [2004]. Also descriptive perfusion parameters are employed, mostly the parameters peak enhancement, time to peak, washin and washout [Sinha et al., 1997, Chen et al., 2006b, Hauth et al., 2006a,b, Williams et al., 2007]. Furthermore, the 3TP method is part of many studies. This method basically comprises the features washin and washout.

5 Although manually derived morphologic features have been successfully employed for classification, their usefulness is hampered by a lack of standardized terminology. Thus, an automatic estimation of morphologic features is not an aim of this thesis. However, the analysis of a breast tumor's morphology should be supported in a qualitative way.

Important Aspects For Evaluation of Longitudinal Brain Tumor Studies. In contrast to breast perfusion MRI, the evaluation of brain perfusion MRI does not aim at an automatic identification of benign or malignant lesions. Instead, the clinical research focus lies on the differentiation of gliomas. Since the grade of gliomas is important for a patient's survival progression time, many studies evaluate the dependency of the quantitative perfusion parameter CBV and the tumor grade. Therefore, an important part of clinical research is the evaluation of longitudinal studies that cover the transformation from LGGs to HGGs. That implies the following aspects:

6 For longitudinal studies, different perfusion acquisitions have to be compared, which is a complex and exploratory analysis task due to the absence of standardized intensity values and the high variability of MRI scanners and patient data. When taking a series of perfusion data (in the context of a longitudinal study) into account, the complexity gets even higher.

7 The exploration with visual analysis techniques within multiple linked views aims at evaluating *single* perfusion studies. However, specific support for longitudinal studies is needed for the comparison of different points in time – taking into account that imaging parameters may have changed.

General Aspects For Evaluation of Breast Tumor DCE-MRI Studies and Longitudinal Brain Tumor DSC-MRI Studies. For both clinical aspects, the following aspects are important:

8 The inter- and intra-observer variability is a limitation of many evaluation methods. Existing approaches are often limited to certain samples, slices or parts of the data set. Therefore, this thesis aims at evaluation of the whole lesion with focus on the most

suspect tumor part. This includes a subdivision of the tumor via clustering and an appropriate representation of the clustering result.

$\boxed{9}$ So far, visual analysis has seen limited use in medical research, although in many applications the magnitude and heterogeneity of the data would strongly benefit from these methods. This aspect comprises the visual analysis of tumor heterogeneity.

The next chapters present dedicated methods that include the given aspects for evaluation of breast and brain tumor perfusion data.

5.

2D Visual Exploration of Breast Tumor Perfusion Data

This chapter is partly based on:

Sylvia Glaßer, Uta Preim, Klaus D. Tönnies, and Bernhard Preim: “A Visual Analytics Approach to Diagnosis of Breast DCE-MRI Data". In Computer and Graphics (34:5), p. 602-611, 2010.

Sylvia Glaßer, Sebastian Schäfer, Steffen Oeltze, Uta Preim, Klaus D. Tönnies, and Bernhard Preim: “A Visual Analytics Approach to Diagnosis of Breast DCE-MRI Data". In Proc. of Vision, Modeling, and Visualization (VMV), p. 351-362, 2009.

Sylvia Glaßer, Kathrin Scheil, Uta Preim, and Bernhard Preim: “The File-Card-Browser View for Breast DCE-MRI Data". In Proc. of Bildverabeitung für die Medizin (BVM), p. 314-318, 2011.

Tobias Böhler, Sylvia Glaßer, and Heinz-Otto Peitgen: “Deformable Registration of Differently-Weighted Breast Magnetic Resonance Images". In Proc. of Bildverarbeitung für die Medizin (BVM), p. 94-98, 2011.

5 2D Visual Exploration of Breast Tumor Perfusion Data

In this chapter, the *PerfusionAnalyzer*, a framework for the visual exploration of breast DCE-MRI perfusion data is presented. The PerfusionAnalyer is a software prototype that integrates conventional views such as parameter maps or subtraction images as well as new developed techniques. As concluded by the previous chapter, the evaluation of the tumor's enhancement kinetics and its predictability for malignancy is a major research focus when evaluating breast perfusion data. Hence, the evaluation of the tumor's enhancement kinetics demands an appropriate exploration of this specific kind of data.

Integrated in the PerfusionAnalyzer, the basic 2D visualization techniques are presented that allow for a precise evaluation of breast DCE-MRI perfusion data. In Section 5.1, the PerfusionAnalyzer framework is described in more detail. Afterwards, in Section 5.2, the embedded breast tumor detection and delineation is explained. For a voxel-wise exploration, a novel glyph-based visualization technique is introduced in Section 5.3. The glyphs are designed to simultaneously map washin and washout of the contrast enhancement. Next, the automatic grouping of voxels into regions is explained in Section 5.4, including dedicated methods how to explore the generated regions. Both approaches focus on the exploration of kinetic features. Their appropriateness is demonstrated with a small case study in a qualitative way.

After these kinetic-oriented exploration techniques, two approaches will be explained that cover the tumor's morphology and histopathology. The first technique is a novel exploration for the investigation of breast tumor boundaries: the *FileCardBrowser View*, described in Section 5.5. Finally, the PerfusionAnalyzer framework is extended with a combined T_1-T_2 view, improving the differential diagnosis by the clinical expert during breast cancer diagnosis, see Section 5.6. The described methods aim at an improved 2D visualization and exploration of the data. The 3D visualization techniques are covered in the next chapter.

5.1 The PerfusionAnalyzer

The PerfusionAnalyzer was developed for the visual exploration of breast tumors. This framework comprises multiple linked views dedicated to breast perfusion DCE-MRI. State of the art for multiple linked views designed for high-dimensional data was generally presented in Section 4.1. In Section 4.1.3, the focus was set on perfusion data in particular. Furthermore, this framework was developed based on the aspects $\boxed{1}$, $\boxed{3}$, $\boxed{4}$, and $\boxed{5}$.

The graphical user interface with the main exploration views is depicted in Figure 5.1. The standard exploration covers the T_1 source image, the subtraction view, 2D parameter maps, and a diagram panel to visualize relative enhancement (RE) curves of a single voxel or a ROI.

These views are in parts known from conventional workstations. Furthermore, novel glyph-based visualizations are created and a region-based analysis of the tumor is provided. These approaches will be described in the following sections in more detail. The 2D parameter maps also includes the three-time-point (3TP) parameter view based on the work by Degani et al. [1997]. Hence, the curve shape is mapped to color (red for washout curve, green for plateau curves and blue to increasing curves) and the initial RE to intensity, recall Figure 4.3.

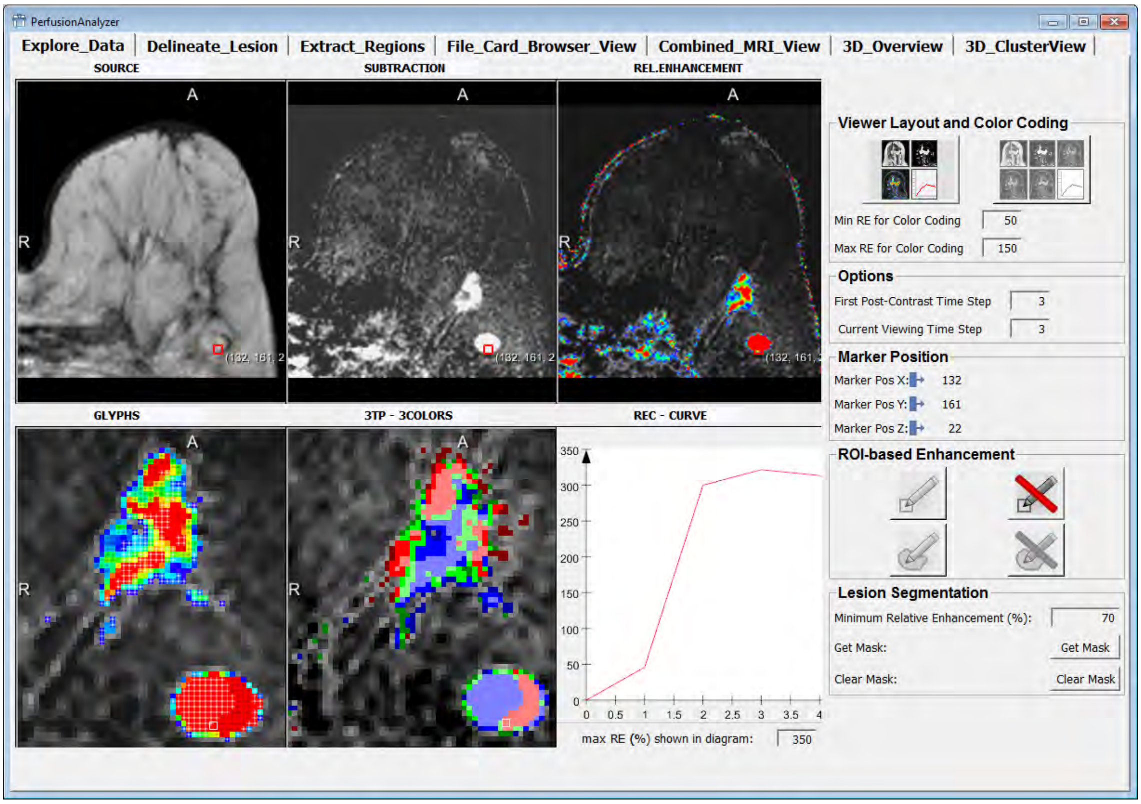

Min RE for Color Coding 50

Max RE for Color Coding 150

First Post-Contrast Time Step 3

Current Viewing Time Step 3

Marker Pos X: 132

Marker Pos Y: 161

Marker Pos Z: 22

Minimum Relative Enhancement (%): 70

Get Mask:

Clear Mask:

max RE (%) shown in diagram: 350

Figure 5.1: *The PerfusionAnalyzer framework with a collection of 2D views. Beyond standard views like the source image, the subtraction image or a 2D color-coded parameter map of RE values, novel visualization techniques are integrated. (Medical image data is courtesy of U. Preim, Municipal Hospital Magdeburg, Germany.)*

The PerfusionAnalyzer comprises the visual exploration of breast data to identify a lesion as well as to segment the lesion. Furthermore, visual analysis techniques to extract important kinetic or morphologic features are included. The PerfusionAnalyzer is a software prototype embedded in the Me*VisLab* framework[1] and implemented in C++, supported by OpenGL and VTK.[2] Hence, a motion correction routine was integrated that based on the combination of rigid and elastic registration [Rueckert et al., 1999]. The lesion detection and in turn delineation from background is described in the next section. The region division was realized via MATLAB.[3]

However, the software is not optimized for speed which leads to long computation times for the analysis of larger lesions. This issue can be tackled with some adapted preprocessing steps in future work. Hence, it is still in the state of a research prototype, e.g., careful workflow-adapted user interface is missing.

---

[1] Product of Fraunhofer MEVIS; www.mevislab.de (12/08/2013)

[2] The Visualization Toolkit, New York, USA; http://www.vtk.org/ (12/08/2013)

[3] Product of the MathWorks, Natick, USA; www.mathworks.de/products/matlab/ (12/08/2013)

5.2 Breast Tumor Detection in DCE-MRI

For the automatic detection of breast tumors in breast DCE-MRI perfusion data, many approaches have been proposed in the last two decades. In the previous chapter, the most important and most related approaches have been listed, recall Section 4.2. Mostly, a preselection of voxels or a segmentation is created as a basis for further analysis, like automatic breast cancer classification.

The major focus of the PerfusionAnalyzer is rather the lesion segmentation than the visual exploration and analysis of the segmented lesion. Therefore, a basic volume growing algorithm is employed. The software prototype needs a one-click user interaction to mark a seed point inside the tumor tissue. Next, a region growing selects all voxels that are spatially connected to the marked seed point with RE values $\geq 60\%$ at the first time step after the early post contrast phase. The early post contrast phase is the phase after contrast agent bolus injection, which is usually characterized by a strong uptake of RE values. After this early phase, the contrast agent enhancement is particularly interesting since contrast agent washout can occur, which is indicative for malignancy, recall also Section 2.1.2. Voxels with RE values $< 60\%$ were considered to belong to the surrounding normal tissue. The RE threshold was defined according to [Kuhl et al., 1999], but the user can change it to adapt it to the data. This limit was established for each lesion. However, the threshold applies only to the border voxels of the tumor. Voxels in the internal space could have values below this threshold, for instance due to necrosis. The radiologist was allowed to edit the segmented lesion by adjusting a rectangular ROI. Thus, the clinical expert could exclude tissue not belonging to the tumor, for instance vessels. In Figure 5.2, an example illustrates RE of voxels forming a contrast-enhancing mass

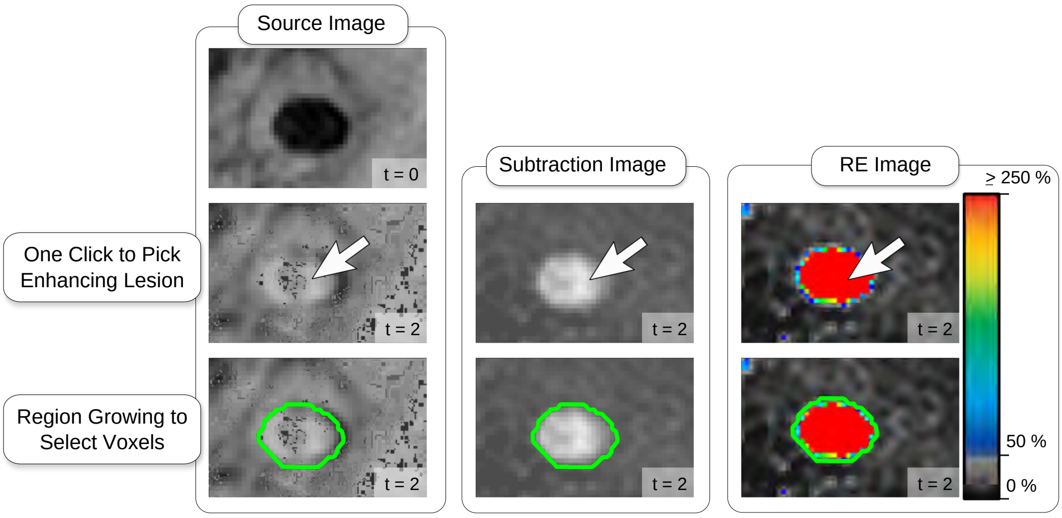

Figure 5.2: *Illustration of the tumor segmentation. At first, a one-click user interaction is necessary to pick the lesion. Afterwards, region growing selects all spatially connected voxels with a user-defined minimum RE value at the first time step after the early post-contrast phase. (Medical image data is courtesy of U. Preim, Municipal Hospital Magdeburg, Germany.)*

This basic segmentation was carried out with an experienced radiologist for a total of 146 small breast lesions yielding satisfying results for all data sets. Small refers to tumors with a maximum slice diameter $\approx 7-8$ *mm*. Such small tumors are often metastases of an existing primary tumor. Due to present contrast enhancement even for these small tumors, they can be better assessed with DCE-MRI than X-ray mammography. Also, the PerfusionAnalyzer segmentation was less time-consuming than manual segmentation. However, for future work, a method that automatically detects supplying vessels or vessel-like structures could be integrated.

5.3 Glyph Visualization

The main drawback of existing approaches, especially color-coded parameter maps, is the missing information about curve shapes. Parameter maps mostly assign only one parameter to color, or combine different color hues, whereas the clinical expert must mentally assign the mix of colors to the amount of enhancement and curve shape. Inspired by existing glyph maps, like the 3TP method, a new glyph map was developed and the two most important attributes for kinetic evaluation are mapped: the washin (the amount of contrast agent at a certain point in time) and the curve course (increasing curve, plateau curve, or washout curve). The glyphs are covering aspects $\boxed{1}$ and $\boxed{4}$. To convey as much information as possible, each voxel is depicted with a glyph. The amount of RE at a certain point in time is color-coded by employing a hue, lightness, and saturation (HLS) color space. To account for the range of the RE values, two thresholds are defined: T_{down} for the minimum RE and T_{up} for the maximum RE value. The color coding is restricted to suspicious enhancement. Thus, $T_{down} = 60\%$ and $T_{up} = 250\%$ are defined as default values according to [Kuhl et al., 1999]. Color coding is carried out by assigning red to RE values greater or equal to T_{up} and blue to values equal to T_{down}. In between, the H value, i.e., the color hue, is extracted via linear interpolation based on T_{up} and T_{down}, see Figure 5.3(b). For context information, voxels exhibiting values $< T_{down}$, are mapped to gray. Their brightness is proportional to the voxels' RE values. However, T_{down} and T_{up} can be adapted for visual analysis. For example, if the sensitivity shall be increased, T_{down} must be decreased.

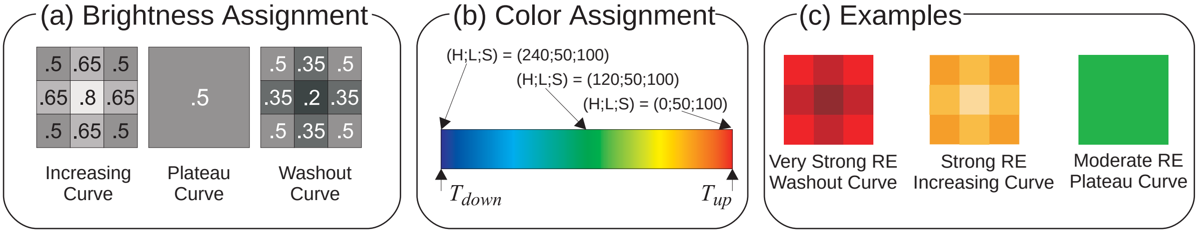

Figure 5.3: *Voxel-wise mapping of RE and RE curve shape to glyphs (image adapted from [Glaßer et al., 2009]). The curve shape determines the L component (a), whereas the RE value determines the hue of the glyphs (b). In (c), glyphs with different RE curve shapes and RE values are presented.*

The curve shape of each voxel is classified based on the 3TP method [Degani et al., 1997, Furman-Haran et al., 2001]. Therefore, an RE change in the interval ±10% during washout will be interpreted as plateau, whereas RE changes higher than 10% and lower than -10% are considered as increasing and decreasing curve, respectively. Mapping of the RE curve shape is realized by applying a 3×3 kernel for brightness modification. The S component (from the HLS color space) of each glyph's color is assigned to 1, since only fully saturated colors for highlighting of the lesion's enhancement are used, see Fiure. 5.4. In contrast to [Englmeier et al., 2004, Hauth et al., 2006b], the RE and the RE curve shape can be directly interpreted from the corners and the center of each glyph. Although the visualization is a little less intuitive more information is provided, which may be important for special cases like a lesion with moderate enhancement but present washout curves. Furthermore, this technique was designed for clinical practice. Hence, the repeated practical use of this technique accounts for the low intuitiveness.

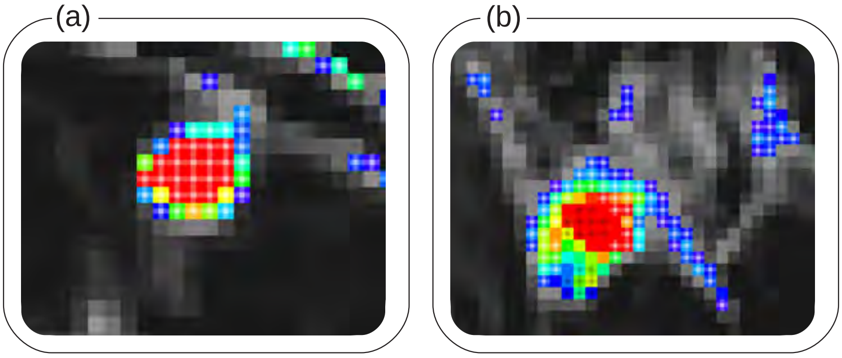

Figure 5.4: *Glyph-based visualization of two lesions. In (a), a benign lesion with high RE values (red colors) and mostly increasing curves (see brighter centers of glyphs) is depicted. In (b), malignancy is indicated by red glyphs (strong washin) with darker centers (washout curve shape), see the center of the lesion.*

When compared to the 3TP method [Degani et al., 1997], the glyph technique allows for a more detailed differentiation between different enhancement kinetics, as demonstrated in Figure 5.5.

At the moment, the presented color scale reflects the rainbow color scale. This is motivated by existing workstations in the clinical practice, which also employ this color scale. However, the rainbow color scale is not recommended in visualization due to the lack of perceptual ordering or its uncontrolled luminance variation [Borland and Taylor, 2007]. Nevertheless, the rainbow color scale is composed from fully saturated colors is well known and established in clinical practice and allows for visual clustering (e.g., a ROI that consists of red voxels can be easily visually separated from other voxels). Since the glyph-based view is intended to provide a quick overview in clinical practice instead thorough analysis in clinical research, the rainbow color scale is chosen.

5.4 Visual Exploration Based on Region Merging

As concluded in Section 5.3, a single voxel-based analysis may provide a fast overview, but single voxels could be outliers and suffering from noise, motion, or blurring artifacts. Therefore, in clinical practice, the radiologist places a ROI in the tumor tissue and qualitatively evaluates the shape of the averaged RE curve. If the ROI extraction should be carried out with a computer-aided framework, it is necessary to group similarly perfused voxels into regions. Due to a tumor's heterogeneity, it is not feasible to subdivide the tumor in equally sized parts.

For a subdivision of a tumor, i.e., the grouping of voxels into regions, various approaches exist, see the different clustering algorithms in Chapter 3 as well as related work about clustering of medical data in Chapter 4. A rather straightforward approach is region merging where neighbored regions are merged together, as long as they fulfill some well-defined similarity criterion.

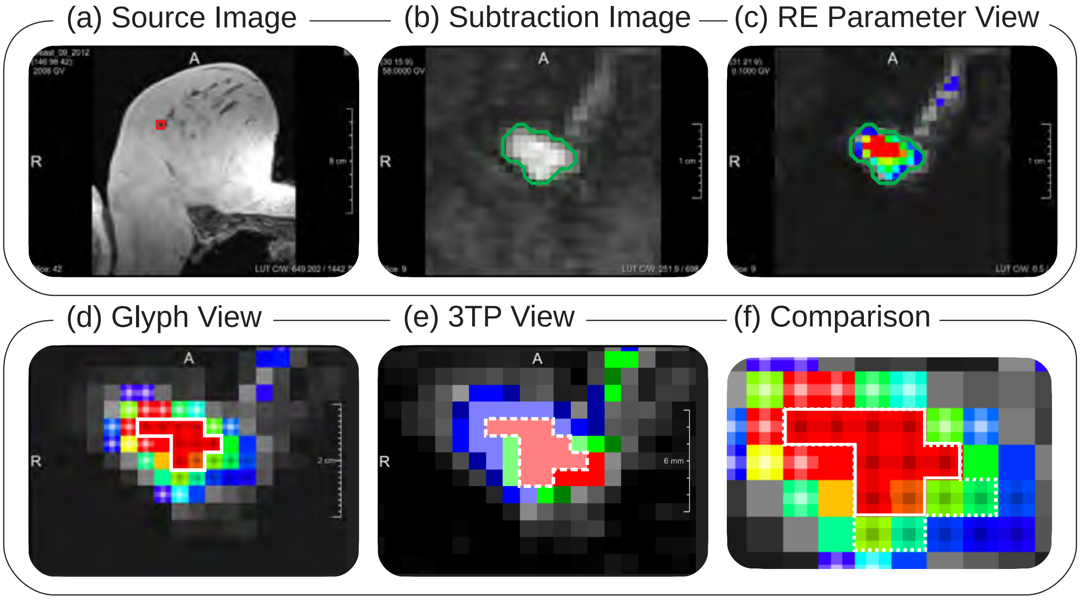

Figure 5.5: *Comparison of the glyph-based view implemented in the PerfusionAnalyzer and the 3TP view. In (a), a small lesion is marked in the source image. In (b) and (c), the subtraction and color-coded RE view is provided, respectively. In (d), the glyph view is presented. Voxels with high enhancement (reddish colors) and washout curves (darker glyph centers) are selected to form a ROI. In (e), the 3TP view is shown. Again, voxels with high enhancement (bright colors) and washout curves (reddish colors) are selected. In (f), the selection are compared. The ROI that is based on the glyph view, is more homogeneous w.r.t. the enhancement kinetics than the ROI from the 3TP view (see green and turquoise color-coded voxels) . Heterogeneous ROIs exhibit distorted averaged RE curves. (Medical image data is courtesy of U. Preim, Municipal Hospital Magdeburg, Germany.)*

The region merging approach has two advantages: it is easy to understand for the clinical expert and it produces spatially connected regions of voxels. A region merging approach must be adapted to breast DCE-MRI such that regions with similar perfusion characteristics form ROIs. Hereby, noise is suppressed through averaging the voxel intensities in the regions and artifacts, i.e., motion or blurring, are not reinforced. Tumorous regions, exhibiting different perfusion characteristics, are kept apart in order to avoid that malignant tumor tissue is neglected because of surrounding benign tissue. The region merging approach is covering aspects $\boxed{3}$ and $\boxed{4}$.

5.4.1 Adaption of Region Merging to Breast DCE-MRI

For a successful adaption of the region merging approach to breast DCE-MRI, voxels with similar perfusion characteristics have to be grouped into regions. Therefore, the following steps have to be carried out:

- Quantification of kinetic enhancement.
- Definition of a distance function based on the quantified kinetic enhancement to steer the merging process.
- Definition of a stopping criterion for the merging procedure.

After choosing a quantification of kinetic enhancement and in turn a distance function (including a similarity criterion) region merging is employed to arrange the voxels into regions. Initially, each voxel is a separate region. Iteratively, the most similar, adjacent regions are merged until the requirements of the stopping criterion are met.

Quantification of Kinetic Enhancement

For the quantification of kinetic enhancement, different approaches exist, recall Section 4.2. For a classification based on kinetic features, the three most widespread approaches cover: quantification based on the 3TP classes via the 3TP method (recall the studies by Hauth et al. [2006a] and Lehman et al. [2006]), quantification based on pharmacokinetic parameters (e.g., the studies by Englmeier et al. [2004] and Hauth et al. [2008]), and the quantification based on descriptive perfusion parameters (e.g., the studies by Sinha et al. [1997] and Williams et al. [2007]). In cooperation with clinical experts, discussions yield a first trend for the last option due to the straightforward extraction of the descriptive perfusion parameters in comparison to pharmacokinetic parameters. Another reason is the temporal resolution of the underlying data. Hence, the employed data sets exhibit five to six time steps, which hardens a model fitting that would be required for pharamcokinetic parameter extraction. A disadvantage of the 3TP method is the restriction to nine classes. Descriptive perfusion parameters like integral or washout allow for a more differentiated characteristic of kinetic enhancement.

Definition of a Distance Function

For characterization of lesion enhancement kinetics, the descriptive perfusion parameters washin, washout, PE, and TTP are employed. Since no ground truth for a grouping of voxels is available, different constellations are tested. The parameters are employed for feature vectors $\vec{v}$. A distance function that assigns a similarity between region R_1 and region R_2 is approximated with the Pearson correlation coefficient (recall Eq. (3.3) in Sect. 3.4.1) of the two feature vectors $\vec{v_1}$ and $\vec{v_2}$ of R_1 and R_2. For the evaluation of descriptive perfusion parameters, z-scoring was applied (recall Eq. (3.8) in Sect. 3.4.2).

The following feature vectors $\overrightarrow{v_{3f}}$ and $\overrightarrow{v_{4f}}$ were integrated in the PerfusionAnalyzer:

$$\overrightarrow{v_{3f}}(R) = \begin{pmatrix} washin(R) \\ washout(R) \\ PE(R) \end{pmatrix}, \tag{5.1}$$

where R denotes the region, washin denotes the average washin value, washout denotes the average washout value, and PE denotes the average peak enhancement value of all voxels contained in R.

$$\overrightarrow{v_{4f}}(R) = \begin{pmatrix} washin(R) \\ washout(R) \\ PE(R) \\ TTP(R) \end{pmatrix}, \tag{5.2}$$

where TTP denotes the average TTP value of all voxels of the region R. Thus, the TTP component implies a stronger focus on the curve shape, since washout curves have a significantly smaller TTP than continuously enhancing curves. For a better estimation of the feature vectors, a comparison with the 3TP method is also provided in the following.

Definition of a Stopping Criterion

Based on the region merging concept, the most similar, adjacent regions are merged until the maximal similarity of all regions falls below a pre-defined threshold or the number of regions is reduced to a pre-defined number. To account for varying tumor sizes and varying heterogeneity, a pre-defined number of regions is not applicable. Since the distance function is based on the Pearson's correlation, a minimum value P_{min} for this correlation is defined. Thus, the merging terminates if all remaining adjacent regions exhibit a similarity lower than P_{min}. Naturally, the region merging result strongly depends on the right choice of P_{min}. For example, a P_{min} value that is too small yields only one region - the complete tumor. If the value is too high, each voxel would form a single region. To support the user, a stopping criterion has to be automatically provided by the PerfusionAnalyzer.

For an optimal value of P_{min}, the region merging results for the two feature vectors $\overrightarrow{v_{3f}}$ and $\overrightarrow{v_{4f}}$ are compared. In addition, a comparison with the 3TP method is provided. With $\overrightarrow{v_{3f}}$, $\overrightarrow{v_{4f}}$, and the 3TP method three sets of regions S_{3f}, S_{4f} and S_{3tp} are obtained:

- S_{3f} denotes the set of regions, extracted with the 3D feature vector $\overrightarrow{v_{3f}}$,
- S_{4f} denotes the set of regions, extracted with the 4D feature vector $\overrightarrow{v_{4f}}$, and
- S_{3tp} denotes the set of regions, extracted with the 3TP method.

The number of regions contained in S_{3f} and S_{4f} strongly depends on the assigned value to P_{min}. The lower P_{min}, the more regions will be merged and less regions will remain. For extraction of an optimal P_{min}, the region merging was applied to a set of 20 breast DCE-MRI lesions, containing 10 small and 10 big lesions. Hence, small refers to lesions only detectable in the MRI perfusion scan (due to their contrast enhancement) and big to lesions that were already classified as primary tumor in the conventional X-ray mammography. The sets S_{3f} and S_{4f} were created for the P_{min}-values $0.9 - 0.99$ (with a step size 0.01) and 0.999, see Figure 5.6. Qualitative analysis of the results with an experienced radiologist indicates that P_{min} should be at least 0.95. For P_{min} values of $0.97 - 0.99$, there are small changes in the average region number and region size (see marked area in Fig. 5.6). For this reason, a value of 0.99 as minimum value for the Pearson correlation is suggested in the PerfusionAnalyzer.

Comparison with Respect to Number of Regions

To assess the quality of $\overrightarrow{v_{3f}}$, $\overrightarrow{v_{4f}}$, and the 3TP method, an overview of the comparison of the total number of regions $\#R_N$ of S_{3f}, S_{4f}, and S_{3tp} is presented in Figure 5.7. For both tumor sizes, the average number of regions in S_{3tp} is the smallest, which may result from the finer division of the tumor based on the region merging method. Moreover, in average, S_{3f} contains more regions than S_{4f} albeit the difference is smaller than the difference between S_{4f} and S_{3tp}. As depicted in Figure 5.7, S_{3f} contains the most regions that consist of one voxel only.

In general, a few larger regions are easier to analyze than a highly fragmented segmentation result with many small regions. Thus, S_{4f} and S_{3tp} seem to be more appropriate, whereas S_{4f} provides a finer subdivision for the early contrast agent accumulation and employs local

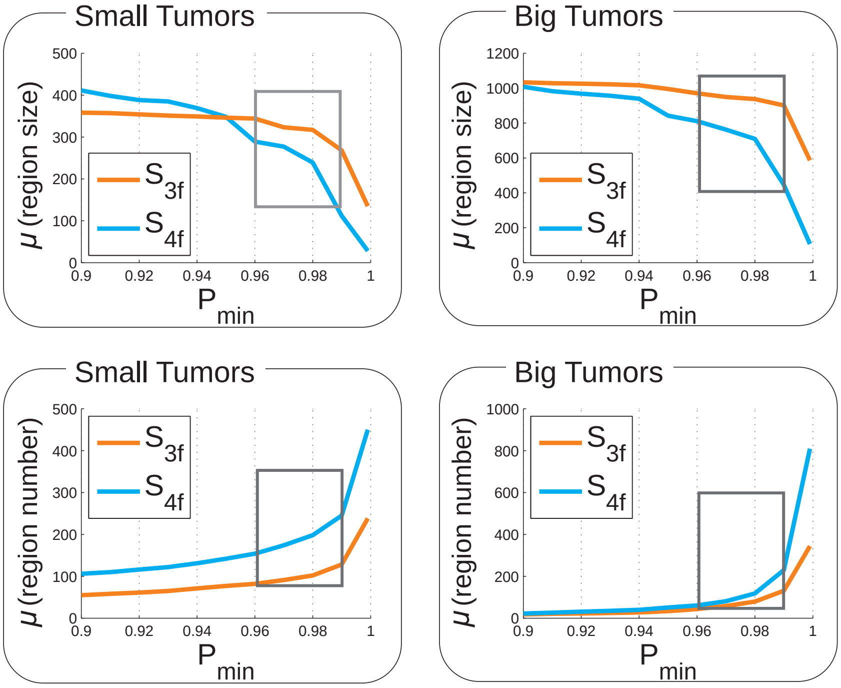

Figure 5.6: *Influence of P_{min} (image adapted and reprinted from [Glaßer et al., 2010] © 2010, Elsevier, with kind permission from Elsevier). For P_{min} values of 0.9, only a few, large regions exist, which is not satisfying for heterogeneous tumors. With increasing P_{min}, a finer division is achieved that means more regions with a smaller average region size are extracted. The best results are achieved for values $0.95-0.99$. Smaller values do not provide enough regions. The step from 0.99 to 0.999 causes a significant increase of regions and decrease of region size.*

information. If only regions are considered that contain more than one voxel, similar results for these two methods are obtained. The small regions (containing only one voxels) are at the tumor's boundary. Hence, the clustering suffered from motion artifacts and blurring. Thus, their RE curve is distorted and there are no similar voxels in the neighborhood. As it was stated in Chapter 4, a ROI for further diagnosis should at least contain three voxels.

Comparison with Respect to Washout Curve Shape

In clinical practice, a ROI with an average washout curve is rated as very indicative for malignancy. Therefore, the number of regions $\#R_W$ with a washout curve shape in S_{3f}, S_{4f}, and S_{3tp} is compared. As shown in Figure 5.8, for larger tumors, S_{4f} exhibits less regions with a washout curve than S_{3tp} in 6 of 8 cases, whereas two tumors do not exhibit any regions with a washout curve. For smaller tumors, S_{4f} has more regions with washout curve in 7 of 10 cases. In average, S_{4f} exhibits more regions with washout curve and containing only 1 voxel than S_{3tp}. A very important fact is the influence of the feature vector $\overrightarrow{v_{4f}}$, see Figure 5.8. S_{3f} provides less regions with washout curves than S_{4f}. More critical, in 13 of 20 cases, no washout regions are existing in S_{3f} which may caused by merging of regions with different curve shapes in the intermediate and late post-contrast phase.

The comparison of the part of the tumor that is covered by the regions with washout curve yields similar results. The percentaged size for this part of each tumor is similar for S_{3tp} and

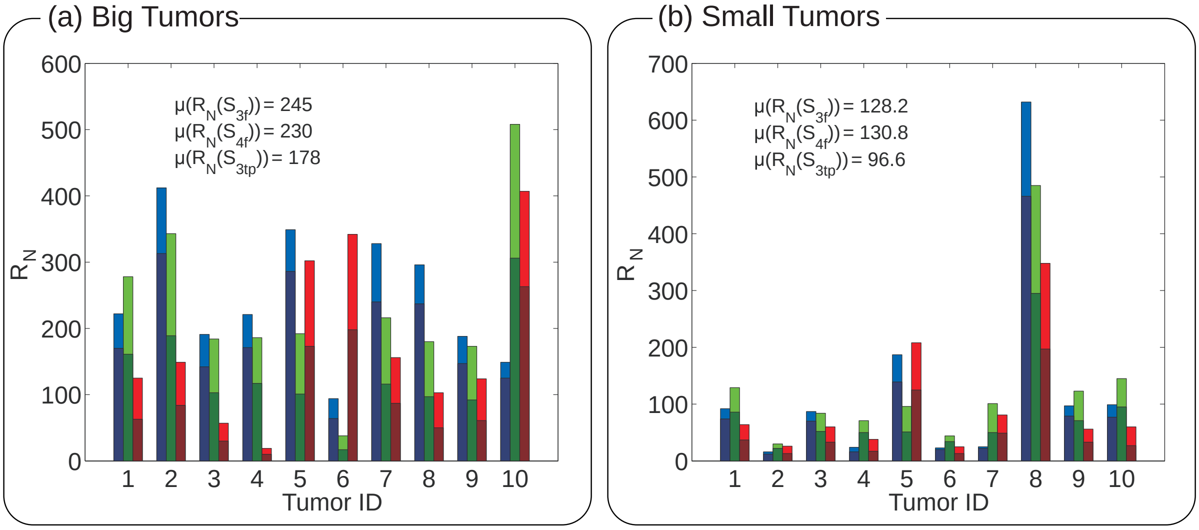

Figure 5.7: *Comparison of the region number R_N for each set S_{3f}, S_{4f}, and S_{3tp} for larger tumors (a) and smaller tumors (b) (image adapted and reprinted from [Glaßer et al., 2010] © 2010, Elsevier, with kind permission from Elsevier). Blue is assigned to $R_N(S_{3f})$, green is assigned to $R_N(S_{4f})$ and red is assigned to $R_N(S_{3tp})$. The overall region number is presented with bright colors. Dark colored bars indicate the number of regions with size equal to 1 voxel for each set. In addition, the average number of regions $\mu(\#R_N)$ is presented.*

S_{4f} with an average difference of 1.89%. The percentaged size of the part covered by washout regions of S_{3f} is in average 12.65% smaller than the part of S_{4f}.

In conclusion, the set S_{4f} extracted with the region merging applying the feature vector $\overrightarrow{v_{4f}}$ in combination with a minimum Pearson correlation value $P_{min} = 0.99$ yields better results than S_{3f}. It achieves equally suited results to S_{3tp} but a finer subdivision of the early contrast agent accumulation. These parameter choices are employed as default values in the PerfusionAnalyzer. During evaluation of the region merging results, all regions have been taken into account, since the clustering result itself has been rated. However, if such a region is employed as ROI for further clinical diagnosis, only regions with a minimum voxel size or a minimum percentage size w.r.t. the whole tumor is employed. For this purpose, in Chapter 7, different approaches for the identification of the most suspect region from a clustering result will be presented.

5.4.2 Visual Exploration of Region Merging Result

For a visual exploration of the region merging result, the PerfusionAnalyzer provides a primitive 2D slice view, see Figure 5.9. Hence, further analysis is only applied to regions with a certain minimum size, e.g. at least 3 voxels or 1% of the lesion's size. This minimum size can be adapted by the user, depending on the level of detail the user is interested in.

For a more detailed analysis of the resulting regions, two diagram-based presentations are provided. First, a quantitative analysis is supported with the RE curve diagram. Second, the perfusion parameter-based qualitative evaluation with the change diagrams provides information of the lesion's heterogeneity as well as the perfusion characteristics of each region.

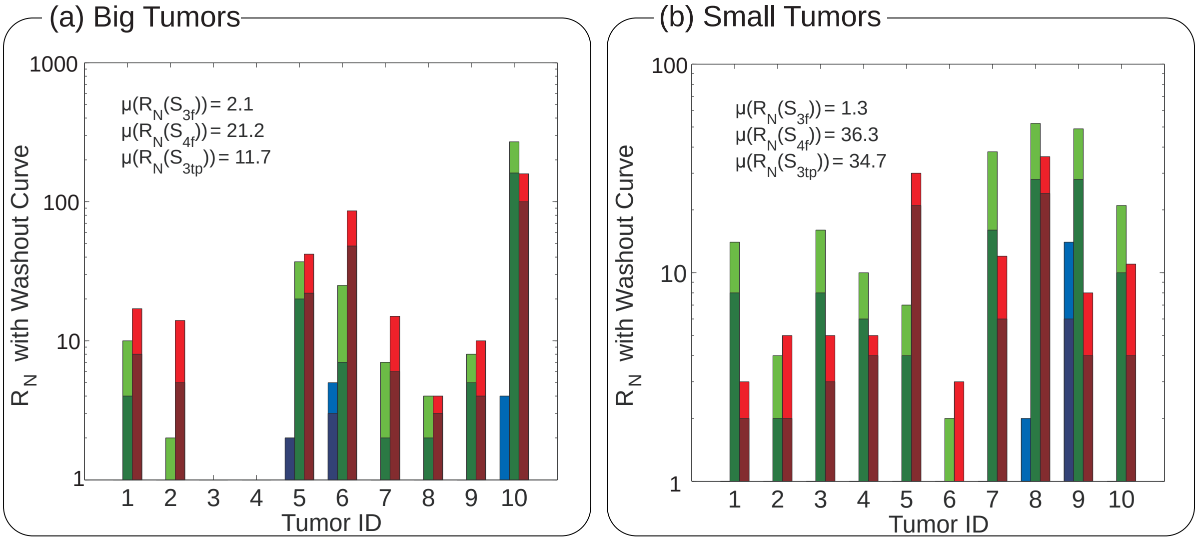

Figure 5.8: *Comparison of the number of regions with an average washout curve for each set* S_{3f}*,* S_{4f}*, and* S_{3tp} *for larger tumors (a) and smaller tumors (b) (image adapted and reprinted from [Glaßer et al., 2010] © 2010, Elsevier, with kind permission from Elsevier). Blue is assigned to* S_{3f}*, green is assigned to* S_{4f}*, and red is assigned to* S_{3tp}*. With bright colors the overall region number with an average washout curve is presented. Dark colored bars indicate the number of washout curve exhibiting regions with size equal to 1 voxel for each set. In addition, the average number of regions* $\mu(R_N)$ *is presented.*

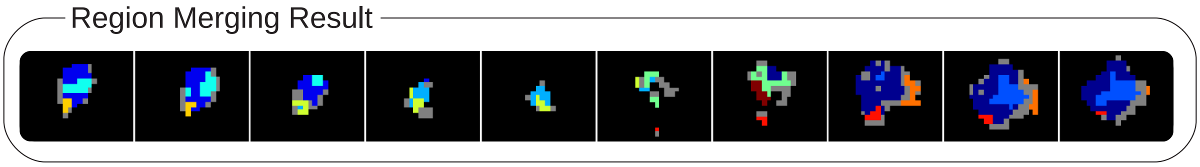

Figure 5.9: *Example of 10 axial slices of a small tumor with color coding of the 11 largest regions, extracted with the region merging method (image adapted from [Glaßer et al., 2009]). Gray is assigned to the remaining regions for the visual separation of surrounding tissue that does not belong to the tumor.*

Region-Based Quantitative Analysis in the RE Curve Diagram

For quantitative analysis of the region merging result, i.e., the enhancement kinetics of each region, the average RE curves are provided in the *RE curve diagram*. The region merging yields n regions R_i, $i = 1 \dots n$, and the whole lesion L as the combination of these regions, see Figure 5.9 for an example of a slice-based view. In Figure 5.10, the average RE curve of L and its regions R_i is depicted. The RE curves are classified into steady, plateau, and washout curves with the adaption of Eq. 2.3 in Section 2.1.2. For information about the region size, the percentaged size of each region in relation to the whole tumor as well as the size of the tumor itself are depicted.

Since washout curves are associated with increased tumor malignancy, RE curves with a washout shape are highlighted with an increased line width. On the contrary, the line width could also be adapted to a region's reliability, as depicted in Figure 5.10(b). The reliability or homogeneity of a region is approximated via a ranking based on the region's perfusion parameters' standard deviation in relation to the whole lesion. Regions with smaller standard deviation values get smaller ranks, i.e., they are more homogeneous. The slice-based view and the RE curve diagram view are linked and assignment of colors is consistent in both views.

The RE curve diagram is linked with an interactive slice view, where each region is color coded according to the average RE curve. To avoid visual clutter, the user can define the number of presented regions, e.g. the user can choose the n largest regions, all regions that contain at least n voxels or all regions with a minimum percentaged size of $n\%$ in relation to the whole tumor.

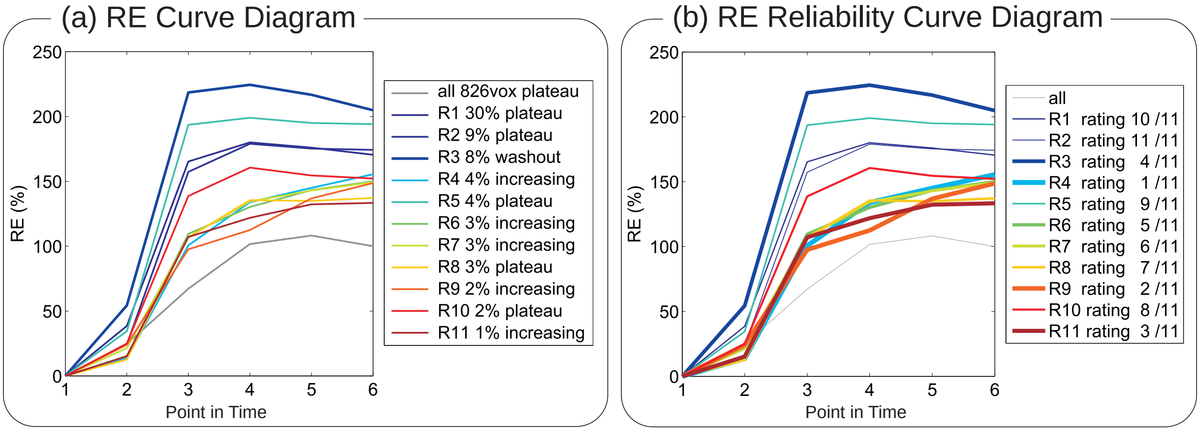

Figure 5.10: *For each larger region, an average RE curve is created. The average RE curve of the overall lesion (including voxels that belong to smaller regions) is depicted in gray and indicates a washout curve shape (image adapted from [Glaßer et al., 2009]). The most suspicious region R_3 is classified as washout curve and an increased line width is assigned to it (a). The line width can also be adapted to each region's reliability (b).*

Parameter-Based Qualitative Analysis in the Change Diagram

In addition to the quantitative evaluation of the RE curve diagram, a qualitative region-wise analysis of the enhancement kinetics is provided in the change diagram. For a fast overview and visual distinction, the measure C_{i_j} is established. C_{i_j} characterizes the change of the average descriptive perfusion parameter value μ_i of the descriptive perfusion parameters P_j, ($j \in \{$ *PE, TTP, Integral, UpSlope, DownSlope* $\}$) of each region R_i. The change of $\mu_L\left(P_j\right)$ is set in relation to the average values for the whole lesion $\mu_L\left(P_j\right)$.

Since the parameters *PE* and *Integral* describe the washin and thus a certain amount of contrast agent accumulation, they are considered as quantitative descriptors. Hence, the relative amount of change (see Eq. (5.3)) is employed, since the comparison should indicate trends instead of providing absolute differences of these descriptors. *UpSlope* and *DownSlope* are derived from the same RE curve and can be simply compared by difference (see Eq. (5.4)). *TTP* describes the point in time where *PE* is achieved. Since breast DCE-MRI data sets typically contain $5-6$ time steps, the difference of L and region R_j is normalized with the number of time steps t_n (see Eq. (5.5)).

Calculation of C_{i_j}, $i = 1 \ldots n$, for $j \in \{PE, Integral\}$:

$$C_{i_j} = \frac{\mu_i(P_j) - \mu_L(P_j)}{\mu_L(P_j)} \cdot 100, \tag{5.3}$$

for $j \in \{UpSlope, DownSlope\}$:

$$C_{i_j} = \mu_i(P_j) - \mu_L(P_j), \tag{5.4}$$

and for $j = TTP$:

$$C_{i_j} = \frac{\mu_i(P_j) - \mu_L(P_i)}{t_n} \cdot 100. \tag{5.5}$$

An example for the change diagram is provided in Figure 5.11. Hence, color coding is synchronized with the RE curve diagram and the slice view (see Fig. 5.9 and Fig. 5.10). In conclusion of Eq. (5.3)-(5.5), the values of $\mu_L(P_j)$ are set at zero along the abscissa. Different perfusion characteristics of a region in comparison to L are indicated by higher bars (considering the absolute height), whereas similar characteristics are indicated by smaller bars (considering the absolute height). In Figure 5.11, the regions R_1, R_2, R_3, and R_5 indicate suspicious enhancement kinetics, since they exhibit a stronger washin (in terms of parameters *PE*, *Integral*, *UpSlope*) and an earlier and stronger washout (high negative magnitudes for *DownSlope*, *TTP*) in comparison to the whole lesion.

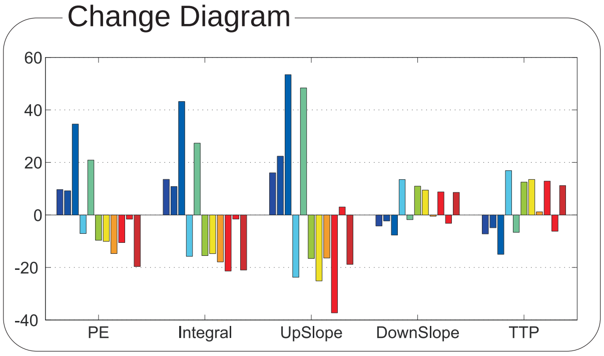

Figure 5.11: *The change diagram for the lesion depicted in Fig. 5.9 and Fig. 5.10 (image adapted from [Glaßer et al., 2009]). The regions R_1, R_2, R_3, and R_5 are very suspicious due to the stronger washin (higher bars for PE, Integral, UpSlope) and a stronger washout (high magnitude for DownSlope, TTP) in comparison to the whole lesion.*

5.4.3 A Case Study for the Visual Exploration based on Glyphs and Regions

In this section, the visual exploration is demonstrated with a small case study. When analyzing a breast tumor with focus on kinetic enhancement, the clinical expert evaluates the presence of regions with strong washin and washout behavior. First, the glyph-based visualization serves as an overview of the lesion. Tumor parts with washout curves, which are indicative for malignancy, should be analyzed in more detail. Thus, the region merging approach is carried out and the lesion is divided into a number of similarly perfused regions. Next, the clinical expert starts the exploration with the quantitative analysis with the RE curve diagram to determine a suspicious tumor part. Next, the search for similarly perfused regions is carried out with the change diagram, which allows for a qualitative region-wise analysis of the enhancement

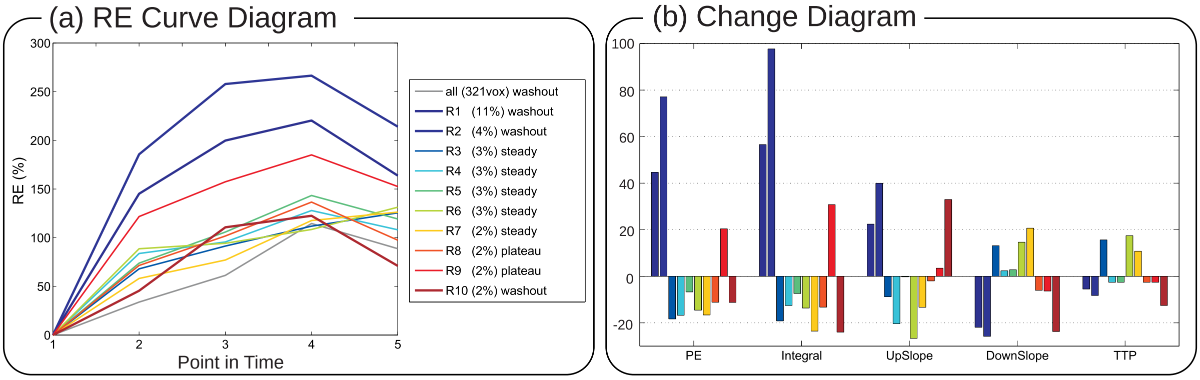

Figure 5.12: *Analysis of regions with similarly perfused voxels (image adapted and reprinted from [Glaßer et al., 2010] © 2010, Elsevier, with kind permission from Elsevier). In (a), the RE curve diagram of the 10 largest regions is presented. For each region, the percentaged size and the curve type is depicted. The curve of the whole tumor is visualized in gray. The most suspicious regions* R_1, R_2, *and* R_{10} *exhibit curves that are classified as washout curve. In (b), the change diagram is presented, which allows for further characterization (color coding is synchronized with the RE curve diagram). The regions* R_1 *and* R_2 *have a strong and rapid washin (higher bars for PE, Integral, UpSlope) and a strong washout (high magnitude for DownSlope, TTP) in comparison to the whole tumor.* R_{10} *has only a moderate washin, since there are smaller values for PE and Integral. Moreover, in the change diagram, the region* R_9 *can also be classified as suspicious, since this region exhibit the same trends like* R_1 *and* R_2 *(compare dark blue, medium blue, and red colored bars).*

kinetics. Further diagnosis and treatment like core needle biopsy can then be adapted to the identified spatially connected regions with suspicious enhancement kinetics.

The case study contains seven different malignant and benign lesions L_1-L_7 and their histopathologic reports, listed in Table 5.1. For each lesion, the results have been approved by a clinical expert. In Figure 5.13, the different views, i.e., the glyph view, the region merging result, the RE curve diagram and the change diagram are provided.

Lesion L_1**.** The region merging result for L_1 contains 826 voxels and 11 main regions. The glyph-based overview (see Fig. 5.13) indicates malignancy with strong RE and washout curves. In the RE curve diagram, the region R_3 is classified as washout. Five regions with an average plateau curve exist and a strong heterogeneity can be observed. By analyzing the

Table 5.1: *Listing of all lesions and their histopathologic reports.*

Lesion ID	Histopathologic Report
L_1	Malignant multicentric, invasive lobular carcinoma.
L_2	Benign lesion.
L_3	Malignant moderate differentiated invasive lobular carcinoma, contains small lobular carcinoma in situ.
L_4	Malignant moderate differentiated invasive ductal carcinoma.
L_5	Malignant inflammatory cancer.
L_6	Malignant mucinous carcinoma, contains benign fibroadenoma.
L_7	Benign lesion with fibroadenomas.

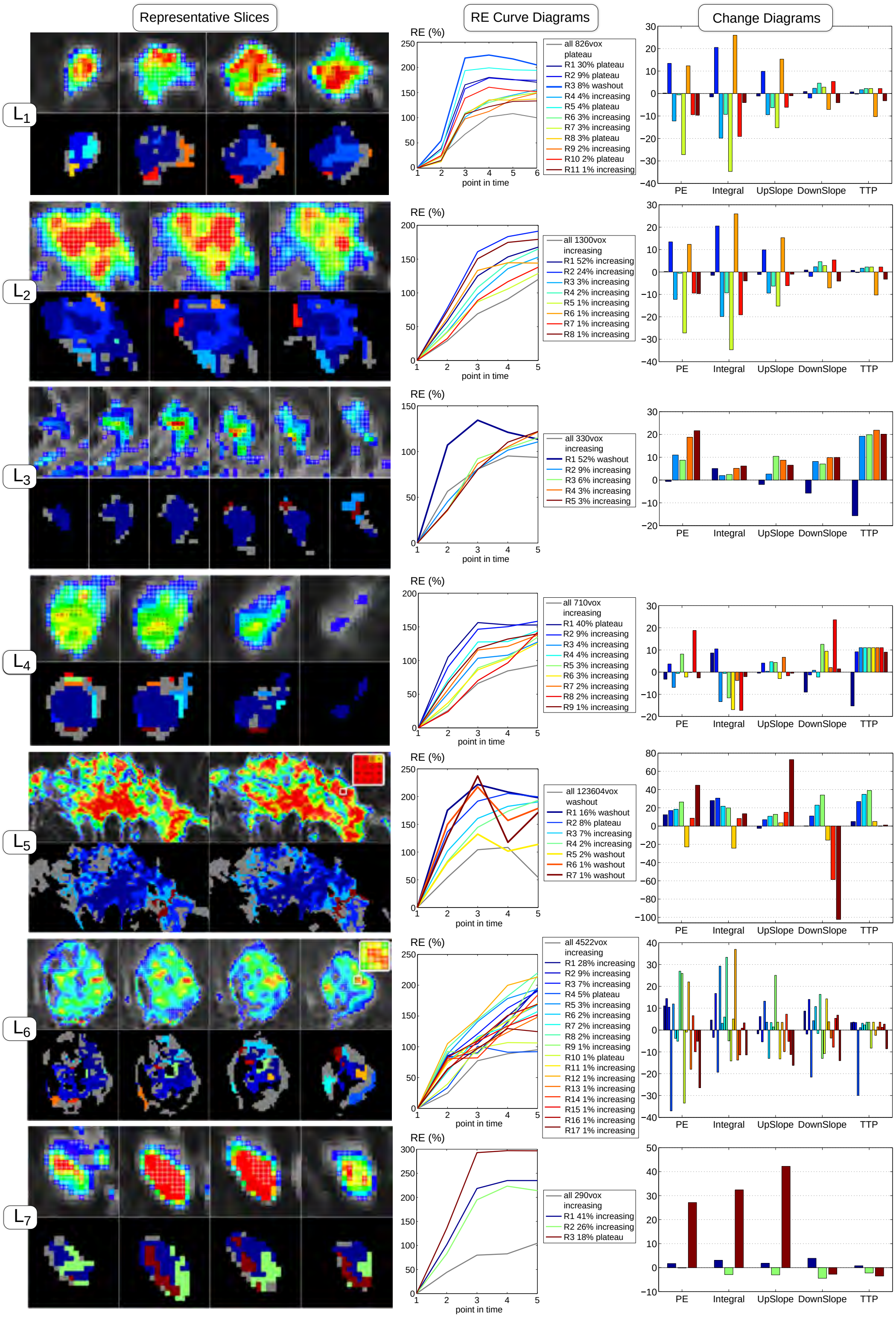

Figure 5.13: *Case Study with a glyph-based overview and the region map for representative slices (left), the RE curve diagram (center), and the change diagram (right) (image adapted from [Glaßer et al., 2009]). For the larger lesions* L_5 *and* L_6*, zooming is necessary for glyph interpretation (see inlays).*

change diagram, R_3 contains a strong washin (maximum *PE, Integral, UpSlope*) and washout (higher negative magnitude for *DownSlope* and earlier *TTP*) in comparison to the whole lesion. In combination with the washout curve, R_3 is highly suspicious and indicates malignancy. Moreover, the change diagram reveals suspicious regions with an average plateau curve R_1, R_2, and R_5, which exhibit similar attributes to R_3 in comparison to the whole lesion. The suspicion of malignancy is confirmed with the histopathologic report of L_1.

Lesion L_2. The segmentation result contains a lesion with 1311 voxels and eight regions. The glyph-based overview indicates continuous enhancement for many voxels. All regions exhibit an increasing curve. The change diagram reveals that the regions differ in terms of *PE*, *Integral*, and *UpSlope*, which is caused by different amounts of contrast agent washin. They do not differ in terms of washout due to the very small changes for *TTP* and *DownSlope*. No regions with suspicious average RE curve exist, indicating a benign lesion, which is confirmed by the report in Table 5.1.

Lesion L_3. The segmentation yields a small lesion with 330 voxels and five regions. The glyph-based overview reveals suspicious enhancement kinetics for R_1. R_1, with a size of 50% and a washout curve, indicates malignancy, whereas other regions are continuously enhancing. The change diagram indicates similar perfusion characteristics of R_2-R_5 and strengthens the suspicion of R_1, since R_1 exhibits the strongest washout. The indications are confirmed with the report in Table 5.1.

Lesion L_4. The segmentation contains a lesion with 710 voxels and nine regions. Although the glyph-based visualization reveals voxels with suspicious washin and washout kinetics, almost all regions exhibit an average increasing curve in the RE curve diagram. Furthermore, only moderate RE (up to 160%) can be observed. The largest region R_1 exhibits a plateau curve. The change diagram shows the lesion's heterogeneity with different lesion enhancement kinetics. Especially the washout characteristics confirm R_1 as suspicious region, because it strongly differs from the other regions as well as the whole lesion. Although no washout curves exist, heterogeneity and general washout perfusion parameter values indicate malignancy, which is confirmed by the report.

Lesion L_5. The glyph-based overview reveals an inflammatory lesion with irregular contours, indicating inflammatory breast cancer. The segmentation for this specific cancer yields a huge (more than 120.000 voxels), highly fragmented lesion. The largest region R_1 contains only 16% of the lesion's voxels, since many very small regions exist. The RE curve and change diagram exhibit heterogeneous regions and many washout curves. The indication of malignancy is confirmed in Table 5.1.

Lesion L_6. For L_6, the segmentation leads to a large (4522 voxels), highly fragmented lesion. The glyph-based overview indicates moderate enhancement, with some small areas containing suspicious curve courses. The RE curve diagram does not reveal a washout RE curve, but it exhibits a strong heterogeneity. Furthermore, R_2 and R_4 are classified as plateau. The change diagram illustrates the lesion's heterogeneity and suspicious perfusion parameter values of R_2 and R_4. Both regions strongly differ from the whole lesion, thus indicating malignancy. The suspect is confirmed by the histopathologic report. L_6 does contain smaller benign lesions, which may have caused regions with an average increasing RE curve shape.

Lesion L_7. The segmentation as well as the glyph-based overview yield a small, enhancing lesion (290 voxels) containing only three regions. Two are continuously enhancing and one ($R3$) is characterized by a plateau. R_3 has a strong RE (up to 300%) but does not exhibit any significant washout characteristic. This is strengthened by the change diagram, which reveals strong differences during washin (in terms of *PE, Integral, UpSlope*), but almost no differences during washout. The non-existence of characteristic washout kinetics indicates a benign lesion, which is confirmed in Table 5.1.

5.5 The File-Card-Browser View

Next to kinetic features, many studies aim at the evaluation of morphological features for lesion characterization, although a standardized terminology is missing. As it was stated by the aspect $\boxed{5}$ regarding breast tumor evaluation in Section 4.4, the evaluation of morphologic features should be supported in a qualitative way.

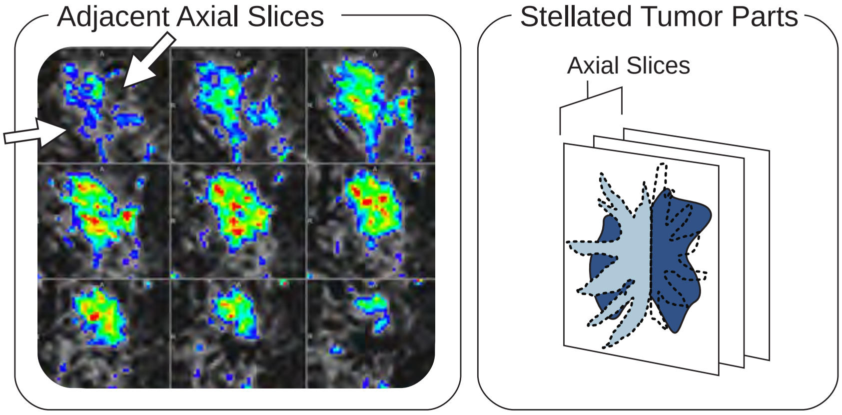

Figure 5.14: In the conventional 2D view, the lesion's morphology is hard to interpret. On the left, it is not clear if the parts (marked with an arrow) stem from a stellated boundary or just from the 2D view. On the right, the stellated parts of the tumor boundary are parallel to the current viewing direction and could be missed (image adapted and reprinted from [Glaßer et al., 2011] © 2011, Springer-Verlag, with kind permission from Springer Science and Business Media).

Therefore, the morphologic evaluation was not employed for an automatic classification process but instead a further view was integrated in the PerfusionAnalyzer: the *File-Card-Browser View* (FCB View). The FCB View was developed to account for the limitations of axial slice-based 2D view. Similar to a conventional file card browser, the FCB View provides 2D views, which can be rotated around the tumor via multiplanar reformation (MPR) views. In general, an MPR view is a 2D intersection plane with the 3D medical tomographic data sets with arbitrarily orientation. Furthermore, MPR views were also adapted to special diagnostic tasks, such as the diagnosis of vascular diseases yielding curved multi planar reconstructions [Kanitsar et al., 2002]. In clinical practice for breast tumor evaluation, stellated parts of a tumor's boundary may not be recognizable in the standard slice-based view, e.g., the axial slice view, see Figure 5.14. An additional MPR view could reduce misinterpretations.

The extraction of the MPR views depends on the tumor extent and consists of three steps, illustrated in Figure 5.15.

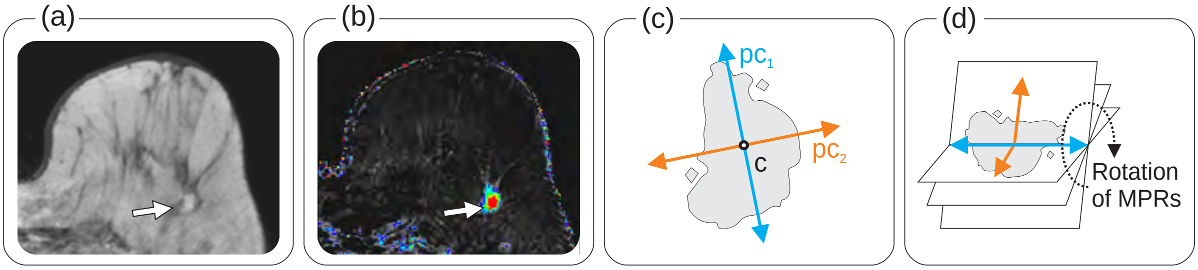

Figure 5.15: *Creation of the FCB View (image adapted and reprinted from [Glaßer et al., 2011] © 2011, Springer-Verlag, with kind permission from Springer Science and Business Media). At first, the lesion and the lesion mask is identified and extracted with one click in the axial slice-based source view (a) or the RE view (b). In (b), the voxels of the tumor with RE values > 50% are color coded. The tumor mask is provided in (c). Also, pc_1 and pc_2 are depicted. The MPR plane is generated with the vectors pc_1 and pc_2. The vector pc_1 is employed as rotation axis, see (d). (Medical image data is courtesy of U. Preim, Municipal Hospital Magdeburg, Germany.)*

The FCB View was tested with 20 DCE-MRI breast tumor data sets from the *Breast Tumor Database 2009*. This study will be explained in more detail in Section 7.1. The lesion identification and segmentation process was carried out with the PerfusionAnalyzer, as it was described in Section 5.2. In contrast to previous described methods, an isotropic voxel size was desired for the MPR generation. The isotropic voxel size is achieved by resampling with a Lanczos kernel (carried out with *MeVisLab*).

For the first step, the binary mask of the tumor is extracted from the segmented lesion. In the second step, the centroid c of the tumor mask is computed. The center c is approximated as mean position of the masked voxels. In the last step, a principal component analysis (PCA) is applied. The PCA is carried out over the set of 3D voxels that belong to the tumor mask. The first and second principal components pc_1 and pc_2 are extracted. Thus, pc_1 and pc_2 correspond to the two 3D main directions of the tumor. Next, the MPR plane is generated based on the plane spanned by pc_1 and pc_2, see Figure 5.15(c). For the generation of the FCB View, the first vector pc_1 is employed as rotation axis. Subsequently, the next MPR planes are generated by rotating pc_2 around pc_1 with origin at the tumor center c. The MPR plane is again spanned by pc_1 and the rotated pc_2 vectors. Thus, the MPR planes are adjusted to the tumor's main directions. The user can rotate around 180° for a complete overview of the tumor's boundary, see Figure 5.15(d). In case of sphere-shaped tumors, the tumor's main extents are quite similar. However, the FCB View employs the perpendicular principal components and the FCB View-based exploration reveals the round boundary as well.

For an informal and qualitative evaluation, the FCB View was created and visually compared to the conventional slice view. In Figure 5.16, the results are provided by the four examples C_1 - C_4. For each case, nine adjacent slices in the conventional slice-based view are presented. In contrast, nine adjacent slices are presented of the same tumor with the FCB View. Color coding is applied to map the RE values to color (the same color scale as introduced in Sect. 5.3).

The first case C_1 presents a small, round benign tumor. As it is depicted, the FCB View also reveals a round boundary. In the second case C_2, a more stellated tumor can be observed in the conventional slice-based view. With the FCB View, two almost non-connected parts of the tumor become visible. Thus, the FCB View yields more details for understanding the tumor's morphology and is therefore more appropriate than the conventional slice view. The example, C_3 serves as representation for different tumor parts with different enhancing characteristics. Although both views present a tumor with an irregular boundary, the FCB View reveals two similarly perfused regions (visualized with similar reddish color coded contrast enhancement kinetics and marked with arrows), whereas the conventional view could not show these spatially connected and similarly perfused parts. Similarly perfused regions of a tumor are necessary for evaluating the tumor's heterogeneity as well as further diagnosis like core needle biopsy. The example C_4 illustrates the improved boundary evaluation. The conventional view reveals parts of the tumor that seem to be suspicious (see arrows). These parts are caused due to 2D axial slice-based view, because the FCB View reveals an almost round boundary.

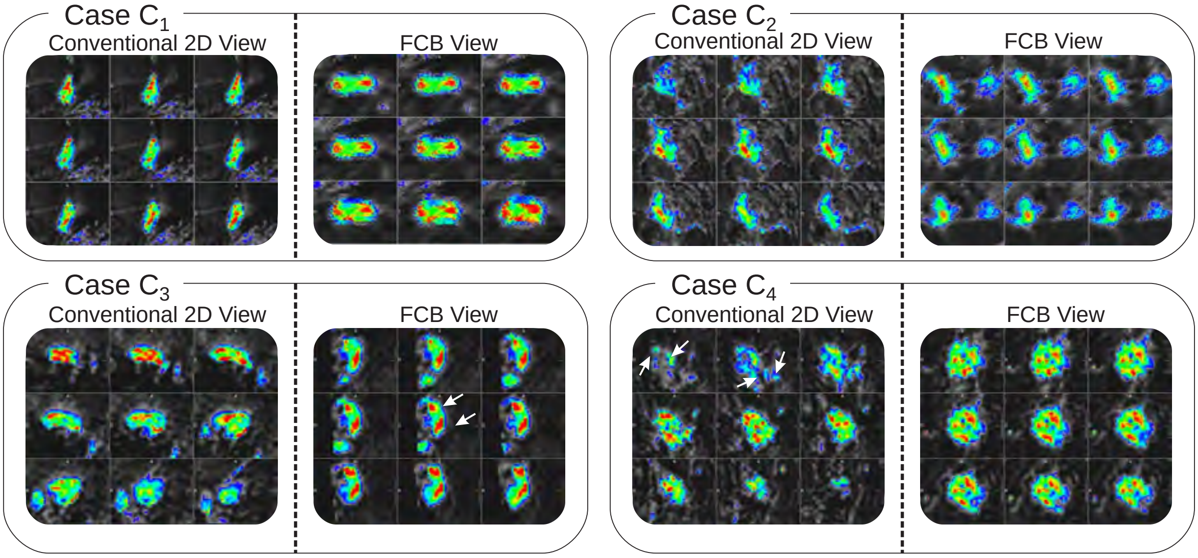

Figure 5.16: *Four example cases C_1, C_2, C_3, and C_4 of the database (image adapted and reprinted from [Glaßer et al., 2011] © 2011, Springer-Verlag, with kind permission from Springer Science and Business Media). On the left, nine adjacent slices in the conventional slice-based view are presented. On the right, nine adjacent slices of the same tumor with the FCB View are shown. Due to the generation process, the slices of the different techniques are not identical, i.e., they cover not the exact same portion of the data. For mapping of RE, color coding is applied.*

In 2 of 20 cases, the center c was not optimally located due to a very strong stellated and irregular morphology. In these cases, the FCB View could not provide the desired improved overview. However, such irregularly shaped tumors can be already evaluated in the conventional slice-based view and do not need further evaluation with an additional MPR view.

As a result, the FCB View is adapted to each tumor, regarding the tumor's spatial extent. Furthermore, it provides additional information about the tumor's morphology and boundary. Additionally, different parts, e.g., two spatially non-connected foci, can be identified. This holds also for different tumor parts that exhibit similar contrast agent accumulations. The FCB View method aims at additional improvement and completion of the conventional axial slice-based view instead of substitution of this clinical evaluation method.

5.6 Combination of T_1- and T_2-Weighted Breast MRI Data

The PerfusionAnalyzer features the analysis of breast perfusion DCE-MRI data. Hence, it strongly focuses on the T_1-weighted sequence. For differential diagnosis in the early lesion detection process, the radiologist also takes the T_2 sequence into account, as it was briefly described in Section 2.1.2. Lesions are recovered by time-consuming manual spatial correlation of both images, i.e., the radiologist has to mentally register the images and locate the lesion from the first image sequence in the second sequence. A simultaneous evaluation could reduce this time and effort, but a co-registration of the T_1 and T_2 sequence would be necessary. Disagreement of T_1- and T_2-weighted sequences of a single patient results primarily from patient motion. Unlike motion correction of a single DCE-MRI T_1-weighted scan, the sequence co-registration must not only account for patient movement, but also for the different image resolutions as well as intensity distributions.

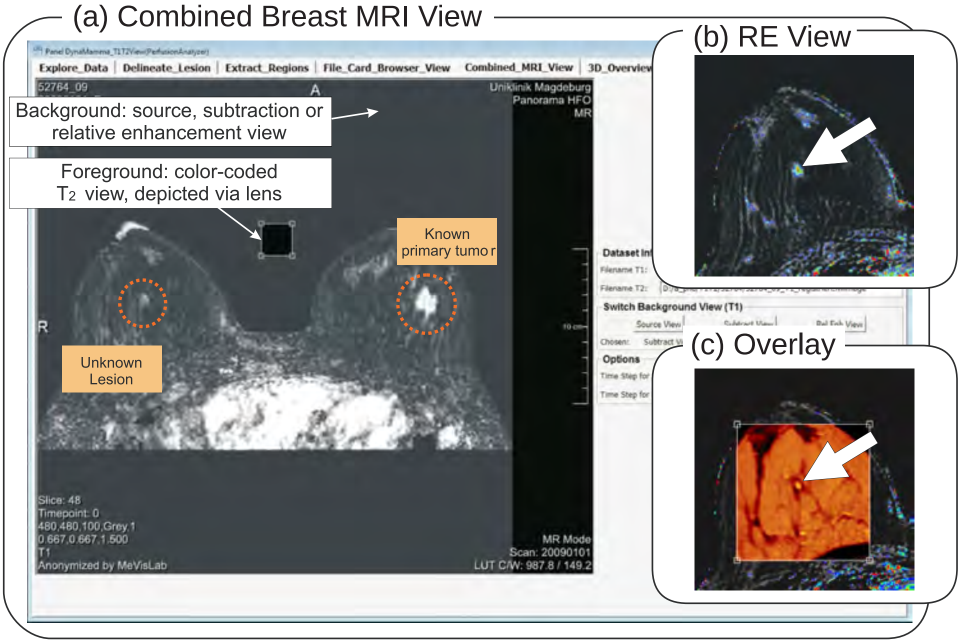

Figure 5.17: *Joint visualization of T_1- and T_2-weighted MRI sequences. In (a), the subtraction view of an T_1-weighted DCE-MRI data set is depicted. A known primary tumor exists and the clinical expert has to evaluate if the tumor has spread. Therefore, all suspicious lesions have to be evaluated, see the marked one. With the PerfusionAnalyzer, the clinical expert can change the background to the RE color-coded parameter map, see (b). Next, the integrated magic lens displays the T_2 data set as overlay and reveals hyper intensity indicating a cyst, see (c). (Medical image data is courtesy of U. Preim, Municipal Hospital Magdeburg, Germany.)*

In cooperation with Fraunhofer MEVIS[4], a deformable image registration method was adapted to T_1 and T_2-weighted MR images of the breast. To support the approach, a landmark-based evaluation was carried out within the PerfusionAnalyzer. Therefore, a clinical expert marked identical structures (small enhancing lesions or characteristic parenchyma patterns) in both sequences. The landmarks were the input for the image registration. The method respects differences in resolution, anisotropy and intensity characteristics. It was developed by Tobias Böhler and is part of his PhD thesis [Böhler, 2011].

---

[4] Fraunhofer Institute for Medical Image Computing MEVIS; www.mevis.fraunhofer.de; (12/01/2013)

In addition to the landmark-based evaluation, a view for the co-registered T_2 image was integrated in the PerfusionAnalyzer. Thus, the clinical expert can evaluate both sequences simultaneously with a magic lens, see the examples in Figures 5.17 and 5.18. This view is just an optional extension and it remains future work to include other modalities or results. For example, first findings of the evaluation of the conventional X-ray mammography could be integrated and presented to the clinical expert.

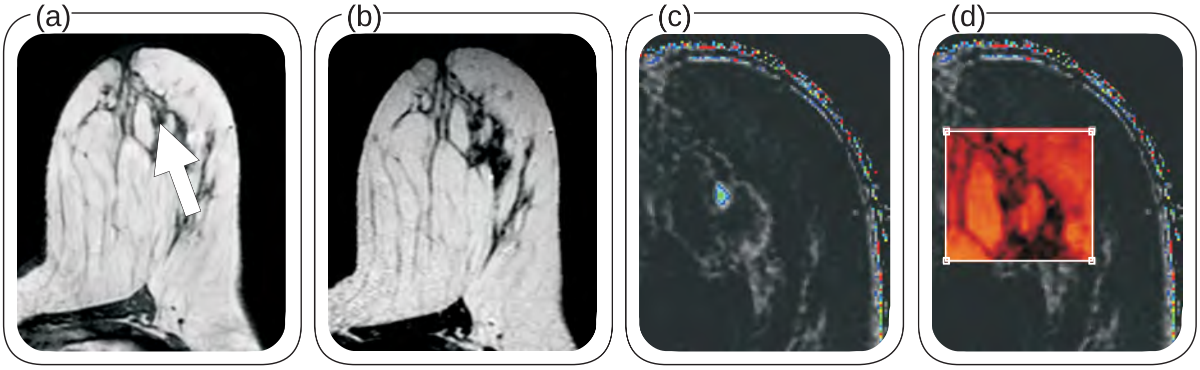

Figure 5.18: *Joint visualization of T_1- (a) and T_2-weighted (b) MRI sequences (image adapted and reprinted from [Böhler et al., 2011] © 2011, Springer-Verlag, with kind permission from Springer Science and Business Media). Note the varying image resolutions and intensity distributions. The RE parameter map of (a) reveals a small enhaning lesion, see (c) and the arrow. When combined with a lens that shows the T_2 view in (d), hypo-intense tissue is depicted, indicating malignancy. (Medical image data is courtesy of U. Preim, Municipal Hospital Magdeburg, Germany.)*

5.7 Summary of 2D Visual Exploration of Breast Tumor Perfusion Data

In this chapter, the PerfusionAnalyzer, a software prototype covering multiple linked views, with the integrated 2D visual exploration techniques for the evaluation of breast tumor perfusion data was presented. Beyond standard views, e.g., color-coded 2D parameter maps of RE values or subtraction views, also novel visualization techniques were integrated. The lesion detection and delineation was implemented with a volume growing method.

The voxel-wise glyph-based visualization allows for a fast overview of data sets. It avoids interpolation and distortion due to average RE curves but is prone to outliers. The classification of the voxel's RE curve is carried out via the adapted 3TP method. As an advantage, the glyphs visualize more different RE values than the adapted 3TP method, which only differentiates the RE values of the early post-contrast phase into three groups.

An automatic subdivision of a suspicious tumor into different regions is established with the region merging method. This approach reduces the influence of outliers. The similarity function is based on a feature vector consisting of descriptive perfusion parameter values. Hence, each region contains voxels with similar perfusion characteristics. An advantage is the connectivity of the remaining regions compared to other classification techniques, e.g., the 3TP method, that neglect spatial connectivity. The clinician is not only interested in the malignancy of special tumor parts but also in the localization of these parts for further treatment. Since a region contains similarly perfused voxels, the distortion of the average RE curve of the ROI as well as the inter-observer variability concerning the ROI's placement is reduced. The number of regions and the diversity of the corresponding RE curves provide valuable information of the physiological heterogeneity of the tumor and reveal benign and malignant parts inside the whole tumor.

In general, the glyph-based voxel-wise overview as well as the region-wise quantitative and qualitative evaluation with the RE curve diagram and the change diagram provide additional information about the tumor enhancement kinetics and thus its malignancy. This is particularly useful, since breast tumors can contain benign and malignant parts at the same time. Moreover, it is possible, that no washout curve can be observed at all. Hence, the clinical expert has to decide about further diagnosis and treatment. A drawback of the region merging is the influence of noise on small regions. Hence, this influence is higher than on larger regions. Although the results are satisfying for the tested lesions, the correlation threshold should be adapted to account for this issue and it is left for further investigation in future work. Also, when analyzing a local neighborhood, regions could be automatically classified as reliable or unreliable. Adequate visualization techniques should be developed to represent this information.

With the PerfusionAnalyzer, the evaluation of a suspicious tumor has been improved, since the radiologist could focus on suspicious regions and avoid the error-prone and time-consuming manual ROI placement. The selection of the suspicious regions could include numerous regions, depending on the tumor's heterogeneity and size, but it is still faster than the manual ROI placement method. The selection is carried out with the RE curve diagram by choosing the largest region that exhibits strong contrast agent accumulation in the early post-contrast phase and an average RE curve with a washout shape. Furthermore, the analysis of the RE curve diagram and change diagram allows for a finer exploration of the data set, in comparison to the nine classes derived with the 3TP method. Similar trends in terms of the descriptive perfusion parameters are determined by analyzing the trends in the change diagram. The region number in relation to the tumor size provides information about a tumor's heterogeneity, which could be indicative for malignancy.

Beyond the kinetic evaluation, a new MPR view was designed and integrated to account for the tumor's morphology. The FCB View is adapted to each tumor, i.e., it creates a new MPR plane that is adapted to the tumor's extent. The presented comparison and examples illustrated the main advantages of this method: the improved boundary evaluation as well as the identification of spatially connected and similarly perfused regions. The first advantage allows for a better evaluation of the tumor's morphology, whereas the second one is important for further treatment planning. Therefore, the kinetic evaluation can be combined with this additional technique.

A further extension is the combination of T_1- and T_2-weighted MRI sequences of the breast. The joint inspection of both sequences is important for differential diagnosis when evaluating breast cancer. In particular, it allows to distinguish between benign cyst-type and malignant lesions. However, in routine diagnostics both images are regarded independently and an immediate image registration is prevented due to patient motion and tissue deformations. With the integrated lens view, the radiologist can visually combine the MRI sequences for a faster diagnosis without the effort of mentally integrate both images.

6. 3D Visual Exploration of Breast Tumors and Clustering Results

This chapter is partly based on:

Sylvia Glaßer, Uta Preim, Klaus D. Tönnies, and Bernhard Preim: “A Visual Analytics Approach to Diagnosis of Breast DCE-MRI Data". In Computer and Graphics (34:5), p. 602-611, 2010.

Sylvia Glaßer, Kai Lawonn, and Bernhard Preim: “Visualization of 3D Cluster Results for Medical Tomographic Image Data”. In Proc. of Conference on Computer Graphics Theory and Applications (VISIGRAPP/GRAPP), p. 169-176, 2014.

6 3D Visual Exploration of Breast Tumors and Clustering Results

The visualization of 3D scenes supports the perception of spatial information. Especially tomographic data, like MRI, are well suited for this kind of visualizations. However, 3D visualizations have to deal with occlusions, e.g., when outer parts hide inner parts. Furthermore, the biomedical expert is experienced with evaluating 2D parameter maps and subtraction views since these are widely employed in clinical routine. In Section 6.1, the region merging result of the PerfusionAnalyzer is explored with the *SimVis* framework by Doleisch et al. [2003]. This framework with multiple linked views was presented in Section 4.1.2. In Section 6.2, a more general 3D view of breast data sets is presented. However, for visual exploration and analysis of tumor data, region of interests (ROIs) should be employed instead of the complete whole lesion analysis and a well-suited 3D visualization is missing, recall Chapter 4. The solution to this problem is presented in Section 6.3: the 3D ClusterView. Although this view was initially developed for breast tumor perfusion studies, it can be adapted to brain tumor data as well since it processes any clustering result extracted of medical tomographic image data.

6.1 3D Exploration via Brushing and Linking

As first step towards 3D visualization, the ROIs that were extracted with the region merging method integrated in the PerfusionAnalyzer, were adapted to the *SimVis* framework. Thus, an overview of the breast tumor is provided, see Figure 6.1. The 3D exploration of the region merging result is based on aspect $\boxed{8}$ of Chapter 4. Hence, an interactive feature definition is carried out in the attribute views, e.g., the parallel coordinates view, the curve view and the scatterplot view.

The exploration was carried out in the following way. First, the exploration is restricted to voxels that exhibit a relative enhancement (RE) value greater than a certain threshold, e.g., 50% after the early post contrast phase. This selection was carried out via brushing in the curve view (see turquoise rectangle at the third time step in Fig. 6.1(d)), and the result is presented in Figure 6.1(a). Hence, only a volume of interest is depicted and the selected voxels in the curve view are mapped to color based on the voxel values for peak enhancement or the different regions.

The second exploration also takes the curve shape into account. For example, a similarity brush to highlight voxels with a fast washin and washout, i.e, a decreasing RE curve, is applied. The similarity brush selects curves that exhibit similar gradients like the two blue parallelograms, where the parallelograms' heights define the size of the similarity interval (see Fig. 6.1(e)). As it is depicted in Figure 6.1(b), many spatially not connected voxels are highlighted.

The third exploration example is based on the region merging result. In the scatterplot diagram in Figure 6.1(f), the regions are arranged based on their ID (the regions are ordered by size and the largest region is assigned to ID 1) and their average RE curve shape. A brush selects regions with small IDs, i.e., larger regions, and a washout curve shape. As a result, the clinical expert yields a portion of the data that contains the most malignant part of the tumor (Fig. 6.1(c)). This part is important for further diagnosis like core needle biopsy.

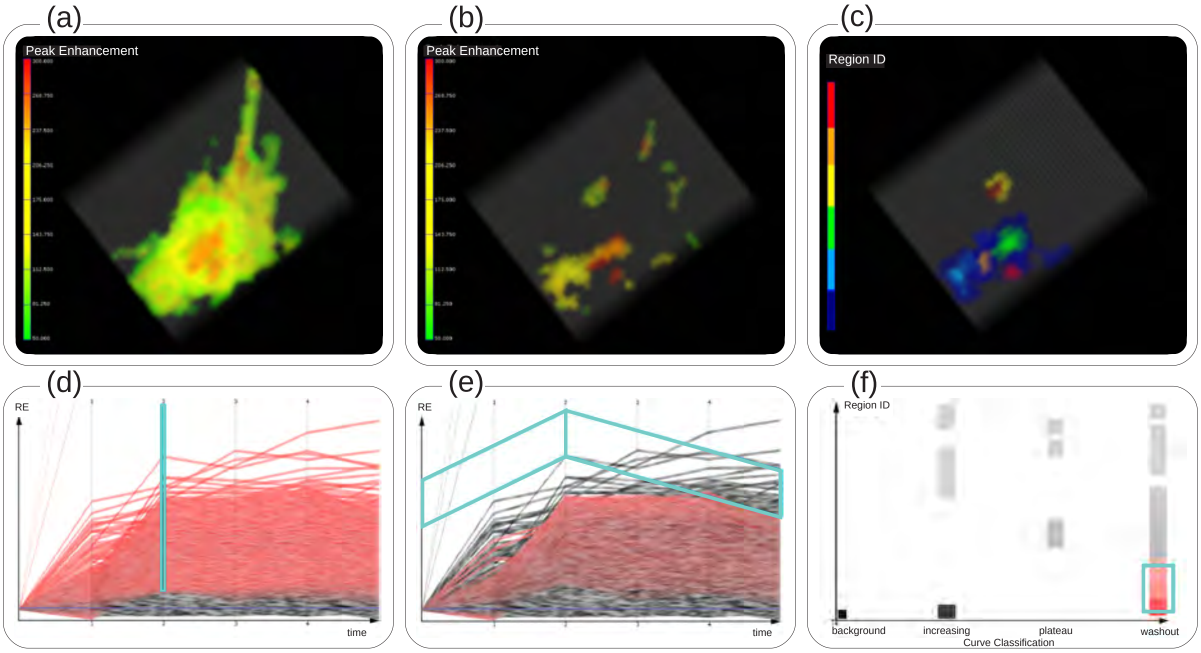

Figure 6.1: *Visual comparison of the exploration of the tumor's most suspicious part (image adapted and reprinted from [Glaßer et al., 2010] © 2010, Elsevier, with kind permission from Elsevier). In the top row, a volume of interest of a breast DCE-MRI data set is depicted. At the bottom row, the corresponding selections are visualized. In (d), all voxels RE* $\geq 50\%$ *at the first point in time after the early post-contrast phase are selected in the curve diagram (see turquoise rectangle at the third time step) yielding the enhancing lesion in (a). In (e), a similarity brush highlights voxels with a fast washin and washout in (b). The similarity brush selects curves that exhibit similar gradients like the two turquoise parallelograms. The parallelograms' heights define the size of the similarity interval. In (b), many small not connected voxels are selected. In (f), regions with an average washout curve are selected, yielding a few regions in (c).*

As an intermediate result, a 3D region-based analysis is well suited to visually detect the most malignant tumor part. For a better spatial orientation, context visualization of the breast is needed, which is described in the next section.

6.2 Adaption of Transfer Functions for 3D Breast Visualization

For the spatial overview of a breast tumor DCE-MRI data set, a direct volume rendering visualization was integrated in the PerfusionAnalyzer, i.e., with the Me*VisLab* platform[1] supported

---

[1] Product of Fraunhofer MEVIS, Bremen; www.mevislab.de (12/08/2013)

by OpenGL and VTK.[2] Examples are provided in Figure 6.2. The generation of the 3D view comprises two steps. First, the breast shape is visualized as gray-colored background visualization for context information. Second, the contrast agent enhancing tumor is visualized as focus object.

For the visualization of the breast, the DCE-MRI data set is employed. A 3D Sobel filter is applied to highlight the air-tissue boundary. In a preprocessing step, Gaussian filtering reduces the influence of outliers and noise. A threshold is employed to mask voxels with Sobel gradient values smaller than this threshold. Afterwards, a ramp window function (from dark gray to light gray) is assigned to the remaining voxel values, yielding a gray shaded context visualization of the breast shape. This threshold can be adapted by the user.

The highlighting of the tumor or any other enhancing tissue is based on the RE extracted from the breast DCE-MRI data set. The RE values of the first post-contrast time step are employed. Furthermore, the descriptive perfusion parameter integral is extracted. Voxels that exhibit high RE values, but low integral values are classified as outliers and are mapped to full transparency. They may arise due to noise or motion artifacts. The threshold for low integral values forms the second user-defined input. Finally, the remaining voxels are mapped to color by employing a ramp window function covering blue (for low enhancement, i.e., 60%, red, orange, and yellow for higher RE values (RE $\geq$ 250%).

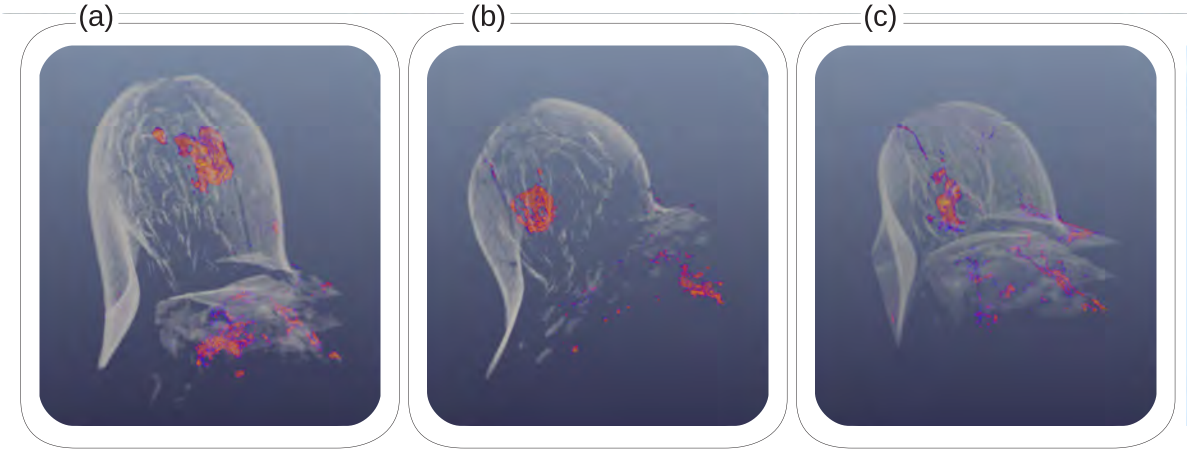

__Figure 6.2:__ Examples of three breast DCE-MRI data sets visualized with the PerfusionAnalyzer. The tumors are highlighted, whereas the surrounding tissue and the skin is provided as context information. (Medical image data is courtesy of U. Preim, Municipal Hospital Magdeburg, Germany.)

The presented view aims at a spatial overview of the breast as well as its enhancing lesions. For a diagnostic evaluation, this view does not provide sufficient information. However, the 3D view does only require two parameter choices to yield satisfying results.

6.3 The 3D ClusterView

Clinical diagnosis of perfusion data sets aims at the identification of areas that exhibit similar characteristics. Therefore, clustering is applied to the perfusion data sets to group objects with

---

[2] The Visualization Toolkit, New York, USA; http://www.vtk.org/ (12/08/2013)

similar attributes, e.g., voxels representing certain tissue types. The appropriateness of a cluster algorithm depends on the medical problem and image parameters. To improve the adoption of a clustering to a specific problem, the biomedical expert has to evaluate the quality of the clustering result like the topology of the clusters and the spatial orientation of the structure that has been decomposed. The 3D ClusterView in the PerfusionAnalyzer is a new clustering visualization that is tailored to tumor cluster results. The tumor voxels are represented such that geometric tubes visualize cluster connections. The spatial information about the voxel positions in the tomographic data set is provided as well. The 3D ClusterView provides the amount of clusters, cluster size, amount of outliers, and – most important – the spatial extent and the orientation of the resulting clusters.

The motivation for developing this view is the need for improved interpretation of a clustering result (e.g., number and size of clusters or their spatial relationship) right after clustering was carried out. In contrast to 2D scatterplots or 2D visualization techniques, a 3D scatterplot clustering visualization allows for a quick spatial overview. A 3D scatterplot has the great advantage of showing one additional data dimension compared to conventional 2D scatterplots. On the other hand, the data exploration requires more user interaction, since only two position attributes can be presented simultaneously on the 2D screen. As it was listed in Section 4.1, no appropriate 3D scatterplot visualization is available for the specific view of clustered tomographic data. In literature, a direct presentation of clustering results usually involves surface representation or a visualization of a reduced high dimensional space. Naturally, only limited spatial information about the clusters and the cluster elements is available due to the dimension reduction.

In contrast, clustering results of medical tumor data cover voxels with an explicit spatial position.To support the spatial perception in the 3D ClusterView, and to fulfill aspect $\boxed{8}$, special geometric primitives, i.e., tubes, were developed to visually represent the connection of clusters. The orientation and attributes of these primitives are very well adapted to the 3D scatterplot. The 3D ClusterView comprises the following parts:

1. A center point-oriented projection of a tumor into a sphere model. Hence, different spheres represent different neighbor layers.
2. A 3D scatterplot visualization for breast clustering employing the sphere model and featuring well adapted geometric primitives to present the clustering structure.
3. Selected shading styles to enhance the different parts of the scatterplot parts.
4. A perception-based color mapping to enhance visual differentiation between the clusters.

The steps of the 3D ClusterView generation are presented in Figure 6.3. At step I, the neighborhood model is extracted (described in Sect. 6.3.1). At step II, the voxel size and tumor extent is determined (see Sect. 6.3.2). At step III, the voxels are projected onto spheres (refer to Sect. 6.3.3), and the cluster elements are connected with their associated cluster center points via tubes (presented in Sect. 6.3.4). Also, the spheres are reshaped according to the tumor's extent. A legend that is based on the necklace map is added to the 3D visualization. It provides additional information about the clusters and is described in Section 6.3.5. Finally, the assignment of color and shading styles is presented in the last part of this section. The extraction of clusters and the generation of surface meshes was realised with MATLAB.[3] The final presentation and the necklace map legend were created with Me*VisLab*.

---

[3] Product of the MathWorks, Natick, USA; www.mathworks.de/products/matlab/ (12/08/2013)

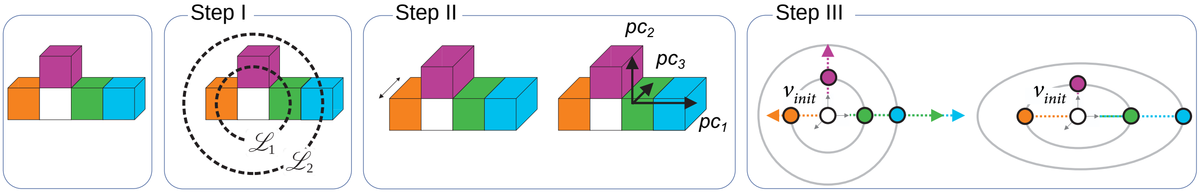

Figure 6.3: *Scheme of the cluster visualization pipeline. The example holds five voxels, each forming its own cluster. In step I, a sphere model is created that holds all voxels of the tumor. In step II, the voxel dimensions are adapted to the image resolution. A principal component analysis yields the main directions of the tumor. In step III, the 3D clustering visualization is generated by positioning the voxels onto spheres. The sphere-shaped visualization is adapted to the main tumor extents that are approximated with the principal components.*

6.3.1 Neighborhood Model for Voxel Ordering

Given a voxel in a 3D tomographic data set, the corresponding neighbors are defined as adjacent voxels that share

- a face (yielding 6 neighbors),
- an edge (yielding 18 neighbors),
- or a vertex (yielding 26 neighbors).

For the 3D ClusterView, the edge-based neighborhood relationship is employed. See Figure 6.4 for an illustration of the edge-based neighborhood in the 2D case. In the 3D case, a voxel with position $p(i,j,k)$ has 18 neighbors. The neighborhood structure is built by an iterative process: First, an initial voxel v_{init} is chosen by employing the centroid of the tumor $\mathscr{T}$. If the centroid is not part of the tumor due to an irregular tumor shape, its nearest neighbor contained in the tumor is chosen. As a result, the first layer $\mathscr{L}_1$ of the neighborhood structure contains only v_{init}. The second layer $\mathscr{L}_2$ includes the neighbors $v_i \in \mathscr{T}$ of v_{init} that are also part of the tumor. For simplicity, $\mathrm{Neigh}(v)$ denotes the neighbors of v in $\mathscr{T}$. The i-th layer can be written as:

$$\mathscr{L}_i = \bigcup_{v \in \mathscr{L}_{i-1}} \mathrm{Neigh}(v) \setminus \mathscr{L}_{i-1}. \tag{6.1}$$

The i-th (with i > 1) layer $\mathscr{L}_i$ comprises a maximum of $4(i-1)(5i-6) + 2$ elements.

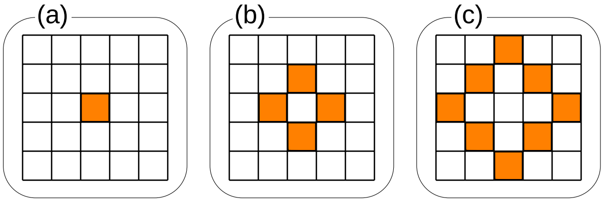

Figure 6.4: *Illustration of the edge-based neighborhood in 2D space. The initial voxel in (a), has four neighbors in (b), which in turn have eight neighbors excluding the initial voxel in (c).*

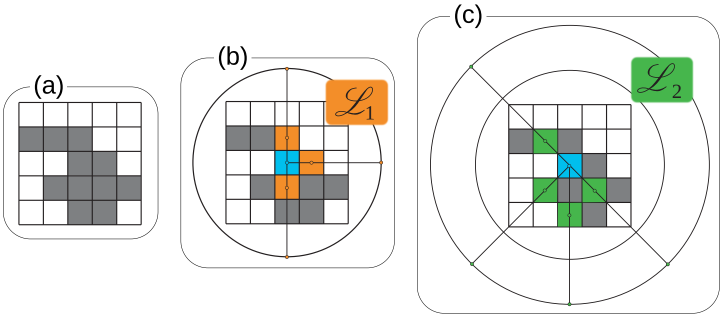

Figure 6.5: *Illustration of the sphere projection. The method starts with the initial voxel (cyan color-coded), see (a). Next,* $\mathscr{L}_1$ *is determined and the intersection point of the line constructed by the initial voxel and an element of* $\mathscr{L}_1$ *with the circle is calculated, see (b). In (c), the intersection points of the second layer* $\mathscr{L}_2$ *are obtained.*

6.3.2 Integration of Voxel and Tumor Extent

The voxel extent is determined by the image matrix that defines the image plane resolution, i.e., the voxel's width and height. The voxel's depth is set down by the slice thickness, which usually differs from the image plane resolution in medical image data sets. In a preprocessing step, the voxel's depth v_z is rescaled such that the voxel's width and height equal uniform length.

The tumor extent is characterized with a principal component analysis (PCA). The voxel's x, y, and z indices serve as input, and z was rescaled with v_z. Hence, the principal components match the eigenvectors of the covariance matrix that was constructed for the PCA. With the three eigenvalues corresponding to the three principal components, the tumor's three main extents are obtained.

6.3.3 Projection onto a Sphere

After the extraction of the neighborhood structure, the cluster visualization is built up. Each layer of neighborhood information is projected onto a sphere. Therefore, a sphere of radius $r = i^2$ is translated to the initial voxel, i.e., the centroid. Afterwards, the intersection point of the sphere with the line, constructed by the initial voxel and an element in the ith layer $\mathscr{L}_i$, is determined. In detail, the voxel is translated such that the initial voxel lies in the origin. Given the midpoint $\mathbf{q}_j^i$ of $v_j \in \mathscr{L}_i$, the intersection point $\mathbf{p}_j^i$ is calculated by:

$$\mathbf{p}_j^i = \mathbf{q}_j^i \sqrt{\frac{r^2}{(\mathbf{q}_j^i)^2}}. \tag{6.2}$$

See Figure 6.5 for an illustration in 2D.

6.3.4 Connection of Cluster Elements and Their Associated Midpoints

To support the perception of clustered elements, all elements are connected with their associated midpoints. The connections, shaped like tubes, are motivated by the natural model of neurons and their dendrites as well as blobby surfaces [Blinn, 1982]. The cluster visualization connects the start points, i.e., the extracted positions for each voxel, with the end point, i.e., the cluster center, by smooth organic linkage. Hence, the algorithm comprises three steps.

At the first step, the start point and the end point are connected with a straight line. As an optional step, several equidistant points on the line are added. Afterwards, the normalized vector, pointing from the origin to the start point, is scaled to one tenth of the length from the end point to the start point. This vector is added to the points on the line. The scaling changes linearly to zero such that the first points are larger translated than the last ones. This approach yields a bending of the tubes and reduced visual clutter. The second step is about generating a cubical spline to connect the end point and the start point via the middle points. The third and last step generates a Frenet frame around the curve. Afterwards, this frame is employed to generate a tube around the curve. Inspired by the following formula:

$$\mathrm{thick}(x) = \mathrm{radius}\left(1 - \left(\frac{x}{\mathrm{d}}\right)^2\right)^2, \tag{6.3}$$

a function which determines the thickness of the tube at every point is generated. Let r_1 be the radius of the sphere at the start position, r_2 the radius of the sphere at the end point, and d denotes the distance between the start and the end position. Furthermore, r' is defined as $r' = 0.25\min(r_1, r_2)$. Then, the thick(x) function with $x \in [0, \mathrm{d}]$ can be written as:

$$thick(x) = \begin{cases} (r_1 - r')\cdot\left(1 - \left(\frac{4x}{\mathrm{d}}\right)^2\right)^2 + r' & \text{if } x \le \frac{\mathrm{d}}{4} \\ (r_2 - r')\cdot\left(1 - \left(\frac{4(\mathrm{d}-x)}{\mathrm{d}}\right)^2\right)^2 + r' & \text{if } x \ge \frac{3}{4}\mathrm{d} \\ r' & \text{otherwise.} \end{cases} \tag{6.4}$$

The construction of thick(x) ensures a smooth change from r_1 for $x = 0$ to r_2 for $x = d$. First, the value thick(x) decreases smoothly from r_1 to r' for $x \in [0, \mathrm{d}/4]$ and keeps its value r' for $x \in [\mathrm{d}/4, 3\,\mathrm{d}/4]$. For $x > 3\,\mathrm{d}/4$ the function smoothly increases to the value r_2. In Figure 6.6, an example for the connections is provided.

6.3.5 Combination with a Necklace Map

To assess a clustering's quality, additional information to the cluster's spatial orientation should be provided. These information may include the cluster's average value of some parameter, its standard deviation, or its size, etc.

For perfusion imaging, the average perfusion enhancement curve is of major interest from the radiologist's point of view. Thus, for each cluster its average curve is provided in a legend that is based on a necklace map [Speckmann and Verbeek, 2010]. The necklace map was developed for 2D maps and is similar to cartograms or choropleth maps. However, it arranges

Figure 6.6: *An example of a visually pleasing tube connecting the start point (i.e., an extracted position for a voxel) and the end point (i.e., the cluster center).*

symbols (e.g., circles) around the initial map in a linear ordering. Thus, the symbols can carry information but no occlusion arises.

The necklace map is perfectly suited for the 3D ClusterView method because additional information for a group of well-defined objects - the clusters - can be displayed in a 3D scene instead of a 2D scene. The according symbol for each cluster is a circle that is color-coded with the corresponding cluster color. All circles are arranged on the necklace ordered by cluster size, starting in the top right. The necklace itself is an ellipse that is obtained by scaling a circle with the tumor extents. The necklace legend is depicted in Figure 6.7. The size of the necklace pearls is linearly decreased, and not proportional to the cluster size due to strong variations of cluster sizes, e.g., a cluster may contain 3 or 500 voxels.

6.3.6 Representation of Clusters

The tubes are rendered with a Phong shading to improve the shape perception. To support the visualization of the start point, and thus, a good differentiation from the Phong-shaded connecting tube, Fresnel shading is applied to the start point.

A specific color is assigned to each cluster and its start points. For the color assignment, the CIELAB color space is employed to establish high perceptual color contrast. The CIELAB color space was defined by the International Commission on Illumination (CIE)[4] and is based on the Lab color space. Hence, L defines the lightness and a and b the color hue. For the proposed method, the first cluster is always assigned to orange with the corresponding CIELAB components $L = 67$, $a = 43$, and $b = 74$. For the n remaining clusters, n colors are extracted with the following routine. A circle is placed in the CIELAB space. The circle's center is set to the origin $(a = 0; b = 0)$. Given the a- and b-value for orange, its radius r is defined with $r^2 = a^2 + b^2$. Then, the angle $\alpha := arcsin(b/r)$ is determined. Next, a new color is extracted by calculating new values for a and b by increasing α with β and $\beta \in \{0, 1 \cdot \frac{2\pi}{n}, 2 \cdot \frac{2\pi}{n}, \cdots, (n-1) \cdot \frac{2\pi}{n}\}$. Thus, $a = r \cdot \cos(\alpha + \beta)$ and $b = r \cdot \sin(\alpha + \beta)$ are extracted and combined with the starting value for L.

For the final representation, the surrounding spheres with the voxels are scaled according to the tumor extent to highlight the tumor's biological form. Thus, a tumor with a biological

---

[4] International Commission on Illumination; cie.co.at (12/01/2013)

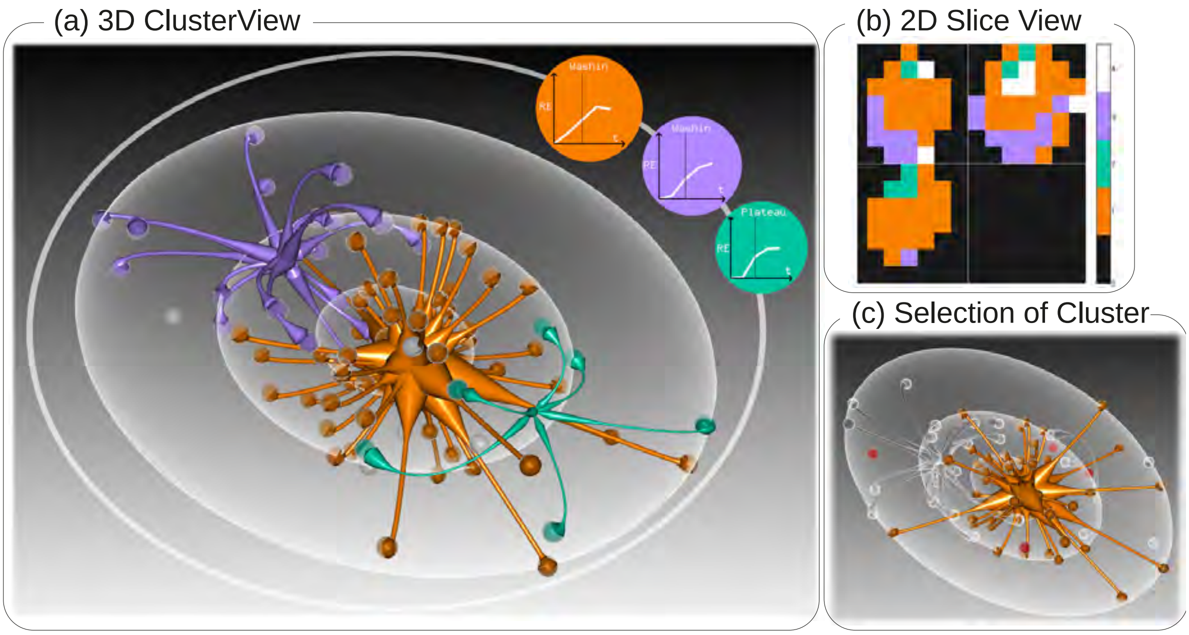
(a) 3D ClusterView

(b) 2D Slice View

(c) Selection of Cluster

Figure 6.7: *Example of a breast tumor clustering of tomographic perfusion data. The 3D cluster visualization (a) and the 2D slice view (b) are integrated in the 3D ClusterView framework and reveal three clusters arranged at three layers. The necklace map (placed around the 3D visualization) and the slice view allow for a fast selection of clusters. Once the user selected a cluster, only this cluster is color-coded, and the remaining clusters are visualized with a Fresnel shading (c). Outliers are highlighted with bright red after selection according to observations from a user study.*

ellipsoid form yields a scaling of the spheres along the main tumor extents, whereas an almost sphere-like tumor will only cause minimal scaling.

6.3.7 Results

The 3D ClusterView approach adapted to a breast tumor is presented in Figure 6.7. There, an overview of the 3D scatterplot-like clustering visualization is provided. The user can examine the spatial extent of the single clusters and their spatial position. The spheres holding the different neighbor layers are visualized with a Fresnel shading. Gray is assigned to these spheres. Outliers are presented with white colored spheres. Further, a standard headlight is applied to the visualization.

The 3D view is accomplished with a necklace map. Thus, the user has a fast overview of all existing clusters and additional information are mapped. As demanded by the medical experts, the cluster's average RE curve is represented in the necklace map. The framework also holds a conventional slice view. To study a cluster's spatial orientation in more detail, the user can pick a cluster by clicking via the necklace map or the 2D view and study its extent in more detail. Now, Fresnel shading is interactively applied to the non-selected clusters with a gray color. This emphasizes the selected clusters and supports the individual examination, recall Figure 6.7.

In Figure 6.8, a brain tumor data set comprising a masked perfusion T_2^*-weighted MRI data set is presented. For brain perfusion, the parameter cerebral blood volume (CBV) is analyzed to detect hot spots, i.e., regions with elevated CBV values. The brain was decomposed into five clusters with a k-means algorithm based on the parameter CBV. Hence, no outliers are present. Instead of presenting the whole contrast agent enhancement curve, the pearls of the necklace map provide average CBV values and identify the pink cluster as cluster with highest averaged CBV value.

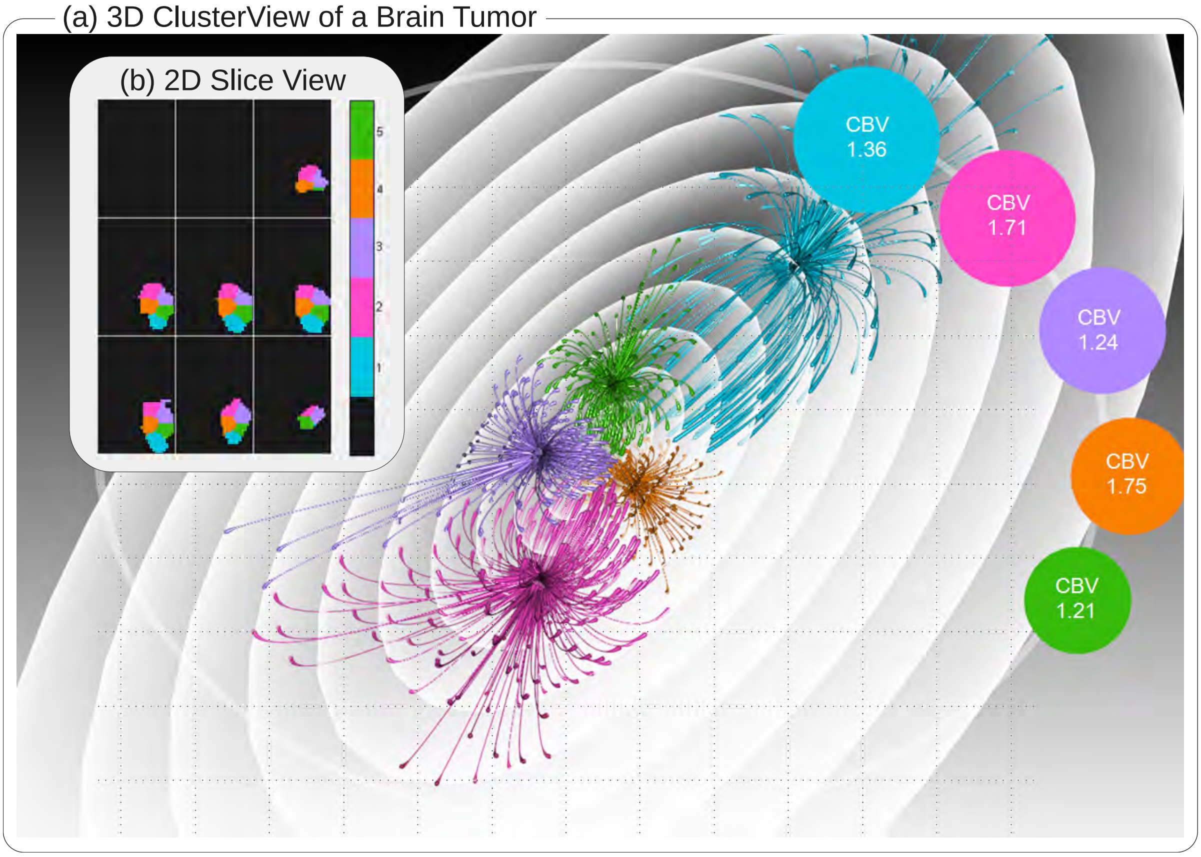

Figure 6.8: *Illustration of the clustering result of a brain tumor. The tumor has an elongated shape and was clustered into five clusters, no outliers exist. The necklace map provides additional cluster information, i.e., the cluster's average parameter value of the cerebral blood volume (CBV), see (a). The slice view was added for a 2D view of the clusters, see (b).*

6.3.8 Evaluation

In the following, a qualitative evaluation of the 3D ClusterView visualization method is presented. The goal was to assess the capability to express the topology of the clustering result in the 3D visualization. Hence, the focus relies on the 3D representation of the clusters in combination with connecting tubes. For comparison, a point-based scatterplot view and a transparent isosurface were presented to the user, see the example in Figure 6.9. The evaluation was conducted with one medical researcher and physician, and ten researchers who are familiar with the visualization and evaluation of medical tomographic image data.

In this study, the participants were asked to handle a few minor tasks about

- the topology of the clustering result,
- the presence of outliers, and

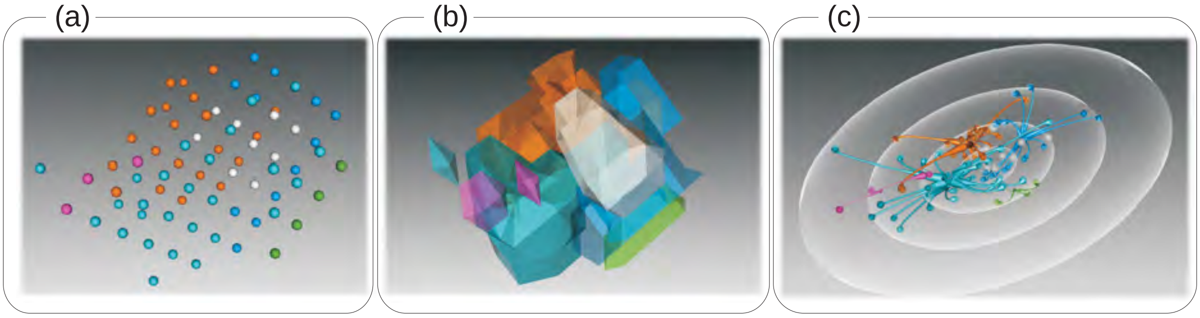

Figure 6.9: The three 3D views of a clustering result, including a point-based view (a), the isosurface view (b), and the 3D ClusterView approach (c).

- the impression about the tumor's boundary and shape.

The topology of the clustering result was covered by the request to identify the largest cluster and to categorize the clustering result's topology in pre-defined categories. It was questioned, if the participants could identify outliers and how many outliers there are with respect to number and percentage to the whole tumor. The last question concerned the tumor's boundary (from round to stellated boundary) and shape (from spherical to ellipsoidal). To make the answers of different participants comparable, well-defined categories were provided for each answer.

First, the participants were introduced to the three techniques by presenting a clustering result of a test data set (recall Fig. 6.9). Next, the subjects solved the tasks for nine examples, created by applying each visualization technique to three new data sets. The visualizations were presented such that no data set was consecutively shown, but after each presentation, another data set with another 3D view was depicted. After answering the questionnaire, the participants rated the techniques due to their appropriateness to evaluate the clusters' topology, the required user interaction, and provided additional feedback.

As a result, all volunteers correctly identified the largest cluster for each example. However, when it comes to the cluster number, the 3D ClusterView technique achieved better results than the other two methods, see the diagram in Figure 6.10. This is very relevant, since a wrong number of clusters implies that some clusters were not detected at all or (very rare) some single, spatially connected, clusters were interpreted as different clusters. The majority of the participants rated the 3D ClusterView method to be the most appropriate for evaluating the clusters' topology (8 out of 11).

Outliers were present in all examples, and with two exceptions (arising from the 3D ClusterView visualization and an isosurface-based view) for two single examples, all participants detected the outliers for each view. When it comes to tumor shape, the volunteers assign higher ratings, i.e., more stellated boundaries based on the presented visualization in comparison to the other two conventional views. This is due to the arrangement of the voxels onto the spheres. Hence, the 3D ClusterView suggests a more stellated boundary, which is a limitation. However, there was no trend with respect to the employed technique present when the participants should evaluate the tumor size via the number of voxels that were clustered. All participants had no difficulty with the interaction or with the visualization. But the majority (9 out of 11) needed less interaction with the 3D scene, e.g., camera rotation, comprising the 3D ClusterView due to the good spatial impression of the connected clusters.

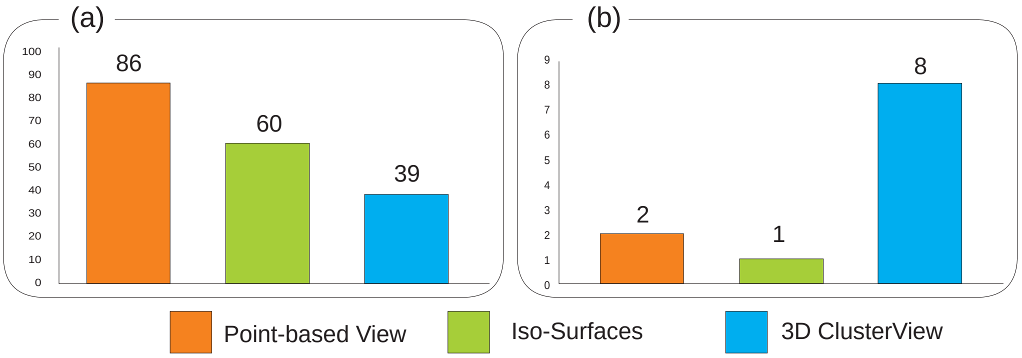

Figure 6.10: *Bar diagrams illustrate the average squared error of the approximated number of clusters (a) by all users for the three techniques: point-based 3D view, isosurface view and the 3D ClusterView with connecting tubes. In (b), the number of users is presented that chose the technique as most appropriate for the evaluation of the clustering's topology.*

However, the study does not allow for a definitive statement. A further evaluation is required with more participants and data sets. In summary, the participants were able to fulfill the assigned tasks with the 3D ClusterView method very well. They rated it as best suited for the evaluation of a clustering topology. Furthermore, they preferred it due to the visual cluster connections via tubes and due to the lesser scene interaction in comparison to the other techniques. They asked for a more prominent color-coding of outliers, like bright red, which was employed in the framework afterwards. It must also be stated that the 3D ClusterView visualization indicates a more stellated boundary due to the spatial representation of the voxels on the spheres. On the other hand, these representations reduce the amount of occlusion and thus the amount of required user interaction.

For future work, in case of a huge number of cluster elements, the 3D ClusterView would benefit from a view-dependent transparency representation similar to the work by Günther et al. [2011]. They reduce the number of displayed lines by smoothly fading them out. Connections very distant to the camera are opaque, whereas connections far away are rendered transparent. This is done to improve the visual appearance of the tubes and to concentrate on the focus of the camera.

6.4 Concluding Remarks of 3D Visualization for Breast Tumors and Clustering Results

The increasing complexity of medical image data induces an increasing demand for visual analytic solutions [Lundström and Persson, 2011]. Albeit their work identified the diagnosis of primary and secondary findings in the image data in an efficient way as key issues, the determination of shape, size, and relative position of different parts of the anatomy were identified as important component of a radiologist's image review work. For this aspect, a 3D view has the great advantage of conveying spatial information when compared to 2D parameter maps.

The visual exploration of breast tumors in 3D (recall Sect. 6.2) provides this spatial information overview, but the advantages are restricted to this overview. A dedicated analysis is hampered due to occlusion of inner tumor parts. In contrast to the 2D representations, including the MPR-based FileCardBrowser View, the tumor's morphology is difficult to analyse regarding its 3D shape. An adaption to multiple linked views (recall Sect. 6.1), like the *SimVis* framework, allow for an exploration of the data set, but unless the spatial overview, no further information can be extracted from the 3D views.

Although conventional analysis is carried out in 2D due to the missing diagnostic information or occlusions, the 2D visualization of clustering results becomes difficult to interpret. The information that should be depicted cover the number of clusters, their size, and how they are spatially aligned. Hence, a 2D view lacks of appropriate visualization for an intuitive representation. With the 3D ClusterView, the clusters can be adequately represented as a 3D scene. Hence, the geometric modeling enhances cluster connections. The 3D ClusterView is completed with a necklace map legend, maintaining that each cluster can be addressed. Hence, the user can select a cluster of interest for further exploration in the 3D view. While the appearance of the selected cluster does not change, color and shading of the remaining clusters change from opaque visibility to Fresnel. The 3D ClusterView was successfully adapted to brain tumor data and is well suited for any clustered medical tomographic image data. Due to the increased complexity of medical image data, the biomedical experts will be definitely confronted with the problem of an effective clustering of their data in the future. In turn, the extracted clustering results have to be qualitatively and quantitatively evaluated. Hence, for the qualitative evaluation, the 3D ClusterView yields the most expressive results since it is specifically tailored to this application area.

7. Breast Tumor Analysis for Automatic Classification

This chapter is partly based on:

Uta Preim, Sylvia Glaßer, Bernhard Preim, Frank Fischbach, and Jens Ricke: "Computer-Aided Diagnosis in Breast DCE-MRI - Quantification of the Heterogeneity of Breast Lesions". In European Journal of Radiology (81:7), p. 1532-1538, 2012.

Sylvia Glaßer, Uli Niemann, Uta Preim, Bernhard Preim, and Myra Spiliopoulou: "Classification of Benign and Malignant DCE-MRI Breast Tumors by Analyzing the Most Suspect Region". In Proc. of Bildverarbeitung für die Medizin (BVM), p. 45-50, 2013.

Sylvia Glaßer, Uli Niemann, Uta Preim, Bernhard Preim, and Myra Spiliopoulou. "Can we Distinguish Between Benign and Malignant Breast Tumors in DCE-MRI by Studying a Tumors Most Suspect Region Only?" In Proc. of IEEE Symposium on Computer-Based Medical Systems (CBMS), p. 59-64, 2013.

Sylvia Glaßer, Sophie Roscher, and Bernhard Preim. "Adapted Spectral Clustering for Evaluation and Classification of DCE-MRI Breast Tumors". In Proc. of Bildverarbeitung für die Medizin (BVM), p. 198-203, 2014.

7 Breast Tumor Analysis for Automatic Classification

In this chapter, the automatic classification of breast tumors in DCE-MRI data is examined with a strong focus on heterogeneity and lesion enhancement kinetics. These approaches are strongly motivated by the high sensitivity for the detection of breast cancer in contrast to the problematic specificity of breast DCE-MRI. The specificity is hampered by overlapping enhancement kinetics of some benign and malignant lesions [Kuhl et al., 1999] as well as ambiguous morphologic features [Wedegärtner et al., 2001]. Therefore, the presented approaches do not only employ features related to the enhancement kinetics, but also measures for the heterogeneity of the feature values. Therefore, additional criteria to distinguish benign and malignant lesions can be found. The heterogeneity of breast tumors is strongly associated with malignancy. This is due to the increased angiogenetic activity of malignant lesions. Especially for very small breast lesions, the heterogeneity has not been examined in detail. In larger malignant lesions, central necrosis might occur and cause heterogeneous contrast enhancement, which can be visually assessed by the clinician. This does not hold for the small lesions due to limited spatial resolution of the MRI scan. Furthermore, small malignant lesions may not develop necrotic areas in an early tumor stage. Nevertheless, they are expected to be more heterogeneous than benign ones, a hypothesis that will be assessed with the classification approaches in this chapter.

For the extraction of features regarding the contrast enhancement kinetics, a group of voxels with similar perfusion characteristics has to be extracted because the contrast enhancement of the individual voxels is noisy by nature. Hence, a major challenge lays in grouping the voxels to homogeneous and spatially contiguous regions. This chapter comprises four different classification approaches. In Section 7.1, the database containing the breast tumor data sets is explained. For the sake of comparability, all four classification approaches were applied to this database. First, the region merging result, embedded in the PerfusionAnalyzer, is employed for automatic classification in Section 7.2. Second, the grouping of regions is extended and different density-based clustering approaches are used, see Section 7.3. Hence, the results of the first approach are integrated such that features with high discriminative power are selected as well as features that proved to be well suited for an automatic classification approach. Inspired by the second classification approach, the third classification approach studies how the formation of regions of similar voxels contributes to distinguishing between benign and malignant tumors, see Section 7.4. Furthermore, an adaption of spectral clustering is presented in Section 7.5, since this classification is well suited to create spatially connected regions. Whereas the first classification approach employs the receiver operating characteristics, the second, third, and fourth classification approaches extend the classification process by learning a decision tree model. The decision tree has the strong advantage of being human-readable and it reveals the most important features, i.e., features that are closer to the root.

Integrated in the classification approaches is the detection of the most suspect part of the tumor. This part is referred to as MSRegion. The identification of the MSRegion does not only play an important role for the feature extraction, it furthermore substitutes the manual and error-prone definition of a ROI by the clinical expert.

At the end of this chapter, the conclusions of the classification approaches with focus on the clinical research on DCE-MRI tumor enhancement kinetics are summarized.

7.1 The Breast Tumor Database 2009

The *Breast Tumor Database 2009* comprises breast DCE-MRI data sets with benign and malignant lesions. The DCE-MRI data were clinically indicated, i.e., a suspicious finding was found with conventional X-ray mammography or the patients suffered from other, breast cancer-related symptoms. The patients gave their informed consent to the MRI exam and to the fact that the data might be used for research purposes. The retrospective study was performed according to the guidelines of the ethics committee. The breast DCE-MRI data sets were enrolled from January 2008 to December 2009.

Table 7.1: *Histology of the lesions of the Breast Tumor Database 2009.*

Histology	Number	%
Invasive ductal carcinoma	15	22.1
Invasive lobular carcinoma	13	19.1
Fibroadenoma (histology: 4, follow up: 6)	10	14.7
Adenosis	6	8.8
Fibrosis	5	7.3
Ductal carcinoma in situ	4	5.9
Invasive ductal / lobular carcinoma	3	4.4
Papilloma	2	2.9
Undifferentiated carcinoma	2	2.9
Breast tissue	2	2.9
Fibrocystic changes	1	1.5
Hemangioma	1	1.5
Lymph node	1	1.5
Inflammation	1	1.5
Benign (follow up)	2	2.9

7.1.1 Patients and Lesions

The *Breast Tumor Database 2009* comprises lesions that were only detected in MRI. Hence, palpable lesions or lesions detected in X-ray mammography or ultrasound were excluded. The database consists of 68 breast tumors, arising from 50 patients with a mean age of 55 years (range: 36 - 73). From these 68 lesions, 31 (45.6%) lesions proved to be benign and 37 (54.4%) to be malignant. The mean diameter was 8 *mm* (range: 4 - 18 *mm*). 60 lesions were confirmed by histopathology of specimens obtained by core needle biopsy. All biopsies were performed under MRI guidance with an MR-compatible fully automatic biopsy gun 100 *mm*, 14G invivo

Germany. Eight lesions with MR-BI-RADS classification three confirmed to be benign by follow up after six to nine months. The histology of all lesions is listed in Table 7.1.

7.1.2 MRI Protocol

The breast DCE-MRIs were performed on a $1.0T$ open MR scanner (Philips Panorama HFO) with a dedicated breast coil (Philips SenseBreast). The imaging sequence was an axial T_1-weighted 3D gradient echo sequence (TR 11, TE 6, flip angle 25 °, voxel size $0.67mm \times 0.67mm$, matrix 528×528, slice thickness 1.5 - 3 mm without gap). Fat suppression was not employed. During and immediately after the bolus injection of contrast agent (0.1 $mmol/kg$ bodyweight), one pre-contrast and four or five post-contrast images were acquired per series with a temporal resolution of ≈ 80 s. The contrast medium (Magnevist, Schering, Germany) was administered using an automated pump (Accutron MR MEDTRON 2007) with a flow of $1ml/s$. 16 of the 50 patients were premenopausal. In this subpopulation, the MR exam was performed in the 2^{nd} week of the menstrual cycle.

7.1.3 Image Interpretation and Data Analysis

The breast DCE-MRIs were evaluated by experienced radiologists. First, the data sets were examined at a commercially available workstation (Philips ViewForum) using subtraction and parameter images in order to detect lesions unknown from ultrasound and X-ray mammography. The radiologists assessed each lesion according to the MR-BI-RADS classification. The morphologic features (shape and margin) were evaluated and the lesion size was recorded. At this time, the histology of the lesions was unknown to the radiologists. For the study, lesions with MR-BI-RADS (recall Table 2.1 at page 18) classification 3 - 5 were included.

7.1.4 Adaption of the 3TP Method

The main advantage of the three-time-point (3TP) method is the quantitative analysis of the relative enhancement (RE) curves instead of the subject and error-prone qualitative evaluation. The 3TP classification is adapted to the data sets to provide a quantitative analysis of the curve shape in the intermediate and late post-contrast phase. In contrast to the study by Degani et al. [1997], the *Breast Tumor Database 2009* exhibits different average total acquisition times of $\approx$ 400 s, since another protocol was applied and the scan times depended on different parameters, e.g., the size of the scanned breast. With this scanning protocol, the early post-contrast phase lasts until the third point in time t_3. In agreement with an experienced radiologist, t'_1 is assigned to the first point in time, t'_2 to t_3 and t'_3 to the last point in time.

7.1.5 Challenges and Limitations

In this breast tumor database, only lesions with follow up or histology were included. However, 8 lesions with the BI-RADS classification 3 had a follow up only after 6-9 months. Due to the retrospective fashion and the limited period of this study, further follow up with MRI or targeted ultrasound was not performed. However, this time frame is not sufficient to downgrade a lesion to BI-RADS 2. According to the BI-RADS lexicon, a time frame of two years or longer is necessary. Furthermore, motion correction was carried out with the combined rigid and elastic registration introduced by Rueckert et al. [1999] and integrated in Me*VisLab*.[1] Motion correction is very important to establish a valid inter-pixel correspondence over time, because breathing, heartbeat, patient movement, and muscle relaxation can occur. Nevertheless, motion correction can also lead to artifacts like blurring and loss of small details. Furthermore, in some cases the motion artifacts cannot be completely removed.

In summary, this database comprises small breast tumors that are only detectable in DCE-MRI, and cannot be classified with conventional mammography. Thus, they are inherently difficult to separate, even for a human expert, since all lesions were suspicious enough to justify biopsy or follow up studies. As a result, typical benign lesions are not part of this database.

7.2 Heterogeneity Analysis Based on Region Merging

In this section, the first classification approach to distinguish between benign and malignant breast tumors is presented. It is based on the methods integrated in the PerfusionAnalyzer and thus employs a classification based on the region merging methods adapted to the *Breast Tumor Database 2009*. The ground hypothesis was that - due to neoangiogenesis - malignant lesions are more heterogeneous than benign lesions, also when the lesion size is so small that necrosis not yet occurred.

This hypothesis arose, since malignant lesions show rim enhancement or heterogeneous enhancement due to necrosis and fibrosis mainly in the tumor center and angiogenetic activity predominantly at the periphery of the tumor [Buadu et al., 1996]. Benign tumors are predominantly more homogeneous [Okafuji et al., 2008] and exhibit a lower vessel density than recurrent invasive breast cancer lesions [Obermair et al., 1994]. Yet, fibroadenomas as well may display a heterogeneous internal enhancement due to mucinous or myxoid degeneration [Kuhl, 2007]. However, such heterogeneous regions are most often found in larger tumors that are already known from mammography and ultrasound and histologically confirmed by ultrasound-guided biopsy. Smaller lesions, depicted only with breast DCE-MRI, show predominantly a homogeneous internal enhancement, when evaluated visually.

Related studies for the breast cancer MRI classification have been presented in Section 4.2, and in the conclusion of Chapter 4. The evaluation of heterogeneity has been identified as important issue (aspect $\boxed{2}$). This issue has been accompanied by three more aspects which are integrated in the following way: the kinetic features (aspect $\boxed{1}$) are employed based on extracted descriptive perfusion parameters (aspect $\boxed{4}$) and the analysis is carried out over the whole lesion ensuring to hold the most malignant tumor part (aspect $\boxed{3}$).

The classification approach in this section is based on the region merging method described in Section 5.4, integrated in the PerfusionAnalyzer. The approach aims at the evaluation of small differences of the perfusion characteristics that are not perceptible in conventional MR images. Hence, it also intends to define a *score*, to provide the radiologist with a parameter combination that automatically determines tumor malignancy.

---

[1] Product of Fraunhofer MEVIS, Bremen; www.mevislab.de (12/08/2013)

To quantify the RE value for each voxel at each point in time, the percentage signal intensity increase was calculated. From the resulting RE curve, the descriptive perfusion parameters washin (the steepness of the ascending curve), washout (the steepness of the descending curve), peak enhancement (the maximum RE value), Integral (the area under the curve) and time to peak (the time when peak enhancement occurs), were extracted. These parameters are substitutes for physiological parameters like tumor perfusion and vessel permeability, recall Section 2.1.2. Without the parameter Integral, these kinetic features have also been employed in the related studies in literature, for example by Hauth et al. [2006b] as well as by Williams et al. [2007].

The voxels were grouped into regions, by applying the region merging method described in Section 5.4. For the first classification approach, a minimum Pearson's correlation of 0.99 was employed and the four-dimensional feature vector $\overrightarrow{v_{4f}}$ was employed. Furthermore, regions must contain at least three voxels according to the recommendation for the optimal ROI setting [Kuhl, 2007]. Smaller regions were neglected, because they are predominantly influenced by noise and artefacts.

7.2.1 Feature Selection

For this first classification method, a combined feature set was employed that covers morphologic features, the descriptive perfusion parameters, numbers of regions, and numbers of 3TP classes. The features are listed in detail in Table 7.2 and 7.3. Hence, Table 7.2 covers the global tumor attributes regarding tumor size, patient age and morphology as well as margin type. Table 7.3 covers the kinetic features extracted for all regions. It must be stated that for this classification approach a multitude of features was employed to detect important features and to achieve initial results about the discriminating power of the features.

Table 7.2: *Features for the first classification approach that include tumor and patient attributes. Margin and boundary classification were based on the MR-BI-RADS protocol.*

General Features		
1	*#Reg*	Number of regions with at least three voxels.
2	*age*	Age of patient.
3	*diameter*	The lesion's size, approximated as maximum slice diameter of the lesion (in *mm*).
4	*quadrant*	Breast quadrant where the tumor is located.
5	*morphology*	The morphology of the tumor.
6	*margin*	Tumor's margin.

Since the first classification approach also aims at identification of a score for an automatic classification, the combination of the descriptive perfusion parameters are included as $\overline{pc_1}$ and $\overline{pc_2}$. Therefore, a principal component analysis (PCA) was carried out over the descriptive perfusion parameters of all tumors of the *Breast Tumor Database 2009*, and the first two principal components were selected.

Table 7.3: *Region-based and kinetic features for the first classification approach. Hence the 3TP classification is employed to classify RE curves based on their washin with* $Washin_{3TP}$ *and based on the curve shape with* $Washout_{3TP}$.

Features for each Region of the Region Merging Result		
1	$\#RegVoxel$	Number of voxels of the region.
2	$Washin_{3TP}$	Rated washin, a value of 1 is assigned to 3TP curves 1-3; a value of 2 to 3TP classes 4-6, and a value of 3 otherwise.
3	$Washout_{3TP}$	Rated washout, a value of 1 is assigned to increasing curves, i.e., 3,6,9; a value of 2 to plateau curves, i.e., 2,5,8; and a value of 3 to washout curves, i.e., 3TP classes 7,4,1.
4	$3TP_{region}$	The 3TP class of the region's average RE curve.
5	$\overline{pc_1}$	The average value of the region's voxels for $\overline{pc_1}$.
6	$\overline{pc_2}$	The average value of the region's voxels for $\overline{pc_2}$.
7	$\#Present_{3TP}$	Number of different 3TP classes existing in the region.
8..16	$Exist_{3TP}(1..9)$	Binary attribute that flags the existence of voxels with 3TP curve 1..9 in the region.
17	$Washout$	The average value for washout.
18	$Integral$	The average value for the parameter integral.
19	PE	The average value for the parameter PE.
20	TTP	The average value for time to peak.
21	$Washin$	The average value for washin.
22	$\sigma Washout$	The standard deviation value for washout.
23	$\sigma Integral$	The standard deviation for the parameter integral.
24	σPE	The standard deviation for the parameter peak enhancement.
25	σTTP	The standard deviation for time to peak.
26	$\sigma Washin$	The standard deviation for washin.
27..31	RE_t	The region's average RE value at time step t, $t = 2..6$

7.2.2 Experimental Settings and Results

The Mann-Whitney U test [Mann and Whitney, 1947] was applied to examine statistically significant differences between benign and malignant lesions considering significance for $p < 0.05$. Receiver operating characteristic (ROC) curve analysis and calculation of the area under the curve (AUC) were performed. The IBM SPSS Statistics software package[2] was employed for statistical analysis.

As a result, malignant lesions showed a significantly higher number of regions $\#Reg$ compared to benign ones (median 17 versus 8, $p = 0.005$), see the feature description in Table 7.2(1). Therefore, malignant lesions were more heterogeneous. With a cut-off of ten regions, sensitivity and specificity were 0.8 and 0.58, respectively. The lesion's diameter of benign and malignant lesions was similar (mean 7.6 *mm* and 7.8 *mm*, respectively), see Table 7.2(3). The analysis of the 3TP classes revealed significant differences between the groups as well. Malignant lesions had more present 3TP classes, i.e., a higher value for $\#Present_{3TP}$, compared to benign lesions (mean 6.2 versus 5.3, $p = 0.007$), see Table 7.3(7). Hence, the malignant

---

[2] Product of IBM, New York, USA; http://www-01.ibm.com/software/analytics/spss/ (12/08/2013)

lesions also turned out to be more heterogeneous. With a cut-off of five different 3TP classes existing, sensitivity and specificity were 0.78 and 0.45, respectively.

The perfusion parameters (peak enhancement, wash-in, wash-out, integral, and time to peak) revealed no significant differences between the groups, listed in Table 7.3(17)-(26). The 3TP class 7 (Tab. 7.3(14)), i.e., strong early enhancement and following washout, occurred significantly more often in malignant lesions (18/37) than in benign ones (14/31). The p-Value and AUC were 0.04 and 0.57, respectively. The sensitivity was determined to be 1.0, but the specificity was very poor (0.13). In Figure 7.1(a) and (b), the ROC curves for the features *#Reg* and $\#Present_{3TP}$ are depicted. Figure 7.1(c) demonstrates the box plots of the number of regions *#Reg* of benign and malignant lesions. Median, mean, standard deviation, and p-values are displayed in Table 7.4. AUC values, sensitivity and specificity of selected cut-offs can be seen in Table 7.5.

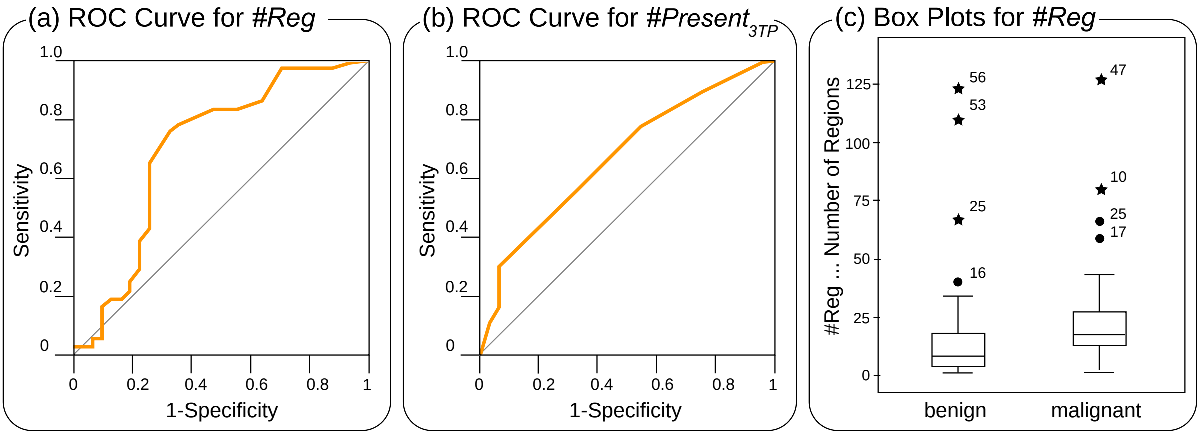

Figure 7.1: *Depiction of the ROC curves for the feature #Reg in (a), and* $\#Present_{3TP}$ *in (b). In (c), the box plots for benign and malignant lesions and #Reg is depicted. (Image adapted and reprinted from [Preim et al., 2012] © 2012, Elsevier, with kind permission from Elsevier.)*

Table 7.4: *Median, mean, standard deviation* σ*, and* p *(U-test). The RE value at the third time point* $RE(t_3)$*, Washin, Washout, Integral, and TTP values are average values for the most suspect region.*

	Benign			Malignant			p
	Median	Mean	σ	Median	Mean	σ	
age	61	57.5	10.5	54	53.7	8.3	0.032
diameter	6	7.6	2.9	7	7.8	2.4	0.37
MR-BI-RADS	4	3.7	0.5	4	4.4	0.5	< 0.001
#Reg	8	19.6	29.5	17	25.3	24.3	0.005
$\#Present_{3TP}$	6	5.3	1.4	6	6.2	1.4	0.007
RE_3	245.3	330.7	265.5	242.8	251.3	92.4	0.3
Washin	120	152.3	125	117	121.7	48.3	0.6
Washout	−8.9	−8.5	25.3	−8.7	−9.4	12.7	0.95
Integral	788.8	974.2	695	805.5	820.3	363.7	0.8
TTP	3.2	3.7	1	3.2	3.5	0.56	0.8

Despite the exclusive evaluation of lesions $< 2cm$, shape and margin were significantly different. Malignant lesions showed more often an irregular shape 22/37 (59.5 %), but rarely

Table 7.5: *AUC, sensitivity, and specificity for the significant parameters.*

	AUC	Cutoff	Sensitivity	Specificity
$\#Reg$	0.7	10	0.8	0.58
$\#Present_{3TP}$	0.68	5	0.78	0.45
$Exist_{3TP}(7)$	0.57	n.a.[a]	1.0	0.13

[a] Not applicable.

a round 6/37 (16.2 %), oval 8/37 (21.6 %), or lobulated 1/37 (2.7 %) shape. Benign lesions were more often characterized by a round shape 17/31 (54.8 %), but rarely by an irregular 6/31 (19.4 %), oval 4/31 (12.9%), or lobulated shape 4/31(12.9 %). The difference was highly significant ($p < 0.001$). The margin showed significant differences as well ($p = 0.007$). Malignant lesions showed more often a blurred margin 25/37 (67.6 %) and rarely a well-defined margin 12/37 (32.4 %). Benign lesions displayed more often a well-defined margin 21/31 (67.7 %) and rarely a blurred margin 10/31(32.3 %). The detailed histology of the lesions can be found in Table 7.1 at the beginning of this chapter.

Diagnostic criteria in breast DCE-MRI include assessment of morphological features like shape, margin and heterogeneity (internal architecture) as well as analysis of time-intensity curves. Heterogeneity is known to be a feature of malignant tumors because larger tumors develop necrotic areas [Wedegärtner et al., 2001]. Those necrotic areas can be estimated visually. However, in small lesions without apparent necrosis the visual analysis may not be sufficient. For that purpose, the region merging-based classification allows for a novel assessment of heterogeneity for this specific data sets, i.e., small enhancing lesions only detectable in DCE-MRI. Furthermore, it enables the analysis of the whole lesion. In the *Breast Tumor Database 2009*, the number of regions as well as the number of 3TP classes showed significant differences between benign and malignant lesions. Therefore, malignant lesions turned out to be more heterogeneous than benign ones. The region analysis revealed better results compared to the analysis of the 3TP classes. The reason could be that the 3TP classification has only nine classes, whereas the region analysis has much more regions and is thus more sophisticated.

Examples for a benign and a malignant lesion are given in Figures 7.2 and 7.3. The regions were color-coded and displayed in region images embedded in the PerfusionAnalyzer. Figure 7.2 shows images of a 63-year-old woman who underwent mastectomy of the right breast. Breast DCE-MRI revealed another lesion of the left breast. The lesion of 6 *mm* with oval shape and sharp margin was classified as MR-BI-RADS 3. 3TP classes 4, 5, 7, and 8 occurred. The lesion contained 3 regions suggesting homogeneity of a benign lesion. In follow up MRIs, the lesion did not change and was considered to be a fibroadenoma. Figure 7.3 shows images of a 45-year old woman with newly diagnosed breast cancer. Breast DCE-MRI revealed an additional lesion of 6 *mm* in a distance of 2 *cm* to the known tumor. The lesion had an irregular shape and blurred margin and was classified as MR-BI-RADS 4. 3TP classes 4-9 occurred indicating suspect strong enhancement and following wash-out. The lesion contained 41 regions, suggesting suspect heterogeneity. Histology revealed ductal carcinoma in situ, i.e., malignancy.

Several studies showed that the heterogeneity can be a helpful parameter, recall Section 4.2. This first classification approach is important, since the heterogeneity analysis is missing in current commercially available workstations. The presented first classification approach combines five single descriptive perfusion parameters as well as takes the whole lesion into account. Hence, the analysis of the heterogeneity provided better results compared to the eval-

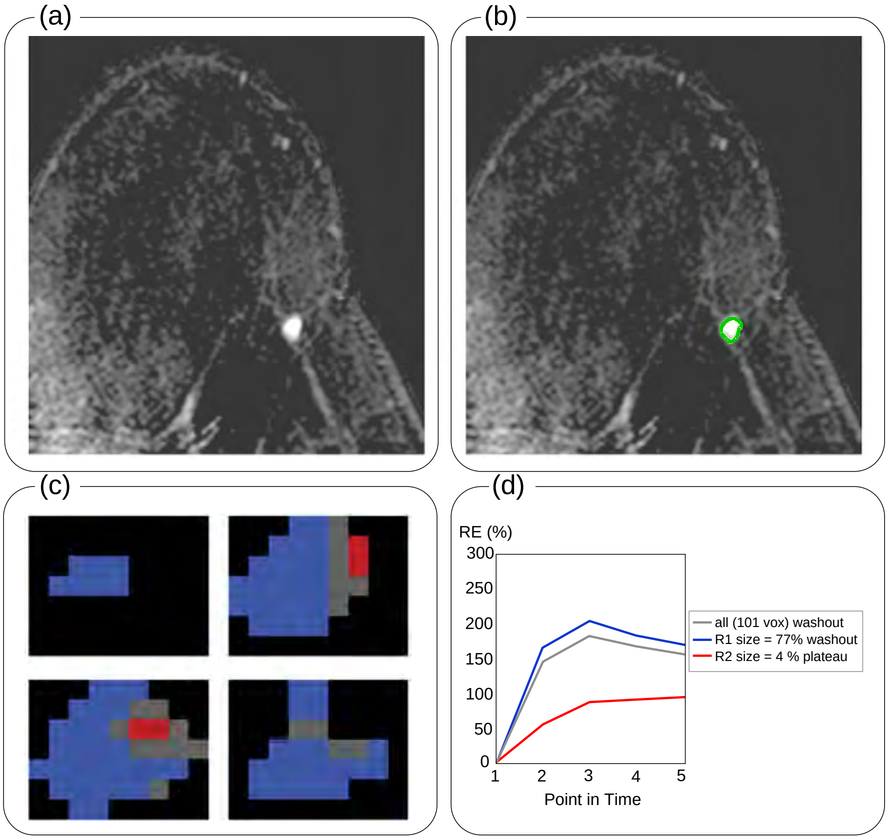

Figure 7.2: *Benign lesion, (a) subtraction image, (b) segmented subtraction image, (c) region image, (d) RE curve view (image adapted and reprinted from [Preim et al., 2012] © 2012, Elsevier, with kind permission from Elsevier). The images show a lesion of 6 mm with oval shape and sharp margin, which was classified as MR-BI-RADS 3. 3TP classes 4, 5, 7, and 8 occurred. The lesion contained 3 regions suggesting homogeneity of a benign lesion. In follow up MRIs, the lesion did not change and was considered to be a fibroadenoma. (Medical image data is courtesy of U. Preim, Municipal Hospital Magdeburg, Germany.)*

uation of the enhancement kinetics. The results indicate that the evaluation of heterogeneity is more robust and reliable. Another advantage of the region merging approach is that manual ROI setting can be avoided. Although commercially available software tools can guide manual ROI setting, they cannot avoid or replace it. Since the regions consist of voxels with similar perfusion parameters, partial volume averaging due to adjacent necrotic tissue or normal tissue is prevented. Early strong contrast enhancement and following wash-out were not capable to predict dignity. Although the 3TP class 7 (early strong contrast enhancement and following wash-out) revealed significant differences between the groups with a sensitivity of 1.0, the specificity was very poor (0.13). This is in contrast to other studies [Kuhl et al., 1999, Schnall et al., 2006, Hauth et al., 2008]. Also, the reported sensitivity and specificity rates for the Göttinger score (recall Sect. 4.2.2) could not be achieved. However, a study of Williams et al. [2007] also failed to show significant differences between benign and malignant lesions.

The results of this classification approach are influenced by a long acquisition time and poor temporal resolution of the MRI data. Furthermore, the *Breast Tumor Database 2009* mainly consists of lesions with histology confirmed by biopsy. That means the included lesions were suspicious enough to justify a biopsy. Thus, typical benign lesions were not included. Another possible reason is, that with computer aided detection and a 3D analysis voxels with suspect

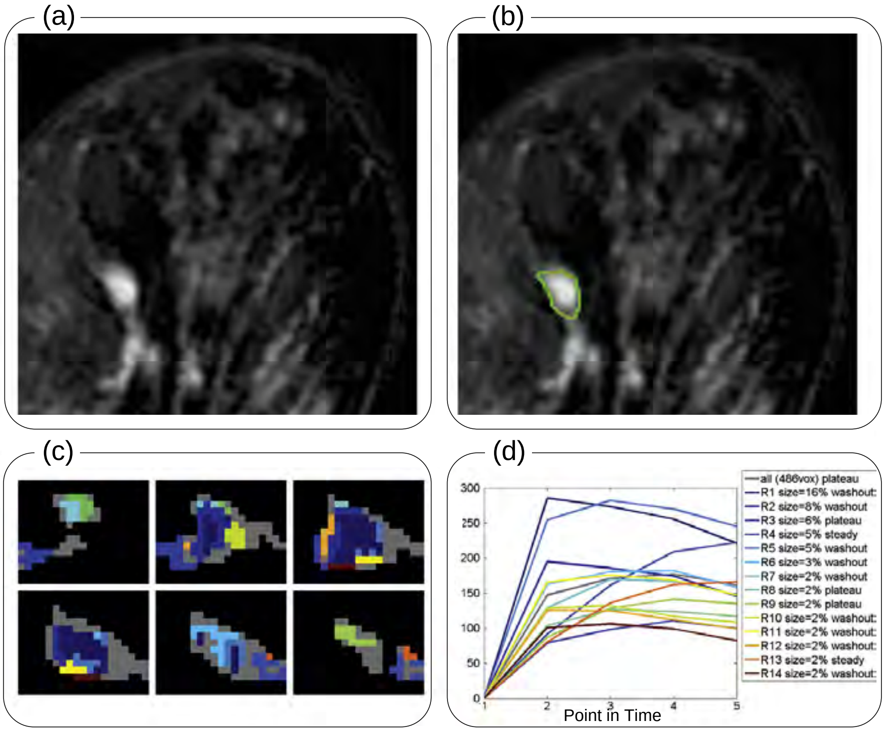

Figure 7.3: *Malignant lesion, (a) subtraction image, (b) segmented subtraction image, (c) region image, (d) RE curve view (image adapted and reprinted from [Preim et al., 2012] © 2012, Elsevier, with kind permission from Elsevier). The images display an additional lesion of 6 mm in a distance of 2 cm to a known breast cancer. The lesion had an irregular shape and blurred margin and was classified as MR-BI-RADS 4. 3TP classes 4 - 9 occurred indicating suspect strong enhancement and following washout. The lesion contained 41 regions, suggesting suspect heterogeneity. Histology revealed ductal carcinoma in situ. (Medical image data is courtesy of U. Preim, Municipal Hospital Magdeburg, Germany.)*

curves are detected without fail. These curves could have been missed with the manual ROI placement.

7.2.3 Findings of the Region Merging-Based Classification

In conclusion, the 3D quantification of the heterogeneity of small lesions detected in breast DCE-MRI showed significant differences between benign and malignant lesions. The analysis of heterogeneity was superior to the analysis of single perfusion parameters and enhancement curve types. Therefore, despite of an overlap of the number of regions in benign and malignant lesions, the quantification of the heterogeneity can be a helpful method in differential diagnosis and should be further evaluated.

Based on the first results, indicating the opportunity of heterogeneity, two more classification approaches are carried out with a strong focus on heterogeneity based on kinetic features. Since margin and shape evaluation of tumors suffer from inter- and intra-observer variability (as reported in [Wedegärtner et al., 2001]), these features are not further investigated. The study by Sinha et al. [1997] reported better discriminative power for boundary features in comparison to kinetic features and texture features. However, even with pre-defined choices via a standard terminology, a considerable variability of morphologic features for breast tumor

DCE-MRI description was reported by Stoutjesdijk et al. [2005]. This is also expressed by aspect $\boxed{5}$ of Chapter 4. Thus, the following classification approaches yield a more general data analysis, which is also more independent of the manual evaluation by the clinical expert.

7.3 The Second Classification Approach Integrating Density-Based Clustering

Despite the promising results of the clinical analysis of the first classification approach, the classification of breast tumors solely based on DCE-MRI is a challenge in clinical research. Therefore, the second classification approach, described in this section, focuses on distinguishing between benign and malignant tumors based on kinetic features as well as considering the tumor's heterogeneity.

Since the RE curves of the individual voxels are noisy by nature, a major challenge lays in grouping them to homogeneous and spatially contiguous regions. Thus, the extraction of the MSRegion is improved. Voxels are grouped via three density-based clustering techniques that have been adapted to partition a breast tumor into clusters. The MSRegion is chosen to bet the most suspect cluster or region delivered by the most stable clustering algorithm. The presented classification approach combines extracted features of the MSRegion as well as the tumor and yields predictive tumor characteristics that hold for multiple tumors.

At the end of this section, preliminary results are listed that show that the classifier separates between benign and malignant tumors and returns predictive attributes that are intuitive to the clinical expert.

7.3.1 Adaption of Density-Based Clustering

In this section, the adaption of density-based clustering techniques is described. The RE plotted over time yields RE curves. Similar to the first classification approach, the descriptive perfusion parameters washin, washout, peak enhancement, integral, and time to peak are extracted. Since peak enhancement and integral strongly correlate, peak enhancement is excluded from the feature space that forms the basis for density based clustering.

The following density-based clustering algorithms were adapted to breast tumor perfusion MRI:

- the *Density-based Spatial Clustering of Applications with Noise* (DBSCAN) algorithm presented by [Ester et al., 1996],
- the *Density-Connected Subspace Clustering* (SUBCLU) algorithm introduced by [Kailing et al., 2004], and
- the *Ordering Points to Identify the Clustering Structure* (OPTICS) presented by [Ankerst et al., 1999].

The algorithms separate objects into clusters based on estimated density distributions and were described in more detail in Section 3.3.

These density-based clustering algorithms yield clusters with arbitrary shapes, instead of restricting the cluster shape to convex objects. This is very advantageous for irregular and heterogeneous tumor parts. Objects that do not feature similar objects (i.e., objects with similar parameters) in a given neighborhood are marked as outliers. That is a further advantage, since outliers may be caused by a missing inter-voxel-correspondence over time due to motion artifacts. Based on these two advantages, density-based clustering approaches are well suited for breast tumor perfusion clustering.

Each voxel of a tumor is interpreted as a data *object* and the descriptive perfusion parameters are employed as *attributes*. Each of the three algorithms requires two parameters: the minimum number of points to build a cluster *MinPoints* and the maximum radius ε defining the neighborhood of a point. Since no automatic generation of *MinPoints* was available, *MinPoints* is empirically set to 4, 6, and 8. The calculation of ε depends on the clustering algorithm. All clustering algorithms were implemented in MATLAB.[3]

Adaption of DBSCAN. For the DBSCAN algorithm and each *MinPoints* value $\in \{4,6,8\}$, ε was automatically determined as suggested in [Daszykowski et al., 2001]. Hence, an artificial data set is generated based on the original data. The artificial data set exhibits the same dimensionality in the feature space, but a uniform distribution (within the original data's range). Then, the k-distance is extracted for each of the artificial objects. The k-distance is the distance from an object to its k nearest neighbors. When setting k = *MinPoints*, then each artificial object's k-distance is sorted, an ε is assigned to the 95% quantile of all sorted k-distances.

Adaption of SUBCLU. For SUBCLU, ε was extracted from the k-distances graph that maps the k-distance of an object to its k next neighbors [Ester et al., 1996]. Thus, objects that form clusters, exhibit smaller values for k-distance than outliers. In the k-distances graphs, the k-distances are sorted, i.e., the object with the smallest k-distance is mapped first. The best-suited ε can be found where the k-distance graph has an increasing slope, see in Figure 7.4. Thus for each *MinPoints* value, a k-distance graph was created (with k = *MinPoints*) for all four perfusion parameter sets. The ε value is automatically determined by choosing the point with the largest distance perpendicular to a line g connecting the first and the last point of the graph (see Fig. 7.4). This approach was well suited for the employed database. However, for a more general approximation for ε, the L-method by Salvador and Chan [2004] can be employed. It detects the knee in a graph and achieved similar results for the *Breast Tumor Database 2009*.

After extracting four values for each descriptive perfusion parameter, ε was assigned to the mean. Since the SUBCLU algorithm analyzes subspaces of the data, the ε values were estimated based on the one-dimensional perfusion parameter sets. The ε approximation based on the k-distances graph was empirically tested, and yielded better results for the SUBCLU algorithm than the ε approximation employed for the adapted DBSCAN.

Adaption of OPTICS. For OPTICS, ε was empirically set to 0.5 and 0.75 for the first classification approach. For a more expanded analysis, the OPTICS parameter choice was refined, which will be explained in more detail in Section 7.4.1.

---

[3] Product of the MathWorks, Natick, USA; www.mathworks.de/products/matlab/ (12/08/2013)

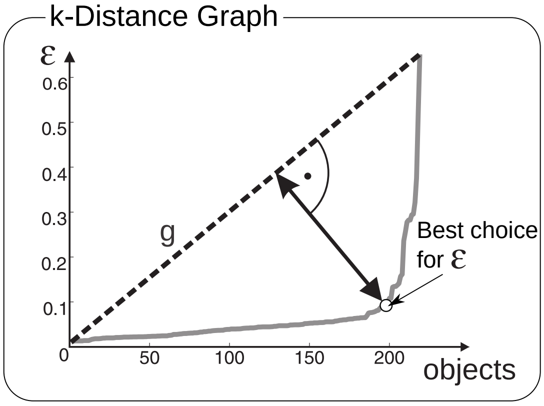

Figure 7.4: Determination of ε: for an example data set (a small breast tumor with ≈ 220 voxels) the k-distances graph for a MinPoints value equal to 4 was extracted (image adapted and reprinted from [Glaßer et al., 2013b] © 2013, Springer-Verlag, with kind permission from Springer Science and Business Media). The graph maps the distance of an object to its k next neighbors (with k = MinPoints). A well suited ε can be detected at a position with increased slope, i.e., the point with a maximum distance perpendicular to g. Objects with a k-distance ≤ ε will be assigned to clusters, otherwise they are classified as noise.

7.3.2 Extraction of the MSRegion

The actual classification approach strongly focuses on the most suspect tumor part, i.e., the MSRegion. The MSRegion is extracted via density-based clustering over the descriptive perfusion parameters, taking also the 3TP classification in account, see Figure 7.5.

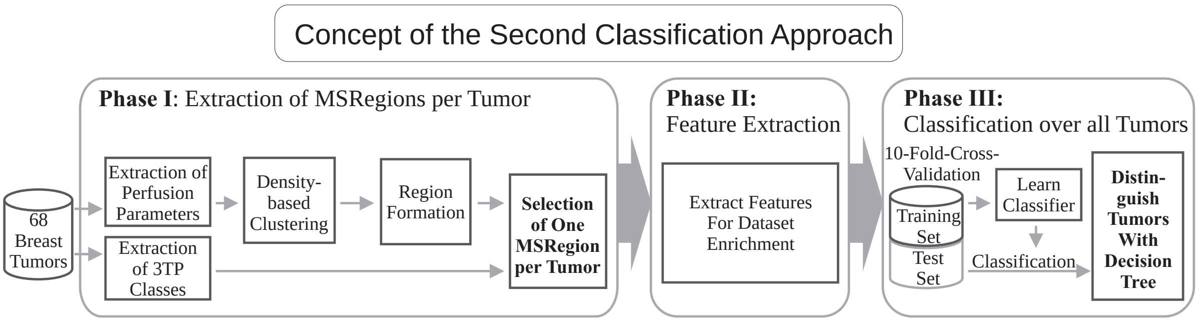

Figure 7.5: Schematic overview of the second classification approach. First, each tumor's MSRegion is extracted from the density-based clustering results. Second, a classifier is learned to predict malignancy.

With *MinPoints* $\in \{4,6,8\}$, and the parameter choices described in the previous Section 7.3.1, twelve clustering results per data set are obtained: three configurations for DBSCAN and SUBCLU and six configurations for OPTICS. Connected component analysis is applied to the clustering results such that a cluster that contains spatially not connected groups is split into these groups yielding only spatially connected voxels per region.

To select the MSRegion, the clustering with the least outliers is chosen. Next, all regions that contain less than three voxels are rejected. From the remaining regions, the largest region with an average RE curve of 3TP class 7 is declared as MSRegion. If no such region exists, a search is carried out for the biggest region with average RE curve 3TP class 9, 8, 4, 6, 5, 1, 3, 2 in that order. Although this is a user-defined ranking, this empirical ranking worked well for all tested data sets and is furthermore based on definitions of the most malignant tumor enhancement kinetics: a present washout in combination with a strong washin.

7.3.3 Feature Selection Including Purity, Jaccard Coefficient and F_1 score

For the classification step of the second classification approach, a number of features is extracted. The selection of features is based on the results of the first classification approach. Thus, features describing the boundary of the tumor are excluded and the focus is set on kinetic and heterogeneity-based features. Similar to the first classification approach, patient's age and lesion size is kept. In contrast to the first approach, the tumor size is automatically extracted as 3D volume in mm^3.

Hence, data enrichment is carried out by including attributes of the tumor and its MSRegion. To strengthen the influence of the tumor's heterogeneity

- the purity P,
- the Jaccard coefficient J, and
- the F_1 score

are employed as heterogeneity measurements. The approximation of P, J, and F_1 are explained in the following. As a result, all employed features are listed in Table 7.6.

To extract the heterogeneity measurements, the clustering result is compared with the 3TP classes yielding a supervised evaluation method. The three criteria will be described in more detail in the following. Hence, the term *class* is employed for a group of voxels that belong to the same 3TP class, i.e., which exhibit RE curves with the same 3TP class. The term *region* is employed for a group of spatially connected voxels that were derived from the density-based clustering result. The measurements P, F_1, and J are employed as external validation indices, since their values are based on the extra knowledge about the data, i.e., the 3TP classes.

The Jaccard coefficient J. The value for the Jaccard coefficient (J) can be determined by:

$$J = \frac{f_{11}}{f_{01} + f_{10} + f_{11}}, \tag{7.1}$$

where f_{01} denotes the number of pairs of voxels of different classes but the same region, f_{10} denotes the number of pairs of voxels of the same class but different regions, and f_{11} denotes the number of pairs of voxels of the same class and the same region. The value of J lies in the interval $[0, 1]$. Higher values indicating a better result, i.e., a higher match of 3TP classes and clustering result.

Table 7.6: *Features for the second classification approach.*

Features of MSRegion		
1	$TumorSize$	size (in mm^3).
2	$\#RegVoxel$	Number of voxels of the MSRegion.
3	$RelRegSize$	The percentaged MSRegion size (with respect to the tumor size).
4..6	P, J, $F1$	The value for P, J, and $F1$ based on the 3TP class division and the clustering result.
7..9	$P_{outlier}$, $J_{outlier}$, $F1_{outlier}$	The value for P, J, and F_1 based on the 3TP class division and the group of all outliers of the chosen clustering.
10..14	RE_t	The MSRegion average RE value at time step t, t = 2..6
15	$Integral$	The average value for the parameter integral.
16	$Washin$	The average value for washin.
17	$Washout$	The average value for washout.
18	TTP	The average value for time to peak.
19	$3TP_{region}$	The 3TP class of the MSRegion's average RE curve.
20..28	$\#Voxels_{3TP(1..9)}$	Number of MSRegion voxels that have a 3TP curve 1..9.
29	$\#Present_{3TP}$	Number of different 3TP classes existing in the MSRegion.
30	$Majority_{3TP}$	3TP class with the most voxels in the region.
31..33	$P_{MSRegion}$, $J_{MSRegion}$, $F1_{MSRegion}$	The value P, J, and $F1$ based on the 3TP class division and the MSRegion.
34	$\#R_{3TP(7)}$	The number of regions with an average RE curve classified as 3TP class 7.
35	age	Age of patient.

The F_1 score. The value for the F_1 score (also called F - measure) is based on the values precision and recall:

$$\begin{aligned} F_1 &= \frac{2 \cdot precision \cdot recall}{precision + recall}, \text{ and} && (7.2)\\ precision &= \frac{f_{11}}{f_{11} + f_{10}}, \text{ with} && (7.3)\\ recall &= \frac{f_{11}}{f_{11} + f_{01}}. && (7.4) \end{aligned}$$

Likewise to the domain of J, the values of F_1 lie in the interval $[0,1]$ and values equal to 1 are the best possible result.

The Purity P. The purity P approximates the amount of pairs of voxels of a region that belong to the same class. Hence, p_{ij} denotes the probability that a voxel of region i exhibits the 3TP class j:

$$p_{ij} = \frac{m_{ij}}{m_i}, \tag{7.5}$$

where m_i is the number of voxels in region i and m_{ij} is the number of voxels in region i that have the 3TP class j. Next, the purity p_i for region i is extracted by choosing the highest value of p_{ij}, i.e., over all 3TP classes j and employed to extract P:

$$p_i = \max_j p_{ij}, \text{ and} \tag{7.6}$$

$$P = \sum_{i=1}^{K} \frac{m_i}{m} p_i, \tag{7.7}$$

where m is the number of voxels of all regions, i.e., the whole tumor. A P value equal to 1 means that for each cluster of a clustering result, all voxels exhibit the same 3TP class. Features covering the values for P, F_1, and J are employed for the further classification step.

As it can be interfered from Table 7.6, the value for P, J, and $F1$ are extracted based on the comparison between:

- the whole clustering result and the 3TP classification of the tumor, see Table 7.6(4) - (6),
- the group of outliers and the 3TP classification of the voxels belonging to this group, see Table 7.6(7) - (9),
- the MSRegion and the 3TP classes of the MSRegion's voxels, see Table 7.6(31) - (33).

7.3.4 Experimental Settings and Results

In contrast to the first classification approach, where ROC and AUC analysis was employed (recall Sect. 7.2), for the following classification approaches a decision tree is created. The decision tree is a supervised learning method, i.e., a model that is employed for classification. Each tumor of the *Breast Tumor Database 2009* forms an item, the extracted features are the attribute values and the class label is extracted by the report. Then, the decision tree model is constructed from the study by dividing the database into training and test set. The decision tree classifier has the strong advantage of being human-readable. Furthermore, it reveals the most important features, i.e., features that are closer to the root. Thus, it allows for identification of features with high discriminative power for clinical practice. Decision trees are very similar to diagnostic algorithms medical physicists and in particular radiologists are familiar with since they are frequent parts of medical publications and guidelines. The decision tree is usually visualized as node-link diagram and each internal node represents a test on a feature (e.g., a feature of Tab. 7.6). The test results are represented via the links between the nodes. Finally, each leaf node contains a class label.

For the presented approach, the J4.8 classification algorithm was employed to learn a decision tree classifier. The J4.8 algorithm is based on the C4. 5 decision tree classification [Quinlan, 1993] and integrated in the *Waikato Environment for Knowledge Analysis* (Weka) library - a Java software library that encompasses algorithms for data analysis and predictive modeling [Holmes et al., 1994]. It performs 10-fold or 5-fold cross validation and requires at least two instances (two tumors) for each tree leaf. Cross validation means that for a k-fold cross validation the database is splitted into k equally-sized partitions [Tan et al., 2006]. Then, k runs are carried out. During each run, one of the partitions is employed for testing, and the remaining ones are used for training. The total error of the k-fold cross validation is extracted by summing up the error for each run.

As a result, the second classifier was obtained, see Figure 7.6. Hence, the decision tree is presented as node-link diagram. A test (or a range of values) is assigned to each internal node where the links represent the test value. The leaf nodes contains the class labels, i.e., benign and malignant.

The C4. 5 decision tree classifier [Quinlan, 1993] employs 18 of the original ca. 40 features. The evaluation criterion is the number of *Correctly Classified Instances* (*#CCI*). The best decision tree employs eight features only, namely the features (5), (8), (12), (17), (25), (28), (30), and (35) of Table 7.6. It yields a *#CCI* of 46 of the 68 (67.65%) lesions. 22 (32,35%) instances were classified incorrectly. The true positive (TP) and false positive (FP) rate are:

- for benign tumors: TP = 0.548 and FP = 0.216, and
- for malignant tumors: TP = 0.784 and FP = 0.452.

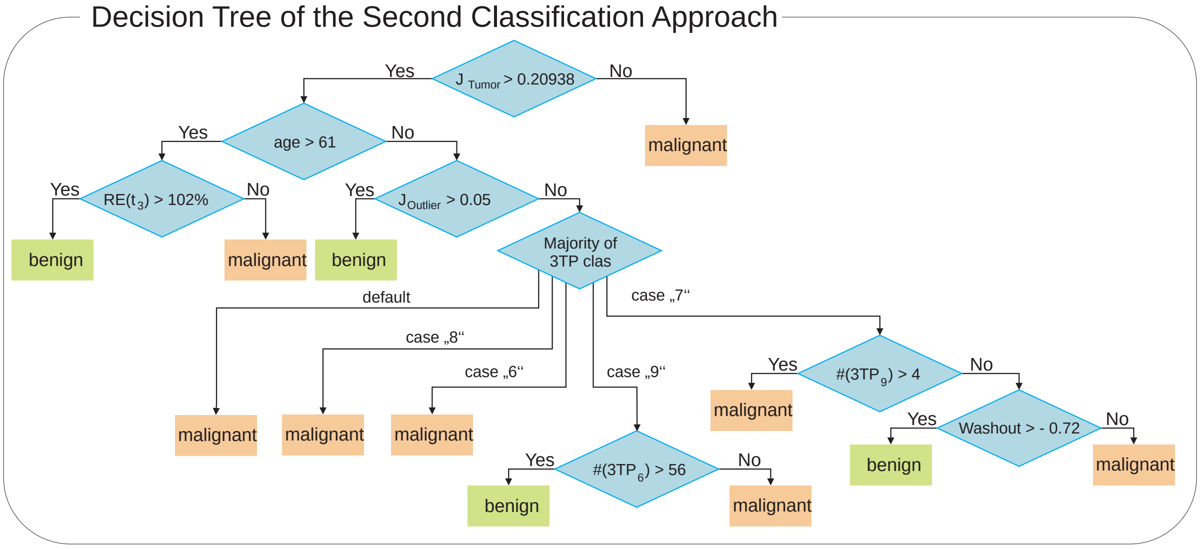

Figure 7.6: *Learned decision tree: the attributes at the upper part of the tree, i.e., close to the root, are the most important ones since they influence the classification of more objects than attributes at the lower part.*

Features closer to the root of the tree are more important than those at lower levels, because the former help in splitting a larger set of tumors. Very important is the fact that the most important attributes are the heterogeneity of the tumor, represented by J_{Tumor} and $J_{Outlier}$, and the age of the patient. The most prominent 3TP class, the number of voxels in the 3TP class 9 ($\#(3TP_9)$) and 6 ($\#(3TP_6)$), the contrast agent washin ($RE(t_3)$), and washout are also important.

7.3.5 Findings of the Density-Based Classification

In the presented classification approach, a novel combination of within-tumor clustering and tumor classification to predict tumor malignancy was carried out yielding preliminary results on the *Breast Tumor Database 2009* with 68 breast tumors. These first results indicate that the identification of the most suspect region or tumor part with clustering and the exploitation of this region's features in classification are promising steps in tumor separation. The focus of the second classification approach was the kinetic features of the tumor.

The low sensitivity of the results must be attributed to the specific tumor type, for which it is difficult to distinguish between benignity and malignancy. The next step examines how features of clusters derived from different clustering algorithms affect the discriminative power of a classifier.

7.4 The Third Classification Approach Including Ensembles

Since the intermediate results indicate a relationship between tumor heterogeneity in terms of contrast enhancement kinetics and malignancy, this work is extended by learning classifiers on different sets of derived features. This means, it is analyzed how the formation of regions of similar voxels contributes to distinguishing between benign and malignant tumors. Hence, the focus is set on features of an MSRegion found through clustering, rather than the features of all clusters, i.e., the whole lesion. This classification approach aims at answering the research question: *Is it feasible to automatically assess tumor malignancy by identifying and characterizing the tumor's most suspect (i.e., malignant) region?*

As expected, such an approach would be sensitive to the (clustering) algorithm that forms the regions. Therefore, not only the density-based clustering algorithms were employed, but also different MSRegions were extracted. Thus, it is possible to study how the formation of regions of similar voxels contributes to distinguishing between benign and malignant tumors. The MSRegions' features are employed to train different classifiers and combine them into ensembles. The different kind of classifiers exploit different combinations of features for learning. As a result, features are determined that contribute to the classification and should therefore be considered in clinical practice. To make the results comparable, the same database, i.e., the *Breast Tumor Database 2009* is employed (recall Sect. 7.1). In Figure 7.7, the three phases of the extended classification approach are illustrated.

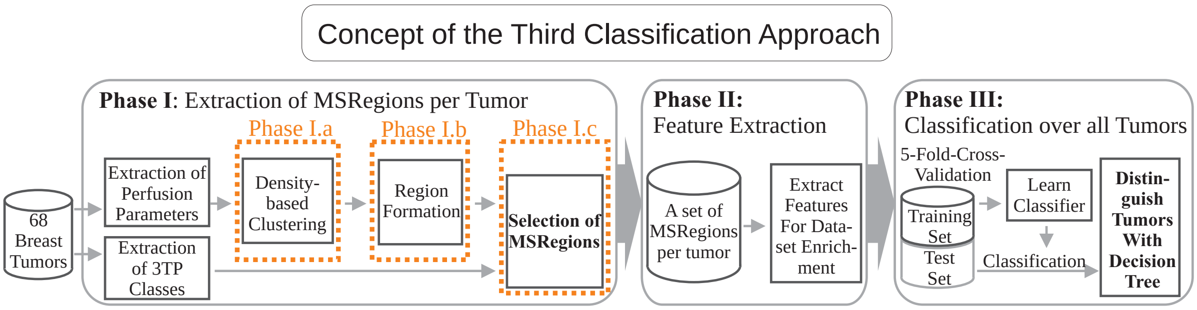

Figure 7.7: *Schematic overview of the presented approach (image adapted and reprinted from Glaßer et al. [2013a] © IEEE 2013 with kind permission from IEEE). In phase I, several clustering runs are carried out (I.a) to form regions (I.b), of whom the MSRegions were selected (I.c). Second, for each MSRegion features were extracted for data enrichment (II). In phase III, learners over the set of all tumors and their MSRegions are trained.*

In phase I, several clustering runs employing density-based clustering algorithms with different parameter settings are performed. For each run, voxels that exhibit similar perfusion characteristics are grouped into clusters (I.a). Then, clusters with spatially non-connected parts are split into spatially connected regions (I.b). Finally, the MSRegion per clustering type is selected (I.c). This step will be described in Section 7.4.1.

In phase II, a set of features that reflect the homogeneity of the region is extracted. Informally, a region is homogeneous if all its voxels exhibit the same washin / washout behavior. Hence, a region consisting only of 3TP class 8 voxels is more homogeneous than one with voxels from 3TP classes 7 and 8. The extraction of this feature set will be described in Section 7.4.2.

In phase III, classifiers are trained on subsets of the features extracted from the data in phase II. Since phase I delivers one MSRegion per clustering run on the same tumor, the classifiers are combined and each of them considers the MSRegion of a different clustering run and predicts tumor malignancy (the label). A combination of such classifiers is an *ensemble*, which collectively decides on the label of a tumor by majority voting; each ensemble member has one vote. The classifier specification will be provided in Section 7.4.3.

7.4.1 Extended Extraction of MSRegions

For the subsequently applied tumor classification, a set of MSRegions is extracted and the classification features are derived from this set later on. The adaption of density-based clustering is almost identical to the previous approach. The segmentation of the voxels belonging to the breast tumor was carried out with the PerfusionAnalyzer. Next, the four descriptive perfusion parameters washin, washout, time to peak, and integral were extracted. As it was reported in Section 7.3.1, values for peak enhancement and integral were correlating. For autoscaling, z-scoring was applied, which was described in Section 3.4.2. The DBSCAN algorithm and the SUBCLU algorithm were adapted as described in Section 7.3.1. However, for OPTICS, more parameter choices were employed. Hence, ε was experimentally determined by successively applying 20 potential ε values (in the range from 0.05 to 2) to the clustering algorithm. If a OPTICS run for one of the 20 values showed the best result compared to the 19 other ones, the score of this ε value was incremented. To assess the quality of a run, the sums of weighted values for Jaccard coefficient, F_1 score and Purity were computed based on the actual clustering and the 3TP division. Then, the two best ε values were picked.

Again, with $MinPoints \in \{4, 6, 8\}$, twelve configuration for clustering algorithms are obtained: three configurations for DBSCAN and SUBCLU and six configurations for OPTICS. Also, clusters that cover spatially not connected voxels (w.r.t. an 18 neighborhood) are split into different groups of spatially connected voxels.

Next, for each clustering algorithm type (i.e., DBSCAN, SUBCLU, and OPTICS), the best clustering result is selected by choosing the clustering result with the least outliers. Thus, the three best clustering runs A_{DB}, A_{SC}, and A_{OP} are obtained. From the results of A_{DB}, A_{SC}, and A_{OP}, all regions that contain less than three voxels are rejected. From the remaining regions, the largest region with an average RE curve of 3TP class 7 is chosen. If no such region exists, a search for the 3TP class 9, 8, 4, 6, 5, 1, 3, and 2 in that order, is performed. Although this is a user-defined ranking, this empirical ranking is based on definitions of the most malignant tumor enhancement kinetics: a present washout in combination with a strong washin. Thus, for each tumor and each clustering type (i.e., for A_{DB}, A_{SC}, and A_{OP}) the three most suspect regions MSRegion$_{DB}$, MSRegion$_{SC}$, and MSRegion$_{OP}$ are extracted.

7.4.2 Extended Feature Selection

The complete feature space describing a patient's tumor is based on the actual MSRegion and the tumor attributes. Hence, the following sets of features are obtained:

- the features concerning the MSRegion's size for each of the clusterings A_{DB}, A_{SC}, and A_{OP} (listed in Tab. 7.7),
- the features concerning homogeneity of these clusterings (listed in Tab. 7.8), and
- the features on washin and washout behavior based on the MSRegion and the corresponding clustering (listed in Tab. 7.10) as well as
- features associated with the whole tumor (listed in Tab. 7.9).

Table 7.7: *Features of the MSRegion of a clustering; these features reflect the region size.*

General features of MSRegion		
1	*#RegVoxel*	Number of voxels of the MSRegion for a given clustering.
2	*RelRegSize*	The percentaged region size (with respect to the tumor size).

Table 7.8: *Homogeneity features over the regions of a clustering.*

Features on Homogeneity and 3TP Class		
1	P	Purity value based on the comparison of the 3TP class division and a given clustering.
2	J	Jaccard coefficient based on the 3TP class division and a given clustering.
3	$F1$	F1-score value based on the 3TP class division and a given clustering.
4	$\#R_{3TP(7)}$	The number of regions with an average RE curve classified as 3TP class 7.

Table 7.9: *Listing of global tumor features.*

Global Tumor Features		
1	*#Voxel*	Number of tumor voxels.
2	*age*	Age of patient.

7.4.3 Extended Classifier and Ensemble Specification

Based on the presented feature set, three base classifiers L_1 - L_3 for the three most suspect regions MSRegion$_{DB}$, MSRegion$_{SC}$, and MSRegion$_{OP}$ are defined. Next, the intersection of these three regions is extracted yielding the MSRegion$_{\cap}$. The MSRegion$_{\cap}$ is the starting point for the fourth base classifier L_4. Furthermore, L_1-L_4 are combined into two more classifiers: L_5 and L_6. The detailed description of L_1-L_6 is listed in Table 7.11. Each of these classifiers learns a decision tree.

The analysis is extended to combinations of classifiers into the ensembles $C_1(a) - C_1(d)$ described in the upper part of Table 7.12. Finally, two baseline classifiers C_2 and C_3 are learned that assign the label according to some intuitive but simplistic rule (see lower part of Tab. 7.12).

Table 7.10: *Selection of washin and washout features for the MSRegion.*

Washin and Washout Features for the MSRegion		
1	RE_{t_3}	The RE at the third time step.
2	*Integral*	The average value for the parameter integral.
3	*Washin*	The average value for washin.
4	*Washout*	The average value for washout.
5	*TTP*	The average value for time to peak.
6	$3TP_{region}$	The 3TP class of the region's average RE curve.
7..15	$\#Voxels_{3TP(1..9)}$	Number of region voxels that have an 3TP curve 1..9.
16	$\#Present_{3TP}$	Number of different 3TP classes existing in the region.
17	$Majority_{3TP}$	3TP class with the most voxels in the region.

Table 7.11: *Table of learners L_1 - L_6.*

Decision Tree Classifiers	
L_1	All features of the MSRegion$_{DB}$ of Table 7.7-7.10 are applied.
L_2	All features of the MSRegion$_{SC}$ of Table 7.7-7.10 are applied.
L_3	All features of the MSRegion$_{OP}$ of Table 7.7-7.10 are applied.
L_4	All features of the MSRegion$_{\cap}$ (Tab. 7.10), all tumor attributes (Tab. 7.9) and region size attributes (Tab. 7.7) are applied.
L_5	Two features from each of the four MSRegions of L_1 - L_4 are applied: the region's size (Tab. 7.7(2)) and average 3TP class (Tab. 7.10(6)).
L_6	Extension of L_5. For each of the four MSRegions (of $L_1 - L_4$) the relative region size (Tab. 7.7(2)) and average 3TP curve (Tab. 7.10(6)) is used. For the clustering with the least outliers from A_{DB}, A_{SC}, and A_{OP}, the homogeneity measures (Tab. 7.8)(1)-(3) are extracted. Also, the tumor attributes are used (Tab. 7.9).

7.4.4 Experimental Settings and Results

The learners and classifiers were applied to the data sets to study the influence of the different clusterings and features. Again, the evaluation criterion is the number of correctly classified instances *#CCI*. Hence, the specificity and sensitivity are considered as less important, because the *Breast Tumor Database 2009* lacks of typical benign tumors. Thus, the sensitivity and specificity measures would be misleading, as it was also indicated by the previous classification result (see Sect. 7.3.5).

Hence, the same experimental setup was created, applying again the Weka library and the included J4.8 decision tree classification algorithm (recall Sect. 7.3.4). To create a classifier covering a strong variety of features, three runs were carried out.

In the first run, the classification algorithm was applied to all complete attribute sets. For the second run, feature subsets of L_1-L_6 were mined to optimize the achieved *#CCI* value. For feature subset search, two approaches were adapted, yielding run 2(a) and run 2(b), based on methods already available in Weka:

a) The information gain of each attribute in all respective feature sets is evaluated. An attribute is excluded if its information gain is zero.

Table 7.12: *Table of classifiers* C_1 *(*$C_1(a) - C_1(d)$*),* C_2*, and* C_3 *based on* L_1 *-* L_6 *from Tab. 7.11.*

Ensemble Classifiers $C_1(a) - C_1(d)$	
The classifiers $C_1(a)$ - $C_1(d)$ carry out a majority voting based on their inputs. If 50% of each classifier's inputs predict malignancy, then the classifier labels the tumor as malignant. The following inputs (based on Tab. 7.11) are employed:	
$C_1(a)$	$C_1(a)$ was created from $L_1 - L_6$.
$C_1(b)$	$C_1(b)$ was created from $L_1 - L_5$.
$C_1(c)$	$C_1(c)$ was created from $L_1 - L_4$ and L_6.
$C_1(d)$	$C_1(d)$ was created from $L_1 - L_4$.

Rule-based Classifiers C_2 and C_3	
C_2	Labels the tumor based on the MSRegion$_{\cap}$. If its average curve type equals 3TP class 1, 4, or 7 the tumor is labeled as malignant. Otherwise it is labeled as benign.
C_3	If the number of voxels with an RE curve classified as 3TP class 1, 4, or 7 is greater or equal to 3 then the tumor is labeled as malignant. Otherwise it is labeled as benign.

b) The wrapper approach, described in [Kohavi and John, 1997], is used to neglect irrelevant attributes. It delivers an attribute subset with the highest possible accuracy.

Since *age* and #*Voxel* show a high significance to almost every constructed decision tree, the third run investigates the impact of these two global tumor attributes on the classification results. Therefore, the full attribute set is applied initially. Next, the classification is conducted such that the features *age*, #*Voxel*, or both were excluded. It becomes apparent that their influence on #*CCI* is very high. The restriction to attributes of the MSRegion only (run 3) results in a drastic decrease of maximum and average #*CCI*.

In the following, the results for each run are described. For the first run, L_2 yields the best decision tree and achieves 53 of 68 ($\approx$ 78%) #*CCI*. Hence, the attributes $Majority_{3TP}$, *age*, and #*Voxel* are employed.

The second run covers the runs 2(a) and 2(b). For the run 2(a), the maximum #*CCI* is 50 ($\approx$ 74%), achieved by L_2, $C_1(b)$, and $C_1(d)$. L_2 is based on the MSRegion$_{SC}$. The decision tree of L_2 contains the attributes J_{SC}, $F1_{SC}$, $3TP_{region}$, $Majority_{3TP}$, and *age*. For the run 2(b), L_2 also yields the best result with #*CCI*= 56 ($\approx$ 82%). This is the overall maximum of all runs as well. The corresponding decision tree (see Fig. 7.8(a)) consists of the attributes $Majority_{3TP}$, *age*, and #*Voxel*. Both runs 2(a) and 2(b) yield an increased number of average #*CCI*.

The best tree solely based on MSRegion features (run 3) was produced by L_4 and yields 45 ($\approx$ 66%) #*CCI*, see Figure 7.8(b). The two baseline classifiers C_2 and C_3 achieved 33 ($\approx$ 49%) #*CCI* and 38 ($\approx$ 56%) #*CCI*, respectively. Thus, simple rules of thumb are not adequate to predict malignancy of lesions on this difficult data set.

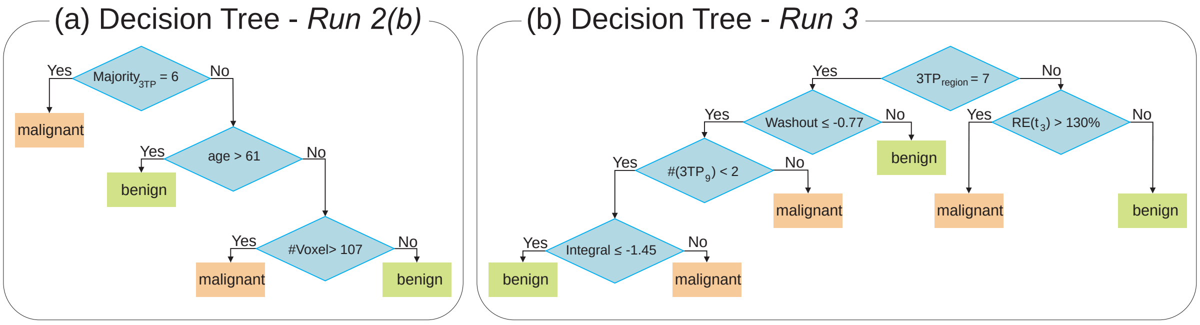

Figure 7.8: *The presented decision tree in (a) achieved the best #CCI value. The decision tree in (b) is the best among the classifiers that did not consider the features age and #Voxel.*

7.4.5 Findings of the Extended Classification Analysis

In this section, the third classification approach, which is an extension of the second approach, has been presented. Thus, density-based clustering algorithms with slightly different parametrizations have been employed and the same database, i.e., the *Breast Tumor Database 2009*, was used for training of different classifiers. Hence, the focus relied on the clustering, i.e., how the formation of similar regions of similar voxels contributes to distinguishing between benign and malignant tumors. As a result, it has been shown that for the final classification step only a few features have to be employed. Another finding is the influence of patient age and tumor size. Both attributes strongly correlate with tumor malignancy and thus prove the challenges of automatic DCE-MRI breast tumor classification solely based on perfusion data. However, the presented analysis identified features that correspond to tumor heterogeneity (i.e., Jaccard coefficient and Purity) and are also suited to predict malignancy.

In conclusion, the adapted specific density-based clustering is much more important for classification instead of the extraction of complex ensembles. The analysis yields a feature set that is best suited to automatically determine tumor malignancy. This feature set has a much higher discriminative power than simple rules of thumb, i.e., the two baseline classifiers C_2 and C_3.

Finally, the features of the MSRegion alone cannot distinguish between benign and malignant tumors, yet the properties of this region are indicative for tumor malignancy for the data set of the *Breast Tumor Database 2009*. The presented classification approach is still limited by the number of tested tumor data sets and the techniques as well as the feature sets should be applied to a larger study. Furthermore, the tumors of this database are hard to classify even for a human expert (recall also the limitations described in Sect. 7.1.5).

7.5 The Fourth Classification Approach in the Spectral Domain

As it was demonstrated by the previous classification approaches, the clustering result of breast tumors strongly depends on the chosen clustering algorithm and its parameter settings. The goal of the adapted spectral clustering approach is an improved spatial connectivity of the remaining regions. In theory, the most homogeneous clusters may be formed by voxels that are not spatially connected. This case may occur with the presented density-based approaches in Section 7.3 and Section 7.4. In practice, the clinician demands spatially connected voxels to form a ROI for further diagnosis like core needle biopsy. With the presented fourth classification approach in the spectral domain, the clustering result is improved in a qualitative way by sorting only spatially connected voxels into clusters.

7.5.1 Adaption of *k*-Means Clustering in the Spectral Space

Like the previous classification approaches, the clustering is applied to the normalized (via z-scoring) perfusion parameters peak enhancement, time to peak, washin, and washout. Based on the descriptive perfusion parameters per voxel, a spectral clustering is applied.

Spectral clustering carries out a dimension reduction, i.e., the objects are transformed into the spectral domain, recall Section 3.4.3. In this new representation, clusters can be easier separated (regarding the high-dimensional space) by applying simple clustering techniques like *k*-means.

For the presented approach, the Ng-Jordan-Weiss Algorithm is employed to directly partition the data into *k* groups. The similarity graph is constructed based on the descriptive perfusion parameters. Each node of the graph represents a voxel of the corresponding breast tumor. Hence, the tumor data are represented in a regular orthogonal 3D grid and each node is connected to its adjacent nodes within a 26-neighborhood. This is a crucial part during clustering process since the 26-neighborhood maintains clusters with spatially connected voxels. As proposed by Von Luxburg [2007], the Gaussian similarity function is employed:

$$s(x_i,x_j) = exp\left(-\frac{dist(x_i,x_j)}{2\sigma^2}\right)$$

to represent the local neighborhood relationships. The distance $dist(x_i,x_j)$ between two voxels x_i and x_j is measured by using the cosine similarity of their corresponding perfusion parameter values [Tan et al., 2006]:

$$dist(x_i,x_j) = cos(x_i,x_j) = \frac{x_i \cdot x_j}{\|x_i\|\|x_j\|}. \tag{7.8}$$

This distance function yields best clustering results w.r.t. the internal cluster indices that will be presented in the following. The scaling parameter σ describes how rapidly the affinity decreases with the distance between x_i and x_j. Instead of manually selecting σ, the approach by Zelnik-Manor and Perona [2004] is employed to calculate a local scaling parameter for each data point. Hence, the number *neigh* of neighbors that should be considered to compute this scale has to be determined. For the presented approach, *neigh* is empirically determined, i.e., different values for *neigh* are used. Afterwards the *neigh* which yields the best clustering result is selected. To assess the clustering result's quality, three internal cluster validation measurements are extracted [Rendón et al., 2011]:

- the Davies-Bouldin index,
- the Dunn index, and
- the Calinski-Harabasz index.

In contrast to external validation indices, internal cluster validation evaluate the clustering result with respect to the information intrinsic to the data alone.

The Davies-Bouldin Index. The Davies-Bouldin index DB is a measure for the average similarity between each cluster and its most similar cluster. It is approximated as [Davies and Bouldin, 1979]:

$$DB = \frac{1}{N}\sum_{i=1}^{N} R_i, \tag{7.9}$$

where R_i is the similarity between each cluster and its most similar cluster c_i, i.e.:

$$\begin{aligned} R_i &= \max{}_{j=1..N, i\neq j}\{R_{ij}\}, \\ R_{ij} &= \frac{s_i + s_j}{d(v_i, v_j)}, \text{ and} \\ s_i &= \frac{1}{m_i}\sum_{k=1}^{m_i} d(x_k, v_i), \end{aligned}$$

where s_i denotes the scatter within cluster c_i, m_i refers to the number of voxels in cluster i, v_i refers to the centroid of cluster i, N to the number of clusters, and x to a data element, i.e., a voxel. The smaller the value of DB is, the better is the clustering result, i.e., the clusters are well separated.

The Dunn Index. The Dunn index is a measure for the smallest cluster distance in relation to the largest intra-cluster distance in a clustering result. Several variations of this index have been proposed. Hence, the Dunn index is computed by [Dunn, 1973]:

$$Dunn = \frac{\min_{i=1..N}\{\min_{j=1..N, i\neq j} d(c_i, c_j)\}}{\max_{k=1..N} diam(c_k)}, \text{with} \tag{7.10}$$

$$\begin{aligned} d(c_i, c_j) &= \min_{x\in c_i, y\in c_j}\{dist(x,y)\}, \text{ and} \\ diam(c_i) &= \max_{x,y\in c_i}\{dist(x,y)\}. \end{aligned}$$

Here, c_i and c_j refer to the clusters i and j. Larger values of the Dunn index indicate a better, i.e., compact and well-separated, clustering result.

The Calinski-Harabasz index. The Calinski-Harabasz CH index [Caliński and Harabasz, 1974] is calculated by:

$$CH = \frac{SSB}{SSW} \cdot \frac{M - N}{N - 1}, \tag{7.11}$$

where SSB and SSW refer to the sum of squared distances between the clusters and the sum of squared distances within a cluster, respectively. They are calculated by:

$$\begin{aligned} SSW &= \sum_{i=1}^{N}\sum_{j=1}^{M_i} d(x_j, v_i)^2 \\ SSB &= \sum_{i=1}^{N}(M_i \cdot d(v_i, \bar{v})^2). \end{aligned}$$

Here, M is the number of all voxels, M_i is the number of voxels in cluster c_i, v_i is the centroid of cluster c_i, $\bar{v}$ is the centroid of the whole data set. Larger values of the Calinski-Harabasz index indicate a better clustering result (larger values for SSB and smaller values for SSW yield increased inter- but reduced intra-cluster variances).

For the empirical determination of *neigh*, it is varied in the range of $[3\dots11]$. Best results w.r.t. the three internal cluster validation indices are obtained for $neigh = 3$, see Figure 7.9. Next, an automatic approximation of the number of clusters k is carried out. Several methods to automatically determine k have been proposed, e.g., a look for the eigengap. Unfortunately, the tumor data sets of the *Breast Tumor Database 2009* are noisy due to their small size and this criterion becomes less effective. Therefore, the three internal cluster validation indices are employed again. For each data set, the spectral clustering is computed several times with different number of clusters k ($k \in \{3..9\}$) and the optimal k is selected according to the validation indices via majority voting. If no majority exists, the Davies-Bouldin index is considered, as suggested by Rendón et al. [2011].

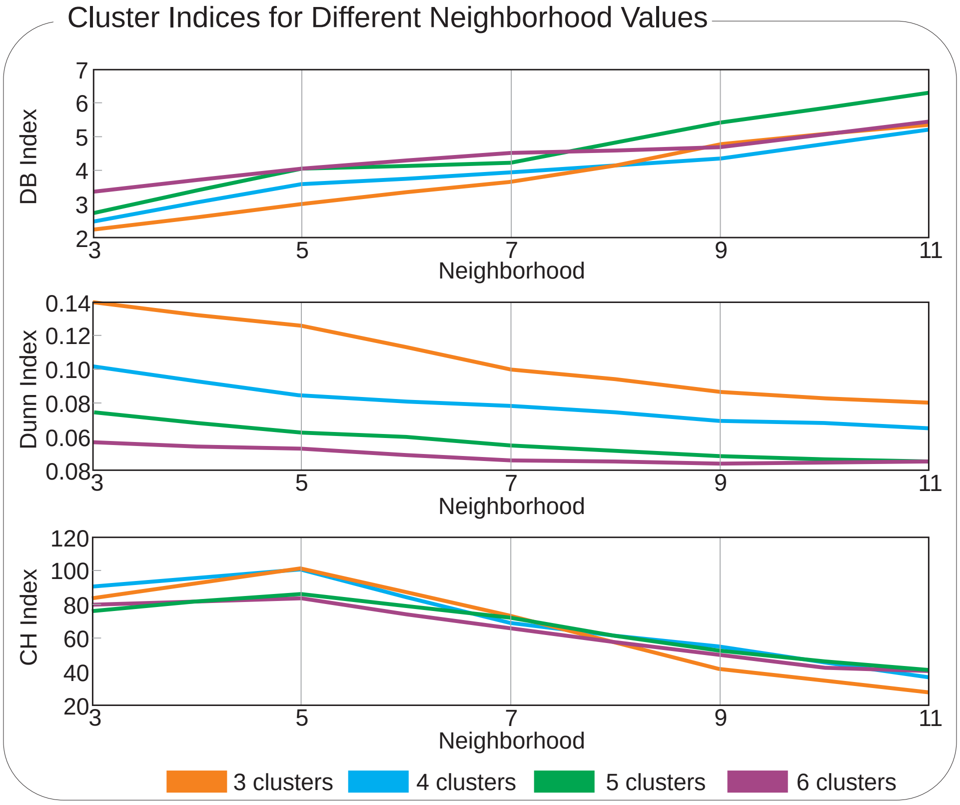

Figure 7.9: *Result of the average Davies-Bouldin (DB), Dunn, and Calinskie Harabasz (CH) index for a varying number of neighbors (n*$\in \{3,5,7,9,11\}$*) and a fixed cluster number. For n=3, all indices show good results (a minimal DB, a maximal Dunn, and a maximal CH index).*

In summary, the distance function $dist(x_i, x_j)$ detects similar descriptive perfusion parameter values and the 26-neighborhood yields the spatial connectivity of voxels in a cluster. With the internal cluster validation indices, automatic parameter choices are extracted for *neigh*, i.e., a local scaling parameter and the cluster number k.

7.5.2 Feature Selection

Based on the spectral clustering result, features are extracted to learn a classifier. Hence, the feature selection is closely adapted to the previous feature selection of the second and third classification approach. Likewise, one cluster is chosen as most suspect region MSRegion. Therefore, the 3TP class ranking is employed for the obtained clusters. The largest cluster with an average RE curve of 3TP class 7 is chosen. If no such cluster exists, a search for the 3TP class 9, 8, 4, 6, 5, 1, 3, and 2 in that order, is performed, recall the description in Section 7.4.1.

From the MSRegion the following features for each tumor are extracted (see also Tab 7.13):

- biological features, i.e., age and tumor size in mm^3,
- features of the MSRegion and its average RE curve, i.e., washin, washout, integral, time to peak, and 3TP class as well as the percentage region size (when compared to the whole tumor), and
- the number of clusters, the separability (i.e., the inter-cluster variance) and the homogeneity (i.e., the averaged intra-cluster variance) of the clustering result (see [Zhao et al., 2009] for more information), and
- the similarity measures Purity P, Jaccard index J, and F_1 score based on the comparison of the clustering result and the 3TP method classification of all tumor voxels.

Table 7.13: *Features for the fourth classification approach.*

Features of MSRegion		
1	*size*	*size* (in mm^3).
2	*age*	Age of patient.
3	*RelRegSize*	The percentaged MSRegion size (with respect to the tumor size).
4..6	$P, J, F1$	The value for P, J, and $F1$ based on the 3TP class division and the clustering result.
7..11	RE_t	The MSRegion average RE value at time step t, $t = 2..6$
12	*Integral*	The average value for the parameter integral.
13	*Washin*	The average value for washin.
14	*Washout*	The average value for washout.
15	*TTP*	The average value for time to peak.
16	$Majority_{3TP}$	3TP class with the most voxels in the region.
17	*#cluster*	The number of clusters.
18	*Separability*	The inter-cluster variance.
19	*Homogeneity*	The intra-cluster variance (average of all clusters).

7.5.3 Experimental Settings and Results

The adapted spectral clustering approach was employed for all tumor data sets of the *Breast Tumor Database 2009*. For the classification based on the spectral clustering approaches, the same experimental setup was employed, i.e., the Weka library and the included J4.8 decision tree classification algorithm (recall Sect. 7.3.4). Again, the evaluation criterion is the number of correctly classified instances *#CCI*. Also, the specificity and sensitivity are considered as less important, because the data set lacks of typical benign tumors and these measures would be misleading, as it was also indicated by the previous classification result (see Sect. 7.3.5). In Figure 7.10, the learned classification model with the best results, i.e., highest *#CCI* is depicted.

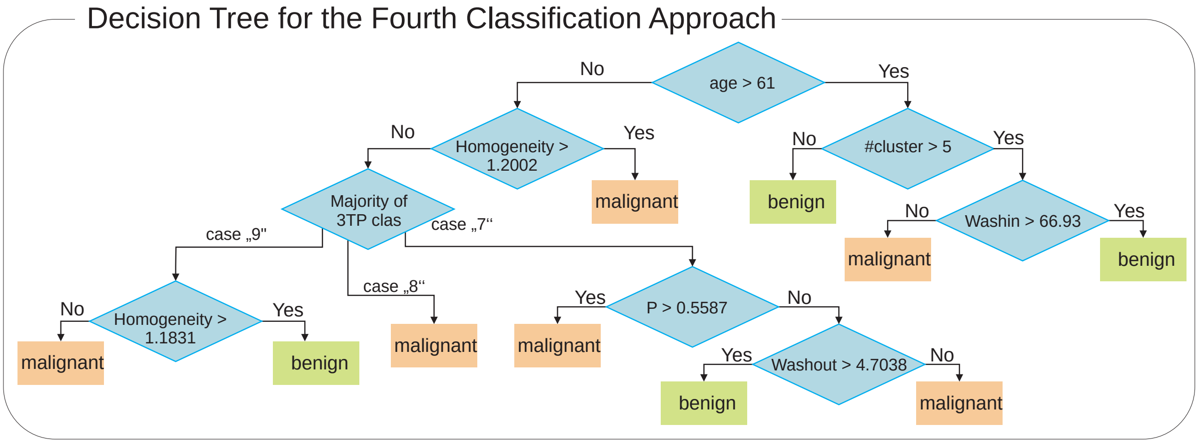

Figure 7.10: *Learned decision tree: the attributes at the upper part of the tree are the most important ones (image adapted and reprinted from [Glaßer et al., 2014b] © 2014, Springer-Verlag, with kind permission from Springer Science and Business Media).*

The best decision tree correctly classifies 56 of 68 tumors, i.e., 82.24%. Inherent to decision trees, the most important features are at top levels, i.e., closer to the root, since they split a larger set of tumors. Hence, the feature *patient age* was employed as most important feature. However, all other attributes characterize the tumor's heterogeneity and kinetic contrast enhancement behavior.

7.5.4 Findings of the Fourth Clustering Approach

The contribution of the fourth classification approach is the adaption of spectral clustering to breast DCE-MRI tumors. To be more precise, k-means was carried out in the spectral domain of the descriptive perfusion parameter space extracted from breast tumor voxels and their RE curves. For the employed algorithms, automatic parameter choices were provided for the input parameters. The learned classifier achieves classification results that can be ordered between the second and the third classification approach. However, it has the great advantage that spatially connected homogeneous regions are obtained. In Figure 7.11, an example of the clustering result is presented. This is in contrast to the approaches described in Sections 7.3 and 7.4 where a connected component analysis is necessary to guarantee spatial connectivity. When compared to the first classification approach described in Section 7.2, the similarity function of the spectral clustering is better suited, since the constructed similarity graph compares each voxel. The region merging averages the parameter values over all voxels that are contained in one region which may induce errors due to this averaging.

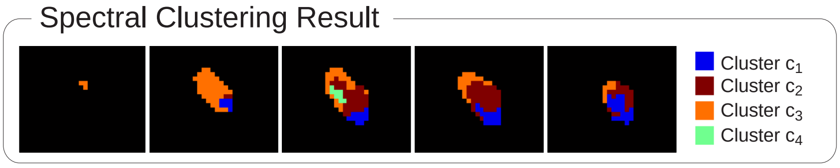

Figure 7.11: *Five slices showing the clustering result for a small breast tumor (image adapted and reprinted from [Glaßer et al., 2014b] © 2014, Springer-Verlag, with kind permission from Springer Science and Business Media).*

7.6 Summary of Heterogeneity Analysis

In this chapter, an important contribution for the clinical research focus on DCE-MRI tumor enhancement kinetics based on four different classifications approaches has been presented. All classification approaches have been carried out on the *Breast Tumor Database 2009* to achieve comparable results. This database is special since the comprising data sets are small breast tumors that could only be detected in DCE-MRI and are even hard to separate for a human expert. Based on the requirements of ROIs, i.e., groups of spatially connected voxels with similar perfusion characteristics, the methods in this chapter analyze how such ROIs can be employed for automatic classification.

The first classification approach is a general classification approach combining kinetic and morphological features and was conducted within the clinical environment. Based on ROC analysis, the first classification approach yields a better discriminative power for heterogeneity related features than the analysis of single perfusion parameters and enhancement curve types. These finding inspired the second and third classification approaches. The region concept was refined due to these first results and the focus was set on detecting the most suspect region MSRegion of a tumor as well as heterogeneity analysis adapted to enhancement kinetics. To make a transition to a machine learning problem, and to reduce the influence of subjective criteria, tumor margin and shape evaluation was removed from the feature set. The second classification approach combines the concept of formation of regions with the extraction of heterogeneity with respect to enhancement kinetics. An adaption of density-based clusterings was introduced to account for outliers, to speed up the segmentation process, and to extend the previous region merging method. Furthermore, a decision tree model is learned for the classification. Thus, the employed feature set is human readable and the most important features for the classification become visible. Although only 46 of 68 tumors could be correctly classified by the learned decision tree of the second classification approach, the most important features for distinguishing between benign and malignant tumors were again related to the heterogeneity of the tumor enhancement kinetics beyond the patient's age. The new aspect of the third classification approach is the focus on the features of the MSRegions found through clustering, rather than the features of all cluster, i.e., the whole lesion. As a result, the clustering, i.e., the grouping of voxels into regions is more important for classification instead of the extraction of complex ensembles. Most important, the method yields a feature set that is best suited to automatically determine tumor malignancy (with 56 of 68 correctly classified tumors) based on the heterogeneity of tumor enhancement kinetics and patient's age as well as tumor size. The contribution of the fourth classification approach is the adaption of spectral clustering to breast DCE-MRI tumors. Thus, spatially connected homogeneous regions are obtained.

In summary, the spectral clustering approach may be best suited for the clinician to identify a ROI for further diagnosis like core needle biopsy. For an automatic classification approach, the third classification approach yields a higher discriminating power for the *Breast Tumor Database 2009*. Hence, outliers can be identified, but a connected component analysis may be necessary to guarantee spatial connectivity. Although the region merging approach does provide a division into spatially connected regions as well, its similarity function is inferior compared to the other approaches. The region merging averages the parameter values over all voxels that are contained in one region which may induce errors due to this averaging.

The presented approaches evaluate all the whole lesions (in terms of global features) as well as the tumor's MSRegion. Furthermore, they are superior to simple rules of thumb, for example the C_2 and C_3 classifiers test during the third classification approach in Section 7.4.3. Beyond the semi-automatic extraction of the lesion, all classification approaches are fully automatic, i.e., no user input is necessary like pre-definition of number of clusters etc. Therefore, the presented method could be adapted to breast tumor data sets independent of specific scanning protocols or parameters.

When evaluating the achieved classification results, it must also be stated that the classification was only covering DCE-MRI data for the clinical research focus. In clinical practice, rather the combination of different image modalities (e.g., X-ray and MRI) with patient-specific attributes (e.g., genetic risk factors) is indispensable for a complete diagnosis. It was not possible to create a *score* for automatic tumor classification solely based on perfusion MRI, but the best suited kinetic features to distinguish between benign and malignant tumors have been identified.

In conclusion, a combination of the reported features and the region formation could be easily integrated within the clinical workflow and can support the radiologist when finding a tumor's most malignant part and to rate the tumor's malignancy. The detection of the MSRegion has great importance for further diagnosis like core needle biopsy. As limitations for the presented classification approaches, the adapted 3TP classification and the strong influence of patient's age and tumor size have to be mentioned. However, an extensive clinical study is needed to assess, whether the adapted 3TP method classification is reliable with current DCE-MRI scanning protocols and to make sure that no critical exceptions exist. In future, the investigation how the clinical expert could direct the clustering (e.g., set the clustering's parameters) bears great potential for a semi-automatic classification approach. The presented classification approaches strongly depend on the important breast cancer classification aspects $\boxed{1}$, $\boxed{2}$, $\boxed{3}$ and $\boxed{4}$, recall Chapter 4. Without the morphologic features (aspect $\boxed{5}$), a more standardized classification approach is provided.

8. Visual Analysis of Brain Tumor Data

This chapter is partly based on:

Sylvia Glaßer, Steffen Oeltze, Atle Bjørnerud, Uta Preim, Bernhard Preim, and Helwig Hauser: “Visual Analysis of Longitudinal Brain Tumor Perfusion". In Proc. of SPIE 8670 Medical Imaging, p. 86700Z, 2013.

8 Visual Analysis of Brain Tumor Data

In clinical research on diagnosis and evaluation of brain tumors, longitudinal perfusion MRI studies are acquired for tumor grading as well as to monitor and assess treatment response and patient prognosis. Within this chapter, it is demonstrated how visual analysis techniques can be adapted to multidimensional data sets from such studies. The developed framework supports the computer-aided diagnosis of low grade gliomas (LGGs) and high grade gliomas (HGGs). It includes two innovations. First, a pipeline is introduced that yields comparative, co-registered quantitative perfusion parameter maps over all time steps of the longitudinal study. Second, based on these time-dependent parameter maps, visual analysis methods were developed and adapted to reveal valuable insight into tumor progression, especially regarding the clinical research area of LGG transformation into HGGs. The framework underwent an informal evaluation based on four longitudinal brain studies, which demonstrates the suitability of the presented visual analysis methods and comprises new possibilities for the clinical researcher to characterize the development of LGGs. The framework was created with the Me*VisLab* platform[1], supported by OpenGL and VTK.[2]

Related studies for the evaluation of LGGs and HGGs have been presented in Section 4.3, and in the conclusion of Chapter 4. Hence, the important aspects $\boxed{6}$ and $\boxed{7}$ have been identified which will be taken into account in the next sections. Furthermore, an approximation of heterogeneity will be presented, as demanded by aspect $\boxed{9}$.

8.1 Clinical Motivation

MRI is used for evaluating brain tumors due to its high soft-tissue contrast. In addition to morphologic aspects represented by conventional MRI, the dynamic susceptibility contrast (DSC) perfusion imaging enables the characterization of dynamic aspects, recall Chapter 2. In particular, the evaluation is based on the cerebral microvasculature that is represented by the quantitative perfusion parameter relative cerebral blood volume (rCBV), see Figure 8.1. DSC-MRI, in combination with conventional MRI, is a good presurgical indicator for glioma grade and may identify the most malignant parts of a tumor for guiding stereotactic biopsy as well as to monitor and assess treatment response and patient prognosis. Gliomas – tumors with a glial cell origin – are the most common primary brain tumors. They histopathologically vary from LGGs to HGGs.

Grading of gliomas and thus the differentiation between LGGs and HGGs plays an important role for treatment planning and patient outcome [Covarrubias et al., 2004]. Furthermore, LGGs may transform into HGGs at some point in time and an early detection of such a transformation is of significant clinical importance. If a surgical removal or radiation treatment

---

[1] Product of Fraunhofer MEVIS, Bremen; www.mevislab.de (12/08/2013)

[2] The Visualization Toolkit, New York, USA; http://www.vtk.org/ (12/08/2013)

is not possible, e.g., due to the tumor's location or patient's request, patients with LGGs are commonly subject to a life-long MRI monitoring. Here, the clinical research focus lies on the detection of LGG transformation in longitudinal brain data acquired over several years. Furthermore, the evaluation of rCBV is a clinical research focus as well. It is an important indicator for a patient's survival and gliomas with high rCBV values have a significantly faster progression time [Law et al., 2008]. Since HGGs have in general foci of higher rCBV values and rCBV correlates with the tumor grade, rCBV is also employed for differentiation between LGGs and HGGs [Law et al., 2003, Emblem et al., 2008, Law et al., 2008].

As it was stated in Section 4.3, longitudinal rCBV evaluation is a challenge since rCBV maps of different acquisitions have to be compared. This is a complex and exploratory analysis task due to the absence of standardized intensity values and the high variability of MRI scanners and patient data. Thus, longitudinal studies are in general assessed with software intended for the diagnosis of a patient at one point in time. In contrast, the framework presented in this chapter comprises dedicated support for longitudinal LGG studies. It provides the normalization of the image data and a visual comparison of the data from different points in time.

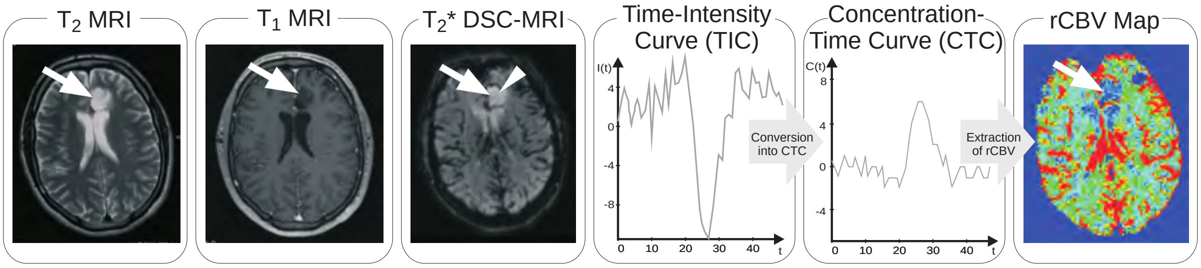

Figure 8.1: *MRI slices with a tumor (see arrow). For a single voxel (see arrowhead) of the DSC-MRI data, the time-intensity curve is extracted and converted into the concentration-time curve (see diagrams). From the concentration-time curve, the parameter CBV is extracted, yielding a CBV map (low values are mapped to blue, high values to red). Note the varying data size, orientation, and image resolution. (Data is courtesy of Atle Bjørnerud, Department of Medical Physics, Rikshospitalet-Radiumhospitalet Medical Centre and Department of Physics, University of Oslo, Norway.)*

In Section 4.3, a detailed description about the ROI-based evaluation of rCBV values was provided. Hence, different recommendations about the optimal size and placement of the ROI were reported. Furthermore, no gold standard for a cut-off value between LGGs and HGGs based on a ROI's average rCBV value is available.

Finally, the strong focus on tumor heterogeneity discussed in the previous chapter influences the demand for assessment of brain tumor heterogeneity. Hence, first results indicated that tumorous areas with increased heterogeneity might reflect the most suspicious tumor part, see the examples in Figure 8.2. This illustration was created with the *SimVis* framework presented by Doleisch et al. [2003]. Note that after excluding voxels with high-correlating rCBV and rCBF, only voxels with increased integral parameter values are remaining.

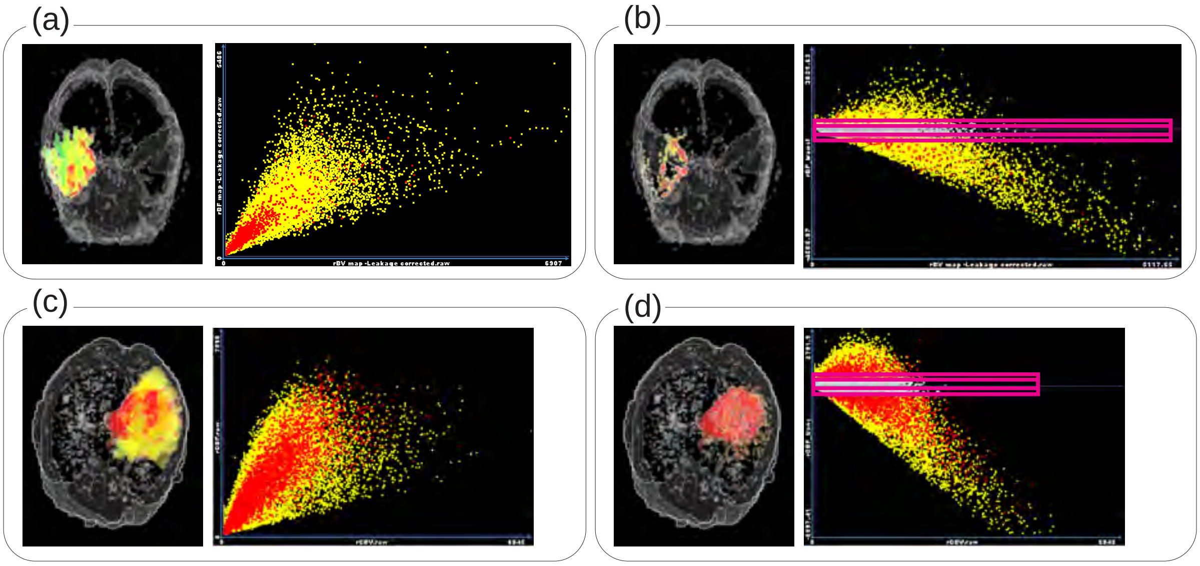

Figure 8.2: *Exploration of rCBV and rCBF via* SimVis. *Two different brains are depicted and the brain tumor is visualized with color-coding (mapping integral from red to green values). The scatterplots on the left show all brain voxels' rCBV and rCBF values in yellow. Values of tumor voxels are visualized in red revealing a stronger correlation for tumor voxels. After transforming the scatterplot along the correlation line, a brush (see pink boxes) is defined such that voxels with strong correlating rCBV and rCBF are excluded, see (b) and (d). Hence, the LGG exhibits a smaller part at the right boundary with high integral values. This is a possible indication for high neoangiogenetic activity at the tumor boundary. The HGG at the bottom exhibits a larger area of voxels without rCBV and rCBF correlation. This might indicate a higher neoangiogenetic activity. (Data is courtesy of Atle Bjørnerud, Department of Medical Physics, Rikshospitalet-Radiumhospitalet Medical Centre and Department of Physics, University of Oslo, Norway.)*

8.2 Application Scenario and Image Data

This section introduces the application scenario in more detail. Therefore, clinical research questions regarding LGGs and their development are presented. Furthermore, the longitudinal brain perfusion studies are described.

8.2.1 Clinical Research Questions

The comparison of rCBV maps is the most important question of the clinical experts. As a prerequisite, preprocessing has to be carried out to incorporate rCBV maps from different perfusion scans. Since LGG transformation relates to increased tumor heterogeneity, the evaluation of the tumor's heterogeneity based on quantitative perfusion parameters is demanded as well. Tumor transformation is also related to tumor growth, which should be visualized. In summary, there are four clinical research question and a last question regarding the visual analysis framework:

1. How can a comparative rCBV evaluation be achieved for a longitudinal brain perfusion study?

2. When does the LGG transformation start based on the evaluation of rCBV maps?
3. How is the tumor's heterogeneity characterized in terms of local rCBV and rCBF correlation?
4. How does the tumor grow and develop during the longitudinal study?
5. How can visual exploration and analysis of longitudinal studies be carried out?

8.2.2 Image Data

The case study consists of a selection of four patients fulfilling two special conditions. First, each patient had a confirmed diagnosis of an inoperable grade II glioma, i.e., an LGG, and was thus monitored over several years. Second, during this time period, a transformation into an HGG took place. The brain MRI data of these four patients was evaluated resulting in four longitudinal studies L_1 – L_4. For each study, up to five MRI protocols including perfusion T_2^*-weighted DSC-MRI sequences, T_1 pre- and post-contrast scans, T_2 scans, and Fluid Attenuated Inversion Recovery (FLAIR) MRI were acquired. Typical sequence parameters for the T_2^* DSC-MRI perfusion studies are gradient-echo echo planar imaging (GRE-EPI) with a temporal resolution TR of $1.4-1.72$ s, echo time TE $30-52$ ms, image matrix 128×128, slice thickness 6.5 mm, in-plane resolution 1.8 mm $\times 1.8$ mm, number of slices $12-19$, number of acquisitions $50-75$, and a total acquisition time ranging from 73 s to 119 s.

For each study, the point in time of the LGG transformation was estimated by an experienced radiologist. The estimation is based on *all* MRI protocols – instead of the single perfusion scan – of all time steps for each study.

The Study L_1. L_1 was acquired over almost three years at four time steps $t_1 - t_4$ for monitoring of an LGG. The transformation into an HGG started between t_1 and t_2.

The Study L_2. The patient of study L_2 underwent surgical intervention and the remaining LGG was monitored for four years. MRI data was acquired at five time steps and the LGG transformation started between t_3 and t_4.

The Study L_3. L_3 contains an oligodendroglioma, a glioma type exhibiting foci of high CBV values irrespective of the tumor grade [Lev et al., 2004]. MRI scans have been acquired at four time steps during two and a half years. The transformation started between t_3 and t_4.

The Study L_4. Image data for L_4 has been acquired at five time steps t_1-t_5 to supervise an LGG over a time period of three and a half years. The transformation into an HGG started after t_3.

8.3 Visual Analysis of Longitudinal Brain Tumors

The framework for computer-aided diagnosis of longitudinal brain tumor studies includes two innovations: a *preprocessing pipeline* for the MRI perfusion scans and the *framework* containing the adapted visual analysis techniques.

8.3.1 Preprocessing Pipeline

The preprocessing pipeline facilitates the comparison of the different perfusion data sets (with possible different image parameters) of a longitudinal brain perfusion study. It comprises five steps, which are described in the following.

Co-Registration of Perfusion Data Sets

Motion artifacts in brain perfusion imaging typically result from patient movement. With the skull as static reference object, rigid registration algorithms allow for co-registration of brain perfusion data. First, each T_2^*-weighted DSC-MRI perfusion scan was motion corrected with the software package *nordicICE*.[3] Second, each study's perfusion DSC-MRI data set was co-registered to the study's DSC-MRI data set acquired last in time with *RView*[4], employing a rigid registration algorithm [Studholme et al., 1999]. Thus, a concurrent analysis of all perfusion scans of a longitudinal study is supported.

Extraction of CBV and CBF maps

To assess CBV and cerebral blood flow (CBF), the distribution of the contrast agent is analyzed. The contrast enhancement results in time-intensity curves for each voxel (see Fig. 8.1). Hence, the software package *nordicICE* is employed to transform these curves into concentration-time curves, applying the regularized singular value decomposition for deconvolution [Rosen et al., 1990]. The arterial input function was extracted from the arteria cerebri media [Østergaard et al., 1996b]. Contrast agent leakage correction was carried out due to possible contrast agent extravasation in regions of blood-brain barrier (BBB) disruption [Boxerman et al., 2006], caused by the tumor. CBV is approximated as the area under the concentration-time curve and defined as the total volume of blood traversing a given region of the brain. It is measured in *ml* of blood per 100 *g* of brain tissue. CBF is defined as the volume of blood traversing a given region of brain per unit time. It is measured in *ml* of blood per 100 *g* of brain tissue per minute. Although in ischemic stroke diagnosis, CBF is thoroughly analyzed, the role of this parameter in brain tumor diagnosis has not been as extensively studied as CBV [Covarrubias et al., 2004].

However, since tumor heterogeneity indicates tumor malignancy, the framework includes heterogeneity evaluation in terms of correlation between CBV and CBF. While a small decrease in CBF is expected as a consequence of normal aging in a longitudinal study, the transformation from LGG to HGG is expected to involve significant stronger changes. However, a gold standard for CBV and CBF evaluation seems hard to establish due to different imaging modalities, age, and gender [Bjørnerud and Emblem, 2010].

Normalization of CBV and CBF maps

For comparison of CBV and CBF values from DSC-MRI scans, normalization has to be carried out. In the framework, the general approach is employed where CBV and CBF maps are

---

[3] Product of NordicNeuroLab, Bergen, Norway; www.nordicneurolab.com (12/08/2013)

[4] By C. Studholme, Seattle, USA; rview.colin-studholme.net (12/08/2013)

normalized with the averaged white matter's values of the contralateral side [Wetzel et al., 2002], yielding relative CBV (rCBV) and relative CBF (rCBF) values. Visual inspection and ROI placement are realized with Me*VisLab*.

Exclusion of Vessels and Adapted Smoothing

Next, vessels were excluded from the rCBV and rCBF maps since brain vessels exhibit higher values than the surrounding tissue. They can be identified and removed based on the earlier and stronger contrast enhancement in the T_2^*-weighted DSC-MRI data. A vessel mask is extracted with *nordicICE* based on the cluster analysis of the estimated perfusion-related parameters to separate vessels (both arteries and veins) from other tissue. For each rCBV and rCBF map the corresponding vessel mask is applied. Afterwards, a 3×3 modified average filter is applied to smooth the data as well as to reduce holes caused by the vessel mask. This filter empirically accounts best for rCBV changes due to noise or subtle artifacts. The modified filter only averages over non-vessel voxels in the 3×3 neighborhood of the current filter kernel. Hence, outliers, i.e., isolated voxels with rCBV values higher than a certain threshold, are removed. The 0.995 quantile of a data set's rCBV value is employed as cut-off value for outliers.

Extraction of Tumor Masks

In a last step, a tumor mask for each of the perfusion data sets was created. Hence, the T_2 and FLAIR images were co-registered to the perfusion data sets acquired at the same point in time of the studies with *RView*. Next, binary tumor masks based on hyperintense areas in T_2 and FLAIR data for each study's time step were extracted and applied to the rCBV maps. Tumor mask creation was manually carried out. Afterwards, it was validated by an experienced radiologist.

8.3.2 A Framework for Visual Analysis of Longitudinal Brain Tumors

Based on the preprocessed longitudinal scans, a framework was developed for the longitudinal evaluation of brain perfusion data. The framework contains color-coded 2D and 3D visualizations, a local heterogeneity map, and a parallel coordinates plot view. The related work for these concepts was provided in Section 4.1.

Direct 2D and 3D Visualizations

The 2D and 3D visualizations directly map each voxel's rCBV value to color. For direct rCBV extraction, a standard 2D slice view of the brain tumor with voxelwise rCBV is presented. All tumor slices of a study's scans are provided. A modified rainbow color scale from blue to red is applied, see Figure 8.3. The color scale is based on the scale suggested by Wetzel et al. [2002]. Red highlights critical rCBV values (values > 5), and suspicious rCBV values greater than 1 are mapped to cyan. Although rainbow color scales do in general lack an intuitive visual interpretation of the data's order, they support visual clustering. Hence, regions with mostly red colors (and thus high rCBV values) or blue regions can be observed. Based on the rCBV maps a selection of voxels, – *the rCBV threshold selection* – can be defined. This selection consists of all voxels with an rCBV value greater than a user-defined threshold and can be combined with all other views.

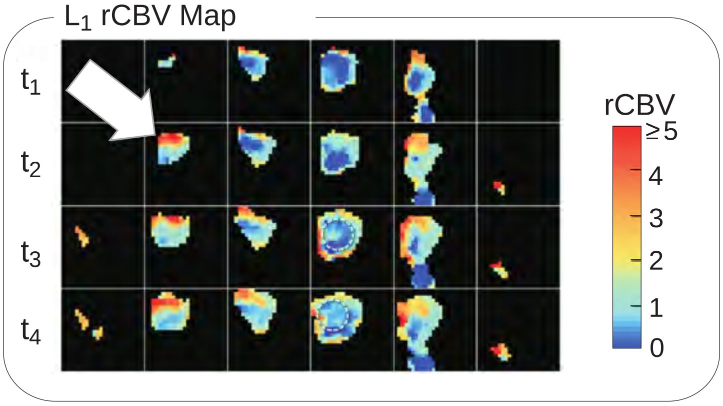

Figure 8.3: *2D rCBV maps of all slices (horizontally aligned) of study L_1 for all four time steps (vertically aligned). At t_1 and t_4, the tumor is covered by four and six slices, respectively. Note the hot spot with high rCBV values (arrow). The encircled regions exhibit lower rCBV values.*

The 3D overview provides a direct volume rendering applying the same color scale (see Fig. 8.3) for highlighting tumor voxels. A linear opacity transfer function assigns α-values of 0.2 to low rCBV values ≤ 1 and α-values of 1 to rCBV values ≥ 5. The brain is displayed as isosurface context object and was extracted from the perfusion data set with thresholding. The tumor is presented as focus object. The visibility of the focus object from all viewing points is maintained with a simple cut-out technique, see Figure 8.4. Hence, the tumor's enclosing sphere is slightly enlarged and employed to cut the isosurface of the brain. The 3D overview visualizes the tumor's progression as well as its spatial localization in the brain. However, only limited information about a tumor's malignancy can be provided since no exact quantification of rCBV hot spots is possible. The 3D overview reveals the spatial variability of rCBV hot spots. They may occur at slightly different positions across all scans of a longitudinal study due to tumor growth (see Fig. 8.4).

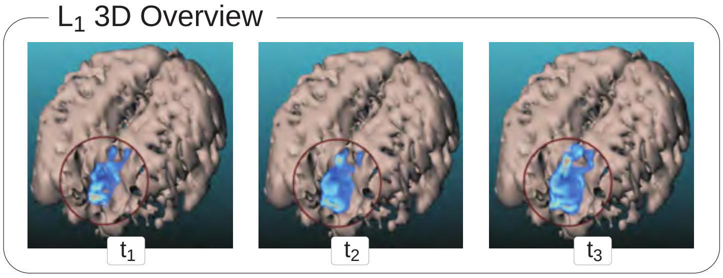

Figure 8.4: *3D view of tumor growth of L_1 at t_1, t_2, and t_3. The brain is depicted as context object and the tumor is emphasized with a cut-out technique.*

Visual Analysis of Local Tumor Heterogeneity

In clinical research, tumor growth and malignancy are associated with increased tumor heterogeneity due to necrosis mainly in the tumor center. Also, some neoangiogenetic tumor parts are expected to exhibit increased heterogeneity. For an assessment of local heterogeneity, approximated as correlation of rCBV and rCBF, the local correlation coefficient (LCC) measure [Cachier and Pennec, 2000] is extracted. An important property of LCC is the independence of scaling of the data value range. Thus, the LCC maps are independent of rCBV and rCBF normalization factors, which had been used to normalize CBV and CBF maps. The LCC values are extracted from the preprocessed rCBV and rCBF parameter maps yielding a color-coded 2D LCC parameter map, see Figure 8.5. LCC values of 1 indicate an increasing linear relationship. Values equal to 0 illustrate a missing linear dependency. A heat color map from dark red to bright orange is applied to map increasing values of LCC.

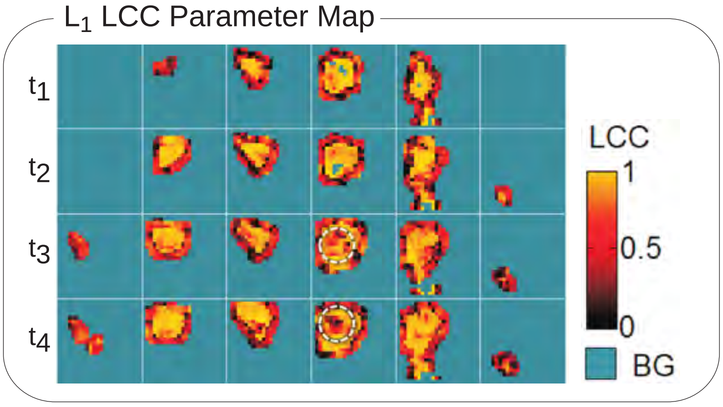

Figure 8.5: *LCC parameter maps of L_1. Heterogeneous areas are mapped to dark red. The encircled regions at time steps t_3 and t_4 exhibit low rCBV values, see Figure 8.3.*

The rCBV Profile Parallel Coordinates Plot

A parallel coordinates plot allows for the exploration of multivariate data where each axis presents a data dimension. Recall Sect. 4.1.2 for related work regarding parallel coordinates plots. The parallel coordinates plot is adapted as follows: For each voxel, the rCBV values over time (i.e., the scans at different time steps of a study) are extracted yielding rCBV curves. In Figure 8.6, the rCBV profile view of L_1 is presented (the same color scale is applied, recall Fig. 8.3). According to discussions with the clinical experts, the rCBV changes, i.e., the voxel's rCBV differences between two subsequent time steps were of great interest resulting in the rCBV change profile view, see Figure 8.6. Hence, shadows support depth perception. The rainbow color scale's hue changes support the differentiation between rCBV values. The data's order can be easily inferred from the curves' height. In addition, height lines support direct quantitative rCBV or rCBV change extraction and curve differentiation is supported by contour lines and Fresnel shading.

To obtain groups of similar curves, different strategies to sort the curves were empirically tested. Hence, the best result (i.e., the lowest amount of occlusions of curves in the background and the easiest detection of trends) was achieved with a sorting based on the squared differences of each rCBV change curve's integral. The order is applied to both rCBV profile views. Tumors with larger extents and thus a larger amount of voxels yield a higher number of rCBV change curves, which may lead to visual clutter. To reduce the curve number, the user can apply the rCBV threshold selection and only curves that have at least one rCBV value greater than this threshold are included. In addition, the rCBV profile views allow for the

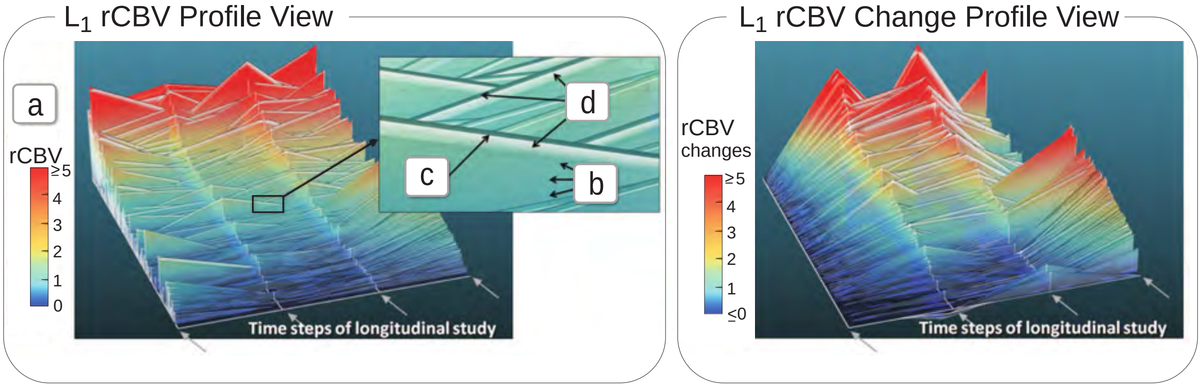

Figure 8.6: *The rCBV profile view (left) with all voxels' rCBV curves. The rCBV values are color-coded (a) and height lines support direct measurement (b). Differentiation of curves is supported by dark contour lines (c), with Fresnel shading attached to (d). The rCBV change profile view presents the rCBV parameter curves' differences (right). Thus, all differences are mapped to zero for t_1.*

rCBV curve index selection. Hence, all voxels with a corresponding curve index inside the selected range of curve indices are combined. The curve indices are sorted depending on the rCBV profile view. Although the rCBV profile views allow for simultaneous display of all voxels' rCBV changes, the spatial connectivity of the voxels is lost, as the voxels' order purely depends on the rCBV curves and not on their spatial position.

8.3.3 Combination of Visual Analysis Techniques

The presented techniques can be combined via the rCBV threshold selection and the rCBV curve index selection. Then, a tumor voxel is only mapped to color or represented as curve when it is part of all chosen selections. Furthermore, the 2D views can be combined with lenses to allow for simultaneous evaluation of rCBV and LCC values.

8.4 Informal Evaluation with Clinical Research Questions

In this section, the studies $L_1 - L_4$ were discussed with two physicians regarding the clinical research questions (recall Sect. 8.2.1).

How Can a Comparative rCBV Evaluation Be Achieved?

With the presented pipeline, a concurrent evaluation of each study's perfusion scans can be achieved. User interaction is only necessary during ROI placement in the contralateral healthy brain tissue. The pipeline can be applied to all brain DSC-MRI data sets independent of MRI scanner or specific scanning protocol parameters. Also, distortion of a ROI's rCBV values due to vessel voxels is prevented.

When Does the LGG Transformation Start Based on the Evaluation of rCBV Maps?

In general, rCBV maps are evaluated with the hot spot method. If the hot spot's average rCBV value is greater than a certain threshold, e.g., > 1.5 [Covarrubias et al., 2004], the tumor is expected to be an HGG. The transformation of the LGG of L_1 started between t_1 and t_2 since a hot spot occurs at t_2 with an average rCBV value > 1.5. The patient of L_2 was monitored after surgical intervention. In Figure 8.7(a), the development of the recurrent LGG can be observed. First, there is a lesion dominated by radiation necrosis and low rCBV values. Next, the rCBV view at t_4 reveals some rCBV hot spots, whereas at t_5 increased extents of hot spots with higher rCBV are visible. The reported rCBV differences of oligodendrogliomas in comparison to other brain gliomas is reflected by L_3 since foci with high rCBV values do occur at all time steps (see Fig. 8.8(a)). Study L_4 comprises an LGG and between t_3 and t_4 more hot spots with increased rCBV values occur, see Figuer 8.9(a). However, in clinical research, it is not always clear at which extent and number of hot spots and which threshold of rCBV, a glioma is graded as HGG [Law et al., 2003, Covarrubias et al., 2004, Emblem et al., 2008]. Furthermore, the normalization of rCBV with a possibly too low or too high normalization factor (extracted on the contralateral brain side) could strongly hamper this analysis and ROI placement suffers from inter-observer variability [Wetzel et al., 2002]. These limitations also hold for the 2D parameter maps.

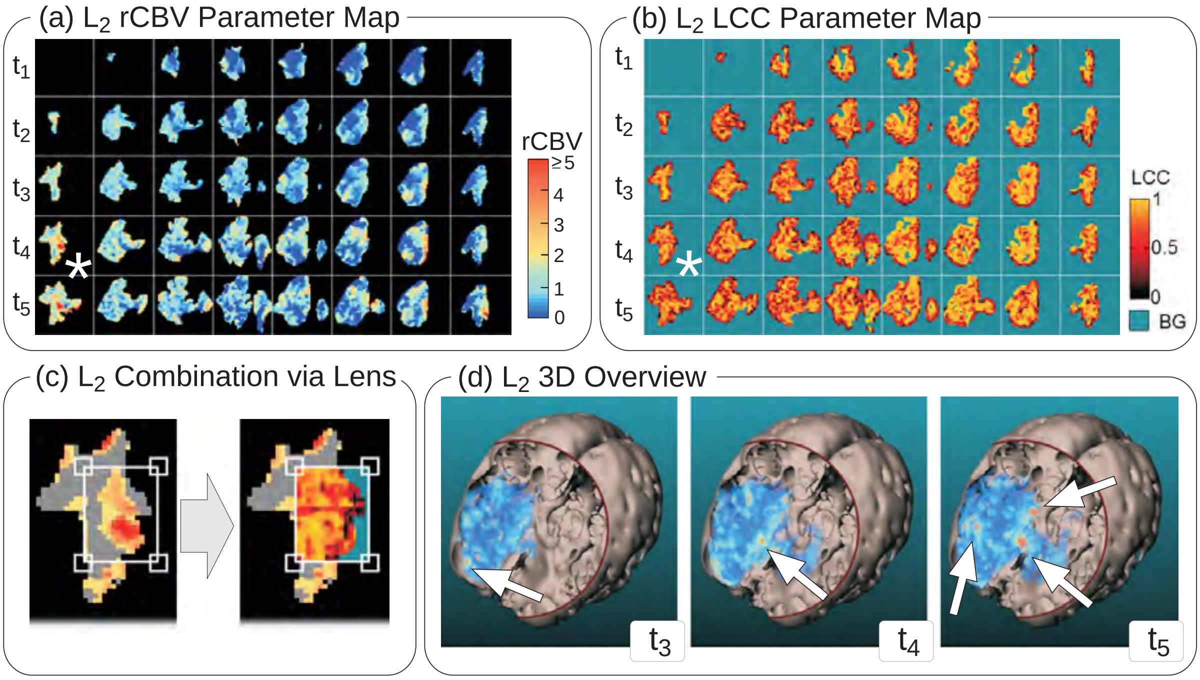

Figure 8.7: *The rCBV map (a) with corresponding LCC map (b) and 3D overview (d) of L_2. To improve readability, the first and the last 2 tumor slices are not presented. The combination of (a) and (b) with a lens for a selected slice (marked with *) is depicted in (c), revealing a hot spot with increased local heterogeneity at the tumor's boundary. An rCBV threshold selection (rCBV threshold = 1.5) is applied, mapping lower rCBV values to gray. In (d), increased rCBV values and larger hot spots (see arrows) are revealed.*

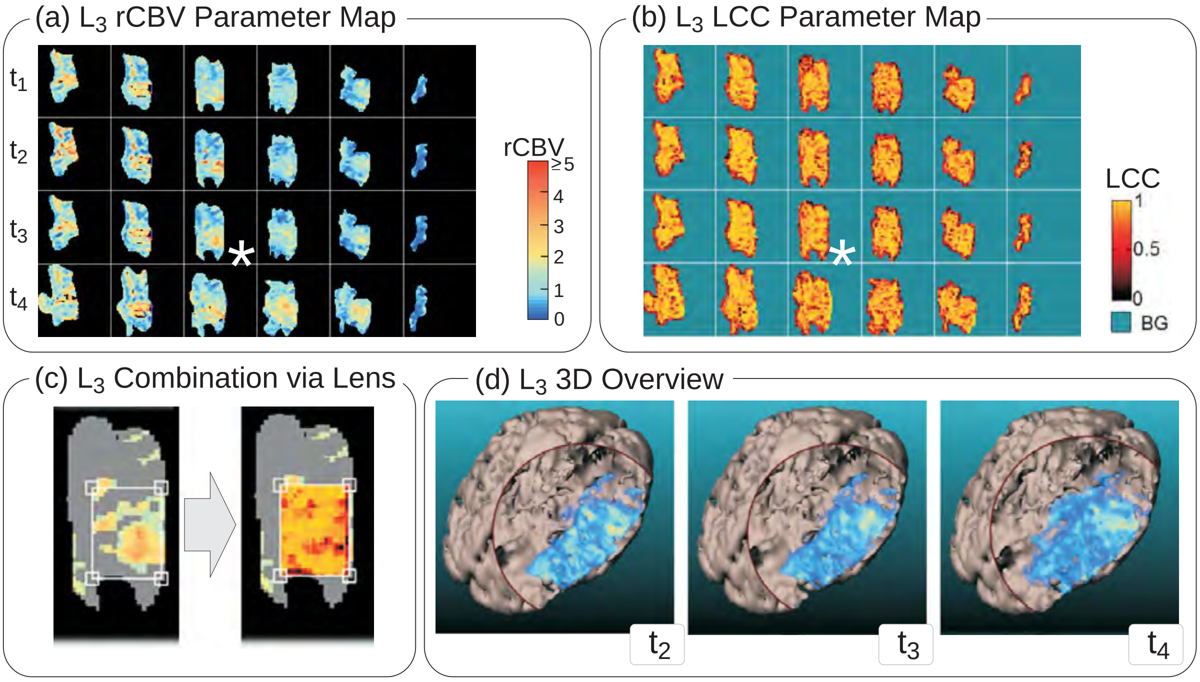

*Figure 8.8: Presentation of the rCBV map (a) with corresponding LCC map (b) and 3D overview (d) of L_3. To improve readability, the first and the last 2 tumor slices are not presented. In c), the combination of (a) and (b) via a lens for a selected slice (marked with *) is depicted, revealing a hot spot with increased local heterogeneity in the tumor's center. An rCBV threshold selection (rCBV threshold = 1.5) is applied, mapping lower rCBV values to gray. In (a) and (d), increased rCBV values and larger hot spots (marked with arrows) are revealed.*

How is the Tumor's Heterogeneity Characterized in Terms of Local rCBV and rCBF Correlation?

To support stereotactic biopsy, the most malignant tumor parts have to be determined. These parts are characterized by areas with increased angiogenesis and therefore with highest rCBV values. Furthermore, the clinical research partners presumed increased heterogeneity and thus uncorrelated rCBV and rCBF values for these parts. The LCC maps of L_1 are presented in Figure 8.5 and of L_2-L_4 in Figures 8.7(a), 8.8(a), and 8.9(a). Hence, also the combination of LCC maps and rCBV maps with lenses (see Fig. 8.7(c) and 8.8(c)) is demonstrated. Two facts can be observed. First, with increased tumor growth, heterogeneous areas in the tumor center become visible, which may be caused by necrotic areas. Second, at the tumor's boundary, areas with uncorrelated rCBV and rCBF values exist. During tumor growth, necrotic areas in the tumor center show up with typical low rCBV values, see the encircled regions in Figures 8.3 and 8.5. Necrotic tumor parts typically exhibit low rCBV values. For stereotactic biopsy, these parts should be explicitly spared. In contrast, areas with high rCBV and high heterogeneity in terms of LCC should be aimed at. These areas can be defined by applying an rCBV selection first. Next, a ROI is set in the remaining rCBV map (see Fig. 8.7(c)). Another finding of the LCC maps is the lack of relationship between LGG transformation and the amount of LCC approximated heterogeneity.

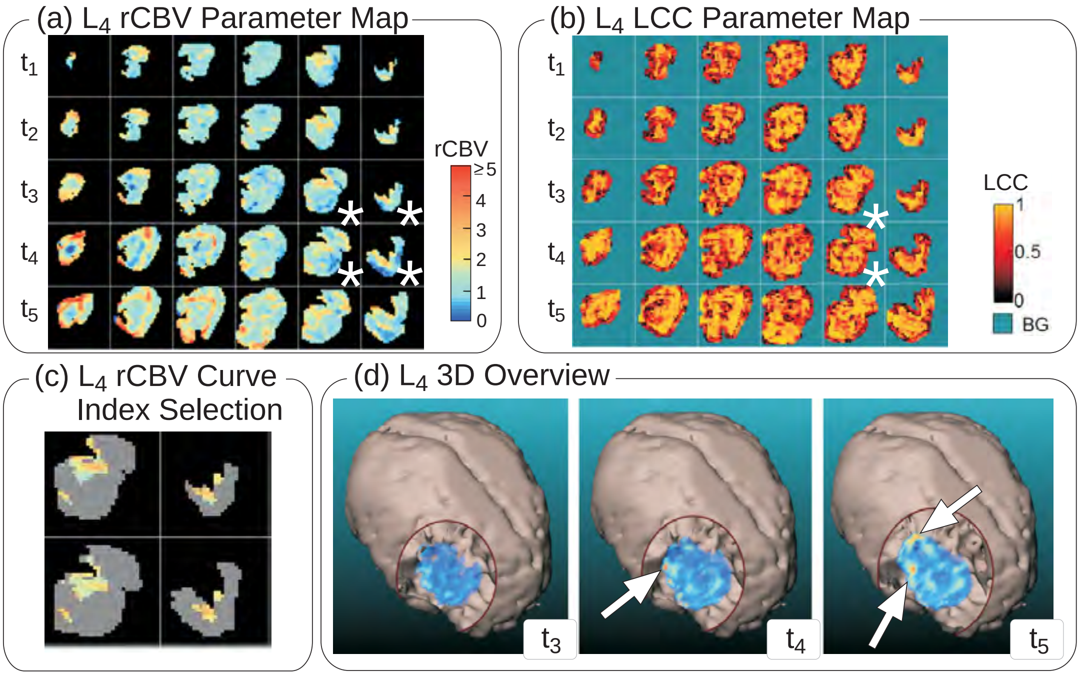

*Figure 8.9: Presentation of the rCBV map (a) with corresponding LCC map (b) and 3D overview (d) of L_4. In c), the rCBV curve index selection is applied to the slices marked with *. Only the voxels, which were selected in the rCBV profile view in Figure 8.10(c). In (d), increased rCBV values are marked with arrows.*

How Does the Tumor Grow and Develop?

For a qualitative overview of tumor growth, the 3D view is provided (see Fig. 8.4, 8.7(d), 8.8(d), and 8.9(d)). Although the medical expert has fast access to the spatial extent of the tumor, no quantitative evaluation is possible. Quantitative information is provided in the 2D parameter maps and the rCBV profile views. Furthermore, the rCBV profile views provide a fast overview of significantly changing rCBV values and thus a possible LGG transformation. This relationship is illustrated in Figure 8.10. Hence, the rCBV values and the rCBV changes of L_4 suddenly increase after t_3 matching the estimated transformation point in time. Due to the large tumor extent of L_3, a reduction of the number of curves is necessary, see Figure 8.11. Still, no rapid rCBV value increase can be observed due to the oligodendroglioma type.

How Can Visual Exploration and Analysis of Longitudinal Studies Be Carried Out?

A possible user scenario is carried out in the following way. First, the preprocessing pipeline provides co-registered rCBV parameter maps. Now, the clinical researcher starts with the spatial 3D cut-out view for a first overview. Next, the data sets are analyzed in the rCBV profile curve view and the 2D rCBV maps. Hence, the transformation time step can be estimated by examining the rCBV curves, the rCBV change curves, or scalar values of rCBV. The analysis involves combinations of the rCBV threshold selection and the rCBV curve index selection (see Fig. 8.7(c), 8.8(c), 8.9(c), and 8.10(c)) to determine the most malignant tumor part for tumor grading or stereotactic biopsy. Hence, the region marked with an arrow in Figure 8.9(c) exhibits only moderate rCBV, but these voxels belong to the selected curve indices. Thus, this

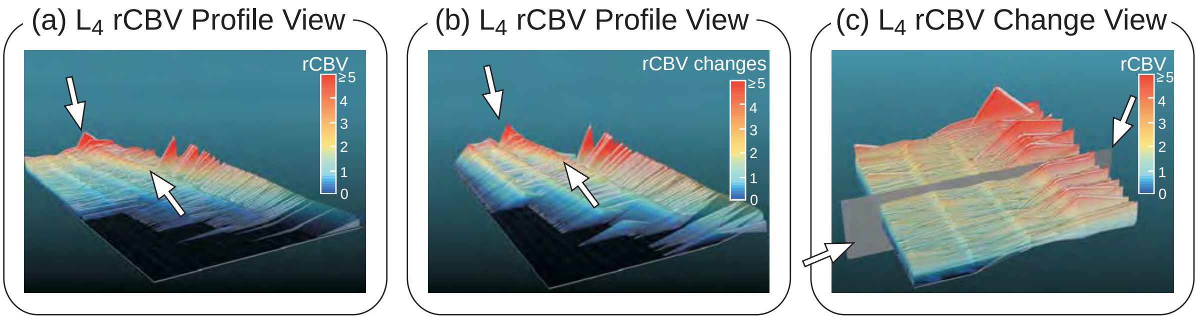

Figure 8.10: *The rCBV profile view (a) and the rCBV change profile view (b) of L_4 reveal increased rCBV values and changes, marked with arrows, after t_3 – matching the estimated transformation starting time. In (c), an rCBV curve index selection is carried out by applying the selection plane (see arrows). From all rCBV curves, the n (n=300) curves, ordered by their integral, are selected. The selection for L_4 yields the example in Figure 8.9(c).*

tumor part may be one of the most malignant parts since these voxels correspond to rCBV curves with the highest curve indices, i.e., the highest integrals.

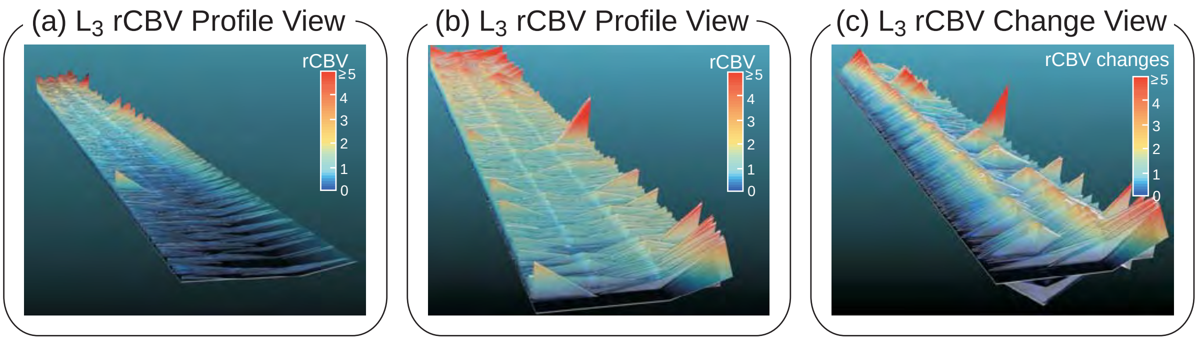

Figure 8.11: *Depiction of the rCBV profile view in (a). In (b), the rCBV threshold selection is applied and thus, the number of curves is reduced. In (c), the rCBV change view for selected curves is provided.*

In summary, for all tumors but the oligodendroglioma of L_3, the transformation time step (which initially was estimated also based on structural MRI sequences) could be approximated with the application employing only the perfusion data sets (recall Sect. 8.2.2).

8.5 Conclusion

In this chapter, an application for the evaluation of longitudinal brain perfusion studies focusing on the development of LGGs within the context of clinical research was presented, recall also the two brain tumor aspects in the conclusion of Chapter 4. A preprocessing pipeline enables the simultaneous evaluation of tumor localization, tumor size, and rCBV values of all perfusion scans. The visual analysis techniques include linked 2D parameter maps, a 3D overview, and the new 3D rCBV profile view that represents all rCBV values of all voxels at all time steps. Once the user examined the LGGs temporal development and the point in time of a starting LGG transformation, the analysis can be restricted to foci with high rCBV values and local tumor heterogeneity. Combination of the different views as well as selecting a set of voxels, which may represent the most malignant tumor part is carried out with lenses in the 2D views, the rCBV threshold selection, and the rCBV curve index selection. The resulting voxel set can be used for ROI placement for tumor grading or stereotactic biopsy.

Without the presented application, a clinician would have to mentally integrate scans of the same study acquired at earlier time steps to evaluate the LGG progression. In addition, the application prevents vessel voxels to be integrated in ROIs and thus avoids distortions of rCBV averaging. The clinical partners did especially like the rCBV change profile view depicting each voxel's rCBV changes due to their ability to visualize the temporal development. Hence, the tumor changes are analyzed for a retrospective evaluation. However, with the heterogeneity analysis based on the LCC, additional information is provided to guide a stereotactic biopsy.

The framework is a prototype application for clinical research and may be adapted to longitudinal studies of breast and prostate tumors where perfusion data is acquired for diagnosis and treatment monitoring. Due to the growing number of longitudinal medical image data and the general need of comparison of sequenced image data (e.g., cohort study data), an increasing demand for visual exploration and analysis of this kind of medical data is expected.

9. Summary and Outlook

9 Summary and Outlook

The diagnosis of cancer includes the detection of signs and symptoms, screening tests, and medical imaging. Especially the medical imaging has gained increased importance due to substantial improvements regarding the image quality. These data sets become larger and more complex. To improve and support the radiologist's work, advanced methods including visual analytic solutions are required. Hence, perfusion imaging plays an important role for the evaluation of breast cancer due to its high sensitivity as well as for monitoring low grade gliomas in brain tumor imaging. This thesis contributes to an improved diagnosis of low grade gliomas and breast tumor perfusion MRI data sets. The contributions, motivated by the nine aspects $\boxed{1}$ - $\boxed{9}$ in Chapter 4 can be summarized as follows:

1. Visual Analysis and Exploration of Breast Tumor DCE-MRI Data.
2. Visual Analysis and Exploration of Longitudinal Brain Tumor DSC-MRI Data.
3. Region-based Division and Analysis of the Whole Lesion.
4. Characterization of Tumor Heterogeneity via Kinetic Features.
5. Suitability of Heterogeneity Features for the Automatic Classification of Breast Tumors.

9.1 Summary

In this section, the contributions will be explained in more detail.

1. Visual Analysis and Exploration of Breast Tumor DCE-MRI Data.

The PerfusionAnalyzer is a software prototype covering multiple linked views with the integrated 2D visual exploration techniques for the evaluation of breast tumor perfusion data. Beyond standard views, e.g., color-coded 2D parameter maps of relative enhancement (RE) values or subtraction views, also novel visualization techniques were integrated. The lesion detection and delineation was implemented with a volume growing method. The voxel-wise glyph-based visualization allows for a fast overview of data sets and allows for a finer classification of RE values than the three-time-point (3TP) method. The voxel-wise glyph assignment avoids interpolation and distortion due to average RE curves. The region merging segmentation on the other hand reduces the influence of outliers. With the integrated region merging method, employing a descriptive perfusion parameter-based feature vector, a semi-automatic subdivision of a suspicious tumor into different regions is established. The most suspect region can be employed as region of interest (ROI). Since a region contains similarly perfused voxels, the distortion of the average RE curve of the ROI as well as the inter-observer variability concerning the ROI's placement is reduced.

Beyond the kinetic evaluation, a new multiplanar reformation (MPR) view was designed and integrated to account for the tumor's morphology. The FileCardBrowser View is adapted to each tumor, i.e., it creates a new MPR plane that is adapted to the tumor's extent. The presented examples illustrated the main advantages of this method: the improved boundary evaluation as well as the identification of spatially connected and similarly perfused regions. While the first one allows for a better evaluation of the tumor's morphology, the second one is important for further treatment planning. Therefore, the kinetic evaluation can be combined with this additional technique.

A further extension is the combination of T_1- and T_2-weighted breast MRI scans. The joint inspection of both sequences is important for differential diagnosis when evaluating breast cancer. In particular, it allows to distinguish between benign cyst-type and malignant lesions. In clinical practice, both images are regarded independently and immediate correlation is prevented by patient motion and tissue deformations. With the integrated lens view, the radiologist can visually combine the MRI sequences for a faster diagnosis without the effort of mentally integrating both images.

2. Visual Analysis and Exploration of Longitudinal Brain Tumor DSC-MRI Data.

The presented application for the evaluation of longitudinal brain DSC-MRI perfusion studies focuses on the development of LGGs within the context of clinical research. A preprocessing pipeline enables the simultaneous evaluation of tumor localization, size, and rCBV values of all perfusion scans. The visual analysis techniques include linked 2D parameter maps, a 3D overview, and the new 3D rCBV profile view that represents all rCBV values of all voxels at all time steps. Once the user examined the LGGs temporal development and the point in time of a starting LGG transformation, the analysis can be restricted to foci with high rCBV values and local tumor heterogeneity. The combination of the different views as well as the selection of a set of voxels which may represent the most malignant tumor part is carried out with lenses in the 2D views, the rCBV threshold selection, and the rCBV curve index selection.

3. Region-Based Division and Analysis of the Whole Lesion.

The presented frameworks and approaches have the important advantage that the whole lesion is taken into account. In contrast, existing approaches are mostly limited to certain samples, slices, or parts of the data set. The presented classification approaches for breast tumor data took the whole lesion into account (in terms of global features) as well as the tumor's most suspect region (MSRegion). The region-based division of the data and the automatic identification of the MSRegion avoid inter- and intra-observer variability. Hence, the error-prone and time-consuming manual ROI placement is obsolete. The MSRegion can be employed for further diagnosis like core needle biopsy.

Likewise, the framework for exploration of longitudinal brain tumors allows for a selection of a voxel set with high rCBV values. This set can be used for ROI placement for tumor grading or stereotactic biopsy. Without the framework, a clinician would have to mentally integrate scans of the same study acquired at earlier time steps to evaluate the LGG progression.

With the 3D ClusterView, a well-suited visualization of the region-based tumor division has been presented. Hence, the geometric modeling enhances cluster connections. Conventional

3D views are often hampered due to occlusion of inner tumor parts. Moreover, no further information can be extracted. Therefore, the 3D ClusterView is completed with a necklace map legend and each cluster can be easily selected. The 3D ClusterView was successfully adapted to brain tumor data and is well suited for any clustered medical tomographic image data. Due to the increased complexity of medical image data, the biomedical expert will be definitely confronted with the problem of an effective clustering of her or his data in the future. For the qualitative evaluation of the clustering result, the 3D ClusterView should be the visualization of choice.

4. Characterization of Tumor Heterogeneity via Kinetic Features.

The presented techniques within the two different application areas of breast and brain tumor diagnosis have a strong focus on the heterogeneity of the kinetic contrast enhancement.

The clustering results for breast tumor data sets were compared with external cluster validation indices. A variety of features with focus on kinetic contrast enhancement were extracted and their usefulness was demonstrated with further classification approaches.

For the longitudinal brain perfusion scan, the heterogeneity was assessed in a qualitative way by analyzing the correlation of the quantitative perfusion parameters CBV and CBF via the linear correlation coefficient measure (LCC) [Cachier and Pennec, 2000]. The clinical expert can explore the CBV as well as the LCC parameter maps with lenses. However, with the heterogeneity analysis based on the LCC, additional information is provided to guide a stereotactic biopsy.

5. Suitability of Heterogeneity Features for the Automatic Classification of Breast Tumors.

For the small breast tumors, a quantitative heterogeneity analysis was carried out including four complex automatic classification approaches. All classification approaches have been carried out on the *Breast Tumor Database 2009* to achieve comparable results. This database is special since it contains small breast tumors that could only be detected in DCE-MRI and are even hard to separate for a human expert. Based on the requirements of ROIs, i.e., groups of spatially connected voxels with similar perfusion characteristics, the methods in Chapter 7 analyze how such ROIs can be employed for automatic classification.

The first classification approach is a general approach combining kinetic and morphological features and was conducted within the clinical environment. The first classification approach yields a better discriminative power for heterogeneity related features than the analysis of single perfusion parameters and enhancement curve types. These findings inspired the following classification approaches. The focus was set on detecting the MSRegion of a tumor as well as on improved heterogeneity analysis based on the enhancement kinetics.

The second classification approach adapts the density-based clustering. A decision tree classifier is learned to ensure that the model is human readable and the most important features for the classification become visible. Although only 46 of 68 tumors could be correctly classified by the learned classifier, the most important features for distinguishing between benign and malignant tumors were related to the heterogeneity of the tumor enhancement kinetics and the patient's age.

The new aspect of the third classification approach is the concentration on the features of the MSRegion found through clustering, rather than the features of all clusters, i.e., the whole lesion. As a result, the clustering, i.e., the grouping of voxels into regions is more important for classification instead of the extraction of complex ensembles. Most important, the method yields a feature set that is best suited to automatically determine tumor malignancy (with 56 of 68 correctly classified tumors) based on the heterogeneity of tumor enhancement kinetics and patient's age as well as tumor size.

The contribution of the fourth classification approach is the adaption of spectral clustering to breast DCE-MRI tumors. Thus, spatially connected homogeneous regions are obtained. Although the classification result could not be improved, this approach is well suited for identification of appropriate tumor parts for core needle biopsy.

The presented classification approaches are superior to simple rules of thumb. Apart from the semi-automatic extraction of the lesion, all classification approaches are fully automatic, i.e., no user input is necessary like the pre-definition of number of clusters etc. Therefore, the classifiers are well suited and universally compatible for breast tumor data sets independent of specific scanning protocols or parameters. In conclusion, a combination of the reported features and the region formation can be easily integrated within the clinical work flow and support the radiologist when finding a tumor's most malignant part and to rate the tumor's malignancy.

In summary, a very special property of the thesis at hand (originating with a strong focus on visualization and visual analysis), is the adaption to a broad range of patients, covering a breast tumor database with 68 lesions as well as a rare set of 4 longitudinal brain tumor perfusion studies that all consist of low grade gliomas that transform into high grade gliomas. Thus, the proposed methods could be tested with real application data. The second remarkable attribute is the concrete clinical research focus on automatic classification of breast cancer. The developed visualizations and techniques were employed as input for a classification approach, which was step by step refined and yields results that are comparable or even better to related studies in literature.

9.2 Drawbacks and Limitations

The presented techniques were closely adapted to the DCE-MRI and DSC-MRI data sets. Although these concrete clinical scenarios bear great potential for application-oriented software development, they are also accompanied by some drawbacks and limitations. These are grouped into

- data-based constraints,
- application-based constraints, and
- medical constraints.

9.2.1 Data-Based Constraints

Data-based constraints comprise the moderate temporal resolution for breast DCE-MRI and the moderate spatial resolution for brain DSC-MRI, respectively. Futhermore, MRI is prone to various artifacts, e.g, inhomogeneities of the magnetic field. More important, motion artifacts hamper the evaluation of the contrast enhancement per voxel. Improved imaging modalities will reduce these obstacles. Also, dedicated motion correction approaches could further improve the inter-pixel correspondence. The promising approach by Schäfer et al. [2011] includes pharmacokinetic modelling for an improved motion correction of breast DCE-MRI data. However, as it is stated by Behrens et al. [2007], an appropriate fitting would require a higher temporal resolution. On the other hand, high spatial resolution is necessary for identification of small lesions.

9.2.2 Application-Based Constraints

The presented approaches are based upon the evaluation of a clustering result and thorough analysis of perfusion parameter values, i.e., the relative cerebral blood volume. Hence, a gold standard for clustering is missing. Furthermore, ”the validation of clustering structures is the most difficult and frustrating part of cluster analysis [Jain and Dubes, 1988]“. A sophisticated study with medical experts that manually subdivide a tumor in MRI data with respect to histopathologic differences within a clinical environment would be a great gain for this application area. Likewise to the lack of a clustering ground truth, the adapted 3TP classification should be raised to question. An extensive clinical study is needed to asses whether the adapted 3TP method classification is reliable with current DCE-MRI scanning protocols. Other concepts for an external cluster validation are needed to confirm the appropriateness of the presented clustering methods. Also, no gold standard for rCBV cut-off values exists. However, with increasing MRI studies of brain tumors and more standardized evaluation criteria, such cut-off values might be formed in the future.

9.2.3 Medical Constraints

The main drawback of the proposed case studies is the missing of typical benign tumors or healthy patients. Although the longitudinal studies of the brain give insight to a transformation from low grade to high grade tumor, the low grade tumors were acquired at an advanced stage, i.e., no scan of the same patient without any tumor burden was available. Likewise, the *Breast Tumor Database 2009* contains benign lesions. However, the benign lesions were suspicious enough to justify biopsy or follow-up evaluation. In future, a systematic evaluation should be combined with a cohort study like the SHIP study [Völzke et al., 2011], comprising MRI scans of the body. Then, the adaption of computer-aided detection and diagnosis can be carried out on a whole new level.

It is expected that the limited standardized evaluation of tumor morphology will be improved in the next years. Hence, morphology-based features will be gain more importance for automatic tumor classification approaches.

Another drawback is the supplemental character of perfusion imaging. This thesis strongly focuses on this imaging modality. However, in clinical practice, rather the combination of different image modalities (e.g. X-ray and MRI) with patient-specific attributes (e.g. genetic risk factors) is indispensable for a complete diagnosis. Finally, an important restriction of the presented methods for breast tumor evaluation is the focus on kinetic contrast agent enhancement features. As presented by Jansen et al. [2008] for breast tumors in DCE-MRI, these features are inappropriate for non-mass like enhancing lesions. Future work could include a preselection. Dependent on the tumor's properties, different feature sets (e.g. a feature set describing the tumor's morphology and another feature set with focus on kinetic features) could be employed for further analysis. Hence, the study by Montemurro et al. [2007] reports poor classification results for the Göttinger score [Fischer et al., 1999] of intermediate-low suspicious DCE-MRI lesions, which further strengthens the need for lesion adapted feature sets.

9.3 Future Potential

For future work, the extension of the presented methods for breast and brain tumor MRI is dicussed first. Afterwards, the transferability to other medical application areas is described.

For the improved evaluation of breast tumor perfusion data, an automatic extraction of morphology features should be developed. Based on the Göttinger score [Fischer et al., 1999], automatic computer-based classification algorithms should extract the values for the lesion margin and the lesion shape (based on the DCE-MRI sequence) and combine it with the presented classification approaches of this thesis. Furthermore, Malich et al. [2005] extended the Göttinger score with features from the T_2-weighted breast MRI data. Also, Behrens et al. [2007] suggested a combination of T_2-based features for improved classification results. With the co-registration of T_2-weighted breast MRI as proposed by Böhler [2011], a software framework could *automatically* extract these features. Thus, our approach described in [Boehler et al., 2011] can be integrated in the classification step. Then, automatically derived T_2-based features will be included in the feature set. The next step for brain tumor evaluation is an adaption of the classification methods that were developed for the breast tumor data sets. Although the evaluation of brain tumor DCS-MRI strongly focuses on rCBV analysis, a feature set (like rCBV mean, rCBV median etc.) can be built up by employing the rCBV histogram as proposed by Friedman et al. [2012].

For future work, the presented methods can be transferred to other medical application areas involving MR perfusion data. An example is prostate cancer evaluation. Hence, T_2-weighted MR images are acquired to locate the cancer. Franiel et al. [2011] presented a comprehensive overview dealing with the importance of DCE-MRI for prostate cancer due to the additional DCE-MRI-derived features. DCE-MRI is increasingly employed for extraction of pharmacokinetic parameters and for assessment of the tumor's aggressiveness. Prostate cancer also exhibits neoangiogenesis, increased heterogeneity, and vessel permeability with increased malignancy [Franiel et al., 2011]. Therefore, this research area is well-suited for the adaption of the presented classification approaches. In a first step, the feature sets proposed in this thesis can be extended with the pharmacokinetic parameters. Next, clustering can be employed. Hence, the same concepts for heterogeneity assessment can be applied. Prostate cancer and abnormal but non-cancerous conditions like fibrosis, prostatitis or hemorrhage exhibit similar signal intensities in T_2-weighted MRI. Thus, in a second step, a classifier (by extending the presented classifiers in this thesis) can be trained to discriminate between prostate cancer and these pathologies. Another promising application area is renal perfusion data [Zöllner et al., 2009]. Here, k-means clustering is employed for the subdivision into different kidney compartments (i.e., cortex, medulla, and pelvis). This analysis could be extended with the presented heterogeneity-based methods of this thesis. Therefore, the k-means clustering can be compared to a density-based clustering result. Next, features (e.g., the Jaccard coefficient) describing the heterogeneity of perfusion can be extracted.

In general, the visual analysis and exploration adapted to specific medical applications has great potential. The increasing amount and size of medical data sets demands for computer-aided support. For the group of cancer-related diseases, incidence rates increase due to improved cancer screening and medical image acquisitions. Visual analysis techniques for breast and brain tumors play an important role for the detection of cancer as well as its most suspect tumor part and may replace the error-prone manual ROI definition. Furthermore, with increasing number of longitudinal studies, visual analysis techniques are appropriate to evaluate a tumor's temporal development. On the other side, clinical applications for automatic tumor classification are usually rated based on the comparison with the diagnosis result of medical doctors. Published studies in literature do not contain a solution for the perfect tumor classification based on perfusion MRI. This is also reflected by the results of this thesis: the character of perfusion MRI remains supplemental to the prevailing imaging methods in clinical practice. However, the presented frameworks could successfully improve the current state-of-the-art evaluation.

Bibliography

W. Aigner, S. Miksch, W. Müller, H. Schumann, and C. Tominski. Visual Methods for Analyzing Time-Oriented Data. *IEEE Transaction on Visualization and Computer Graphics (TVCG)*, 14(1):47–60, 2008.

American College of Radiology. *Breast Imaging Reporting and Data System Atlas (BI-RADS(r) Atlas)*. Reston, Va, 2003.

M. Ankerst, M. M. Breunig, H.-P. Kriegel, and J. Sander. OPTICS: Ordering Points to Identify the Clustering Structure. In *Proc. ACM SIGMOD Int. Conf. on Management of Data*, volume 28, pages 49–60, 1999.

M. Aono and M. Kobayashi. Text Document Cluster Analysis Through Visualization of 3D Projections. Technical report, IBM Research - Tokyo, 2011.

J. Ashburner, J. G. Csernansk, C. Davatzikos, N. C. Fox, G. B. Frisoni, and P. M Thompson. Computer-Assisted Imaging to Assess Brain Structure in Healthy and Diseased Brains. *The Lancet Neurology*, 2(2):79 – 88, 2003.

S. Bachthaler and D. Weiskopf. Continuous Scatterplots. *IEEE Transactions on Visualization and Computer Graphics (TVCG)*, 14(6):1428–1435, 2008.

P. A. T. Baltzer, D. M. Renz, P. E. Kullnig, M. Gajda, O. Camara, and W. A. Kaiser. Application of Computer-Aided Diagnosis (CAD) in MR-mammography (MRM): Do We Really Need Whole Lesion Time Curve Distribution Analysis? *Acad Radiol*, 16(4):435–442, 2009.

E. L. Barbier, J. A. den Boer, A. R. Peters, A. R. Rozeboom, J. Sau, and A. Bonmartin. A Model of the Dual Effect of Gadopentetate Dimeglumine on Dynamic Brain MR Images. *J Magn Reson Imaging*, 10(3):242–253, 1999.

S. Behrens, H. Laue, M. Althaus, T. Boehler, B. Kuemmerlen, H. K. Hahn, and H.-O. Peitgen. Computer Assistance for MR Based Diagnosis of Breast Cancer: Present and Future Challenges. *Computerized Medical Imaging and Graphics*, 31(4-5):236 – 247, 2007.

T. Böhler, S. Glaßer, and H.-O. Peitgen. Deformable Registration of Differently-Weighted Breast Magnetic Resonance Images. In *Proc. of Bildverarbeitung für die Medizin (BVM)*, pages 94–98, 2011.

E. A. Bier, M. C. Stone, K. Pier, W. Buxton, and T. D. DeRose. Toolglass and Magic Lenses: the See-Through Interface. In *Proc. of ACM SIGGRAPH*, pages 73–80, 1993.

S. Bisdas, M. Kirkpatrick, P. Giglio, C. Welsh, M. V. Spampinato, and Z. Rumboldt. Cerebral Blood Volume Measurements by Perfusion-Weighted MR Imaging in Gliomas: Ready for Prime Time in Predicting Short-Term Outcome and Recurrent Disease? *AJN*, 30(4):681–688, 2009.

A. Bjørnerud. The ICE Software Package: Direct Co-Registration of Anatomical and Functional Datasets Using DICOM Image Geometry Information. In *Proc. of Human Brain Mapping*, volume 19, page 1018p, 2003.

A. Bjørnerud and K. E. Emblem. A Fully Automated Method for Quantitative Cerebral Hemodynamic Analysis Using DSC–MRI. *Journal of Cerebral Blood Flow & Metabolism*, 30: 1066–1078, 2010.

J. Blaas, C. P. Botha, and F. H. Post. Interactive Visualization of Multi-Field Medical Data Using Linked Physical and Feature-Space Views . In *IEEE/Eurographics Symposium on Visualization (EuroVis)*, pages 123–130, 2007.

James F. Blinn. A Generalization of Algebraic Surface Drawing. *ACM Trans. Graph.*, 1(3): 235–256, 1982.

T. Boehler, S. Glaßer, and H.-O. Peitgen. Deformable Registration of Differently-Weighted Breast Magnetic Resonance Images. In *Proc. of Bildverarbeitung für die Medizin*, pages 94–98, 2011.

M. Bögl, W. Aigner, P. Filzmoser, T. Lammarsch, S. Miksch, and A. Rind. Visual Analytics for Model Selection in Time Series Analysis. *IEEE Transactions on Visualization and Computer Graphics (TVCG)*, 19(12):2237–2246, 2013.

T. Böhler. *Deformable Image Registration Methods for Clinical Applications of Magnetic Resonance Mammography*. PhD thesis, University of Bremen, 2011.

D. Borland and R. M Taylor. Rainbow Color Map (Still) Considered Harmful. *IEEE Computer Graphics and Applications*, 27(2):14–17, 2007.

J. L. Boxerman, L. M. Hamberg, B. R. Rosen, and R. M. Weisskoff. MR Contrast due to Intravascular Magnetic Susceptibility Perturbations. *Magn Reson Med*, 34(4):555–566, 1995.

J. L. Boxerman, K. M. Schmainda, and R. M. Weisskoff. Relative Cerebral Blood Volume Maps Corrected for Contrast Agent Extravasation Significantly Correlate With Glioma Tumor Grade, Whereas Uncorrected Maps Do Not. *AJN*, 27(4):859–867, 2006.

L. D. Buadu, J. Murakami, S. Murayama, N. Hashiguchi, S. Sakai, K. Masuda, S. Toyoshima, S. Kuroki, and S. Ohno. Breast Lesions: Correlation of Contrast Medium Enhancement Patterns on MR Images With Histopathologic Findings and Tumor Angiogenesis. *Radiology*, 200(3):639–649, 1996.

P. Cachier and X. Pennec. Non-rigid Registration by Gradient Descent on a Gaussian-windowed Similarity Measure Using Convolutions. In *Proc. of IEEE Mathematical Methods in Biomedical Image Analysis (MMBIA)*, pages 182–189, 2000.

F. Calamante. Quantification of Dynamic Susceptibility Contrast T_2^* MRI in Oncology. In A. Jackson, D. L. Buckley, and G. J. M. Parker, editors, *Dynamic Contrast-Enhanced Magnetic Resonance Imaging in Oncology*, pages 53 – 67. Springer-Verlag Berlin Heidelberg, 2005.

F. Calamante, D. L. Thomas, G. S. Pell, J. Wiersma, and R. Turner. Measuring Cerebral Blood Flow Using Magnetic Resonance Imaging Techniques. *J Cereb Blood Flow Metab*, 19(7): 701–735, 1999.

Tadeusz Caliński and Jerzy Harabasz. A Dendrite Method for Cluster Analysis. *Communications in Statistics-theory and Methods*, 3(1):1–27, 1974.

P. Caravan, J. J. Ellison, T. J. McMurry, and R. B. Lauffer. Gadolinium(III) Chelates as MRI Contrast Agents: Structure, Dynamics, and Applications. *Chem Rev*, 99(9):2293–2352, 1999.

W. Chen, M. L. Giger, L. Lan, and U. Bick. Computerized Interpretation of Breast MRI: Investigation of Enhancement-Variance Dynamics. *Medical Physics*, 31:1076, 2004.

W. Chen, M. L. Giger, and U. Bick. A Fuzzy C-Means (FCM)-Based Approach for Computerized Segmentation of Breast Lesions in Dynamic Contrast-Enhanced MR Images. *Academic Radiology*, 13(1):63–72, 2006a.

W. Chen, M. L. Giger, U. Bick, and G. M. Newstead. Automatic Identification and Classification of Characteristic Kinetic Curves of Breast Lesions on DCE-MRI. *Medical Physics*, 33 (8):2878–2887, 2006b.

W. Chen, M. L. Giger, H. Li, U. Bick, and G. M. Newstead. Volumetric Texture Analysis of Breast Lesions on Contrast-Enhanced Magnetic Resonance Images. *Magn Reson Med*, 58 (3):562–571, 2007.

W. S. Cleveland. *The Elements of Graphing Data*. Wadsworth, Monterey, 1985.

Collaborative Group on Hormonal Factors in Breast Cancer. Breast Cancer and Breastfeeding: Collaborative Reanalysis of Individual Data from 47 Epidemiological Studies in 30 Countries, including 50302 Women with Breast Cancer and 96973 Women without the Disease. *Lancet*, 360(9328):187–195, 2002.

E. Coto, S. Grimm, S. Bruckner, E. Gröller, A. Kanitsar, and O. Rodriguez. Mammo Explorer: An Advanced CAD Application for Breast DCE-MRI. In *Proc. of Vision, Modeling, and Visualization (VMV)*, pages 91–98, 2005.

D. J. Covarrubias, B. R. Rosen, and M. H. Lev. Dynamic Magnetic Resonance Perfusion Imaging of Brain Tumors. *The Oncologist*, 9(5):528–537, 2004.

P. Craig, A. Cannon, R. Kukla, and J. Kennedy. MaTSE: The Microarray Time-Series Explorer. In *Proc. of IEEE Biological Data Visualization (BioVis)*, pages 41–48, 2012.

A. Dasgupta and R. Kosara. Pargnostics: Screen-Space Metrics for Parallel Coordinates. In *Proc. of IEEE Visual Analytics Science and Technology (VAST)*, volume 16, pages 1017–1026, 2010.

A. Dasgupta, R. Kosara, and L. Gosink. Meta Parallel Coordinates for Visualizing Features in Large, High-Dimensional, Time-Varying Data. In *Proc. of IEEE Large Data Analysis and Visualization*, pages 85–89, 2012.

M. Daszykowski, B. Walczak, and D. L. Massart. Looking for Natural Patterns in Data. Part 1: Density Based Approach. *Chemometrics and Intelligent Laboratory Systems*, 56:83–92, 2001.

I. Davidson and S. S. Ravi. Clustering with Constraints: Feasibility Issues and the k-Means Algorithm. In *Proc. of SIAM Int. Conf. on Data Mining*, 2005.

G. E. Davidyan. Interactive Agricultural Ecological Atlas of Russia and Neighboring Countries. Economic Plants and their Diseases, Pests and Weeds. [Online], 2008. URL `http://www.agroatlas.ru/en/content/pests/Chaetocnema_concinna/`.

D. L. Davies and D. W. Bouldin. A cluster separation measure. *IEEE Transactions on Pattern Analysis and Machine Intelligence*, 1(2):224–227, 1979.

H. Degani, V. Gusis, D. Weinstein, S. Fields, and S. Strano. Mapping Pathophysiological Features of Breast Tumors by MRI at High Spatial Resolution. *Nat Med*, 3:780–782, 1997.

A. P. Dempster, N. M. Laird, and D. B. Rubin. Maximum Likelihood from Incomplete Data via the EM Algorithm. *Journal of the Royal Statistical Society. Series B (Methodological)*, pages 1–38, 1977.

H. Doleisch and H. Hauser. Smooth Brushing for Focus+Context Visualization of Simulation Data in 3D. In *Proc. of Winter School of Computer Graphics (WSCG)*, pages 147–154, 2002.

H. Doleisch, M. Gasser, and H. Hauser. Interactive Feature Specification for Focus+Context Visualization of Complex Simulation Data. In *Joint Eurographics / IEEE TCVG Symposium on Visualization (VisSym)*, pages 239–248, 2003.

K. M. Donahue, H. G. Krouwer, S. D. Rand, A. P. Pathak, C. S. Marszalkowski, S. C. Censky, and R. W. Prost. Utility of Simultaneously Acquired Gradient-Echo and Spin-Echo Cerebral Blood Volume and Morphology Maps in Brain Tumor Patients. *Magn Reson Med*, 43(6): 845–853, 2000.

J. C. Dunn. A Fuzzy Relative of the ISODATA Process and Its Use in Detecting Compact Well-Separated Clusters. *Journal of Cybernetics*, 3(3):32–57, 1973.

C. W. Elston and I. O. Ellis. Pathological Prognostic Factors in Breast Cancer. I. The Value of Histological Grade in Breast Cancer: Experience from a Large Study with Long-Term Follow-Up. *Histopathology*, 19(5):403–410, 1991.

K. E. Emblem, B. Nedregaard, T. Nome, P. Due-Tonnessen, J.K. Hald, D. Scheie, O. Casar Borota, M. Cvancarova, and A. Bjørnerud. Glioma Grading by Using Histogram Analysis of Blood Volume Heterogeneity from MR-derived Cerebral Blood Volume Maps. *Radiology*, 247(3):808–817, 2008.

K. H. Englmeier, G. Hellwig, J. Griebel, S. Delorme, M. Siebert, and G. Brix. Morpho-Functional Visualization of Dynamic MR-Mammography. *Stud Health Technol Inform*, 107(2):838–841, 2004.

G. Ertaş, H. O. Gülçür, and M. Tunaci. Improved Lesion Detection in MR Mammography: Three-Dimensional Segmentation, Moving Voxel Sampling, and Normalized Maximum Intensity-Time Ratio Entropy. *Acad Radiol*, 14(2):151–161, 2007.

M. Ester, H.-P. Kriegel, J. Sander, and X. Xu. A Density-Based Algorithm for Discovering Clusters in Large Spatial Databases with Noise. In *Proc. of Knowledge Discovery and Data Mining*, pages 226–231, 1996.

B. Fischer and J. Modersitzki. Curvature Based Registration with Applications to MR-Mammography. In *Computational Science —ICCS*, pages 202–206. Springer, 2002.

U. Fischer, L. Kopka, and E. Grabbe. Breast Carcinoma: Effect of Preopartive Contrast-enhanced MR Imaging on the Therapeutic Approach. *Radiology*, 213:881–888, 1999.

J. Folkman. What is the Evidence That Tumors are Angiogenesis Dependent? *J Natl Cancer Inst*, 82(1):4–6, 1990.

J. Folkman. Angiogenesis in Cancer, Vascular, Rheumatoid and other Disease. *Nat Med*, 1(1): 27–31, 1995.

T. Franiel, B. Hamm, and H. Hricak. Dynamic Contrast-Enhanced Magnetic Resonance Imaging and Pharmacokinetic Models in Prostate Cancer. *European Radiology*, 21(3):616–626, 2011. ISSN 0938-7994.

S.N. Friedman, P.J. Bambrough, C. Kotsarini, N. Khandanpour, and Hoggard N. Semi-Automated and Automated Glioma Grading Using Dynamic Susceptibility-Weighted Contrast-Enhanced Perfusion MRI Relative Cerebral Blood Volume Measurements. *Br J Radiol*, 85:e1204 – 11, 2012.

E. Furman-Haran, D. Grobgeld, R. Margalit, and H. Degani. Response of MCF7 Human Breast Cancer to Tamoxifen: Evaluation by the Three-Time-Point, Contrast-Enhanced Magnetic Resonance Imaging Method. *Clin Cancer Res*, 4(10):2299–2304, 1998.

E. Furman-Haran, D. Grobgeld, F. Kelcz, and H. Degani. Critical Role of Spatial Resolution in Dynamic Contrast-Enhanced Breast MRI. *J Magn Reson Imaging*, 13:862–867, 2001.

R. Fusco, M. Sansone, C. Sansone, and A. Petrillo. Segmentation and Classification of Breast Lesions Using Dynamic and Textural Features in DCE-MRI. In *Proc. of Computer-Based Medical Systems (CBMS)*, pages 1–4, 2012.

Y. Ge, R. I. Grossman, J. K. Udupa, J. S. Babb, D. L. Kolson, and J. C. McGowan. Magnetization Transfer Ratio Histogram Analysis of Gray Matter in Relapsing-Remitting Multiple Sclerosis. *AJNR*, 22(3):470–475, 2001.

P. Gibbs and L. W. Turnbull. Textural Analysis of Contrast-Enhanced MR Images of the Breast. *Magn Reson Med*, 50(1):92–98, 2003.

S. Glaßer, K. Scheil, U. Preim, and B. Preim. The File-Card-Browser View for Breast DCE-MRI Data. In *Proc. of Bildverabeitung für die Medizin (BVM)*, pages 314–318, 2011.

S. Glaßer, U. Niemann, B. Preim, and M. Spiliopoulou. Can we Distinguish Between Benign and Malignant Breast Tumors in DCE-MRI by Studying a Tumor's Most Suspect Region Only? In *Proc. of Symposium on Computer-Based Medical Systems (CBMS)*, page to appear, 2013a.

S. Glaßer, U. Niemann, U. Preim, B. Preim, and M. Spiliopoulou. Classification of Benign and Malignant DCE-MRI Breast Tumors by Analyzing the Most Suspect Region. In *Proc. of Bildverarbeitung für die Medizin (BVM)*, pages 45–50, 2013b.

S. Glaßer, S. Oeltze, A. Bjørnerud, U. Preim, B. Preim, and H. Hauser. Visual Analysis of Longitudinal Brain Tumor Perfusion. In *Proc. of SPIE 8670 Medical Imaging*, page 86700Z, 2013c.

S. Glaßer, K. Lawonn, and B. Preim. Visualization of 3D Cluster Results for Medical Tomographic Image Data. In *Proc. of Conference on Computer Graphics Theory and Applications (VISIGRAPP/GRAPP)*, pages 169–176, 2014a.

S. Glaßer, S. Roscher, and B. Preim. Adapted Spectral Clustering for Evaluation and Classification of DCE-MRI Breast Tumors. In *Proc. of Bildverarbeitung für die Medizin (BVM)*, pages 198–203, 2014b.

S. Glaßer, S. Schäfer, S. Oeltze, U. Preim, K. D. Tönnies, and B. Preim. A Visual Analytics Approach to Diagnosis of Breast DCE-MRI Data. In *Proc. of Vision, Modeling, and Visualization (VMV)*, pages 351–362, 2009.

S. Glaßer, U. Preim, K. Tönnies, and B. Preim. A Visual Analytics Approach to Diagnosis of Breast DCE-MRI Data. *Computers & Graphics*, 34(5):602–611, 2010.

H. Gray. *Anatomy of the Human Body. Philadelphia: Lea & Febiger, 1918.* Bartleby.com, 2000.

D. L. Gresh, B. E. Rogowitz, R. L. Winslow, D. F. Scollan, and C.K. Yung. WEAVE: A System for Visually Linking 3-D and Statistical Visualizations, Applied to Cardiac Simulation and Measurement Data. In *Proc. of IEEE Visualization*, pages 489–92, 2000.

I. S. Gribbestad, K. I. Gjesdal, G. Nilsen, S. Lundgren, M. H. B. Hjelstuen, and A. Jackson. An Introduction to Dynamic Contrast-Enhanced MRI in Oncology. In A. Jackson, D. L. Buckley, and G. J. M. Parker, editors, *Dynamic Contrast-Enhanced Magnetic Resonance Imaging in Oncology*, pages 3 – 22. Springer-Verlag Berlin Heidelberg, 2005.

T. Günther, K. Bürger, R. Westermann, and H. Theisel. A View-Dependent and Inter-Frame Coherent Visualization of Integral Lines Using Screen Contribution. In *Proc. of Vision, Modeling, Visualization (VMV)*, pages 215–222, 2011.

Y. Guo, R. Sivaramakrishna, C.-C. Lu, J. S. Suri, and S. Laxminarayan. Breast Image Registration Techniques: A Survey. *Medical and Biological Engineering and Computing*, 44 (1-2):15–26, 2006.

S. Hadlak, H. Schumann, C. H. Cap, and T. Wollenberg. Supporting the Visual Analysis of Dynamic Networks by Clustering associated Temporal Attributes. *IEEE Transactions on Visualization and Computer Graphics (TVCG)*, 19(12):2267–2276, 2013.

B. Hakyemez, C. Erdogan, I. Ercan, N. Ergin, S. Uysal, and S. Atahan. High-Grade and Low-Grade Gliomas: Differentiation by Using Perfusion MR Imaging. *Clinical Radiology*, 60 (4):493–502, 2005.

J. Han, M. Kamber, and J. Pei. *Data Mining: Concepts and Techniques*. Morgan Kaufmann, 2011.

E. A. M. Hauth, H. Jaeger, S. Maderwald, C. Stockamp, A. Mühler, R. Kimmig, and M. Forsting. Evaluation of Quantitative Parametric Analysis for Characterization of Breast Lesions in Contrast-Enhanced MR Mammography. *European Radiology*, 16(12):2834–2841, 2006a.

E. A. M. Hauth, C. Stockamp, S. Maderwald, A. Mühler, R. Kimmig, H. Jaeger, J. Barkhausen, and M. Forsting. Evaluation of the Three-Time-Point Method for Diagnosis of Breast Lesions in Contrast-Enhanced MR Mammography. *Clinical Imaging*, 30(3):160–165, 2006b.

E. A. M. Hauth, H. J. Jaeger, S. Maderwald, A. Muehler, R. Kimmig, and M. Forsting. Quantitative 2- and 3-Dimensional Analysis of Pharmacokinetic Model-Derived Variables for Breast Lesions in Dynamic, Contrast-Enhanced MR Mammography. *Eur J Radiol*, 66(2): 300–308, 2008.

C. Hayes, A. R. Padhani, and M. O. Leach. Assessing Changes in Tumour Vascular Function Using Dynamic Contrast-Enhanced Magnetic Resonance Imaging. *NMR Biomed*, 15(2): 154–163, 2002.

P. M. Hayton. *Analysis of Contrast-Enhanced Breast MRI.* PhD thesis, University of Oxford, 1998.

C. Healey, R. Stamant, and J. Chang. Assisted Visualization of E-Commerce Auction Agents. In *Proc. of Graphics Interface*, pages 201–208, 2001.

J. Heinrich and D. Weiskopf. State of the Art of Parallel Coordinates. In *Eurographics 2013-State of the Art Reports*, pages 95–116, 2013.

A. Hennemuth, S. Behrens, C. Kuehnel, S. Oeltze, O. Konrad, and H.-O. Peitgen. Novel Methods for Parameter Based Analysis of Myocardial Tissue in MR-Images. In *Proc. of SPIE Conf. on Medical Image Computing Bd. 6511*, 2007.

S. H. Heywang, A. Wolf, E. Pruss, T. Hilbertz, W. Eiermann, and W. Permanetter. MR Imaging of the Breast with Gd-DTPA: Use and Limitations. *Radiology*, 171(1):95–103, 1989.

S. H. Heywang-Köbrunner. Contrast-Enhanced Magnetic Resonance Imaging of the Breast. *J Investigative Radiology*, 29(1):94–104, 1994.

S. Heywang-Köbrunner and I. Schreer. *Diagnostic Breast Imaging*. TIS, 2001.

P. Hoffman, G. Grinstein, K. Marx, I. Grosse, and E. Stanley. DNA Visual and Analytic Data Mining. In *Proc. of IEEE Visualization*, pages 437–441, 1997.

G. Holmes, A. Donkin, and I.H. Witten. WEKA: A Machine Learning Workbench. In *Proc. of the Australian and New Zealand Conf. on Intelligent Information Systems*, pages 357 –361, 1994.

S. Ingram, T. Munzner, V. Irvine, M. Tory, S. Bergner, and T. Möller. DimStiller: Workflows for Dimensional Analysis and Reduction. In *Proc. of IEEE Visual Analytics Science and Technology (VAST)*, volume 16, pages 3 –10, 2010.

A. Inselberg and B. Dimsdale. Parallel Coordinates: A Tool for Visualizing Multi-Dimensional Geometry. In *Proc. of IEEE Visualization*, pages 361–378, 1990.

International Agency for Research on Cancer. World Cancer Report, 2008.

B. Issa, D. L. Buckley, and L. W. Turnbull. Heterogeneity Analysis of Gd-DTPA Uptake: Improvement in Breast Lesion Differentiation. *J Comput Assist Tomogr*, 23(4):615–621, 1999.

A. K. Jain and R. C. Dubes. *Algorithms for Clustering Data.* Prentice-Hall, Inc., 1988.

A. K. Jain, M. N. Murty, and P. J. Flynn. Data Clustering: A Review. *ACM Computing Surveys (CSUR)*, 31(3):264–323, 1999.

S. A. Jansen, X. Fan, G. S. Karczmar, H. Abe, R. A. Schmidt, M. Giger, and G. M. Newstead. DCE MRI of breast lesions: Is kinetic analysis equally effective for both mass and nonmass-like enhancement? *Medical physics*, 35:3102, 2008.

H. Järnum, E. G. Steffensen, L. Knutsson, E.-T. Fründ, C. W. Simonsen, S. Lundbye-Christensen, A. Shankaranarayanan, D. C. Alsop, F. T. Jensen, and E.-M. Larsson. Perfusion MRI of Brain Tumours: A Comparative Study of Pseudo-Continuous Arterial Spin

Labelling and Dynamic Susceptibility Contrast Imaging. *Neuroradiology*, 52(4):307–317, 2010.

K. Kailing, H.-P. Kriegel, and P. Kröger. Density-Connected Subspace Clustering for High-Dimensional Data. In *Proc. of SIAM Conf. on Data Mining*, pages 246–57, 2004.

W. A. Kaiser and E. Zeitler. MR Imaging of the Breast: Fast Imaging Sequences with and without Gd-DTPA. Preliminary Observations. *Radiology*, 170(3 Pt 1):681–686, Mar 1989.

A. Kanitsar, D. Fleischmann, R. Wegenkittl, P. Felkel, and M. E. Gröller. CPR: Curved Planar Reformation. In *Proc. of IEEE Visualization*, pages 37–44, 2002. ISBN 0-7803-7498-3.

A. Karahaliou, K. Vassiou, N. S. Arikidis, S. Skiadopoulos, T. Kanavou, and L. Costaridou. Assessing Heterogeneity of Lesion Enhancement Kinetics in Dynamic Contrast-Enhanced MRI for Breast Cancer Diagnosis. *British Journal of Radiology*, 83(988):296–306, 2010.

A. Kassner, D. J. Annesley, X. P. Zhu, K. L. Li, I. D. Kamaly-Asl, Y. Watson, and A. Jackson. Abnormalities of the Contrast Re-Circulation Phase in Cerebral Tumors Demonstrated Using Dynamic Susceptibility Contrast-Enhanced Imaging: A Possible Marker of Vascular Tortuosity. *J Magn Reson Imaging*, 11(2):103–113, 2000.

L. Kaufman and P. J. Rousseeuw. *Finding Groups in Data: An Introduction to Cluster Analysis*. Wiley and Sons, 1990.

J. Kehrer and H. Hauser. Visualization and Visual Analysis of Multifaceted Scientific Data: A Survey. *IEEE Transactions on Computers and Graphics*, 19(3):495–513, 2012.

D. A. Keim, F. Mansmann, J. Schneidewind, J. Thomas, and H. Ziegler. Visual analytics: Scope and challenges. In M. H. Böhlen S. J. Simoff and A. Mazeika, editors, *Theory, Techniques and Tools for Visual Analytics. Chapter 6.*, 2008.

C. Kühnel, A. Hennemuth, S. Oeltze, T. Boskamp, S. Krass, B. Preim, and H.-O. Peitgen. New Software Assistents for Cardiovascular Diagnosis. In *Proc. of GI Workshop - Softwareassisten - Computerunterstützung für die medizinische Diagnose und Therapieplanung*, volume 1, pages 491–498, 2006.

M. V. Knopp, F. L. Giesel, H. Marcos, H. von Tengg-Kobligk, and P. Choyke. Dynamic Contrast-Enhanced Magnetic Resonance Imaging in Oncology. *Top Magn Reson Imaging*, 12(4):301–308, 2001.

R. Kohavi and G.H. John. Wrappers for Feature Subset Selection. *Artificial Intelligence*, 97 (1-2):273–324, 1997.

S. Kohle, B. Preim, J. Wiener, and H.-O. Peitgen. Exploration of time-varying data for Medical Diagnosis. In *Proc. of Vision, Modeling, Visualization (VMV)*, pages 31–38, 2002.

R. Kosara, G. N. Sahling, and H. Hauser. Linking Scientific and Information Visualization with Interactive 3D Scatterplots. In *Proc. of Winter School of Computer Graphics (WSCG) Short Communication Papers*, pages 133–140, 2004.

M. Krstajic, E. Bertini, and D. Keim. CloudLines: Compact Display of Event Episodes in Multiple Time-Series. *IEEE Transactions on Visualization and Computer Graphics (TVCG)*, 17 (12):2432–2439, 2011.

C. K. Kuhl. The Current Status of Breast MR Imaging, Part I. *Radiology*, 244(2):356–378, 2007.

C. K. Kuhl and H. H. Schild. Dynamic Image Interpretation of MRI of the Breast. *J Magn Reson Imaging*, 12(6):965–974, 2000.

C. K. Kuhl, H. Bieling, J. Gieseke, T. Ebel, P. Mielcarek, F. Far, P. Folkers, A. Elevelt, and H. H. Schild. Breast Neoplasms: T2* Susceptibility-Contrast, First-Pass Perfusion MR Imaging. *Radiology*, 202(1):87–95, 1997.

C. K. Kuhl, P. Mielcareck, S. Klaschik, C. Leutner, E. Wardelmann, J. Gieseke, and H. H. Schild. Dynamic Breast MR Imaging: Are Signal Intensity Time Course Data Useful for Differential Diagnosis of Enhancing Lesions? *Radiology*, 211(1):101–110, 1999.

M. Law, S. Yang, H. Wang, J. S. Babb, G. Johnson, S. Cha, E. A. Knopp, and D. Zagzag. Glioma Grading: Sensitivity, Specificity, and Predictive Values of Perfusion MR Imaging and Proton MR Spectroscopic Imaging Compared with Conventional MR Imaging. *AJNR*, 24:1989–1998, 2003.

M. Law, S. Yang, J. S. Babb, E. A. Knopp, J. G. Golfinos, D. Zagzag, and G. Johnson. Comparison of Cerebral Blood Volume and Vascular Permeability from Dynamic Susceptibility Contrast-Enhanced Perfusion MR Imaging with Glioma Grade. *AJN*, 25(5):746–755, 2004.

M. Law, R. Young, J. Babb, M. Rad, T. Sasaki, D. Zagzag, and G. Johnson. Comparing Perfusion Metrics Obtained from a Single Compartment Versus Pharmacokinetic Modeling Methods Using Dynamic Susceptibility Contrast-Enhanced Perfusion MR Imaging with Glioma Grade. *AJNR*, 27(9):1975–1982, 2006.

M. Law, R. Young, J. Babb, E. Pollack, and G. Johnson. Histogram Analysis versus Region of Interest Analysis of Dynamic Susceptibility Contrast Perfusion MR Imaging Data in the Grading of Cerebral Gliomas. *American Journal of Neuroradiology*, 28(4):761–766, 2007.

M. Law, R. J. Young, J. S. Babb, N.Peccerelli, S. Chheang, M.L. Gruber, D. C. Miller, J. G. Golfinos, D. Zagzag, and G. Johnson. Gliomas: Predicting Time to Progression or Survival with Cerebral Blood Volume Measurements at Dynamic Susceptibility-weighted Contrast-enhanced Perfusion MR Imaging. *Radiology*, 247(2):490–498, 2008.

C. D. Lehman, S. Peacock, W. B. DeMartini, and X. Chen. A New Automated Software System to Evaluate Breast MR Examinations: Improved Specificity Without Decreased Sensitivity. *American Journal of Roentgenology*, 187(1):51–56, 2006.

M. H. Lev, Y. Ozsunar, J. W. Henson, A. A. Rasheed, G. D. Barest, G. R. Harsh, M. M. Fitzek, E. A. Chiocca, J. D. Rabinov, A. N. Csavoy, B. R. Rosen, F. H. Hochberg, P. W. Schaefer, and R. G. Gonzalez. Glial Tumor Grading and Outcome Prediction Using Dynamic Spin-Echo MR Susceptibility Mapping Compared with Conventional Contrast-Enhanced MR: Confounding Effect of Elevated rCBV of Oligodendroglimoas. *AJN*, 25(2):214–221, 2004.

H. Levkowitz. Color Icons – Merging Color and Texture Perception for Integrated Visualization of Multiple Parameters. In *Proc. of IEEE Visualization*, pages 164–170, 1991.

X. Liang, K. Ramamohanarao, H. Frazer, and Q. Yang. A Lesion Shape and Margin Characterization Method in Dynamic Contrast Enhanced Magnetic Resonance Imaging of the Breast. In *Proc. of Biomedical Imaging*, pages 1783 –1786, 2012.

L. Linsen, T. V. Long, P. Rosenthal, and S. Rosswog. Surface Extraction from Multi-Field Particle Volume Data Using Multi-Dimensional Cluster Visualization. *IEEE Transactions on Visualization and Computer Graphics (TVCG)*, 14(6):1483–1490, 2008.

A. A. Lubischew. On the Use of Discriminant Functions in Taxonomy. *Biometrics*, 18:455 – 477, 1962.

F. A. Lucas-Quesada, U. Sinha, and S. Sinha. Segmentation Strategies for Breast Tumors from Dynamic MR Images. *Journal of Magnetic Resonance Imaging*, 6(5):753–763, 1996.

C. Lundström and A. Persson. Characterizing Visual Analytics in Diagnostic Imaging. In *Proc. of EuroVA: International Workshop on Visual Analytics*, pages 1–4, 2011.

J.M. Lupo, S. Cha, S. M. Chang, and S. J. Nelson. Dynamic Susceptibility-Weighted Perfusion Imaging of High-Grade Gliomas: Characterization of Spatial Heterogeneity. *AJNR*, 26(6): 1446–1454, 2005.

R. Maciejewski, I. Woo, W. Chen, and D. Ebert. Structuring Feature Space: A Non-Parametric Method for Volumetric Transfer Function Generation. *IEEE Transactions on Visualization and Computer Graphics (TVCG)*, 15(6):1473–1480, 2009.

R. Maciejewski, Y. Jang, I. Woo, H. Janicke, K. Gaither, and D. Ebert. Abstracting Attribute Space for Transfer Function Exploration and Design. *IEEE Transactions on Visualization and Computer Graphics (TVCG)*, 19(1):94–107, 2013.

J. MacQueen. Some Methods for Classification and Analysis of Multivariate Observations. In *Proc. of the Berkeley Symposium on Mathematical Statistics and Probability*, volume 1, page 14, 1967.

E. Maguire, P. Rocca-Serra, S.-A. Sansone, J. Davies, and M. Chen. Taxonomy-Based Glyph Design—with a Case Study on Visualizing Workflows of Biological Experiments. *IEEE Transactions on Visualization and Computer Graphics (TVCG)*, 18(12):2603–2612, 2012.

A. Malich, D. R. Fischer, S. Wurdinger, J. Boettcher, C. Marx, M. Facius, and W. A. Kaiser. Potential MRI Interpretation Model: Differentiation of Benign from Malignant Breast Masses. *American Journal of Roentgenology*, 185(4):964–970, 2005.

A. N. Mamelak and D. B. Jacoby. Targeted Delivery of Antitumoral Therapy to Glioma and Other Malignancies with Synthetic Chlorotoxin (TM-601). *Expert Opin Drug Deliv*, 4(2): 175–186, 2007.

H.B. Mann and D.R. Whitney. *On a Test of Whether One of Two Random Variables is Stochastically Larger Than the Other*. Institute of Mathematical Statistics, 1947.

C. Marrocco, M. Molinara, F. Tortorella, P. Rinaldi, L. Bonomo, A. Ferrarotti, C. Aragno, and S. Schiano lo Moriello. Detection of Cluster of Microcalcifications Based on Watershed Segmentation Algorithm. In *Proc. of IEEE Computer-Based Medical Systems (CBMS)*, pages 1–5, 2012.

K. Matkovič, D. Gračanin, Z. Konyha, and H. Hauser. Color Lines View: An Approach to Visualization of Families of Function Graphs. In *Proc. of IEEE Information Visualization (InfoVis)*, pages 59 –64, 2007.

M. Mavroforakis, H. Georgiou, N. Dimitropoulos, D. Cavouras, and S. Theodoridis. Significance Analysis of Qualitative Mammographic Features, Using Linear Classifiers, Neural Networks and Support Vector Machines. *European Journal of Radiology*, 54(1):80–89, 2005.

K. T. McDonnell and K. Mueller. Illustrative Parallel Coordinates. *Computer Graphics Forum*, 27(3):1031–1038, 2008.

K. McPherson, C. M. Steel, and J. M. Dixon. Breast Cancer - Epidemiology, Risk Factors, and Genetics. *British Medical Journal*, 321(7261):624–628, 2000.

M. Mlejnek, P. Ermes, A. Vilanova, R. van der Rijt, H. van den Bosch, F. Gerritsen, and M. E. Gröller. Application-Oriented Extensions of Profile Flags. In *Proc of EuroVis*, pages 339–346, 2006.

B. Moberts, A. Vilanova, and J. J. van Wijk. Evaluation of Fiber Clustering Methods for Diffusion Tensor Imaging. In *Proc. of IEEE Visualization*, pages 65–72, 2005.

F. Montemurro, L. Martincich, I. Sarotto, I. Bertotto, R. Ponzone, L. Cellini, S. Redana, P. Sismondi, M. Aglietta, and D. Regge. Relationship between DCE-MRI Morphological and Functional Features and Histopathological Characteristics of Breast Cancer. *European Radiology*, 17(6):1490–1497, 2007.

S. Mussurakis, D. L. Buckley, and A. Horsman. Dynamic MRI of Invasive Breast Cancer: Assessment of Three Region-Of-Interest Analysis Methods. *J Comput Assist Tomogr*, 21 (3):431–438, 1997.

A. Y. Ng, M. I. Jordan, Y. Weiss, et al. On Spectral Clustering: Analysis and an Algorithm. Chapter 14. In T. Dietterich, S. Becker, and Z. Ghahramani, editors, *Advances in Neural Information Processing Systems*, pages 849–856. MIT Press, 2002.

K. Nie, J.-H. Chen, H. J. Yu, Y. Chu, O. Nalcioglu, and M.-Y. Su. Quantitative Analysis of Lesion Morphology and Texture Features for Diagnostic Prediction in Breast MRI. *Acad Radiol*, 15(12):1513–1525, 2008.

R. Nock and F. Nielsen. Statistical Region Merging. *IEEE Transactions on Pattern Analysis and Machine Intelligence*, 26(11):1452–1458, 2004.

A. Obermair, K. Czerwenka, C. Kurz, A. Kaider, and P. Sevelda. Tumoral Vascular Density in Breast Tumors and Their Effect on Recurrence-Free Survival. *Chirurg*, 65(7):611–615, 1994.

L. O'Donnell and C.-F. Westin. White Matter Tract Clustering and Correspondence in Populations. In *Proc. of Medical Image Computing and Computer-Assisted Intervention (MICCAI)*, pages 140–147, 2005.

S. Oeltze. *Visual Exploration and Analysis of Perfusion Data*. PhD thesis, Otto-von-Guericke-University Magdeburg, 2010.

S. Oeltze, H. Doleisch, H. Hauser, P. Muigg, and B. Preim. Interactive Visual Analysis of Perfusion Data. *IEEE Transactions on Visualization and Computer Graphics (TVCG)*, 13 (6):1392–1399, 2007.

S. Oeltze, A. Hennemuth, S. Glaßer, C. Kühnel, and B. Preim. Glyph-Based Visualization of Myocardial Perfusion Data and Enhancement with Contractility and Viability Information. In *Proc. of the Eurographics Conf. on Visual Computing for Biomedicine (VBCM)*, pages 11–20, 2008a.

S. Oeltze, A. Malyszczyk, and B. Preim. Intuitive Mapping of Perfusion Parameters to Glyph Shape. In *Proc. of Bildverarbeitung für die Medizin*, pages 262–266, 2008b.

S. Oeltze, H. Hauser, J. Rørvik, A. Lundervold, and B. Preim. Visual Analysis of Cerebral Perfusion Data – Four Interactive Approaches and a Comparison. In *Proc. of the Symposium on Image and Signal Processing and Analysis (ISPA)*, pages 588–595, 2009.

H. Ohgaki and P. Kleihues. Epidemiology and Etiology of Gliomas. *Acta Neuropathol*, 109 (1):93–108, 2005.

T. Okafuji, H. Yabuuchi, H. Soeda, Y. Matsuo, T. Kamitani, S. Sakai, M. Hatakenaka, S. Kuroki, E. Tokunaga, H. Yamamoto, and H. Honda. Circumscribed Mass Lesions on Mammography: Dynamic Contrast-Enhanced MR Imaging to Differentiate Malignancy and Benignancy. *Magn Reson Med Sci*, 7(4):195–204, 2008.

L. Østergaard, A. G. Sorensen, K. K. Kwong, R. M. Weisskoff, C. Gyldensted, and B. R. Rosen. High Resolution Measurement of Cerebral Blood Flow Using Intravascular Tracer Bolus Passages. Part II: Experimental Comparison and Preliminary Results. *Magn Reson Med*, 36(5):726–736, 1996a.

L. Østergaard, R. M. Weisskoff, D. A. Chesler, C. Gyldensted, and B. R. Rosen. High Resolution Measurement of Cerebral Blood Flow Using Intravascular Tracer Bolus Passages. Part I: Mathematical Approach and Statistical Analysis. *Magnetic Resonance in Medicine*, 36 (5):715–725, 1996b.

J. E. Perthen, F. Calamante, D. G. Gadian, and A. Connelly. Is Quantification of Bolus Tracking MRI Reliable Without Deconvolution? *Magnetic Resonance in Medicine*, 47(1):61–67, 2002.

H. Piringer, R. Kosara, and H. Hauser. Interactive Focus+Context Visualization with Linked 2D/3D Scatterplots. In *Proc. of IEEE Coordinated and Multiple Views in Exploratory Visualization*, pages 49–60, 2004.

J. Poco, R. Etemadpour, F. V. Paulovich, T. V. Long, P. Rosenthal, M. C. F. Oliveira, L. Linsen, and R. Minghim. A Framework for Exploring Multidimensional Data with 3D Projections. *Computer Graphics Forum*, 30(3):1111–1120, 2011.

B. Preim and C. P. Botha. Visual Exploration and Analysis of Perfusion Data. Online Chapter. In *Visual Computing for Medicine (Morgan Kaufmann Series in Computer Graphics): Theory, Algorithms, and Applications. 2nd Edition.*, 2013.

B. Preim, S. Oeltze, M. Mlejnek, E. Gröller, A. Hennemuth, and S. Behrens. Survey of the Visual Exploration and Analysis of Perfusion Data. *IEEE Transactions on Visualization and Computer Graphics (TVCG)*, 15(2):205–220, 2009.

U. Preim, S. Glaßer, B. Preim, F. Fischbach, and J. Ricke. Computer-aided Diagnosis in Breast DCE-MRI – Quantification of the Heterogeneity of Breast Lesions. *European Journal of Radiology*, 81(7):1532 – 1538, 2012.

J. M. Provenzale, G. R. Wang, T. Brenner, J. R. Petrella, and A. G. Sorensen. Comparison of Permeability in High-Grade and Low-Grade Brain Tumors Using Dynamic Susceptibility Contrast MR Iimaging. *American Journal of Roentgenology*, 178(3):711–716, 2002.

A. J. Quigley. Large Scale 3D Clustering and Abstraction. In *Selected Papers from the Pan-Sydney Workshop on Visualisation*, pages 117–118, 2001.

J. R. Quinlan. *C4.5: Programs for Machine Learning*. Morgan Kaufmann Publishers, 1993.

A. Radjenovic, B. J. Dall, J. P. Ridgway, and M. A. Smith. Measurement of Pharmacokinetic Parameters in Histologically Graded Invasive Breast Tumours Using Dynamic Contrast-Enhanced MRI. *Br J Radiol*, 81(962):120–128, 2008.

K. A. Rempp, G. Brix, F. Wenz, C. R. Becker, F. Gückel, and W. J. Lorenz. Quantification of Regional Cerebral Blood Flow and Volume with Dynamic Susceptibility Contrast-Enhanced MR Imaging. *Radiology*, 193(3):637–641, 1994.

E. Rendón, I. Abundez, A. Arizmendi, and E. Quiroz. Internal versus External Cluster Validation Indexes. *International Journal of Computers and Communications*, 5(1):27–34, 2011.

H. C. Roberts, T. P. L. Roberts, R. C. Brasch, and W. P. Dillon. Quantitative Measurement of Microvascular Permeability in Human Brain Tumors Achieved Using Dynamic Contrast-Enhanced MR Imaging: Correlation with Histologic Grade. *American Journal of Neuroradiology*, 21(5):891–899, 2000.

T. Rohlfing, C. R. Maurer Jr, D. A. Bluemke, and M. A. Jacobs. Volume-Preserving Nonrigid Registration of MR Breast Images Using Free-Form Deformation with an Incompressibility Constraint. *IEEE Transactions on Medical Imaging*, 22(6):730–741, 2003.

B. R. Rosen, J. W. Belliveau, J. M. Vevea, and T. J. Brady. Perfusion Imaging with NMR Contrast Agents. *Magnetic Resonance in Medicine*, 14(2):249–265, 1990.

D. Rueckert, L. Sonoda, C. Hayes, D. L. G. Hill, M. O. Leach, and D. J. Hawkes. Non-rigid Registration Using Free-Form Deformations: Application to Breast MR Images. *IEEE Trans Med Imaging*, 18(8):712–721, 1999.

S. Salvador and P. Chan. Determining the Number of Clusters/Segments in Hierarchical Clustering/Segmentation Algorithms. In *Proc. of IEEE Tools with Artificial Intelligence (ICTAI)*, pages 576–584, 2004.

H. Sanftmann and D. Weiskopf. Illuminated 3D Scatterplots. *Computer Graphics Forum*, 28 (3):751–758, 2009.

A. J. Sasco, A. B. Lowenfels, and P. P.-D. Jong. Review Article: Epidemiology of Male Breast Cancer. A Meta-Analysis of Published Case-Control Studies and Discussion of Selected Aetiological Factors. *International Journal of Cancer*, 53(4):538–549, 1993.

S. Schäfer, U. Preim, S. Glaßer, B. Preim, and K. D. Tönnies. Local Similarity Measures for Lesion Registration in DCE-MRI of the Breast. *The Annals of the British Machine Vision Association and Society for Pattern Recognition (BMVA)*, 3:1–13, 2011.

M. D. Schnall, J. Blume, D. A. Bluemke, G. A. DeAngelis, N. DeBruhl, S. Harms, S. H. Heywang-Köbrunner, N. Hylton, C. K. Kuhl, E. D. Pisano, P. Causer, S. J. Schnitt, D. Thickman, C. B. Stelling, P. T. Weatherall, C. Lehman, and C. A. Gatsonis. Diagnostic Architectural and Dynamic Features at Breast MR Imaging: Multicenter Study. *Radiology*, 238(1): 42–53, 2006.

T. Schultz and G. L Kindlmann. Open-Box Spectral Clustering: Applications to Medical Image Analysis. *IEEE Transactions on Visualization and Computer Graphics (TVCG)*, 19 (12):2100–2108, 2013.

H. Schumann and W. Müller. *Visualisierung: Grundlagen und Allgemeine Methoden*. Springer, 2000.

J. H. Shin, H. Kyu Lee, B. Duk Kwun, J.-S. Kim, W. Kang, C. Gon Choi, and D. Chul Suh. Using Relative Cerebral Blood Flow and Volume to Evaluate the Histopathologic Grade of Cerebral Gliomas: Preliminary Results. *American Journal of Roentgenology*, 179:783–789, 2002.

S. Sinha, F. A. Lucas-Quesada, N. D. Debruhl, J. Sayre, D. Farria, D. P. Gorczyca, and L. W. Bassett. Multifeature Analysis of Gd-Enhanced MR Images of Breast Lesions. *Journal of Magnetic Resonance Imaging*, 7(6):1016–1026, 1997.

L. H. Sobin and C. H. Wittekind. UICC TNM Classification of Malignant Tumours. 6th Ed., 2002.

B. Speckmann and K. Verbeek. Necklace Maps. *IEEE Transactions on Visualization and Computer Graphics (TVCG)*, 16(6):881–889, 2010.

M.D. Steenwijk, J. Milles, M.A. Buchem, J.H. Reiber, and C.P. Botha. Integrated Visual Analysis for Heterogeneous Datasets in Cohort Studies. In *IEEE VisWeek Workshop on Visual Analytics in Health Care*, 2010.

G. N. Stewart. Researches on the Circulation Time in Organs and on the Influences which Affect It, Part I-III. *J Physiol*, 15:1–89, 1894.

M. J. Stoutjesdijk, J. J. Fütterer, C. Boetes, L. E. van Die, G. Jager, and J. O. Barentsz. Variability in the Description of Morphologic and Contrast Enhancement Characteristics of Breast Lesions on Magnetic Resonance Imaging. *Investigative Radiology*, 40(6):355–362, 2005.

C. Studholme, D. L. G. Hill, and D. J. Hawkes. An Overlap Invariant Entropy Measure of 3D Medical Image Alignment. *Pattern Recognition*, 32(1):71–86, 1999.

R. Stupp, W. P. Mason, M. J. van den Bent, M. Weller, B. Fisher, M. J. B. Taphoorn, K. Belanger, A. A. Brandes, C. Marosi, U. Bogdahn, J. Curschmann, R. C. Janzer, S. K. Ludwin, T. Gorlia, A. Allgeier, D. Lacombe, J. G. Cairncross, E. Eisenhauer, and R. O. Mirimanoff. Radiotherapy Plus Concomitant and Adjuvant Temozolomide for Glioblastoma. *N Engl J Med*, 352(10):987–996, 2005.

T. Sugahara, Y. Korogi, M. Kochi, Y. Ushio, and M. Takahashi. Perfusion-Sensitive MR Imaging of Gliomas: Comparison Between Gradient-Echo and Spin-Echo Echo-Planar Imaging Techniques. *AJNR Am J Neuroradiol*, 22(7):1306–1315, 2001.

J. S. Suri, A. X. Falcao, L. Reden, and S. Laxminarayan. *Review on Real-Time Magnetic Resonance GAD-Enhanced Breast Lesion Characterization*, volume 155, chapter 23, pages 764 – 785. SPIE press, 2006.

B. K. Szabo, P. Aspelin, M. K. Wiberg, and B. Bone. Dynamic MR Imaging of the Breast. Analysis of Kinetic and Morphologic Diagnostic Criteria. *Acta Radiolgoica*, 44:379 – 386, 2003.

P.-N. Tan, M. Steinbach, and V. Kumar. *Introduction to Data Mining*. Pearson/Addison-Wesley: Boston (MA), 2006.

A. Tatu, F. Maas, I. Farber, E. Bertini, T. Schreck, T. Seidl, and D. Keim. Subspace Search and Visualization to Make Sense of Alternative Clusterings in High-Dimensional Data. In *Proc. of IEEE Visual Analytics Science and Technology (VAST)*, pages 63–72, 2012.

F. A. Tavassoli and P. Devilee. *Pathology and Genetics of Tumours of the Breast and Female Genital Organs*, volume 4. World Health Organization, 2003.

The Robert Koch-Institute. Krebs in Deutschland 2007/2008. *Robert Koch-Institut (Hrsg) und die Gesellschaft der epidemiologischen Krebsregister in Deutschland e.V. (Hrsg)*, 8, 2012.

H. Theisel. Higher Order Parallel Coordinates. In *Proc. of Vision, Modeling, and Visualization (VMV)*, pages 415–420, 2000.

H. K. Thompson, Jr, C. F. Starmer, R. E. Whalen, and H. D. McIntosh. Indicator transit time considered as a gamma-variate. *Circ Res*, 14:502–515, 1964.

P. Tiwari, M. Rosen, and A. Madabhushi. A Hierarchical Spectral Clustering and Nonlinear Dimensionality Reduction Scheme For Detection of Prostate Cancer from Magnetic Resonance Spectroscopy (MRS). *Medical Physics*, 36:3927, 2009.

P. S. Tofts and A. G. Kermode. Measurement of the Blood-Brain Barrier Permeability and Leakage Space Using Dynamic MR Imaging. 1. Fundamental Concepts. *Magn Reson Med*, 17(2):357–367, 1991.

P. S. Tofts, B. Berkowitz, and M. D. Schnall. Quantitative Analysis of Dynamic Gd-DTPA Enhancement in Breast Tumors Using a Permeability Model. *Magn Reson Med*, 33(4): 564–568, 1995.

P. S. Tofts, G. Brix, D. L. Buckley, J. L. Evelhoch, E. Henderson, M. V. Knopp, H. B. Larsson, T. Y. Lee, N. A. Mayr, G. J. Parker, R. E. Port, J. Taylor, and R. M. Weisskoff. Estimating Kinetic Parameters from Dynamic Contrast-Enhanced T(1)-Weighted MRI of a Diffusable Tracer: Standardized Quantities and Symbols. *J Magn Reson Imaging*, 10(3):223–232, 1999.

K. D. Tönnies, A. Celler, S. Blinder, T. Möller, and R. Harrop. Scatter Segmentation in Dynamic SPECT Images Using Principal Component Analysis. In *Proc. of SPIE*, pages 507–516, 2003.

C. Turkay, P. Filzmoser, and H. Hauser. Brushing Dimensions - A Dual Visual Analysis Model for High-Dimensional Data. *IEEE Transactions on Visualization and Computer Graphics (TVCG)*, 17(12):2591–2599, 2011a.

C. Turkay, J. Parulek, N. Reuter, and H. Hauser. Interactive Visual Analysis of Temporal Cluster Structures. *Computer Graphics Forum*, 30(3):711–720, 2011b.

M. J. van Osch, E. J. Vonken, C. J. Bakker, and M. A. Viergever. Correcting Partial Volume Artifacts of the Arterial Input Function in Quantitative Cerebral Perfusion MRI. *Magn Reson Med*, 45(3):477–485, 2001.

A. Villringer, B. R. Rosen, J. W. Belliveau, J. L. Ackerman, R. B. Lauffer, R. B. Buxton, Y. S. Chao, V. J. Wedeen, and T. J. Brady. Dynamic Imaging with Lanthanide Chelates in Normal Brain: Contrast Due to Magnetic Susceptibility Effects. *Magn Reson Med*, 6(2):164–174, 1988.

H. Völzke, D. Alte, C. O. Schmidt, D. Radke, R. Lorbeer, N. Friedrich, N. Aumann, K. Lau, M. Piontek, G. Born, C. Havemann, T. Ittermann, S. Schipf, R. Haring, S. E. Baumeister, H. Wallaschofski, M. Nauck, S. Frick, A. Arnold, M. Junger, J. Mayerle, M. Kraft, M. M. Lerch, M. Dorr, T. Reffelmann, K. Empen, S. B. Felix, A. Obst, B. Koch, S. Glaser, R. Ewert, I. Fietze, T. Penzel, M. Doren, W. Rathmann, J. Haerting, M. Hannemann, J. Ropcke,

U. Schminke, C. Jurgens, F. Tost, R. Rettig, J. A. Kors, S. Ungerer, K. Hegenscheid, J. P. Kuhn, J. Kuhn, N. Hosten, R. Puls, J. Henke, O. Gloger, A. Teumer, G. Homuth, U. Volker, C. Schwahn, B. Holtfreter, I. Polzer, T. Kohlmann, H. J. Grabe, D. Rosskopf, H. K. Kroemer, T. Kocher, R. Biffar, U. John, and W. Hoffmann. Cohort Profile: The Study of Health in Pomerania. *International Journal of Epidemiology*, 40(2):294–307, 2011.

U. Von Luxburg. A Tutorial on Spectral Clustering. *Statistics and Computing*, 17(4):395–416, 2007.

K. Wagstaff, C. Cardie, S. Rogers, and S. Schrödl. Constrained k-Means Clustering with Background Knowledge. In *Proc. of Machine Learning*, volume 1, pages 577–584, 2001.

J. Walker, Z. Geng, M. W. Jones, and R. S. Laramee. Visualization of Large, Time-Dependent, Abstract Data with Integrated Spherical and Parallel Coordinates. *EuroVis–Short Papers*, pages 43–47, 2012.

W. Wang, J. Yang, and R. Muntz. STING: A Statistical Information Grid Approach to Spatial Data Mining. In *Proc. of Very Large Data Bases (VLDB)*, pages 186–195, 1997.

J. H. Ward. Hierarchical Grouping to Optimize an Objective Function. *Journal of the American Statistical Association*, 58(301):236–244, 1963.

U. Wedegärtner, U. Bick, K. Wörtler, E. Rummeny, and G. Bongartz. Differentiation Between Benign and Malignant Findings on MR-Mammography: Usefulness of Morphological Criteria. *Eur Radiol*, 11(9):1645–1650, 2001.

R. Wegenkittl, H. Löffelmann, and E. Gröller. Visualizing the Behaviour of Higher Dimensional Dynamical Systems. In *Proc. of IEEE Visualization*, pages 119 –125, 1997.

R. M. Weisskoff, C. S. Zuo, J. L. Boxerman, and B. R. Rosen. Microscopic Susceptibility Variation and Transverse Relaxation: Theory and Experiment. *Magn Reson Med*, 31(6): 601–610, 1994.

S. G. Wetzel, S. Cha, G. Johnson, P. Lee, M. Law, D. L. Kasow, S. D. Pierce, and X. Xue. Relative Cerebral Blood Volume Measurements in Intracranial Mass Lesions: Interobserver and Intraobserver Reproducibility Study. *Radiology*, 224(3):797–803, 2002.

J. I. Wiener, K. J. Schilling, C. Adami, and N. A. Obuchowski. Assessment of Suspected Breast Cancer by MRI: A Prospective Clinical Trial Using a Combined Kinetic and Morphologic Analysis. *American Journal of Roentgenology*, 184(3):878–886, 2005.

T. C. Williams, W. B. DeMartini, S. C. Partridge, S. Peacock, and C. D. Lehman. Breast MR Imaging: Computer-aided Evaluation Program for Discriminating Benign from Malignant Lesions. *Radiology*, 244(1):94–103, 2007.

P. C. Wong and R. D. Bergeron. 30 Years of Multidimensional Multivariate Visualization. In Hagan H. Nielson, G. M. and H. Muller, editors, *Scientific Visualization - Overviews, Methodologies, and Techniques*, pages 3–33. IEEE Computer Society Press, 1997.

X. Xu, N. Yuruk, Z. Feng, and T. A. J. Schweiger. SCAN: A Structural Clustering Algorithm for Networks. In *Proc. of the ACM SIGKDD Conf. on Knowledge Discovery and Data Mining*, pages 824–833, 2007.

Y. Yang, J. X. Chen, and W. Kim. Gene Expression Clustering and 3D Visualization. *Computing in Science and Engg.*, 5(5):37–43, 2003.

H. Younesy, C. B. Nielsen, T. Möller, O. Alder, R. Cullum, M. C. Lorincz, M. M. Karimi, and S. J. M. Jones. An Interactive Analysis and Exploration Tool for Epigenomic Data. *Computer Graphics Forum*, 32(3):91–100, 2013.

S. Zachow, P. Muigg, T. Hildebrandt, H. Doleisch, and H.-C. Hege. Visual Exploration of Nasal Airflow. *IEEE Transactions on Visualization and Computer Graphics (TVCG)*, 15 (6):1407–1414, 2009.

L. Zelnik-Manor and P. Perona. Self-Tuning Spectral Clustering. In *Proc. of Advances in Neural Information Processing Systems*, pages 1601–1608, 2004.

L. Zhang, X. Liu, and W. Sheng. 3D Visualization of Gene Clusters. *Computer Vision and Graphics*, pages 349–354, 2006.

J. Zhao, F. Chevalier, E. Pietriga, and R. Balakrishnan. Exploratory Analysis of Time-Series with ChronoLenses. *IEEE Transactions on Visualization and Computer Graphics (TVCG)*, 17(12):2422–2431, 2011.

L. Zhao, C. P. Botha, J. O. Bescos, R. Truyen, F. M. Vos, and F. H. Post. Lines of Curvature for Polyp Detection in Virtual Colonoscopy. *IEEE Transactions on Visualization and Computer Graphics (TVCG)*, 12(5):885–892, 2006.

Q. Zhao, M. Xu, and P. Fränti. Sum-of-Squares Based Cluster Validity Index and Significance Analysis. In *Adaptive and Natural Computing Algorithms*, pages 313–322. Springer, 2009.

F. G. Zöllner, R. Sance, P. Rogelj, M. J. Ledesma-Carbayo, J. Rørvik, A. Santos, and A. Lundervold. Assessment of 3D DCE-MRI of the Kidneys Using Non-Rigid Image Registration and Segmentation of Voxel Time Courses. *Computerized Medical Imaging and Graphics*, 33(3):171–181, 2009.

Nomenclature

#CCI	Number of Correctly Classified Instances
3TP	Three-Time-Point
AIF	Arterial Input Function
BBB	Blood-Brain Barrier
CBF	Cerebral Blood Flow
CBV	Cerebral Blood Volume
CTC	Concentration-time curve
DCE-MRI	Dynamic Contrast-Enhanced Magnetic Resonance Imaging
DSC-MRI	Dynamic Susceptibility Contrast Magnetic Resonance Imaging
LCC	Local Correlation Coefficient
MPR	Multiplanar Reformation
MR	Magnetic Resonance
MRI	Magnetic Resonance Imaging
MSRegion	Most Suspect Region
MTT	Mean Transit Time
PCA	Principal Component Analysis
PE	Peak Enhancement
rCBF	Relative Cerebral Blood Flow
rCBV	Relative Cerebral Blood Volume
RE	Relative Enhancement
ROC	Receiver Operating Characteristic
ROI	Region of Interest
TIC	Time-intensity Curve
TTP	Time to Peak
XRM	X-Ray Mammography